ELECTROCHEMICAL EVALUATION OF SURFACTANTS RELEVANT TO LIGAND STABILIZED NANOPARTICLES

A Thesis Submitted to the College of

Graduate Studies and Research

In Partial Fulfillment of the Requirements

For the Degree of Doctor of Philosophy

In the Department of Chemistry

University of Saskatchewan

Saskatoon

By

VIVEK JAYAVALLI PADMANABHAN

Permission to Use

In presenting this thesis in partial fulfilment of the requirements for a Postgraduate degree from the University of Saskatchewan, I agree that the Libraries of this University may make it freely available for inspection. I further agree that permission for copying of this thesis in any manner, in whole or in part, for scholarly purposes may be granted by the professor or professors who supervised my thesis work or, in their absence, by the Head of the Department or the Dean of the College in which my thesis work was done. It is understood that any copying or publication or use of this thesis or parts thereof for financial gain shall not be allowed without my written permission. It is also understood that due recognition shall be given to me and to the University of Saskatchewan in any scholarly use which may be made of any material in my thesis.

Requests for permission to copy or to make other use of material in this thesis in whole or part should be addressed to:

Head of the Department of Chemistry

University of Saskatchewan

Saskatoon, Saskatchewan (S7N 5C9)

Canada

ABSTRACT

A very good understanding of nanoparticle-ligand interactions is a key step toward obtaining mechanistic insight into the formation of ligand protected metal nanoparticles and their stability. Since a direct investigation of the processes happening at the nanoparticle/solution interface is practically very difficult, an alternative approach is desirable. The use of interfacial electrochemistry is very promising for this purpose as the ligand interactions on an electrode surface is analogous to those occurring on a nanoparticle surface and, importantly, they can be quantified using the thermodynamics of ideally polarizable electrodes. An attempt to explain certain phenomena in the nanoparticle domain with the help of interfacial electrochemistry is the underlying theme of this thesis. This thesis is primarily focused on two main projects; (1) halide induced aggregation of 4-dimethylaminopyridine (DMAP) stabilized gold nanoparticles and (2) addressing the popular perception concerning the growth mechanism of quaternary ammonium surfactant stabilized gold nanorods.

Halide induced aggregation of DMAP monolayer protected gold nanoparticles is investigated by studying the electrochemical adsorption of DMAP and halide ions on analogous gold electrode surfaces. A quantitative evaluation of the adsorbed species on the electrode surface is provided using the thermodynamics of ideally polarized electrodes and the results explain observations made in the nanoparticle domain. Additionally, a quantitative evaluation of the pH dependent adsorption of dimethylaminopyridine on Au(111) surface is discussed to provide a better understanding of the adsorption behavior of this molecule on gold surfaces.

Interest in quaternary ammonium surfactant adsorption on gold surfaces stems from the unique capability of quaternary ammonium bromide surfactants to facilitate one dimensional

growth of gold nanorods. The current perception on the mechanism of gold nanorod growth is that anisotropy results from the preferential adsorption of this surfactant on different facets of the nanoparticle seed crystal. A systematic evaluation of quaternary ammonium bromide adsorption on different crystal planes of gold is provided to evaluate this popular postulate. As the low index (100) and (111) crystal planes are the most pertinent to these nanorod growth mechanisms, single crystal electrodes with these crystallographic surfaces have been prepared for this investigation. The quaternary ammonium surfactant chosen is octyltrimethylammonium with a nonspecifically adsorbing triflate counterion. An electrochemical evaluation of the adsorption behavior of this surfactant on the respective crystal planes in the absence of any other specifically adsorbing species is provided as an initial survey. Subsequently, a quantitative evaluation of quaternary ammonium bromide adsorption on these crystal planes is also discussed. Accordingly, this project is divided into three major sections for detailed analysis. (1) An electrochemical evaluation of quaternary ammonium triflate adsorption on Au(100) surfaces with an emphasis on surface reconstruction phenomena. (2) An electrochemical evaluation of octyltrimethylammonium triflate (OTA-Tf) adsorption on the Au(111) electrode, highlighting the adsorbate structure and potential induced phase transitions within the adlayer. (3) The effect of bromide on the adsorption behavior of quaternary ammonium surfactant and the relative adsorption of quaternary ammonium bromide on Au(111) and Au(100) surfaces. This last section addresses the popular perception on the mechanism of gold nanorod growth.

ACKNOWLEDGEMENTS

First and foremost, I would like to express my gratitude to Dr. Ian J. Burgess for his immense support and guidance throughout the course of my Ph.D. project.

I would like to extend my appreciation to the members of my advisory committee, Prof. Andrzej Baranski, Dr. Robert Scott and Dr. Aaron Phoenix for their valuable suggestions. I am also very thankful to my examination committee members, Dr. Matthew Paige and Dr. Richard Bowles. Special thanks to my external examiner, Dr. Byron Gates, for his valuable comments and suggestions.

I would like to thank Dr. Shawn Wettig (Pharmacy department) for assistance with Zeta potential measurements, Ms. Sarah Caldwell (Western College of Veterinary Medicine) for TEM training, and Scott Group for the use of UV-vis spectrometer.

My sincere thanks to University of Saskatchewan and the department of chemistry for giving me an opportunity to pursue my Ph.D. research with scholarships and teaching assistantship. I also acknowledge financial support from the Natural Sciences and Engineering Research Council of Canada.

I need to thank all the former and present members of Burgess Group for creating a very good working atmosphere in the lab: Wenbin, Scott, Tyler, Brook, Michelle, Burke, Charlsie, Melanie, Gage, Samuel, Heather, Krysta, Cheryl and Kevin. I would like to express my appreciation to other faculty, staff and students who helped me one way or another. Special thanks to Dr. Alexandra Bartole-Scott and Dr. Valarie MacKenzie.

Finally, my deepest appreciation to my friends, parents, sister and other family members for their unwavering love and support.

DEDICATIONS

This thesis is dedicated to all my teachers.

TABLE OF CONTENTS

LIST OF FIGURES

LIST OF TABLES

LIST OF SYMBOLS AND ABBREVIATIONS

ε	Dielectric permittivity
κ^{-1}	Debye length
π	Surface pressure
θ	Angle
Θ	Surface coverage
λ	Wavelength
μ	Chemical potential
ζ	Zeta potential
Γ	Gibbs surface excess
ω	Angular frequency
γ	Surface tension
ϕ_2	Surface potential (electrochemistry)
ψ_o	Surface potential (colloid chemistry)
ΔG^0_{ads}	Standard Gibbs energy of adsorption
ε_o	Permittivity of free space
ε_r	Static relative permittivity
E_{ac}	Root mean square voltage
q_d	Charge density in the diffused layer
q_i	Charge density in the inner layer
q_s	Excess charge density on the solution side

σ_m	Metal charge density
A	Surface area
ac	Alternating current
AFM	Atomic Force Microscopy
c	Concentration
C	Capacitance
C_H	Helmholtz capacitance
cmc	Critical micellar concentration
CTA-Br	Cetyltrimethylammonium bromide
CV	Cyclic Voltammetry
DC	Differential Capacity
dc	Direct current
DDAP	Dodecyl-N,N-dimethyl-3-ammonio-propanesulfonate
DeTaTf	N-Decyl-N,N,N-trimethylammonium Triflate
DMAP	4-(N,N-dimethylamino)pyridine
DMAP(H^+)	Dimethylaminopyridine and/or Dimethylaminopyridinium
$DMAPH^+$	4-(N,N-dimethylamino)pyridinium
E	Electrode potential
e	Charge of an electron
EC-AFM	Electrochemical Atomic Force Microscopy
EC-STM	Electrochemical Scanning Tunneling Microscopy
E_{pzc}	Potential of zero charge
F	Faraday constant

G	Gibbs function
h	Planck's constant
hex	Hexagonal surface (reconstructed Au(100) surface)
HRTEM	High Resolution Transmission Electron Microscopy
I	Current
IHP	Inner Helmholtz plane
k	Boltzmann constant
LEED	Low Energy Electron Diffraction
MPN	Monolayer Protected Nanoparticle
NMR	Nuclear Magnetic Resonance
OHP	Outer Helmholtz plane
OTA^+	N-octyl-N,N,N-trimethylammonium cation
OTA-Tf	N-octyl-N,N,N-trimethylammonium triflate
pzc	Potential of zero charge
Q	Imaginary component
QELS	Quasi-elastic light scattering
R	Molar gas constant
Ŕ	Real component
RAS	Reflection absorption Spectroscopy
SAED	Selected Area Electron Diffraction
SCE	Saturated Calomel Electrode
SDS	Sodium Dodecyl Sulfate
SEIRAS	Surface Enhanced Infrared Absorption Spectroscopy

SERS	Surface Enhanced Raman Scattering
SPM	Scanning Probe Microscopy
SPR	Surface Plasmon Resonance
STM	Scanning Tunneling Microscopy
T	Absolute temperature
TEM	Transmission Electron Microscopy
TOAB	Tetraoctylammonium bromide
UHV	Ultra High Vacuum
UV-vis	Ultraviolet-visible
V	Voltage
Z	Impedance
Z_i	Valency of ionic species

Chapter 1

1.1 Introduction

An interface is a point or a boundary at which two independent phases interact. The formation of a nanoparticle in solution implies the formation of a new phase within solution, hence an interface. For metal nanoparticles synthesized by wet chemical routes, the interface is that of the metal and the solution. The stability, size and shape of the nanoparticle is determined by the energetics at the nanoparticle interface. At the nanoparticle size regime (1-100 nm), gravity becomes negligible, and van der Waals forces become prominent, causing the nanoparticles in Brownian motion to aggregate. For stable colloids, the attractive forces are opposed by electrostatic repulsive forces, derived from the charge that is developed on the surface for a solid phase dispersed in a polar solvent or an electrolyte solution. For noble metal nanoparticles, the magnitude of van der Waals forces of attraction is relatively large and hence electrostatic repulsion alone cannot prevent aggregation. The presence of ligands at the interface offers additional stability by steric hindrance for metal nanoparticles. These stabilizing ligands are usually organic molecules, and a prerequisite for these molecules is that they should selectively partition at the nanoparticle/solution interface. Consequently, most of the popular metal nanoparticles stabilizing ligands are surfactants; the terms surfactant and ligand are interchangeably used in this thesis.

The nature of the ligand present in the medium, during the nanoparticle synthesis plays a significant role in determining the size and shape of the nanoparticles formed. A good understanding of the nanoparticles' stability, size and shape selectivity can be

obtained with a thorough understanding of the nanoparticle/solution interface and the interaction of the nanoparticle surface with the adsorbed molecule (surfactant/ligand). While a direct evaluation of the interactions of the stabilizing ligands at the nanoparticle interface is challenging due to the limitations because of the smaller size of the nanoparticle, an alternative approach is to study the interactions of these ligands with an analogous macro-surface. Solid surfaces in solutions are usually charged and this surface charge also has a significant influence on the behavior of the surfactant at the nanoparticle interface. Modern electrochemistry provides an excellent platform to study the behavior of molecules at the electrode/solution interface as a function of the charge or electrical potential at the interface. Adsorption of molecules on noble metal surfaces has been widely studied using electrochemical methods over the past several decades, and the theory and methodologies to extract qualitative and quantitative information about adsorbed molecular layers has been well developed over this period.[1-3] In fact, the strategy followed for one of the original gold nanoparticle synthesis protocols was inspired by the knowledge of a stable self-assembled monolayer of alkyl thiol molecules on planar gold surfaces (the terms two dimensional and three-dimensional surfaces are often used in this thesis as convenient short forms representing planar electrode surfaces and nanoparticle surfaces respectively).[4] Clearly, contemporary nanoparticle research can benefit from deeper understanding of the behavior of organic stabilizers on the nanoparticles surfaces.

In this thesis, an electrochemical evaluation of the adsorption behavior of surfactants relevant to gold nanoparticles is discussed. The strategy is to use information obtained from experiments using two-dimensional electrode surfaces to understand the

behavior of molecules on nanoparticle surfaces and to explain certain observations made in the nanoparticle domain.

1.2 Objectives

The following objectives, which reflect different aspects related to nanoparticle stability and structure selectivity, were pursued by studying the adsorption behavior of the surfactant on analogous gold surfaces:

1. To investigate the halide induced aggregation of 4-dimethylaminopyridine (DMAP) stabilized gold nanoparticles by studying the halide-DMAP co-adsorption /competitive adsorption on polycrystalline gold electrodes.
2. To evaluate the influence of surface crystallography and solution pH on the adsorption behavior of DMAP on gold by studying the electrochemical adsorption of DMAP on Au(111) surface.
3. To check the validity of the existing theory on the mechanism of quaternary ammonium bromide stabilized gold nanorod formation by studying the adsorption behavior of quaternary ammonium surfactants in the presence of bromide on Au(111) and Au(100) single crystal surfaces.

1.3 Research Background and Literature Review

The term surfactant (surface active agent) is attributed to those components that accumulate at the interface even at very low bulk concentrations, typically on the order of micro-molar or less. According to classical theory of surfactants, an organic molecule

that behaves as a surfactant in water consists of both hydrophobic and hydrophilic groups.[5] The hydrophilic (polar) group retains the molecule in the aqueous (polar) medium, while the hydrophobic (nonpolar) group determines the molecule's tendency to partition from the aqueous (polar) medium to a relatively less polar medium. Surfactants can be ionic, nonionic or zwitterionic, depending on the type of the hydrophilic group of the molecule. As its name implies, a nonionic surfactant has no charge. An ionic surfactant dissociates into ions upon dissolving in water; the component having amphiphilic nature shows surface activity while the other ions called counter ions typically have very little to no surface activity. If it is the anionic part of the surfactant that is surface active, the surfactant is called anionic and in the opposite case the surfactant is termed cationic. While dissociated organic acids and their salts are anionic, bases such as amines having different degrees of alkylation are cationic in nature upon protonation. If the surfactant contains a headgroup with two opposite charges held together, thus making the molecule electrically neutral overall, it is termed zwitterionic.

From a thermodynamic point of view, surfactants in solution partition to an interface in order to reduce the overall free energy of the system by reducing the interfacial energy (lowering surface tension) and by attenuating the interaction of the hydrophobic group with the hydrophilic solvent. At the critical micellar concentration (cmc), the energy of the interface (surface tension) becomes sufficiently low that the interaction of hydrophobic parts of the surfactant with the polar medium is further decreased by the spontaneous self-assembly of the hydrophobic parts of the surfactant molecules, leading to the formation of "micelles". While most surfactants form geometrically well defined micelles, the ability to form a micelle is not the essential

criterion for a molecule to be termed as a surfactant. The spontaneous aggregation of surfactants into micelles in aqueous solution was first proposed by McBain in 1913.[6] Since then, micellization in solution has been investigated using a variety of spectroscopic techniques and hence the concept of micelle formation in the bulk solution is well understood in terms of structure and energetics. An analogous aggregation behavior of the surfactant at the solid/liquid interfaces was proposed by Fuerstenau and Gaudin in 1955[7,8] and further developments of this postulate were made in their following papers.[9-14] The aggregates formed in the bulk of solution (micelles) can be adsorbed at the solid/liquid interface to form surface aggregates, but more interestingly, even at concentrations well below the cmc of the surfactant, molecules adsorbed at the solid/liquid interface nucleate to form geometrically well defined surface aggregates.[15-17] The structure of these aggregates and the orientation of the molecules itself is often determined by the energetics (or surface charge) of the solid phase, a detailed description of which will be given in the relevant chapters of this thesis.

Empirical models to study the aggregation of surfactants in solution have been proposed by many researchers.[18-20] The invention of scanning probe microscopy promoted a significant breakthrough in the area of surfactant adsorption at the solid/liquid, providing direct visualization of the surfactant aggregates on the surface.[21,22] While the major advantage of the scanning probe based techniques is the direct visualization of the aggregate structures, interaction of the scanning probe with the aggregate structure can be of serious concern.[23,24] The use of an electrified interface i.e., an electrode/electrolyte interface that helps to manipulate the structure of the adsorbed

species by controlling the electric state of the interface provides useful information about the nature of adsorbate/substrate and adsorbate-adsorbate interactions.

Most of the past knowledge concerning the adsorption at the electrode/electrolyte interface came from the thermodynamic studies at the mercury/electrolyte interface.[25] The essential requirement for thermodynamic analysis at the metal/electrolyte interface is that the electrode should behave as an ideally polarizable electrode under the given experimental conditions,[1,25] i.e., the electrode and electrolyte forming the interface behave as an electronic and a dielectric continuum to provide a capacitive interface. For a long time, the thermodynamic measurements performed on solid electrode interfaces were beleaguered by problems related to the surface cleanliness and reproducibility of the surface morphology. For solid electrodes except noble metals, electrode dissolution and hydrogen adsorption/evolution processes restrict their use as ideally polarized electrodes. The development of the flame annealing treatment of noble metal electrodes provided a simple method to generate clean, reliable surfaces with reproducible surface crystallography.[26] Among the noble metal electrodes, the low index surfaces of gold are well known to display ideal or nearly ideal polarizable behavior for a range of potentials that exceed one volt or an equivalent range of surface charge densities that spans ~100 $\mu C/cm^2$. A quantitative analysis of the adsorbates at the interface using thermodynamic treatments of the adsorption process at the liquid electrode (e.g. mercury) /electrolyte interface were based on differential capacity measurements and subsequent integration to obtain charge and surface pressure. Extending this approach to solid electrode interfaces becomes erroneous as the equilibrium capacitance cannot be measured because of the slow kinetics of potential induced surface reconstruction phenomena. Lipkowski and co-

workers developed a chronocoulometric technique for the determination of the equilibrium charge density at the electrode/electrolyte interface that can be applied for a quantitative analysis of processes happening at the solid electrode interface.[27] Consequently, the thermodynamic data measured for a solid electrode interface, particularly for gold electrodes turns out to be nearly as precise as those for mercury/electrolyte interface.[28] Molecular and ionic adsorption on noble metal electrodes were extensively studied by Lipkowski's group over the last twenty five years.[29-31] At the present time, a pool of literature is available concerning the adsorption behavior of ionic,[32-42] zwitterionic[43-45] and neutral[23,38] surfactants. While the study of molecular or ionic adsorption on noble metal surfaces was largely of fundamental interest up to this point, the same methodologies can be applied to study the adsorption of surfactants used to stabilize nanoparticles. For example, the adsorption of citrate on Au(111) has been thoroughly studied using infrared spectroscopy[46,47] and scanning probe microscopy[48,49] to provide qualitative and quantitative information of the citrate adlayer on the surface. The relevance of citrate as a nanoparticle stabilized ligand has also been evaluated using thermodynamic analysis of the electrochemical interface.[50] In this thesis, an electrochemical evaluation of 4-(N,N-dimethylamino)pyridine (DMAP) and quaternary ammonium surfactants is presented to explain certain aspects regarding nanoparticle stability and shape selectivity.

1.4 Review of Essential Theory

1.4.1 Electrical double layer

There is an unequal distribution of electric charges at any interface; as a result, both sides of the interface carry net opposite charges, developing a potential difference

across the interface, which can be called an electrical double layer. The double layer as a whole is electrically neutral, i.e., the net charge on one side of the interface is balanced by an equal and opposite net charge on the other side of the interface. There has been extensive research devoted to understanding the distribution of charge on the solution side of a solid-liquid interface, starting as early as the beginning of the 18th century. Helmholtz's model (proposed in 1879) envisioned that all counterions were lined up parallel to the charged solid surface at a distance of about one molecular diameter. Later Gouy (in 1910) and Chapman (in 1913) modified the Helmholtz model by distributing the counter ions in the solution side of the interface into a diffuse double layer. A more realistic model was proposed by Stern in 1924 in which the solution side of the double layer is divided into two parts: (a) a layer of strongly held counter ions adsorbed close to the charged solid surface and (b) a diffuse layer of counterions as in the Gouy-Chapman model. Grahame added a further modification by dividing the Stern layer into the inner Helmholtz layer and the outer Helmholtz layer.[51] The inner Helmholtz layer corresponds to a plane of non-hydrated specifically adsorbed ions and the outer Helmholtz plane is identical to the Stern plane, i.e., the distance of closest approach of a solvated electrolyte ion. Even after this model, there have been many attempts to further modify these models to give even better realistic pictures of the interface, for example, by taking the discreteness of the charge also into account.[52] In spite of these next generation models, the simple model proposed by Grahame satisfactorily explains most of the processes happening at the interface, at least to the level of precision required for the discussion in this thesis.

A pictorial representation of Grahame's model for the electrical double layer as described by Mohilner is shown in Figure 1.1.[2] The double layer consists of (a) the solid phase, which is the electrode surface, (b) an inner layer which is located next to the solid phase, and (c) an outer or diffuse layer, which extends all the way into the bulk of the solution. The solid phase often carries a charge and the density of excess electronic charge on the solid phase, the charge density is denoted by σ_m. In most electrolyte solutions, the inner layer contains a fraction of a monolayer of unsolvated ions which are said to be specifically adsorbed on the electrode surface, the locus of these ions defines the position of the inner Helmholtz plane (IHP). Some ions, even though electrostatically attracted to the surface, will not be able to get as close to the solid surface as specifically adsorbed ions if the interaction between the ions and the surface is not strong enough to strip the solvation shell, and they are said to be nonspecifically adsorbed. The imaginary plane that crosses the electrical centers of the closest approaching solvated ions is called the outer Helmholtz plane (OHP). Not all nonspecifically adsorbed ions are located at the OHP but rather spread over a three dimensional area beyond the OHP, and extends into the diffuse layer. The diffuse layer is largely disordered and dynamic due to thermal agitation as opposed to the Coulombic forces of attraction and repulsion that generate more ordering. Understandably, the total charge density on the solid surface is equal to the sum of charge densities in the inner and diffuse layers.

i.e., $$\sigma_m = -q_s = -(q_i + q_d) \qquad (1.1)$$

where σ_m is the metal charge density, q_s represents the excess charge density on the solution side, q_i is the charge density in the inner layer and q_d is the charge density in the diffuse layer.

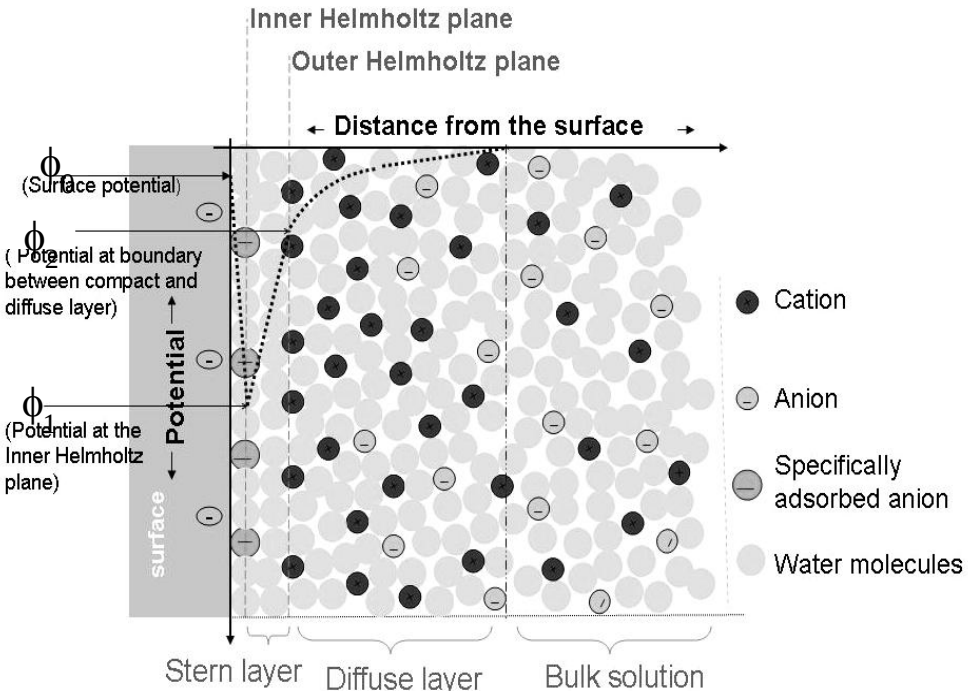

Fig. 1.1 A pictorial representation of the electrical double layer.

A mathematical treatment of the double layer carried out by Adamson[53] provides a useful means to calculate the effective thickness of the diffuse portion of the double layer, which is often called the Debye length (κ).

$$\frac{1}{\kappa} = \left(\frac{\epsilon_0 \epsilon_r RT}{4\pi F^2 \sum_i Z_i^2 c_i} \right)^{1/2} \qquad (1.2)$$

Where ϵ_0 is the permittivity of free space, ϵ_r is the static relative permittivity of the solution, R is the molar gas constant, T is the absolute temperature, F is the Faraday constant, c_i is the molar concentration of the ions in the solution and Z_i is the valency of the ions.

1.4.2 Electrical double layer of a nanoparticle

Nanoparticle dispersions in solution correspond to the distribution of a solid phase in a liquid medium. Because of the large ratio of surface atoms to bulk atoms, colloidal particles are thermodynamically unstable and have a natural tendency to attract each other through van der Waals forces so as to reduce their surface energy, which in turn leads to aggregation of the particles. The stability of classical colloidal systems was understood to arise from interparticle repulsive forces caused by the surface charge on the colloids. A quantitative theory of colloid stability was formulated by Derjaguin and Landau (in 1941) and further developed by Verwey and Overbeek (in 1948), and is now usually referred to as DLVO theory, in recognition of its originators. DLVO theory is considered by many investigators as the definitive theory for electrostatic stabilization of colloidal particles in aqueous solution. Though this theory is often violated in real systems, it is considered as the primary basis of all theories related to colloidal stability, primarily because of the fact that the outer, rather than the inner, layers of the electrical double layer are more important when considering the stability of colloidal particles. Charge stabilization alone is usually not adequate for colloidal dispersions of noble metals having comparatively large values of the Hamaker constant (or in simple terms stronger van der Waals attractive interactions). The additional stability required for metal nanoparticles in solutions is usually provided by protective ligands, which are either chemically (i.e., covalently) or physically adsorbed on the nanoparticle surfaces. The surface coverage of the ligand over the nanoparticle determines the steric stability of the nanoparticles in solution. In addition, the size and shape of the nanoparticle is largely influenced by the interaction of the ligand with the metal core during the nanoparticle

growth process. Hence a good understanding of interactions of the ligand with the metal surface becomes imperative for mechanistic insight into nanoparticle formation and stability. In simple terms, a surfactant covered metal nanoparticle can be treated as a surfactant adsorbed metal surface, and an investigation in this direction is the underlying theme of this thesis. In this thesis, the adsorption of surfactant at an electrified metal/electrolyte interface by means of electrochemical techniques, under conditions identical to the nanoparticle system is discussed in detail.

1.4.3 Adsorption at an electrified solid-solution interface

The extent of surfactant adsorption at the interface can be characterized by interfacial free energy or surface tension. Surface tension is the force needed to oppose the natural pull of the molecules at the interface to minimize the surface area. Measurement of surface tension at the interface is useful to extract information about the energetics and the extent of adsorption of surfactant at the interface. While surface tension at the air/liquid interface can be directly measured (for example, using the Wilhelmy plate method), there is no direct method to measure the surface tension at the solid liquid interface. In this thesis, an indirect method to study the change in surface tension (or surface pressure) at the electrode/electrolyte interface from chronocoulometry measurements is employed. The following sections outline the methodology in detail.

Thermodynamic analysis

The methodology used for the quantitative evaluation of the surfactant adsorption at the electrode-electrolyte interface is based on the method developed in Lipkowski's group. This methodology relies on the extrapolation of the electrocapillary equation to solid-state electrodes. Thermodynamic parameters were obtained from the metal charge

density acquired from chronocoulometric measurements. Since the electrocapillary equation is derived from the Gibbs adsorption isotherm, a brief discussion on the Gibbs model of the interface will be given first. The Gibbs model provides information concerning an imaginary interface that is "infinitely sharp"; i.e., the interface considers no electrical double layer. Therefore it cannot provide the precise location of interfacial quantities; to do so require concepts beyond simple thermodynamics.

In the Gibbs model, two phases of the system are assumed to be completely homogeneous up to a purely mathematical dividing surface having no charge separation, the position of which is arbitrary within the model, and there is no charge separation at the dividing surface. Consider a metal/electrolyte system, represented by α and β phases respectively in the Gibbs model. If the components in each phase were distributed uniformly up to the interface, the total Gibbs function G would be the sum of Gibbs functions for individual phases.

$$G = G_\alpha + G_\beta \qquad (1.3)$$

But for real systems, the components are not uniform at the interface, and hence the sum of two Gibbs functions would differ from the Gibbs function by an amount equal to surface Gibbs function G_δ.

$$G_\delta = G - (G_\alpha + G_\beta) \qquad (1.4)$$

i.e., the properties of the real system have been described with regard to the extensive properties of the real system that exceed those of the model system.

Similarly, the amount of species "j" in the surface phase can be represented in terms of the overall amount n_j and the amount of components in phases α and β.

$$n_j^{\delta} = n_j - (n_j^{\alpha} + n_j^{\beta}) \tag{1.5}$$

The excess amount of components per unit area can be represented by

$$\Gamma_j = \frac{n_j^{\delta}}{A} \tag{1.6}$$

where A is the surface area and Γ_j is the Gibbs surfaces excess.

A general change in *G* brought about by changes in *T*, *p*, *A* and n_j may be expressed by the equation

$$dG = -SdT + Vdp + \gamma dA + \sum_j \mu_j \, dn_j \tag{1.7}$$

where γ is the surface tension, T is the temperature and p is the pressure

For phases α and β, this relation can be written as

$$dG^{\alpha} = -S^{\alpha}dT + V^{\alpha}dp + \gamma dA + \sum_j \mu_j \, dn_j^{\alpha} \tag{1.8}$$

$$dG^{\beta} = -S^{\beta}dT + V^{\beta}dp + \gamma dA + \sum_j \mu_j \, dn_j^{\beta} \tag{1.9}$$

Hence the differential expression for surface Gibbs function can be written as

$$dG^{\delta} = dG - [dG^{\alpha} + dG^{\beta}] \tag{1.10}$$

At constant p,

$$dG^{\delta} = -S^{\sigma}dT + \gamma dA + \sum_j \mu_j \, dn_j^{\sigma} \tag{1.11}$$

On integrating this equation, it transforms to

at constant *T*,

$$G^{\delta} = \gamma A + \sum_j \mu_j \, n_j^{\sigma} \qquad (1.12)$$

The total differential of equation 1.12 is

$$dG^{\delta} = Ad\gamma + \gamma dA + \sum_j \mu_j \, dn_j^{\sigma} + \sum_j n_j^{\sigma} d\mu_j \qquad (1.13)$$

From equations (1.11) and (1.13),

$$Ad\gamma + \sum_j n_j^{\sigma} d\mu_j \; = 0 \qquad (1.14)$$

i.e.,

$$-d\gamma = \sum_j \Gamma_j \, d\mu_j \qquad (1.15)$$

In this relation, surface excess (Γ_j) is related to the change in surface tension ($d\gamma$) and the chemical potentials of the components ($d\mu_j$) present in the solution. This mathematical representation of the thermodynamics of the interface demonstrates that the surface tension of the interface decreases with excess species at the interface, or a positive value of the Gibbs excess.

1.4.4 Electrocapillary equation

Gibbs adsorption described above can be extended to an electrochemical system, provided the electrode is ideally polarized. The Gibbs adsorption isotherm for an electrode-electrolyte interface at constant temperature and pressure can be written as

$$-d\gamma = \sigma_m dE + \Gamma \mathrm{d}\mu \qquad (1.16)$$

where *E* represents the electrode potential.

In the presence of excess supporting electrolyte containing no specifically adsorbing species, and for relatively low concentrations of adsorbate, it can be assumed that the

activity coefficient of the surfactant molecule is constant over a range of concentrations, which allows the substitution of $\mathrm{d}\mu$ with $RT\mathrm{d}(\ln c)$.

$$-d\gamma = \sigma_m dE + RT\Gamma \mathrm{d}(\ln c) \qquad (1.17)$$

where σ_m represents the metal charge density, R is the gas constant and c represents the bulk concentration of the adsorbing species.

At constant electrode potential, the above equation reduces to

$$-d\gamma = RT\Gamma \mathrm{d}(\ln c) \qquad (1.18)$$

Hence the Gibbs excess of the adsorbate at constant electrode potential can be determined using the above relationship if the surface tension at the interface can be measured.

Determination of Gibbs excess at the solid-electrolyte interface

Though it is possible to measure the surface tension for liquid electrodes such as mercury, a direct measurement of surface tension on solid electrodes is impossible. Hence, a method known as the back integration technique was used for gold electrodes, which is discussed below:

The film pressure, π, of the interface can be defined as

$$\pi = \gamma_{c=0} - \gamma_c \qquad (1.19)$$

where γ_c and $\gamma_{c=0}$ are surface tensions corresponding to a given concentration of the adsorbing species and the bare electrode, respectively.

At constant electrolyte composition, equation (1.16) can be integrated over the potential range E_o to E.

$$-\gamma(E) = \int_{E_o}^{E} \sigma_m \, dE - \gamma(E_o) \qquad (1.20)$$

Hence,

$$\pi(E) = \left[-\int_{E_o}^{E} \sigma_m \, dE + \gamma(E_o) \right]_{c=0} - \left[-\int_{E_o}^{E} \sigma_m \, dE + \gamma(E_o) \right]_{c} \qquad (1.21)$$

If there is a potential E_o(commonly referred to as the desorption potential) where no adsorbate species is present on the electrode irrespective of its concentration in the bulk of solution, then

$$[\gamma(E_o)]_{c=0} = [\gamma(E_o)]_c \qquad (1.22)$$

Hence,

$$\pi(E) = \left[\int_{E_o}^{E} \sigma_m \, dE \right]_{c} - \left[\int_{E_o}^{E} \sigma_m \, dE \right]_{c=0} \qquad (1.23)$$

Thus the surface pressure can be determined from the metal charge density data as a function of electrode potential.

By differentiating equations (1.18) and (1.19) with respect to ln*c*,

$$\left(\frac{\delta\pi}{\delta lnc}\right)_E = -\left(\frac{\delta\gamma}{\delta lnc}\right)_E \qquad (1.24)$$

the following expression for the Gibbs excess at a solid electrode/electrolyte interface is obtained,

$$\Gamma = \frac{1}{RT}\left(\frac{\delta\pi}{\delta lnc}\right)_E \qquad (1.25)$$

If the surface pressure can be determined by measuring $\sigma_m\ (E)$ for various bulk concentrations of the adsorbing species, equation (1.25) can be used to determine the surface excess; this methodology is provided in more detail in section 2.4, Chapter 2.

1.5 Overview of the Thesis

This thesis consists of seven chapters. A brief introduction to the research background and literature review is given in Chapter 1 and the details of the experimental methods and data analysis is provided in Chapter 2. Chapter 3 describes an electrochemical evaluation of the halide induced aggregation of 4-(dimethylamino)pyridine (DMAP) stabilized gold nanoparticle. The significance of surface crystallography and solution pH on the adsorption behavior of DMAP is discussed in Chapter 4. In Chapter 5, the influence of surface reconstruction on the adsorption behavior of a quaternary ammonium surfactant on a Au(100) single crystal is discussed. A detailed analysis of the adsorption behavior of a quaternary surfactant on Au(111) electrode, discussing potential induced structural transformation of the surfactant is included in Chapter 6. Studies of the adsorption behavior of quaternary ammonium bromide on Au(111) and Au(100) single crystals (investigated to address gold nanorod growth mechanism) is described in Chapter 7. Finally, concluding remarks on the work presented in this thesis and scope for future research in this direction are discussed in Chapter 8.

Reference List

1. Grahame, D. C. The Electrical Double Layer and the Theory of Electrocapillarity. *Chemical Reviews* **1947,** *41* (3), 441-501.

2. Mohilner, D. M. In *Electroanalytical chemistry: A series of advances*, Bard, A. J., Ed.; Dekker: New York, 1966; Vol. 1, p 242.

3. Damaskin, B.; Frumkin, A.; Chizhov, A. Generalized model of the surface layer for the case of adsorption of inorganic molecules on the electrode. *Journal of Electroanalytical Chemistry* **1970,** *28* (1), 93-104.

4. Brust, M.; Walker, M.; Bethell, D.; Schiffrin, D. J.; Whyman, R. Synthesis of thiol-derivatised gold nanoparticles in a two-phase Liquid-Liquid system. *Journal of Chemical Society , Chemical Communications* **1994,** (7), 801-802.

5. Israelachvili, J. N. *Intermolecular and surface forces;* 2 ed.; Academic Press, London: 1992.pp. 341-385.

6. Schryver, S. B.; Ramsden, W.; Cross, C. F.; Schidrowitz, P.; Dreaper, W. P.; McBain, J. W.; Turner, T.; Worley, F. P.; Martin, C. J.; Bousfield, W. R.; Morse, H. N.; Henri, V.; Freundlich, H.; The, C.; Ostwald, W.; Chapman, C.; Senter, G. Discussion. *Transactions of the Faraday Society* **1913,** *9*, 93-107.

7. Gaudin; Fuerstenau Streaming Potential Studies--Quartz Flotation with Anionic Collectors I. *Transactions of the American Institute of Mining, Metallurgical and Petroleum Engineers* **1955,** *202*, 66-71.

8. Gaudin; Fuerstenau Streaming Potential Studies--Quartz Flotation with Cationic Collectors. *Transactions of the American Institute of Mining, Metallurgical and Petroleum Engineers* **1955,** *202*, 958-965.

9. Fuerstenau, D. W. Streaming Potential Studies on Quartz in Solutions of Aminium Acetates in Relation to the Formation of Hemi- micelles at the Quartz-Solution Interface. *The Journal of Physical Chemistry* **1956,** *60* (7), 981-985.

10. Somasundaran, P.; Healy, T. W.; Fuerstenau, D. W. Surfactant Adsorption at the Solid-Liquid Interface Dependence of Mechanism on Chain Length. *The Journal of Physical Chemistry* **1964,** *68* (12), 3562-3566.

11. Somasundaran, P.; Fuerstenau, D. W. Mechanisms of Alkyl Sulfonate Adsorption at the Alumina-Water Interface1. *The Journal of Physical Chemistry* **1966,** *70* (1), 90-96.

12. Dick, S. G.; Fuerstenau, D. W.; Healy, T. W. Adsorption of alkylbenzene sulfonate (A.B.S.) surfactants at the alumina-water interface. *Journal of Colloid and Interface Science* **1971,** *37* (3), 595-602.

13. Ball, B.; Fuerstenau, D. W. Thermodynamics and adsorption behaviour in the quartz/aqueous surfactant system. *Discuss. Transactions of the Faraday Society* **1971,** *52,* 361-371.

14. Wakamatsu, T.; Fuerstenau, D. W. The Effect of Hydrocarbon Chain Length on the Adsorption of Sulfonates at the Solid/Water Interface. In *Adsorption From Aqueous Solution*, 79 ed.; American Chemical Society: 2011; pp 161-172.

15. Narkiewicz-Michalek, J. On the Nature of the Surface Aggregation in Surfactant Adsorption Onto Polar Surfaces. *Berichte der Bunsengesellschaft physikalische Chemie* **1991,** *95* (1), 85-95.

16. Levitz, P.; Van Damme, H. Fluorescence decay study of the adsorption of nonionic surfactants at the solid-liquid interface. 2. Influence of polar chain length. *The Journal of Physical Chemistry* **1986,** *90* (7), 1302-1310.

17. Naficy, G.; Vanel, P.; Schuhmann, D.; Bennes, R.; Tronel-Peyroz, E. Adsorption on electrodes and micellization of some alkyl sulfates. *The Journal of Physical Chemistry* **1981,** *85* (8), 1037-1042.

18. Nagarajan, R.; Ruckenstein, E. Critical micelle concentration: A transition point for micellar size distribution : A statistical thermodynamical approach. *Journal of Colloid and Interface Science* **1977,** *60* (2), 221-231.

19. Blankschtein, D.; Thurston, G. M.; Benedek, G. B. Theory of phase separation in micellar solutions. *Physical Review Letters* **1985,** *54* (9), 955.

20. Srinivasan, V.; Blankschtein, D. Effect of Counterion Binding on Micellar Solution Behavior. Molecular Thermodynamic Theory of Micellization of Ionic Surfactants. *Langmuir* **2003,** *19* (23), 9932-9945.

21. Nishimura, S.; Scales, P. J.; Biggs, S. R.; Healy, T. W. AFM studies of amine surfactant hemimicelle structures at the mica-water interface. *Colloids and Surfaces A: Physicochemical and Engineering Aspects* **1995,** *103* (3), 289-298.

22. Sek, S.; Chen, M.; Brosseau, C. L.; Lipkowski, J. In Situ STM Study of Potential-Driven Transitions in the Film of a Cationic Surfactant Adsorbed on a Au(111) Electrode Surface. *Langmuir* **2007,** *23* (25), 12529-12534.

23. Grant, L. M.; Ederth, T.; Tiberg, F. Influence of Surface Hydrophobicity on the Layer Properties of Adsorbed Nonionic Surfactants. *Langmuir* **2000,** *16* (5), 2285-2291.

24. Patrick, H. N.; Warr, G. G.; Manne, S.; Aksay, I. A. Self-Assembly Structures of Nonionic Surfactants at Graphite/Solution Interfaces. *Langmuir* **1997,** *13* (16), 4349-4356.

25. Parsons, R. The electrical double layer: recent experimental and theoretical developments. *Chemical Reviews* **1990,** *90* (5), 813-826.

26. Hamelin, A. In *Modern Aspects of Electrochemistry*, Conway, B. E., Bockris, J. O., Eds.; Plenum Press: New York, 2011.

27. Lipkowski, J. In *Adsorption of molecules at metal electrodes*, Lipkoski, J., Ross, P. N., Eds.; VCH: New York, 1992; pp 171-238.

28. 1998 Alcan Award Lecture: Surface electrochemistry - surface science with a joy stick. *Canadian Journal of Chemistry* **1999,** *77*, 1163-1176.

29. Lipkowski, J.; Shi, Z.; Chen, A.; Pettinger, B.; Bilger, C. Ionic adsorption at the Au(111) electrode. *Electrochimica Acta* **1998,** *43* (19-20), 2875-2888.

30. Chen, M.; Burgess, I.; Lipkowski, J. Potential controlled surface aggregation of surfactants at electrode surfaces - A molecular view. *Surface Science* **2009,** *603* (10-12), 1878-1891.

31. Burgess, I.; Zamlynny, V.; Szymanski, G.; Lipkowski, J.; Majewski, J.; Smith, G.; Satija, S.; Ivkov, R. Electrochemical and Neutron Reflectivity Characterization of Dodecyl Sulfate Adsorption and Aggregation at the Gold-Water Interface. *Langmuir* **2001,** *17* (11), 3355-3367.

32. Manne, S.; Gaub, H. E. Molecular Organization of Surfactants at Solid-Liquid Interfaces. *Science* **1995,** *270* (5241), 1480-1482.

33. Maguire, H. J.; Roscoe, S. G. An Electrochemical Study of Antibiotic Ionophores in Self-Assembled Lipid Layers at Platinum. *Langmuir* **1997,** *13* (22), 5962-5968.

34. Manne, S. Visualizing self-assembly: Force microscopy of ionic surfactant aggregates at solid-liquid interfaces. In *Amphiphiles at Interfaces*, 103 ed.; Texter, J., Ed.; Springer Berlin / Heidelberg: 1997; pp 226-233.

35. Jaschke, M.; Butt, H. J.; Gaub, H. E.; Manne, S. Surfactant Aggregates at a Metal Surface. *Langmuir* **1997,** *13* (6), 1381-1384.

36. Wanless, E. J.; Ducker, W. A. Organization of Sodium Dodecyl Sulfate at the Graphite Solution Interface. *The Journal of Physical Chemistry* **1996,** *100* (8), 3207-3214.

37. Wolgemuth, J. L.; Workman, R. K.; Manne, S. Surfactant Aggregates at a Flat, Isotropic Hydrophobic Surface. *Langmuir* **2000,** *16* (7), 3077-3081.

38. Wanless, E. J.; Ducker, W. A. Weak Influence of Divalent Ions on Anionic Surfactant Surface-Aggregation. *Langmuir* **1997,** *13* (6), 1463-1474.

39. Subramanian, V.; Ducker, W. A. Counterion Effects on Adsorbed Micellar Shape:GÇë Experimental Study of the Role of Polarizability and Charge. *Langmuir* **2000,** *16* (10), 4447-4454.

40. Liu, J. F.; Min, G.; Ducker, W. A. AFM Study of Adsorption of Cationic Surfactants and Cationic Polyelectrolytes at the Silica-Water Interface. *Langmuir* **2001,** *17* (16), 4895-4903.

41. Burgess, I.; Jeffrey, C. A.; Cai, X.; Szymanski, G.; Galus, Z.; Lipkowski, J. Direct Visualization of the Potential-Controlled Transformation of Hemimicellar Aggregates of Dodecyl Sulfate into a Condensed Monolayer at the Au(111) Electrode Surface. *Langmuir* **1999,** *15* (8), 2607-2616.

42. Ducker, W. A.; Wanless, E. J. Surface-Aggregate Shape Transformation. *Langmuir* **1996,** *12* (24), 5915-5920.

43. Ducker, W. A.; Grant, L. M. Effect of Substrate Hydrophobicity on Surfactant Surface-Aggregate Geometry. *The Journal of Physical Chemistry* **1996,** *100* (28), 11507-11511.

44. Xu, S.; Chen, M.; Cholewa, E.; Szymanski, G.; Lipkowski, J. Electric-Field-Driven Surface Aggregation of a Model Zwitterionic Surfactant. *Langmuir* **2007,** *23* (13), 6937-6946.

45. Floate, S.; Hosseini, M.; Arshadi, M. R.; Ritson, D.; Young, K. L.; Nichols, R. J. An in-situ infrared spectroscopic study of the adsorption of citrate on Au(1 1 1) electrodes. *Journal of Electroanalytical Chemistry* **2003,** *542*, 67-74.

46. Nichols, R. J.; Burgess, I.; Young, K. L.; Zamlynny, V.; Lipkowski, J. A quantitative evaluation of the adsorption of citrate on Au(111) using SNIFTIRS. *Journal of Electroanalytical Chemistry* **2004,** *563* (1), 33-39.

47. Lin, Y.; Pan, G. B.; Su, G. J.; Fang, X. H.; Wan, L. J.; Bai, C. L. Study of Citrate Adsorbed on the Au(111) Surface by Scanning Probe Microscopy. *Langmuir* **2003,** *19* (24), 10000-10003.

48. Yan, H. J.; Lu, J.; Wan, L. J.; Bai, C. L. STM Study of Two-Dimensional Assemblies of Tricarboxylic Acid Derivatives on Au(111). *The Journal of Physical Chemistry B* **2004,** *108* (31), 11251-11255.

49. Kunze, J.; Burgess, I.; Nichols, R.; Buess-Herman, C.; Lipkowski, J. Electrochemical evaluation of citrate adsorption on Au(111) and the stability of citrate-reduced gold colloids. *Journal of Electroanalytical Chemistry* **2007,** *599* (2), 147-159.

50. Grahame, D. C. Electrode Processes and the Electrical Double Layer. *Annual Review of Physical Chemistry* **1955,** *6* (1), 337-358.

51. Benjamin, I. Chemical Reactions and Solvation at Liquid Interfaces:GÇë A Microscopic Perspective. *Chemical Reviews* **1996,** *96* (4), 1449-1476.

52. Adamson, A. W. In *Physical Chemistry of Surfaces*, 3 ed.; Adamson, A. W., Ed.; Wiley Interscience: New York, 1976.

Chapter 2

Experimental Methods and Data Analysis

2.1 Electrochemical Setup

A computer controlled system, consisting of a HEKA PG590 potentiostat was used for all the electrochemistry experiments. Data were collected using a multifunction DAQ card (PCI 6251 M Series, National Instruments) and in-house software written in the LabVIEW environment.

2.1.1 Electrochemical cell

The electrochemical cell was made of glass and had a solution capacity of 100 mL. It consists of two parts: the bottom part is the electrolyte container with a 50 mm ground joint at the top; this joint is fitted to a glass cover which has six ground joints (five 10 mm and one 15 mm) on the top. One of the 10 mm joints is connected to the salt bridge which is also made of glass. Two joints are used to allow argon purge of the electrolyte solution and an argon blanket on top of the electrolyte surface, which is vented through an exhaust bubbler connected to one of the 10 mm joints. The remaining 10 mm and 15 mm joints are used for the counter and working electrodes respectively. The electrochemical cell was enclosed in a Faraday cage - a grounded conductive shield made of copper mesh - to protect the electrochemical setup against electromagnetic interference from external sources.

All glassware from the electrochemical cell including the salt bridge was washed in a hot acid bath containing a 1:3 v/v mixture of nitric acid and sulfuric acid, and then washed with Milli-Q water and again soaked in fresh Milli-Q water for about 6 h before

use. All glassware used for preparing solutions needed for electrochemical measurements was also washed in the same manner. Milli-Q water of resistivity 18.2 MΩ cm^{-1} was used to prepare electrolyte and all other aqueous solutions.

2.1.2 Electrodes

A saturated calomel electrode (SCE) connected to the electrochemical cell by means of a salt bridge was used as the reference electrode. All potentials reported in this thesis are measured with respect to SCE. A coil of gold wire, which had been flame annealed before each experiment, was used as a counter electrode.

Working electrodes used were either gold bead electrodes or mechanically polished polycrystalline/single crystal electrodes. Gold bead electrodes were formed by melting the end of a gold wire (1 mm diameter, 99.9%) in hydrogen-oxygen flame. Before melting, the gold wire was cleaned by immersing it in freshly prepared piranha solution (a 3:1 v/v mixture of concentrated sulfuric acid and 30% hydrogen peroxide) for 10 min followed by sonication in Milli-Q water for 5 min. After forming the gold bead at the end of the gold wire, it was quenched in Milli-Q water and then etched in *aqua regia* for 1 minute, to remove any trace amount of surface impurities. According to the theory of alloy solidification, the solute atoms remain in the liquid phase (gold melt in this case) on freezing rather than forming as part of the crystal lattice. Thus if any impurities were present in the gold melt, they would migrate to the surface of the gold bead (the impurities can be seen as darker islands in the gold melt) where they can be readily removed by etching the gold bead in *aqua regia* (a 3:1 mixture of hydrochloric acid and nitric acid). Flame annealing, quenching and etching processes were repeated until the melted wire forms a clean spherical gold bead at the end of the gold wire. The as-

prepared electrode was used as the working electrode by immersing the spherical segment as a whole into the electrolyte solution.

Alternatively, a mechanically polished electrode in a hanging meniscus arrangement (Figure 2.1) was also used as the working electrode in some cases, especially for single crystal electrodes. These electrodes were prepared from gold melt in a graphite mold with the use of an inductive furnace, popularly known as the Bridgman technique. A detailed description of the single crystal fabrication using Laue back-reflection method is given in section 2.6.

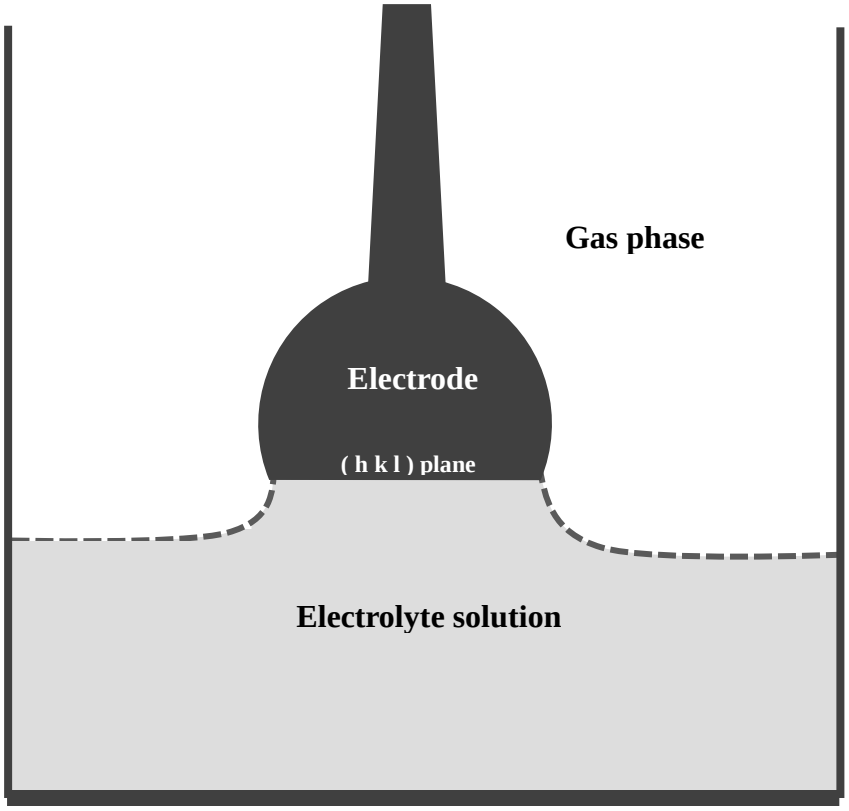

Fig. 2.1
A schematic representation of the hanging meniscus configuration of the single crystal electrode. The "(hkl) plane" represents the polished electrode surface of specific crystallographic orientation.

2.2 Cyclic Voltammetry

To record a cyclic voltammogram, a linear voltage scan (typically 20 mV s^{-1}) was applied to the working electrode and the charging current flowing to the interface was recorded as a function of the electrode potential. The surfactant adsorption at the interface was studied by cycling the potential in the region where charge transfer across the interface does not take place; this region is known as the double layer region. Since the presence of the surfactant at the interface produces characteristic peaks, it is possible to get qualitative information about the changes concerning the adsorbate during the potential scan. The charging current measured using cyclic voltammetry cannot be used for quantitative information about the adsorbate at the interface because it depends not only on the potential but also on the scan rate.

2.3 Differential Capacitance

The dependence of the differential capacity at the interface, on applied potential was used as an additional measure of the processes happening at the interface. Assuming a compact electrical double layer, the interface can be treated as a parallel plate capacitor, the capacitance of which is given by

$$C = \frac{A\varepsilon_o\varepsilon_r}{d} \qquad (2.1)$$

Where A is the plate area, ε_o is the permittivity of free space, ε_r is the relative permittivity and d is the plate spacing or the thickness of the double layer in this case. The adsorption of organic molecules at the interface causes replacement of water and specifically adsorbed ions from the compact layer by the larger organic species, which causes a significant increase in the thickness of the compact layer capacitor. In addition,

organic species have relatively smaller values of permittivity (the capacitances of well formed organic monolayers are typically < 5 μF/cm^2), totaling a significant decrease in the double layer differential capacity. The adsorption of neutral organic species is maximal at the potential of zero charge (pzc). The pzc is determined from the position of the capacity minimum on the differential capacity curve recorded for the surfactant-free electrode in dilute electrolyte. From the position of the characteristic desorption capacitive feature, the potential of the adsorbate desorption can also be determined from DC measurements. The knowledge of both the desorption potential and the potential of zero charge obtained from the differential capacity measurements is important to carry out quantitative measurements using chronocoulometry.

The differential capacity of the double layer (C) formed between the charged electrode carrying an excess charge density of σ_m and the electrolyte solution bearing a balancing charge density $-\sigma_m$ is defined as

$$C = \frac{d\sigma_m}{dE} \qquad (2.2)$$

When there are specifically adsorbed species at the electrode surface, equation (2.2) does not hold true because now σ_m is not only a function of the applied potential (E), but surface excess (Γ) also.

i.e., $$d\sigma_m = \left(\frac{\partial\sigma_m}{\partial\Gamma}\right)_E d\Gamma + \left(\frac{\partial\sigma_m}{\partial \mathrm{E}}\right)_\Gamma d\mathrm{E} \qquad (2.3)$$

Differentiating equation (2.3) with respect to the applied potential gives a description of the interfacial capacity in the presence of adsorbates

$$C = \left(\frac{\partial\sigma_m}{\partial\Gamma}\right)_E \frac{d\Gamma}{d\mathrm{E}} + \left(\frac{\partial\sigma_m}{\partial \mathrm{E}}\right)_\Gamma \qquad (2.4)$$

i.e., there is an additional term in the interfacial capacity that changes as a function of Γ, which is generally called pseudo capacity. The appearance of pseudo capacity peaks in the differential capacity plots indicate the onset of phase transitions or adsorption/desorption processes.

The interfacial capacity can be readily measured by applying a small ac perturbation to the applied electrode potential and measuring the resulting in-phase and out-of-phase components of the resulting current. The differential capacitance technique used is basically a phase-selective ac-voltammetry experiment where a sinusoidal perturbation voltage at a fixed frequency is superimposed on the dc voltage of cyclic voltammetry. An alternating perturbation of 5 mV root-mean-square and 25 Hz was applied to the working electrode on top of a of 5 mV/s linear potential scan. The charging current was analyzed using a lock-in amplifier and the real (in-phase) and quadrature (out of phase) components of the resulting dc current were acquired and converted to dc potential dependent differential capacitance values. Assuming a series resistor-capacitor circuits as the model of the electrode-solution interface, the total impedance across the interface can be calculated using the equation

$$Z = X + \frac{1}{j\omega C} \qquad (2.5)$$

Where X is the resistance of the solution, ω is the angular frequency of the applied alternating current perturbation, C denotes the differential capacity. Using Ohm's law, the current passing though a resistor-capacitor circuit can be shown to be

$$i_{ac} = \frac{V_{ac} X \omega^2 C^2}{1 + X^2 \omega^2 C^2} + j\left(\frac{V_{ac} \omega C}{1 + X^2 \omega^2 C^2}\right) \qquad (2.6)$$

where j^2 = -1. The first term in the above equation is in-phase with the voltage perturbation and the second term corresponds to the out of phase component. During the measurement, the real (R) and quadrature (Q) components were separated using a lock-in amplifier. Thus the differential capacity can be determined as

$$C = \frac{Q}{E_{ac}} \times \frac{1}{\omega} \times \left[1 + \left(\frac{R}{Q}\right)^2\right] \qquad (2.7)$$

Where C denotes the differential capacity of the interface, R and Q are the real and quadrature components of the measured current, respectively, E_{ac} is the root mean square voltage and ω is the angular frequency of the applied alternating current perturbation.

2.4 Chronocoulometry

As its name implies, chronocoulometry is the measurement of charge with time. A schematic diagram outlining the modus operandi of chronocoulometry is shown in Figure 2.2, Panel (a) shows the sequence of potential steps applied to the working electrode. The electrode potential was preset to attain a constant base value (E_b) for time t_b, where the adsorbate forms a stable adlayer. Then the working electrode potential was stepped and held at a variable potential E_c for a specific period of time t_c, sufficiently long enough to allow equilibration of species at the interface. The final phase of a potential step experiment is a potential step from E_c to a potential at which the adsorbates are completely desorbed from the surface (E_{des}). During the step from E_c to E_{des} the current flowing to the interface was acquired over time equal to t_{acq}. After the data acquisition, the working electrode potential was reset to E_b, where the equilibration of the interface takes place, so as to prepare for the next step to a new value of the variable potential E_c.

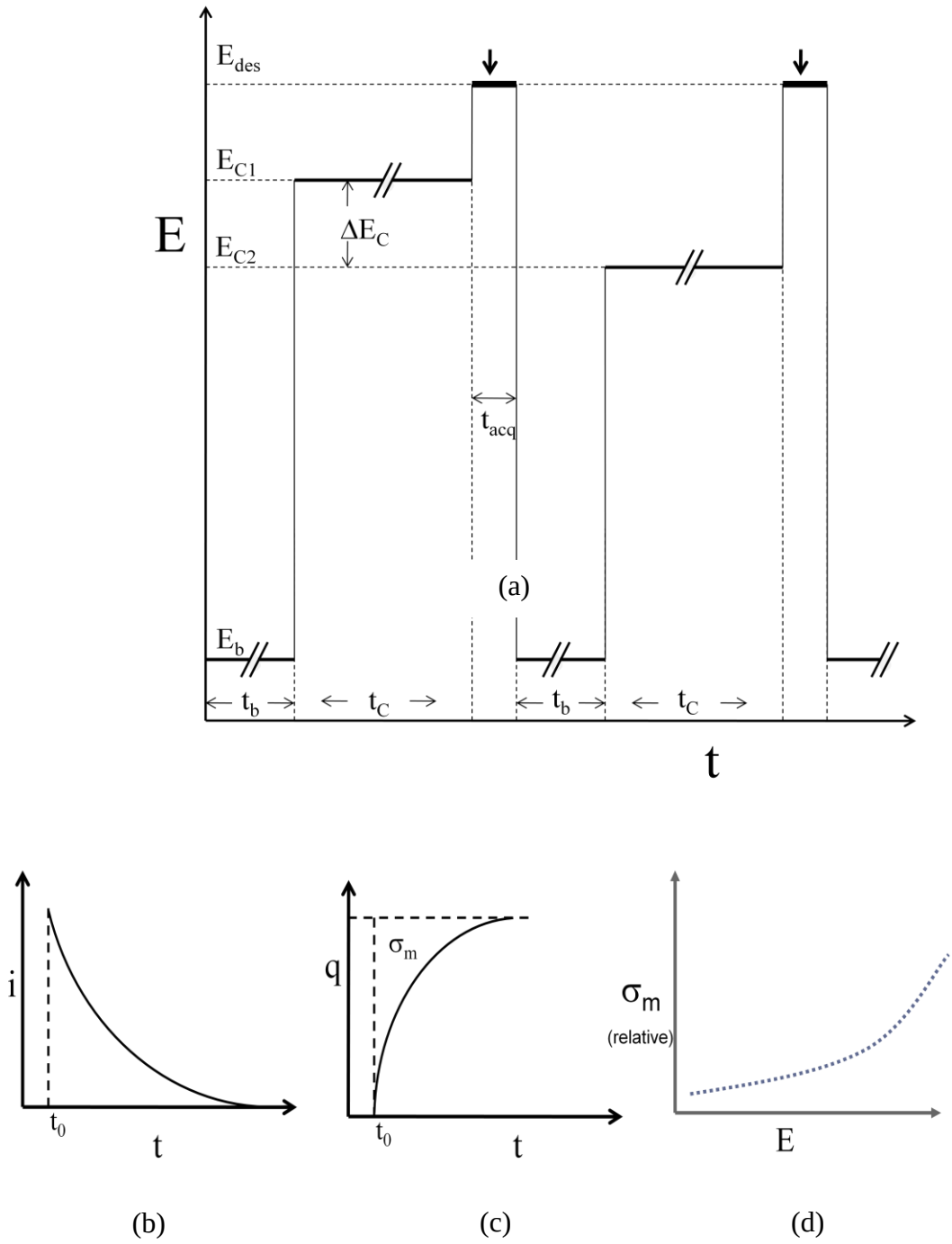

Fig. 2.2

Panel (a) A schematic diagram outlining the step sequences of chronocoulometry measurement. Schematics showing typical current transients obtained at E_{des} in a chronocoulometry experiment (panel b), corresponding charge transient (panel c) and charge density *versus* potential plot (panel d).

A typical current transient that follows exponential decay with time is shown in panel (b), which is then integrated to obtain charge transients as shown in panel (c). The charge transient was then linearly extrapolated to zero time to obtain the corresponding charge density at the potential E_c. This procedure was repeated at different value of E_c to obtain relative charge density ($\Delta\sigma_m$) as a function of electrode potential plots, as shown schematically in panel (d). Knowing the value of the potential of zero charge from the differential capacity measurements, the absolute charge density (σ_m) at the electrode can be obtained by subtracting the relative charge density at the pzc from the relative charge densities at the potential of interest.

2.5 Data Analysis Procedure for the Determination of Gibbs Surface Excess

Figure 2.3 illustrates the data processing procedure used for the determination of Gibbs surface excesses from the chronocoulometry data. Panel (a) shows the family of charge density *versus* potential curves determined from the potential step experiments (described in section 2.4) for electrolyte containing nonspecifically adsorbing ions, and for solutions of increasing adsorbate concentration. As described by equation (1.23), the area contained between the charge curves that correspond to the given concentration of the adsorbate and the pure electrolyte curve is equal to the surface pressure of the adsorbates. Thus integration of the charge density within this area gives surface pressure curves for different adsorbate concentrations as shown in panel (b). Then, the surface pressure taken at constant values of electrode potential are plotted against the logarithm of adsorbate concentration (panel (c)). These curves are differentiated and then divided by RT to get to get Gibbs surface excess (equation (1.25)) as shown in panel (d).

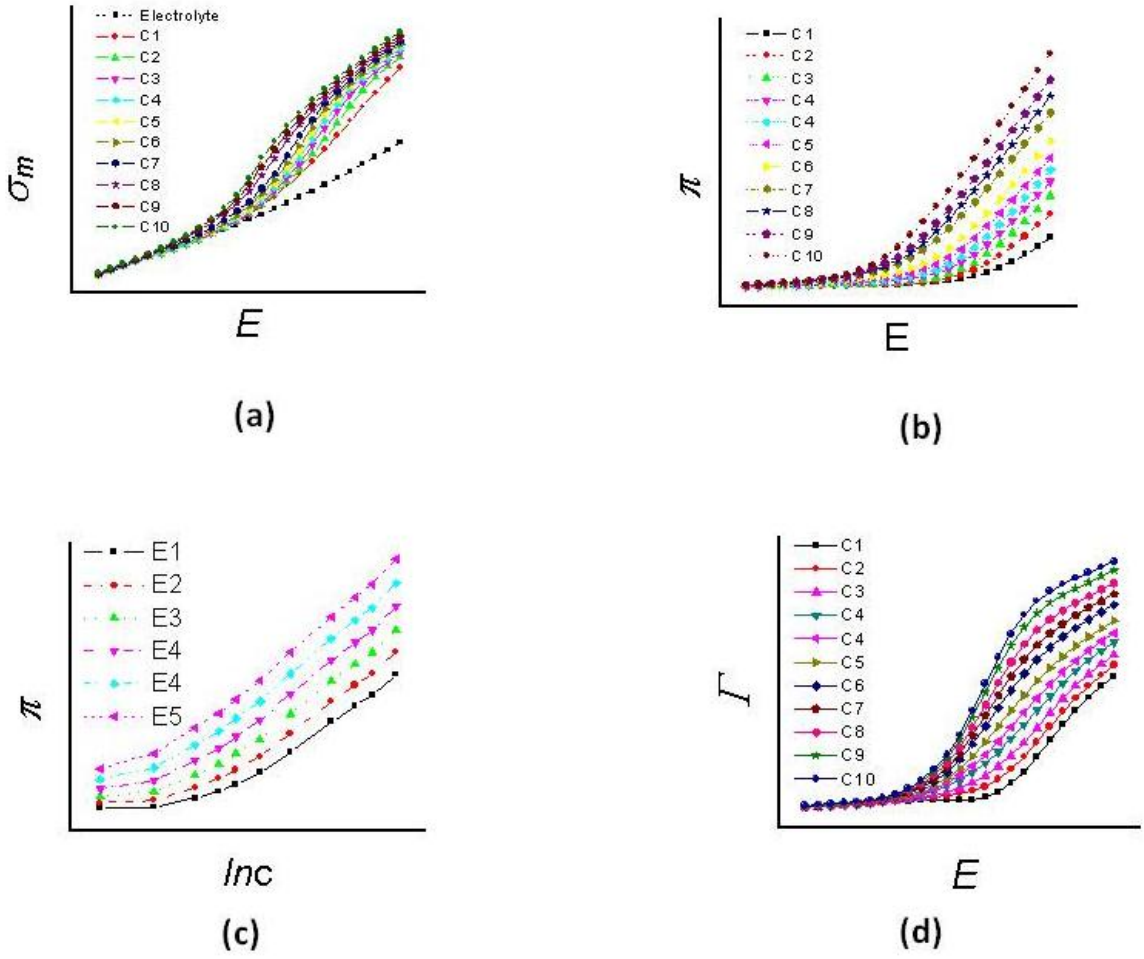

Fig. 2.3

Schematic demonstrating the data analysis procedure for the determination of Gibbs surface excess.

(a) The family of charge density *versus* potential curves determined from the potential step experiments. Dotted line corresponds to electrolyte and the lines with symbols (c_1 to c_2) correspond to variable bulk concentrations of the adsorbing species.

(b) Surface pressure *versus* potential curves that correspond to variable bulk concentrations of the adsorbing species calculated from the charge density *versus* potential curves using equation (1.23).

(c) Surface pressure at constant values of electrode potential plotted against the logarithm of the mole fraction of the adsorbing species.

(d) Gibbs surface excess plot obtained using equation (1.25).

2.6 Single Crystal Preparation and Back-Laue Reflection Method

Commercial gold blocks were pre-etched in *aqua regia* and heated well above its melting temperature in a graphite crucible that is vertically placed in a quartz tube positioned in the coil of an induction oven. The crystallinity and the crystallographic orientation of the electrode depend on the cooling rate and slow cooling is required to ensure the formation of a single crystal. The heating and cooling rates were controlled by means of a PID-controller. A preliminary analysis of the crystallinity of the electrode is done by etching the crystal in *aqua regia* to check for fault-lines corresponding to polycrystallinity.

The orientation of the single crystal electrode with respect to the electrode stem was determined using the back Laue X-ray diffraction technique, which provides the stereographic projection of the lattice planes reflecting X-rays normal to the irradiated crystal surface. In this method a beam of white X-rays is incident on a stationary single crystal and the image of the back reflected X-rays are collected on a photographic plate. These white X-rays are produced with a copper target at an accelerating voltage of 40 kV. The maximum energy of a photon produced by an electron of charge e, accelerated through a voltage V is given by

$$h\nu_{max} = \frac{hc}{\lambda_{min}} = eV \qquad (2.8)$$

Where h is Plank's constant, c is the speed of light and ν_{max} is the highest frequency X-ray produced that corresponds to shortest wavelength λ_{min}. If we use a 40 kV to accelerate the electrons that hit the target,

$$\lambda_{min} = \frac{1239.8}{V} = 0.30 \text{ Å} \qquad (2.9)$$

The λ_{min} value corresponding to this voltage is short enough to determine crystal structure with subnanometer unit cell dimensions. Each crystallographic structure has its own image in reciprocal space. The projection of this image on film and the real space lattice parameters are related through Bragg's law, which gives the relation between the X-ray wavelength λ and the interplanar distance d:

$$2dsin\theta = n\lambda \qquad (2.10)$$

where *n* is the order of the interference.

In Laue back reflection method, since the crystal is exposed to a beam of white radiation, for a given value of *n*, some λ is available in the white radiation to give a Laue spot in a direction making an angle 2θ with the incident X-ray beam. Since *d* and θ are fixed, all orders of the interference *n*, for a given crystal plane will be superimposed on the same spot. Hence the symmetry of the Laue pattern corresponds to the symmetry of the crystal and hence the back-Laue method can be used to identify and orient the crystal of interest.

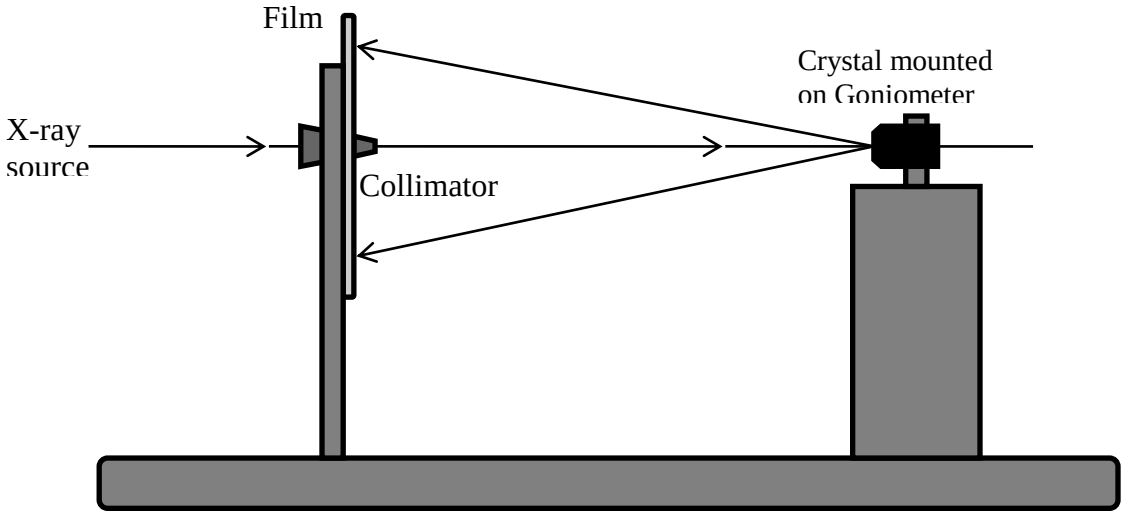

Fig. 2.4
A schematic representation of the Laue back reflection experiment.

A schematic representation of the Laue back reflection experiment used is shown in Figure 2.4. The image of a crystal in reciprocal space can be obtained on a photographic plate. As depicted in the figure, the incident beam of X-rays passes through the collimator, which is fitted at the centre of the cassette containing photographic film. The crystal to be analyzed was placed three centimeters away the film, inside a goniometer on a movable stand with XYZ-translation, and was exposed to the X-ray radiation for fifteen minutes at 40 kV and 20 mA. The crystal was aligned to an estimated 0.1° precision. Typical back-reflection Laue-diffraction patterns for Au(111) and Au(100) crystals are shown in Figure 2.5. An example of the Laue-diffraction pattern before the final orientation is shown in Figure 2.5a, and the Laue-diffraction pattern for a well oriented crystal is shown in Figure 2.5b.

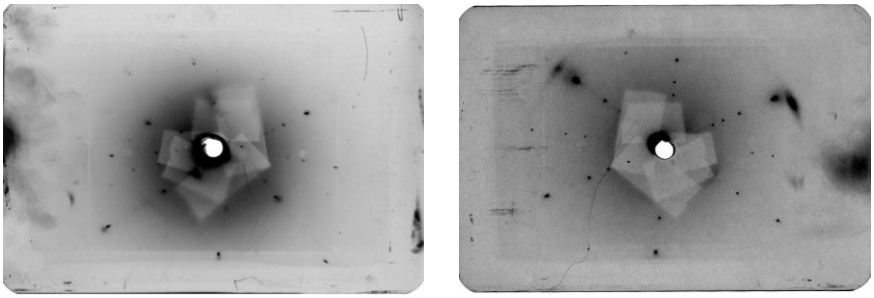

Au(100) **Au(111)**

(a) **(b)**

Fig. 2.5
Panel (a) A typical Laue diffraction pattern from Au(100) single crystal before final orientation.
Panel (b) A typical Laue diffraction pattern from Au(111) single crystal after final orientation**.**

Aligned single crystal electrodes were fixed in a polypropylene holder with epoxy resin, after which the X-ray pattern was taken once more to make sure that the crystal did

not change its orientation during the solidification of the resin. The electrode was then cut and polished using successive grades of sandpaper (120, 220, 320, 400, 600 grit). During this process, care must be taken to prevent the surface edges from becoming rounded. Polishing was done in a figure eight pattern which removes the layers of the surface randomly and uniformly. After sandpaper, a mirror finish on the electrode surface was obtained by polishing the crystal with decreasing size (6, 3, 1, 0.5 μm) diamond pastes (cloth and diamond paste were obtained from LECO). After polishing, the epoxy was removed by soaking the electrode in chloroform. Then the electrode was electropolished by repeated oxidation of the electrode with a current density of 1 mA/cm^{-2} and subsequent dissolution of the oxide thus formed in 10% hydrochloric acid. Further, the electrode was cycled within the typical full oxidation region for about 3 h in perchloric acid electrolyte. Finally, the electrode was repeatedly flame annealed in a natural gas flame until a characteristic cyclic voltammogram of the corresponding low-index electrode is obtained.

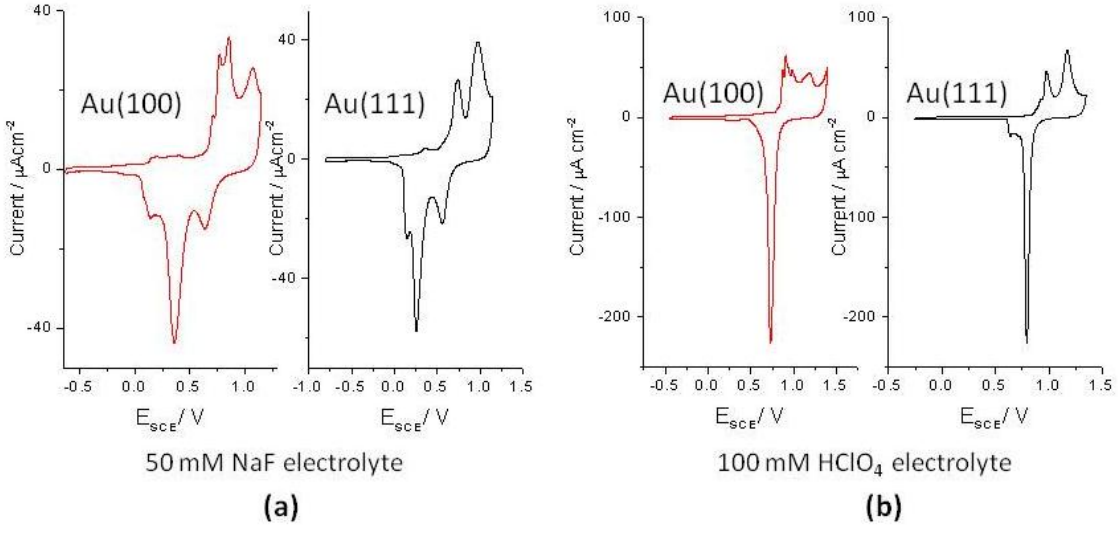

Fig. 2.6
Representative cyclic voltammograms of Au(100) and Au(111) single crystals in sodium fluoride (panel (a)) and perchloric acid (panel (b)) electrolytes.

Characteristic cyclic voltammograms of Au (111) and Au(100) electrodes in both acidic and mildly basic electrolytes are shown in Figure 2.6. These curves are in agreement with the cyclic voltammograms obtained under similar conditions reported in the literature.[1] The potential of zero charge (pzc) has been evaluated for both of these crystals, which would further test the identity of the crystal. Differential capacitance measurements in dilute (5 mM) non-specifically adsorbing NaF electrolytes gave pzc values of 270 mV and 65 mV, respectively, for Au(111) and Au(100) crystals which is comparable with the pzc values reported in the literature as shown in Table 2.1.

	Potential of zero charge vs SCE		**References**
	Present study	**Literature**	
Au(111)	270 mV	260 – 290 mV	3, 4, 5
Au(100)-1x1	65 mV	55 - 80 mV	6, 7, 8

Table 2.1
Comparison of the potential of zero charge of Au(111) and Au(100) electrodes used for the present study with literature reports.

2.7 UV-Vis Analysis of Nanoparticles

Gold nanoparticles of diameter larger than *ca.* 2 nm interact strongly with visible light, giving gold nanoparticle suspensions an intense ruby red color, a phenomenon known as surface plasmon resonance (SPR). The oscillating electric field of light interacts with the conduction electrons at the surface of the nanoparticle, causing them to

collectively oscillate relative to the metal core, resulting in scattering and absorption of the light at the corresponding frequency. The frequency of this oscillation depends on the electron density and on the shape and size of the electronic charge distribution on the nanoparticle surface, and so the dielectric properties of the environment (solvent, ligand shell) are important in determining the SPR frequency. In addition, when plasmonic nanoparticles come close to each other, their surface plasmons couple and the conduction electrons on the nanoparticles begin to oscillate together at a lower frequency. The wavelength (or frequency) corresponds to the surface plasmon resonance (SPR) and can be measured using UV-Vis spectroscopy. UV-Vis spectra were obtained using Varian Cary 50 Spectrophotometer from Agilent Technologies, and a 1 cm path length quartz cuvette was used. Cuvettes were cleaned using warm water with detergent, then with copious amounts of distilled water, finally rinsed thoroughly with Milli-Q water and allowed to dry at room temperature.

Reference List

1. Hamelin, A. Cyclic voltammetry at gold single-crystal surfaces. Part 1. Behaviour at low-index faces. *Journal of Electroanalytical Chemistry* **1996,** *407* (1-2), 1-11.

2. Kolb, D. M.; Schneider, J. Surface reconstruction in electrochemistry: Au(100-(5 x 20), Au(111)-(1 x 23) and Au(110)-(1 x 2). *Electrochimica Acta* **1986,** *31* (8), 929-936.

3. Stolberg, L.; Morin, S.; Lipkowski, J.; Irish, D. E. Adsorption of pyridine at the Au (111)-solution interface. *Journal of Electroanalytical Chemistry and Interfacial Electrochemistry* **1991,** *307* (1-2), 241-262.

4. Kunze, J.; Burgess, I.; Nichols, R.; Buess-Herman, C.; Lipkowski, J. Electrochemical evaluation of citrate adsorption on Au(111) and the stability of citrate-reduced gold colloids. *Journal of Electroanalytical Chemistry* **2007,** *599* (2), 147-159.

5. Brosseau, C. L.; Sheepwash, E.; Burgess, I. J.; Cholewa, E.; Roscoe, S. G.; Lipkowski, J. Adsorption of N-Decyl-N,N,N-trimethylammonium Triflate (DeTATf), a Cationic Surfactant, on the Au(111) Electrode Surface. *Langmuir* **2006,** *23* (4), 1784-1791.

6. Stolberg, L.; Lipkowski, J.; Irish, D. E. Adsorption of pyridine at the Au (100)-solution interface. *Journal of Electroanalytical Chemistry and Interfacial Electrochemistry* **1987,** *238* (1-2), 333-353.

7. Bohnen, K. P.; Kolb, D. M. Charge- versus adsorbate-induced lifting of the Au(100)-(hex) reconstruction in an electrochemical environment. *Surface Science* **1998,** *407* (1-3), L629-L632.

8. Kolb, D. M. Reconstruction phenomena at metal-electrolyte interfaces. *Progress in Surface Science* **1996,** *51* (2), 109-173.

Chapter 3

Insight into Halide Induced Aggregation of Dimethylaminopyridine Stabilized Gold Nanoparticles

3.1 Introduction

In recent years, there have been a number of reports of water-dispersible gold nanoparticles stabilized by charged thiol monolayers,[1-5] citrate ions[6,7] or pyridine derivatives.[8-13] Among these, 4-(dimethylamino)pyridine (DMAP) capped gold nanoparticles have been reported to be stable in aqueous solutions over a much wider range of solution pHs[9,12] compared to other popular water-dispersible gold nanoparticles. In order to predict and control the stability of these nanoparticles, it is essential to have a well understood description of the state of the ligand on the gold surface. Unfortunately, obtaining information on the nanoparticle-ligand interface is technically challenging. However, analogous systems on two-dimensional gold electrodes can be readily treated using the thermodynamics of adsorption on ideally polarized electrodes.[14] In this direction, an electrochemical evaluation of DMAP adsorption on polycrystalline gold has been previously reported by Barlow and Burgess,[15] which demonstrated that DMAP forms a vertical-aligned monolayer on the surface of gold in basic electrolyte solutions. According to this report, in acidic solutions, the adsorbed monolayer consists of flat-lying dimethylaminopyridinium ($DMAPH^+$) ions at negative surface charge densities or a low coverage vertical film of DMAP at positively charged polycrystalline gold surfaces. Both states of adsorption correspond to low surfactant coverages in acidic solutions,

which is consistent with the observed aggregation of DMAP stabilized gold nanoparticles at lower pH.

Apart from pH dependent studies, it is also important to consider the stability of water dispersible MPNs in different chemical environments. A systematic study of the stability of these monolayer protected surfaces in different chemical environments is essential information that will affect application possibilities. For example, many nanoparticle-based nucleic acid[16,17] and protein[18-20] assays rely on colorimetric detection of metal nanoparticle aggregation induced by specific analytes. In these biological assays it is important to discriminate between aggregation induced by the target analyte and aggregation caused by the chloride-containing, physiological matrix. The influence of halides on colloidal metal systems has been investigated with Raman spectroscopy where 2-3 orders of magnitude increases in Surface Enhanced Raman Spectroscopy (SERS) signals have been reported upon the addition of halide ions to silver colloids[21]. Conversely, the presence of halide containing species usually leads to irreversible aggregation of gold nanoparticle systems in both aqueous[22-25] and non-aqueous[26,27] solutions. Historically, the observed aggregation of electrostatically stabilized gold sols upon the addition of halide salt solutions[28] has largely been explained by simple screening effects and little attention is placed on the possibility that the aggregation is caused by the competitive adsorption of halide ions on the metal surface. There is a fundamental difference between these mechanisms as the latter implies the replacement of the stabilizing ligand by halide ions while the former inherently assumes that the original monolayer remains unperturbed.

In this chapter, an electrochemical evaluation of halide-induced aggregation of water-dispersible gold nanoparticles, nominally protected by a monolayer of the DMAP ligand is described. By combining UV-Vis spectroscopic studies of the colloidal domain with electrochemical measurements on two-dimensional gold, the competitive adsorption between DMAP and chloride ions for adsorption sites on the gold surface is described. A qualitative evaluation of halide induced aggregation of DMAP stabilized gold nanoparticles has been carried out using differential capacity measurements, indicating the direct correlation between aggregation of nanoparticles and the competitive adsorption of DMAP and halide at the gold/solution interface. Furthermore, a detailed quantitative analysis of the DMAP/chloride adsorption at the interface has been done using chronocoulometry measurements to provide insight into the surface concentration of DMAP/chloride at the nanoparticle interface.

3.2 Experimental

3.2.1 Synthesis of 4-(N,N-Dimethylamino)pyridine stabilized gold nanoclusters

Gold nanoparticles stabilized with 4-(dimethylamino)pyridine (DMAP) were prepared by ligand exchange and phase transfer (toluene/water) of functionalized nanoparticles by following the method first described by Gittins and Caruso.[9] In a typical nanoparticle synthesis procedure, an aqueous solution of hydrogen tetrachloroaurate (750 mg in 50 mL) was stirred with tetraoctylammoniuim bromide (TOAB, 3.23 g) in 100 mL toluene until all the gold salt is transferred to the organic layer (*ca.* 15 minutes). The gold complex transfers to the organic layer where it is reduced with fresh aqueous sodium borohydride solution (525 mg in 25 mL water) providing ruby red colored gold nanoparticles in the organic layer. After another 12 h of stirring, the gold nanoparticles

in the organic layer are extracted and washed with Millipore water. TOAB stabilized gold nanoparticles thus obtained were phase transferred from the organic phase to the aqueous phase by adding an equal volume of an aqueous solution of DMAP into the organic phase of TOAB protected nanoparticles. Immediate phase transfer of the nanoparticles from the organic layer to the aqueous layer was monitored by the ruby colour transference from the organic to the aqueous layer. The as-prepared DMAP protected gold nanoparticles were water dispersible and were stored at 4 ^{o}C. Nanoparticle formation was further confirmed by UV-Vis spectroscopy and transmission electron microscopy.

3.2.2 UV-Vis analysis of MPN's stability in the presence of halide ions

The effect of chloride on DMAP stabilized nanoparticles was monitored by recording the absorbance spectrum in the 300- 800 nm region with a Varian Cary 50 Bio UV-Vis spectrophotometer in standard quartz cuvettes. The as-synthesized DMAP stabilized nanoparticles were further diluted to adjust the absorbance intensity to approximately unity and the pH was adjusted by adding $HClO_4$. Following the addition of 5 mM sodium halide to the nanoparticle solution the aggregation of the gold nanoparticles was followed by monitoring spectra at equal intervals of time. All glassware used for the synthesis and UV-Vis analysis of the nanoparticles were treated with *aqua regia* (3 parts HCl, 1 part HNO_3), rinsed in Millipore water, and oven dried prior to use.

3.2.3 Zeta potential measurements

Zeta potential measurements and quasi-elastic light scattering (QELS) were performed at room temperature (20±2 °C) using a Malvern Instruments (Worcestershire,

U.K.) ZetaSizer Nano Zs. Estimation of the particle size from QELS revealed that the particles had an average diameter of 10 nm and were reasonably monodisperse (±2 nm). Transmission electron microscopy (TEM) images (*vide infra*) provided the same average size and distribution of the nanoparticles.

3.2.4 TEM measurements

Transmission electron micrographs (TEM) were obtained with a Philips 410 microscope operating at 100 kV. Concentrations of the nanoparticle and halide solutions were the same as that used for UV-vis analysis. Thirty minutes after the addition of halides, the nanoparticle solution was dropcast on a carbon-coated copper TEM grid and evaporated in air.

3.2.5 Electrochemical measurements

Electrochemical experiments were performed to investigate the adsorption and co-adsorption of DMAP and halide ions at the gold/electrolyte interface at various pH. The measurements were carried out using a customized electrochemical setup (details are provided in Chapter 2). The working electrodes in these experiments were polycrystalline gold beads formed by melting gold wire (99.99% Alfa Aesar) with a propane torch. The gold bead, at the end of the gold wire, was immersed in aqua regia (3:1 HCl : HNO_3) to remove surface impurities and then remelted. This procedure was repeated iteratively until the molten gold displayed no visible contaminants. The electrodes then electrochemically polished in 50 mM $KClO_4$ (Aldrich, double-recrystallized) by cycling through the surface oxidation / oxide stripping peaks (-0.8V < E < 1.25V *versus* SCE). The electrolyte solution, 50 mM $KClO_4$, was adjusted to pH 5.5, 7.5 or 9.7 by adding either $HClO_4$ (ultrahigh purity) or KOH (semiconductor grade, 99%) prior to the

electrochemical experiment. The electrolyte solution was deaerated by purging with argon for at least 30 min prior to the experiments, and an argon blanket was maintained over the solution throughout the experiment. Measurements were carried out at room temperature (20±2 ^{o}C).

In the chronocoulometry method (details provided in Chapter 2), the gold electrode was held at a base potential, E_{base}, for 30 s, then the potential was stepped to the variable value of interest, E_c, and held for a sufficient time to achieve adsorption equilibrium (between 180 to 60 s depending on the concentration of DMAP and halide). To desorb DMAP and halide from the electrode interface, a negative potential, E_{des} was applied for 200 ms and the current transient corresponding to desorption was measured. The potential was then stepped back to the base value and the cycle was repeated using a new value of E_c. The values of E_{base} and E_{des} were -450 mV and -900 mV, respectively. To assist mass-transfer, the electrolyte solution was stirred when the electrode potential was at E_c and E_{base}, but the stirring was stopped 10 s before the applying desorption potential, E_{des}.

3.3 Results and Discussions

3.3.1 UV-visible spectroscopy

The stability of DMAP-gold MPNs in the presence of halide ions was investigated by UV-Vis spectroscopy of the particles' surface plasmon. Figure 3.1 presents the effect of halide on the absorption spectra of diluted DMAP-gold nanoparticles at three different representative pHs. In all the panels in Figure 3.1 dotted lines correspond to the spectra before the addition of any halide and solid lines correspond to the spectra recorded 30

mins after the addition of halide; NaF (first column) or NaCl (second column). Corresponding TEM images are shown with the UV-Vis spectra to further confirm the pH / halide dependent aggregation of the nanoparticles. As shown in Figure 3.1a, at pH 9.5, the addition of 5 mM NaF leads to a very slight decrease in the absorbance arising from small dilution effects. Importantly, there is no evidence of a red-shift in the maximum wavelength of absorption (λ_{max} = 520 nm) indicating that the addition of a simple electrolyte has no aggregation affects at this pH. Similarly, no red-shift in the peak is observed upon the addition of NaF, for spectra obtained at pH 7.5 (Figure 3.1b) also. In Figure 3.1c, even in the absence of NaF, the absorbances are systematically lower compared to the equivalent spectra shown in Figures 3.1a and 3.1b. Furthermore, the plasmon absorption maximum has been shifted ~5 nm to 525 nm and there is an increase in absorption at longer wavelengths, which is indicative of particle flocculation.[29] As in the case of the more basic pHs, the addition of NaF has little effect on the UV-Vis and it can be understood that the slight flocculation observed is due to low pH induced changes in the coverage of DMAP (or dimethylaminopyridinium) on the surface of the gold.[15] Gandubert and Lennox observed the lower limit of pH stability for Au-DMAP nanoparticles to be ca. 4.5 based on their titrations using acetic acid.[12] The small discrepancy between their data and the left-hand column of Figure 3.1 most likely stems from the larger DMAP dilutions used in the present study.

The second column in Figure 3.1 presents the results of the analogous experiments described above using 5 mM NaCl in place of 5 mM NaF. The similarity between panels 3.1a and 3.1d reveals that the identity of the halide has little to no effect on the stability of Au-DMAP nanoparticles at high pH values. This is however not the case, when the pH is

lowered to 7.5. Panel 3.1e clearly shows a significant red-shift 30 minutes after the addition of NaCl to the cuvette indicating that the addition of halide ions leads to some form of aggregation. It is important to note that the spectral response is stable over a time interval of at least 6 h and neither a further red-shift nor increased absorbance at longer wavelengths are observed with increasing time. The final panel, f, in Figure 3.1 shows the most dramatic evidence of chloride induced destabilization of the DMAP-Au nanoparticles.

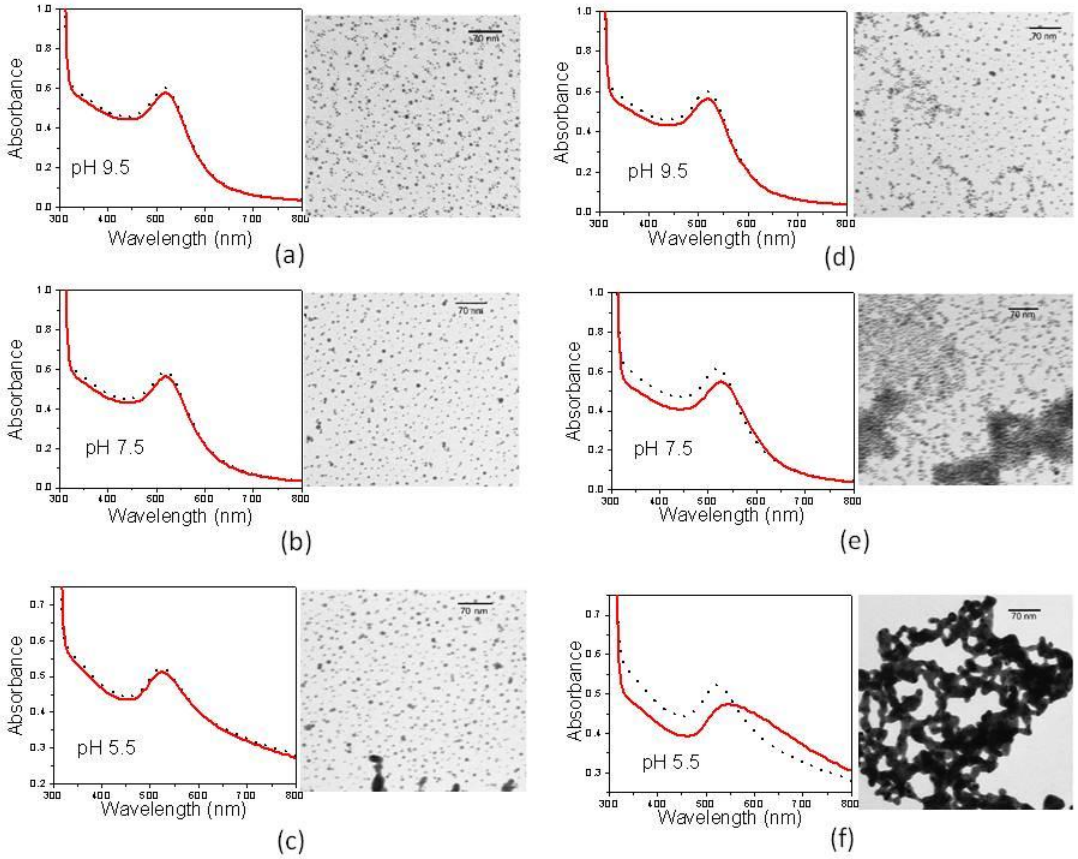

Fig. 3.1

UV-visible absorbance spectra and corresponding TEM images of aqueous dispersions of DMAP stabilized gold nanoparticles in the presence of 5 mM NaF (a,b,c) and 5 mM NaCl (d,e,f). Measurements were made at pH 9.5 (a,d), pH 7.5 (b,e) and pH 5.5 (c,f). (The scale bar on TEM images corresponds to 70 nm).

Thirty minutes after the addition of NaCl the peak maximum has shifted nearly 25 nm toward the red end of the visible spectrum and there is a pronounced increase in absorbance at wavelengths larger than 600 nm. This system is not stable and further red-shifting and increasing long wavelength absorbance is observed with increasing time. The UV-Vis spectral analysis shown in Figure 3.1 demonstrates that the solution pH and the nature of the halide *both* play an important role in the stability of DMAP-Au nanoparticles.

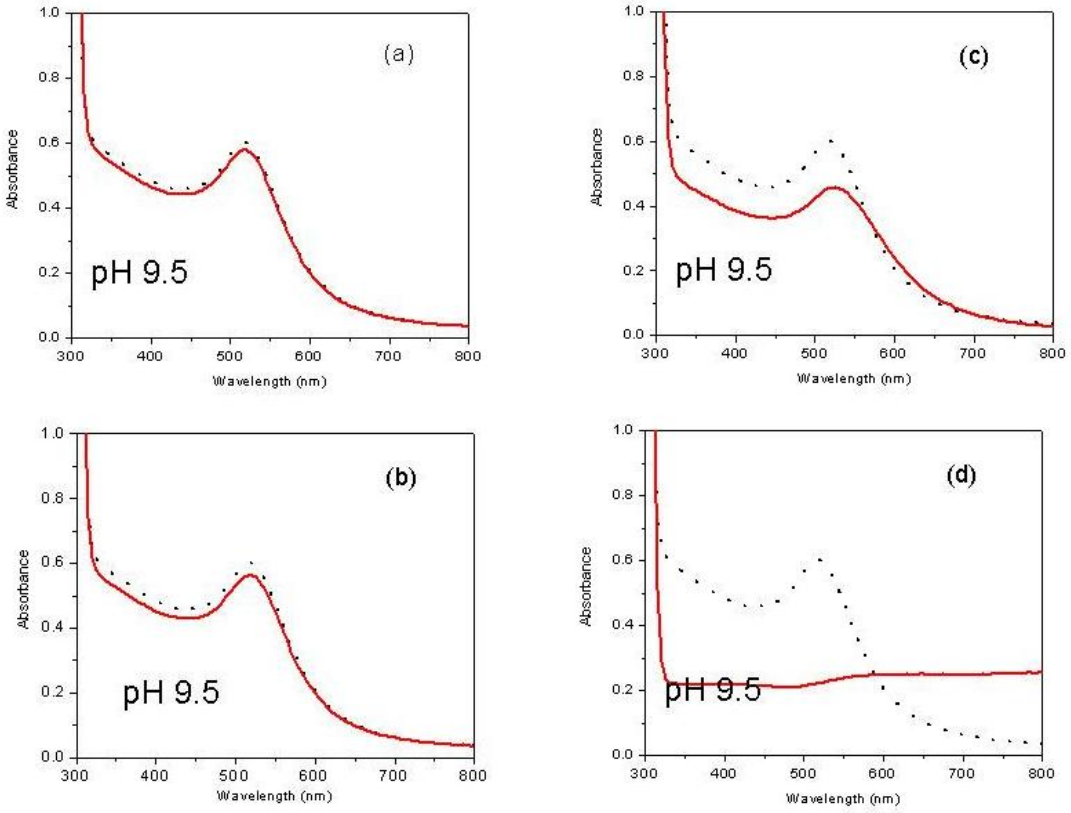

Fig. 3.2

UV-visible absorbance spectra of aqueous dispersions of DMAP stabilized gold nanoparticles in the presence of (a) 5 mM NaF, (b) 5 mM NaCl, (c) 5 mM NaBr, (d) 5 mM NaI, at pH 9.5.

The stability of DMAP-gold nanoparticles in the presence of halide ions was further investigated by measuring the surface plasmon in the presence of other halides. Figure 3.2 presents the absorption spectra of diluted DMAP-gold NANOPARTICLEs at pH 9.5 before (dotted line) and 30 minutes after (solid line) the addition of different halides. As shown in Figure 3.2, the addition of NaF (Figure 3.2a) or NaCl (Figure 3.2b) has little effect in the absorbance spectra, whereas, the peak is seen to be significantly red-shifted and broadened with the addition of NaBr (Figure 3.2c), indicating substantial nanoparticle aggregation in the presence of bromide even at high pH. Additionally, this spectrum recorded after 30 minutes is not stable and further red-shifting is observed with increasing time. The effect is even larger with the addition of NaI (Figure 3.2d) as the plasmon peak has almost disappeared with the addition of NaI. Figure 3.2 demonstrates that the aggregation of nanoparticles is very much dependent on the nature of halide, and follows the order $I^- > Br^- > Cl^- > F^-$.

These results provide some initial insight on the aggregation mechanism. One might suspect that the addition of an electrolyte can destabilize nanoparticles by shielding their electrostatic repulsion forces,[28] in which case all symmetric salts should behave identically. If the stability of these monolayer protected nanoparticles (MPNs) was solely driven by electrostatic considerations the addition of different halides should lead to the same extent of aggregation. On the other hand, even the partial loss of DMAP from the gold surfaces would greatly decrease the steric stability of the MPNs. Given that, the specific adsorption of halides on gold follows the order $I^- > Br^- > Cl^- > F^-$,[30] the UV-Vis spectral analysis indicate that halide ions most likely induces aggregation by competing

with DMAP adsorption sites on the gold surface rather than by electrostatically screening the individual nanoparticles.

3.3.2 Electrochemical experiments

UV-Vis spectral studies demonstrated the influence of halide ions on aggregation of DMAP stabilized gold nanoparticles. In an attempt to understand this observation at the molecular level, the halide induced aggregation of DMAP stabilized MPNs was investigated with the help of electrochemical analysis of DMAP adsorption on two dimensional (centimeter scale) polycrystalline gold. In this approach, differential capacity and chronocoulometry were used to study DMAP-halide co-adsorption on gold electrodes as a function of electrode potential. Differential capacity measurements give a qualitative description of the phenomenon at the interface while quantitative information can be obtained from chronocoulometry experiments. The use of planar gold surfaces provides a reproducible metal surface and allows better control of the concentrations and chemical identity of added species. Successful extrapolation of thermodynamic data obtained from electrochemical measurements to explain the behavior of gold colloids and nanoparticles has been previously reported.[14,15]

3.3.3 Differential capacity

Differential capacity measurements were carried out to obtain an overall qualitative picture of the DMAP/halide adsorption on gold by studying the competitive adsorption of DMAP with fluoride, chloride and bromide on polycrystalline gold. Capacity measurements provide information about the adsorbed species at the interface by comparing changes in capacity due to adsorbed species at the interface. The total

interfacial capacitance, C is composed of the series combination of an inner layer, or Helmholtz capacity C_H and a diffuse layer capacitance, C_D.

$$\frac{1}{C} = \frac{1}{C_H} + \frac{1}{C_D} \tag{3.1}$$

The Helmholtz capacity is given by

$$C_H = \frac{\epsilon_r \epsilon_0}{x} \tag{3.2}$$

where ϵ_r is the relative permittivity, ϵ_0 is the permittivity of free space and x is the thickness of the adsorbed molecules.[31] From equation 3.1, the contribution from C_D can only be neglected when C_H is very small, which is a reasonable assumption when there is a compact organic adlayer at the interface. Similarly, equation 3.2 does not correspond faithfully to the measured capacity when there are ions having high relative permittivity (*viz.* halides) adsorbed at the interface. Nevertheless, it is convenient to consider only the inner layer capacitance for the following qualitative comparison. Hence the displacement of DMAP by halides ions at the interface is indicated by an increase in the measured capacitance; i.e., the Helmholtz capacitance increases with the adsorption of inorganic ions having larger permittivity and smaller size.

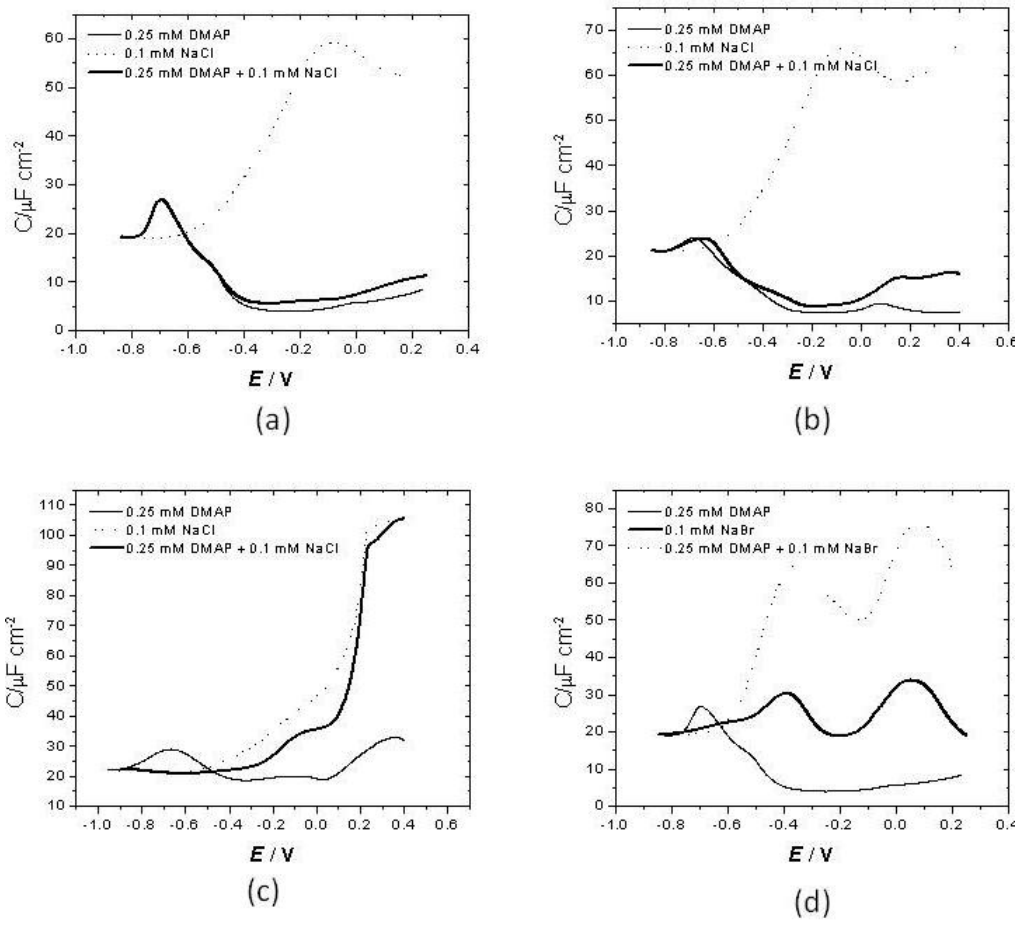

Fig. 3.3

Differential capacity curves showing chloride and DMAP competitive adsorption at the polycrystalline gold electrode at (a) pH 9.5, (b) pH 7.5, (c) pH 5.5, and (d) bromide DMAP competitive adsorption at pH 9.5.

In Figure 3.3, differential capacity curves corresponding to 0.25 mM DMAP bulk concentration (in the absence of halides, indicated by thin solid lines), 0.1 mM NaCl (in the absence of DMAP, indicated by dotted lines) as well as capacity curves corresponding to the addition of 0.1 mM NaCl to the electrolyte containing 0.25 mM DMAP (indicated by bold solid lines) at three representative pHs on polycrystalline gold are shown in panels (a), (b) and (c), respectively. The supporting electrolyte used in all

these experiments was 50 mM $KClO_4$. The low values of the differential capacity at potentials greater than -0.4 V for the DMAP only solution indicate that a DMAP layer is formed on the electrode surface. The differential capacity curves corresponding to 0.1 mM NaCl bulk concentration (dotted lines) are consistent with a monolayer of chloride at the interface. Differential capacity curves corresponding to a solution containing both 0.25 mM DMAP and 0.1 mM NaCl in solution (bold solid lines) qualitatively demonstrate the extent of DMAP replacement by chloride at a given pH. At pH 9.5 (Figure 3.3a), the bold solid line is roughly identical to the thin solid line, indicating the addition of chloride has not significantly influenced the adsorbed DMAP monolayer at the interface. At pH 7.5 (Figure 3.3b), the bold line has notably increased with respect to the thin solid line, clear indication of DMAP replacement by chloride at the interface. At pH 5.5 (Figure 3.3c), the increase in capacity with the addition of chloride is very dramatic (bold solid line) and is more close to the chloride curve (dotted line) than the DMAP only curve (thin solid line). This shows that chloride displaces DMAP from the surface to a larger extent at lower pHs.

The nature of the halide also has a significant influence in the displacement of DMAP at the interface, which is verified by comparing Figures 3.3a and 3.3d. Figure 3.3 shows that, in contrast to the extent of DMAP displacement by chloride at pH 9.5, (Figure 3.3a), the capacity has significantly increased after the addition of bromide even in basic solutions (Figure 3.3d). The extent of DMAP displacement by halide can easily be understood by noting the difference between the thin and bold solid lines. This demonstrates that bromide displaces DMAP more effectively than chloride at the interface, which confirms that the halide induced aggregation of DMAP-Au nanoparticles

is caused by the displacement of DMAP molecules by halide ions at the interface. These differential capacity measurements show that both electrolyte pH and nature of the halide have significant influence in displacing DMAP molecules from the gold surface. The effect of pH and the nature of halide on the DMAP displacement at the gold/solution interface studied using differential capacity measurements show that halide induced aggregation of gold nanoparticles results from the competitive adsorption of halide ions with DMAP molecules at the interface.

The adsorption behavior of DMAP on polycrystalline gold has been thoroughly studied by Barlow and Burgess to reveal the orientation of DMAP on the surface is highly dependent on the electrode potential and electrolyte pH.[15] At pH values at or above the primary pK_a of dimethylaminopyridinium ($DMAPH^+$) (~9.7), the adsorbed species is the deprotonated form of DMAP that adsorbs vertically on the electrode surface via its endocyclic nitrogen. In relatively acidic solutions (pH~4.5), either DMAP or $DMAPH^+$ is adsorbed on the surface, depending on the electrode potential. At relatively negative potentials, the adsorbed species is $DMAPH^+$ that lies nearly flat on the surface. When the electrode is positively charged (i.e., at relatively more positive potentials), the adsorbate undergoes a phase transition to a vertical orientation and concurrently deprotonates to DMAP. The horizontal state of adsorption of $DMAPH^+$ on the surface is termed as state I, and the vertical state of adsorption is termed state II. A detailed description of the orientational changes of DMAP(H^+) with pH, potential and crystallographic orientation of the gold surfaces is discussed in Chapter 4. Though a detailed discussion on the orientational changes of the adsorbed species is not the focus in

this chapter, state I and state II adsorptions are frequently used while describing the adsorption of DMAP on polycrystalline gold at different pHs.

3.3.4 Chronocoulometry

In order to provide quantitative information on the competitive adsorption of DMAP and halide at the interface, this mixed system was investigated using chronocoulometry. Chronocoulometry experiments were performed on two series of solutions. Series I solutions consisted of pH adjusted electrolyte (50 mM $KClO_4$), a constant formal DMAP concentration (0.25 mM), and variable concentrations of sodium chloride. Series II solutions were the complement experiments where the concentration of chloride was held constant (0.25 mM) and the DMAP formal concentration was varied.

Figure 3.4 presents the results of the chronocoulometry experiments performed at pH 9.5. In both panels the dotted black lines represent the charge density data for the pH-adjusted supporting electrolyte in the absence of both chloride and DMAP. Focusing on series I (Figure 3.4a), it can be observed that in the presence of 0.25 mM DMAP (and in the absence of chloride) the charge density curve (black line with symbols) indicates a single state of molecular adsorption on the electrode at this pH[31]. Figure 3.4a shows that the addition of chloride ions to the DMAP containing electrolyte has very little effect, with only a small increase in charge density being observed for E > -0.25V. The family of σ_m-E plots in the presence of 0.25 mM DMAP and variable chloride concentration are essentially superimposable and almost completely independent of the solution concentration of chloride ions. This observation suggests that the surface of the electrode

remains covered with a monolayer of vertically oriented DMAP even with an approximately 30 fold higher concentration of chloride ions in solution.

The situation is markedly different when the chloride concentration is held constant and the DMAP concentration is varied. Figure 3.4b shows a pronounced difference between the charge density curves for 50 mM $KClO_4$ (pH adjusted to 9.5) plus 0.25 mM NaCl in the absence (black line with symbols) and presence of DMAP (lines with colored symbols). It is quite evident that the addition of DMAP causes the σ_m-E plots to appear much like the charge density curves for DMAP in the absence of chloride (see Figure 3.4a). Addition of more DMAP causes the inflection nominally observed at -0.7 V *versus* SCE to shift cathodically. These curves are essentially identical to those obtained in the complete absence of chloride as reported previously[32]. Clearly the electrode responds to incremental changes in the solution DMAP concentration under these conditions. In other words, the chloride ions are not restricting or competing with DMAP for adsorption sites on the gold surface. The cumulative results shown in Figure 3.4 lead to the conclusion that at high pH, the presence of chloride has little to no effect on the adsorbed monolayer of DMAP and should not perturb the stability of DMAP-Au nanoparticles. The experiments described in Figure 3.4 were repeated at pH 5.5 and the results are shown in Figure 3.5. Figure 3.5a corresponds to series I solutions. As the pK_a of its endocyclic nitrogen is 9.7,[33] the molecule exists in the bulk of the electrolyte almost exclusively as the $DMAPH^+$ conjugate acid in neutral and acidic pHs. In this chapter, whenever the concentration of DMAP in solution is mentioned, it represents the formal concentration ($F_{DMAP} = c_{DMAP} + c_{DMAPH^+}$). DMAP/$DMAPH^+$ is used when the adsorbed species can be either the base or conjugate acid.

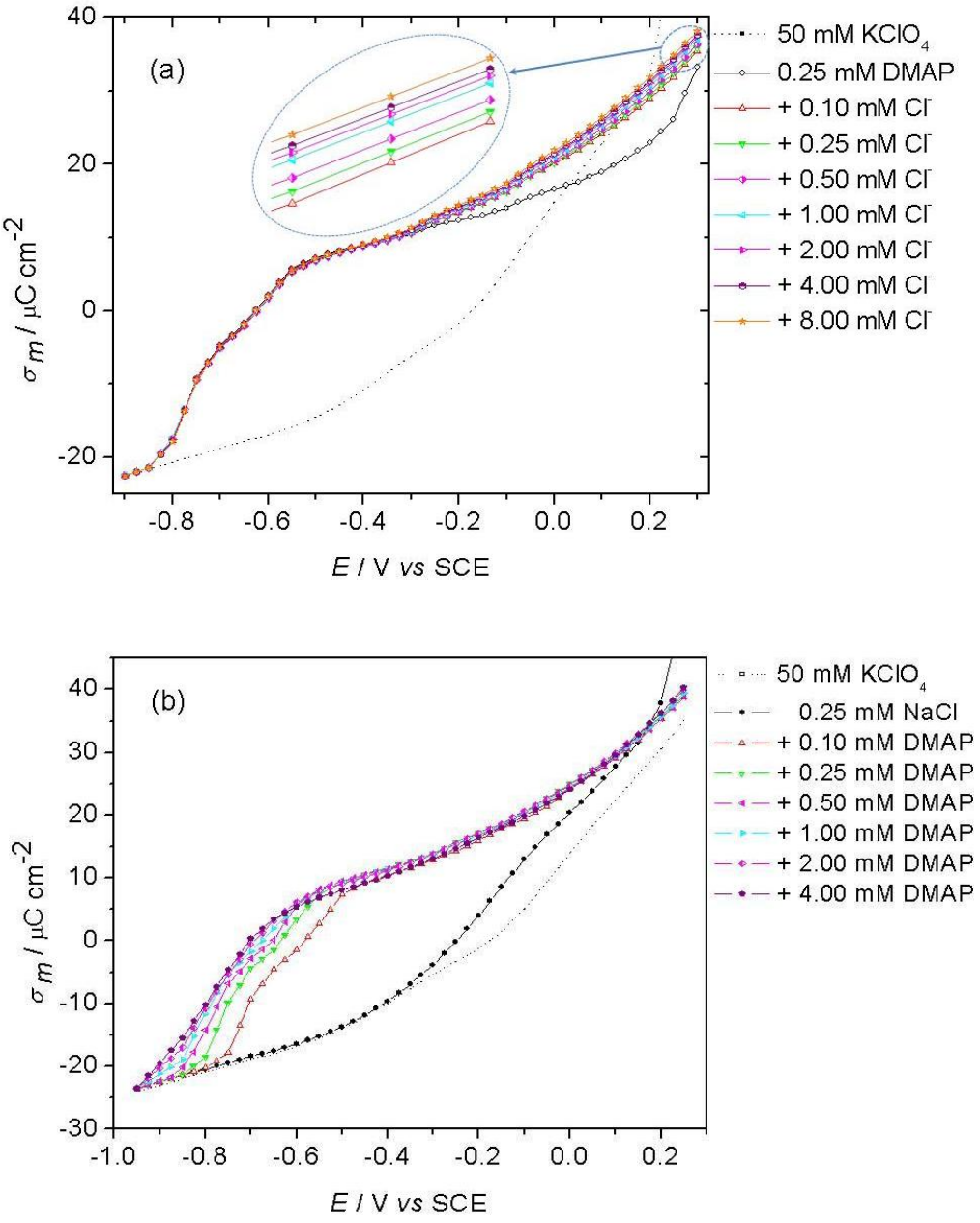

Fig. 3.4

Charge density versus electrode potential curves for polycrystalline gold in 50 mM $KClO_4$ supporting electrolyte at pH 9.5 (----) and series I and II of solutions.

(a) Series I : 0.25 mM DMAP in the absence (○) and in the presence of the following sodium chloride concentrations 0.1 mM (△), 0.25 mM(▽), 0.5 mM(◆), 1 mM(◁), 2 mM(▷), 4 mM(◓), 8 mM(★).

(b) Series II : 0.25 mM NaCl in the absence (●) and in the presence of the following DMAP concentrations 0.1 mM (△), 0.25 mM (▽), 0.5 mM (◀), 1 mM (▶), 2mM (◆), 4 mM (⬟).

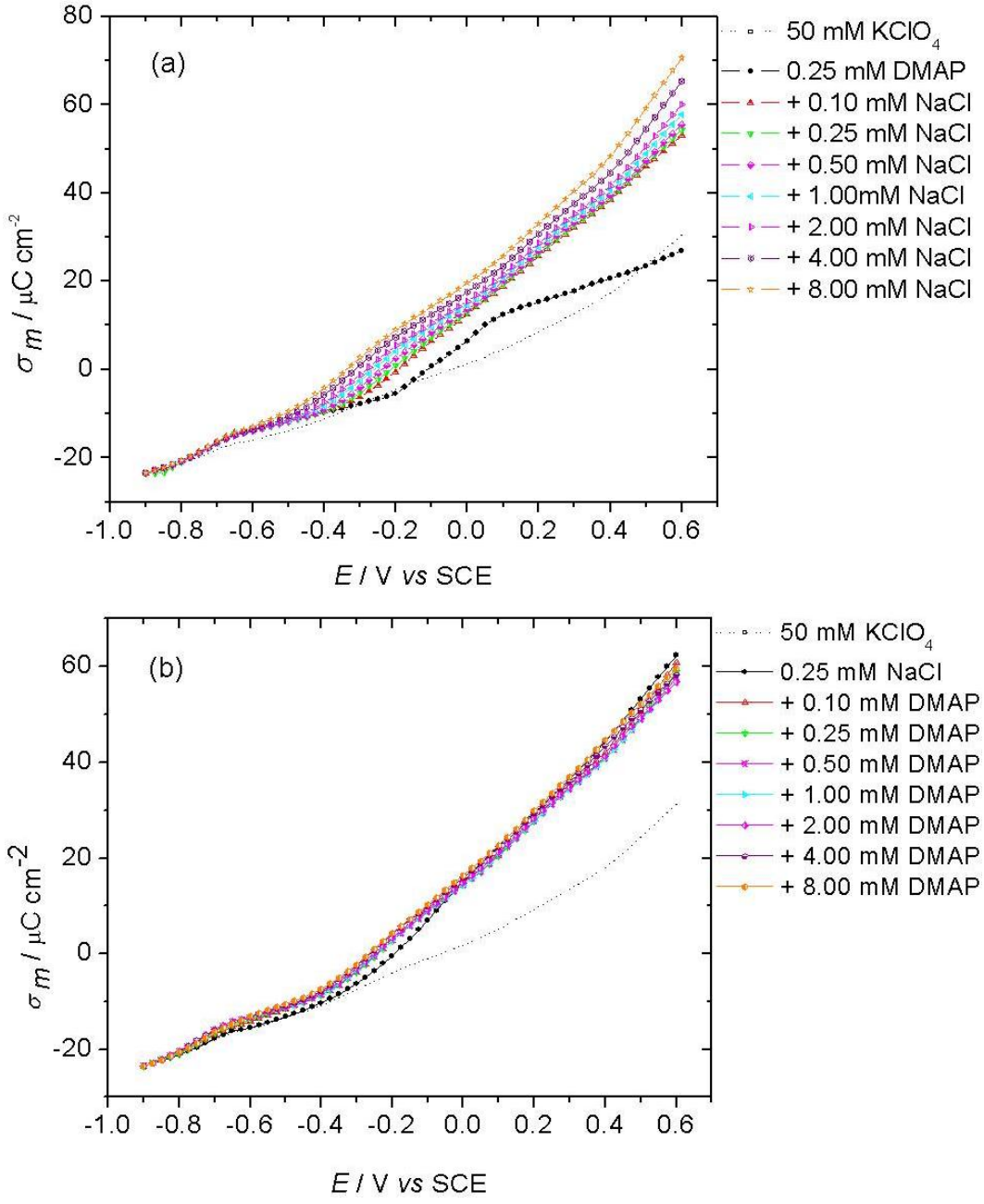

Fig. 3.5

Charge density versus electrode potential curves for polycrystalline gold in 50 mM $KClO_4$ supporting electrolyte at pH 5.5 (----) and series I and II of solutions.

(a) Series I : 0.25 mM DMAP in the absence (●) and in the presence of the following sodium chloride concentrations 0.1 mM (▲), 0.25 mM(◀), 0.5 mM(◆), 1 mM(◀), 2 mM(⊩), 4 mM(⊠), 8 mM(★).

(b) Series II : 0.25 mM NaCl in the absence (●) and in the presence of the following DMAP concentrations 0.1 mM (△), 0.25 mM (▽), 0.5 mM (⊠), 1 mM (▶), 2mM (◆), 4 mM (◒), 8 mM (◐).

In the absence of chloride (black line with symbols) the charge density data for 0.25 mM DMAP is very similar to previous studies of this system at pH 4.5.[15] At the most negative of potentials, the charge of the gold electrode in the presence of $DMAPH^+$ merges with the electrolyte-only curve, which confirms the fact that the organic molecules are desorbed from the surface at very negative electrode polarizations. At more positive potentials (-0.8V < *E* < -0.6V) there is an inflexion in the curve, which results from the adsorption of $DMAPH^+$ onto the gold surface in a flat-lying configuration. This state of adsorption is stable at negative metal charge densities (-0.6V < *E* < -0.2V) but undergoes a transition to a vertical, and *deprotonated*, adsorption state at positive metal charge densities (*E* > 0.1V). The addition of 0.1 mM chloride leads to a pronounced change in the σ_m-*E* plot. At potentials negative of -0.4V the charge overlaps with the 0.25 mM $DMAPH^+$-only curve and this indicates that there is no chloride adsorbed at very negative potentials. At higher potentials the charge density becomes appreciably larger, increases linearly with potential, and there is no evidence of the second inflexion observed between -0.2V < *E* < 0.1V as seen for the $DMAPH^+$-only curve. Unlike the equivalent situation at pH 9.5 (see Figure 3.4a) the charge on the gold electrode now significantly depends on the electrolyte's chloride concentration. With increasing amount of added chloride the onset of the linear portion of the σ_m-*E* curve shifts cathodically and extends over a larger region of potentials indicating that chloride adsorption on gold in the presence of DMAP becomes more favorable, even at increasingly negative potentials. The shape of the curves in the presence of both chloride and DMAP are reminiscent of the charge-density curves obtained by Shi and Lipkowski for the adsorption of chloride on Au(111) electrodes.[32] It was shown therein that chloride adsorbs on bare gold in a

gas-like state at negatively charged surfaces but reorganizes into an ordered (p x $\sqrt{3}$) overlayer at highly positive potentials. It is unlikely that such an ordered monolayer is prevalent on polycrystalline gold, but the similar magnitudes in charge imply that the extent of chloride ion adsorption is the same both in the presence and absence of DMAP species at this pH.

The fact that DMAP/$DMAPH^+$ is only very weakly adsorbed at pH 5.5 in the presence of chloride ions is verified in Figure 3.5b which shows the complement experiment for series II. In the absence of added $DMAPH^+$, the curve for the chloride containing solution merges with the charge density curve for the pure electrolyte at all potentials negative of -0.4V. Further positive potentials show larger charge densities indicative of chloride ion adsorption. The addition of $DMAPH^+$ (lines with coloured symbols) only slightly modifies the appearance of the σ_m-E curves. The most notable changes are the small increases in the measured charge densities in the potential window -0.7V < E < 0V and the very slight decreases for E > 0.4V. It is important to note, however, that these changes are largely independent of the $DMAPH^+$ concentration and varying the amount of conjugate acid added to the cell leads to very little perturbation of the charge-density profiles. It can be concluded from the data shown in Figure 3.5 that chloride has a much greater affinity for the gold surface than DMAP/$DMAPH^+$ at pH 5.5. The fact that chloride adsorption occurs nearly to the same extent in the absence and presence of $DMAPH^+$, combined with the very weak changes in the σ_m-E curves for series II, indicates that at low pH, DMAP species are nearly completely replaced on the gold surface by chloride ions. This observation is consistent with the optical

spectroscopy data obtained for the DMAP-Au MPNs where chloride greatly destabilizes the particles in acidic solutions.

So far charge density data has been described at pHs that correspond to highly favorable DMAP adsorption (pH 9.5) or highly favorable chloride ion adsorption (pH 5.5). It is reasonable to expect that at intermediate pHs, both species could exist simultaneously on the gold surface. Therefore, chronocoulometry experiments were performed at pH 7.5 for series I and II. For series I (Figure 3.6a) all charge curves once again merge at very negative potentials indicating the complete desorption of both Cl^- and DMAP species. However, for $E > -0.4$ V, the presence of halide ions leads to larger charge densities and the effect is pronouncedly dependent on the electrolyte's chloride concentration. This observation can be contrasted to Figure 3.4a where the σ_m-E curves are invariant with changes in the amount of halide present in the electrolyte. In Figure 3.6b it is evident that the presence of DMAP/$DMAPH^+$ causes deviations to the 0.25 mM chloride curve in the potential window $-0.8\text{V} < E < -0.3\text{V}$. Unlike the data shown in Figure 3.5b, here the charge-density plots strongly depend on the $DMAPH^+$ concentration in the aforementioned potential window. The data in Figure 3.6 seem to indicate that at pH 7.5, the charge density of the gold electrode is sensitive to the solution concentration of both the organic and inorganic ions. The sensitivity of the system to incremental changes in the concentration in either species supports the supposition that at intermediate pH (*ca*. 7.5) both DMAP/$DMAPH^+$ and chloride can adsorb on the gold surface.

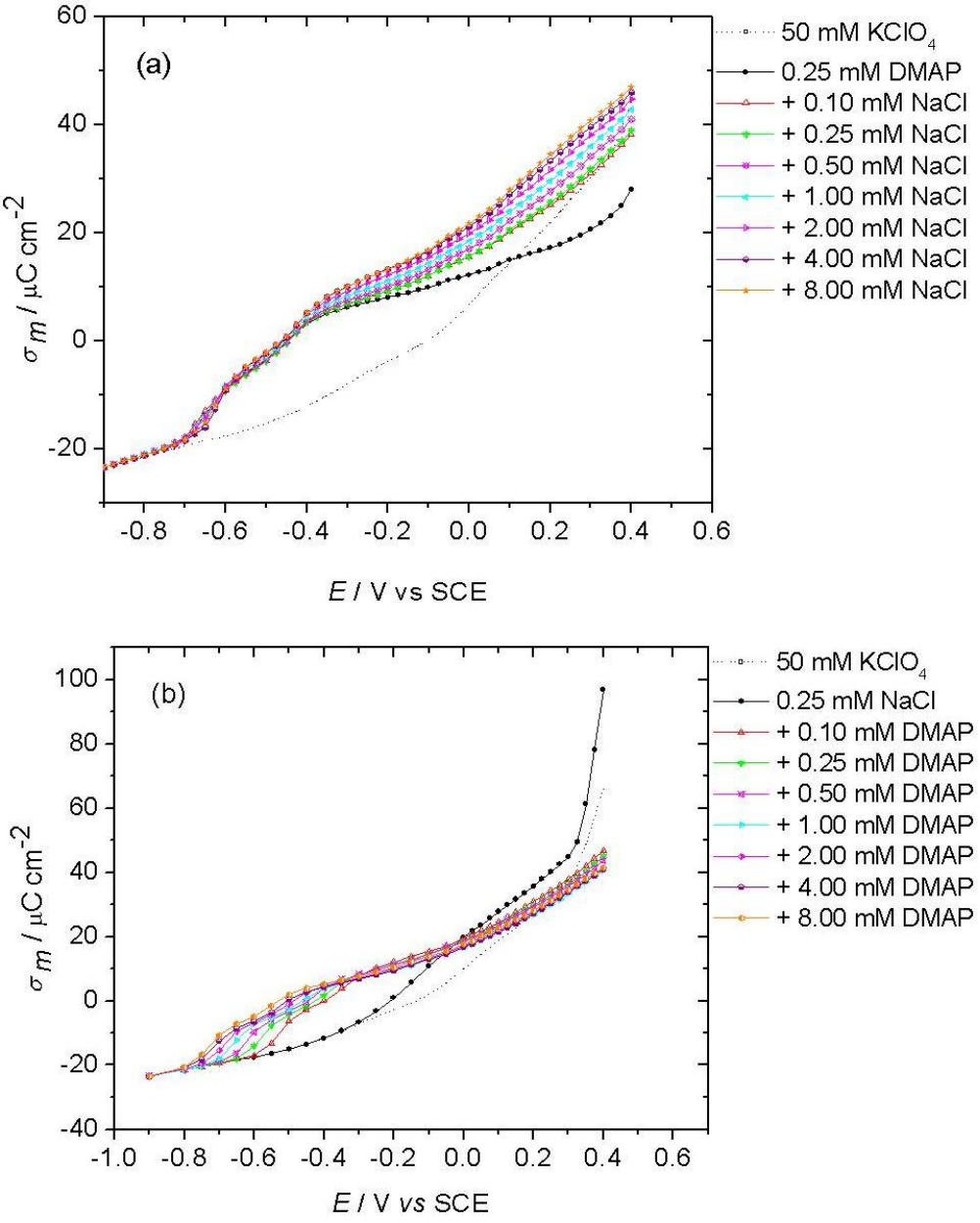

Fig. 3.6

Charge density versus electrode potential curves for polycrystalline gold in 50 mM $KClO_4$ supporting electrolyte at pH 7.5 (----) and series I and II of solutions.

(a) Series I : 0.25 mM DMAP in the absence (●) and in the presence of the following sodium chloride concentrations 0.1 mM (△), 0.25 mM(▽), 0.5 mM(⊠), 1 mM(◁), 2 mM(▷), 4 mM(◒), 8 mM(★).

(b) Series II : 0.25 mM NaCl in the absence (●) and in the presence of the following DMAP concentrations 0.1 mM (△), 0.25 mM (▽), 0.5 mM (⊠), 1 mM (▷), 2mM (◆), 4 mM (◒), 8 mM (◐).

3.3.5 Gibbs surface excesses

The six series of chronocoulometric experiments described above can be used to quantify the surface excess, Γ, for both DMAP species and chloride ions. The analysis of the charge data follows a similar treatment described by Lipkowski and Shi for the co-adsorption of copper and inorganic anions and is based on the electrocapillary equation (3.3) for a multicomponent system.[34]

$$-d\gamma = \sigma_m dE + \Gamma_{Cl^-} d\mu_{NaCl} + \Gamma_{DMAP} d\mu_{DMAP} + \Gamma_{DMAPH^+} d\mu_{DMAPH^+} + \Gamma_{OH^-} d\mu_{OH^-} \qquad (3.3)$$

where γ is the surface energy of the gold-solution interface and μ_i is the chemical potential of the i^{th} species. For series I experiments (Figures 3.4a, 3.5a and 3.6a), as long as the pH is kept constant and under conditions of high electrolyte ionic strength (*i.e.* $d\mu_i = RTd\ln c_i$), Equation (3.3) becomes

$$-d\gamma = \sigma_m dE + RT\Gamma_{Cl^-} d\left(\ln c_{NaCl}\right) \qquad (3.4)$$

Similarly, Equation (3.3) reduces to

$$-d\gamma = \sigma_m dE + RT\Gamma_{DMAP} d\left(\ln c_{DMAP}\right) + RT\Gamma_{DMAPH^+} d\left(\ln c_{DMAPH^+}\right) \qquad (3.5)$$

for series II experiments (Figures 3.4b, 3.5b and 3.6b).

Furthermore, because c_{DMAP} and c_{DMAPH^+} are inter-related through the K_B of DMAP, Equation (3.5) can be re-written as follows

$$-d\gamma = \sigma_m dE + RT\Gamma_{DMAP} d\left(\ln\frac{c_{OH^-}}{K_B} + \ln c_{DMAPH^+}\right) + RT\Gamma_{DMAPH^+} d\left(\ln c_{DMAPH^+}\right) \qquad (3.6)$$

which under conditions of constant pH further simplifies to

$$-d\gamma = \sigma_m dE + RT\left(\Gamma_{DMAP} + \Gamma_{DMAPH^+}\right) d\left(\ln c_{DMAPH^+}\right) \qquad (3.7)$$

It is apparent from Equation (3.7) that the electrocapillary equation alone can't discriminate between the acid and base forms of DMAP but can provide the total surface

excess of both species. From Equations (3.4) and (3.7), integration of the σ_m-E curves provide the relative surface pressure of the interface, π,

$$\pi = \left(\int_{E_{des}}^{E_c} \sigma_m dE \right)_{c_x} - \left(\int_{E_{des}}^{E_c} \sigma_m dE \right)_{c_x=0} \tag{3.8}$$

where c_x is the concentration of the varied additive (either chloride or $DMAPH^+$). Finally, the Gibbs surface excesses of species x can be calculated from the film pressure data for each series of experiments by differentiation of π with respect to $\ln c_x$ at constant electrode potential.

$$\Gamma = \frac{1}{RT} \left(\frac{\partial \pi}{\partial \ln c_x} \right)_E \tag{3.9}$$

In pH 9.5, the very small changes in charge data lead to surface excesses of chloride ions that are very small and suffer from appreciable scatter in the data. A similar result is obtained at pH 5.5 for the analysis of the concentration of adsorbed $DMAP/DMAPH^+$ species. However, as previously described, neutral solutions exhibit characteristics of both $DMAP/DMAPH^+$ and chloride adsorption. In Figure 3.7 *Γ versus E* plots for chloride (Figure 3.7a) and $DMAP/DMAPH^+$ (Figure 3.7b) are shown. At potentials more negative than -0.4V there is no chloride adsorbed on the gold surface. At more positive potentials the curves in Figure 3.7a display two quasi-linear regions, the first extends from -0.4V < E < 0.0 V and a second, of higher slope, is seen for E > 0.0 V. The magnitudes of the chloride surface coverages are in very good, quantitative agreement with chronocoulometric results for chloride adsorption on Au(111)[32] and radiotracer studies of chloride adsorption on polycrystalline gold[35,36]. Additionally, the smaller sloped, or so-called "foot", portion of the isotherms commonly reported for low chloride

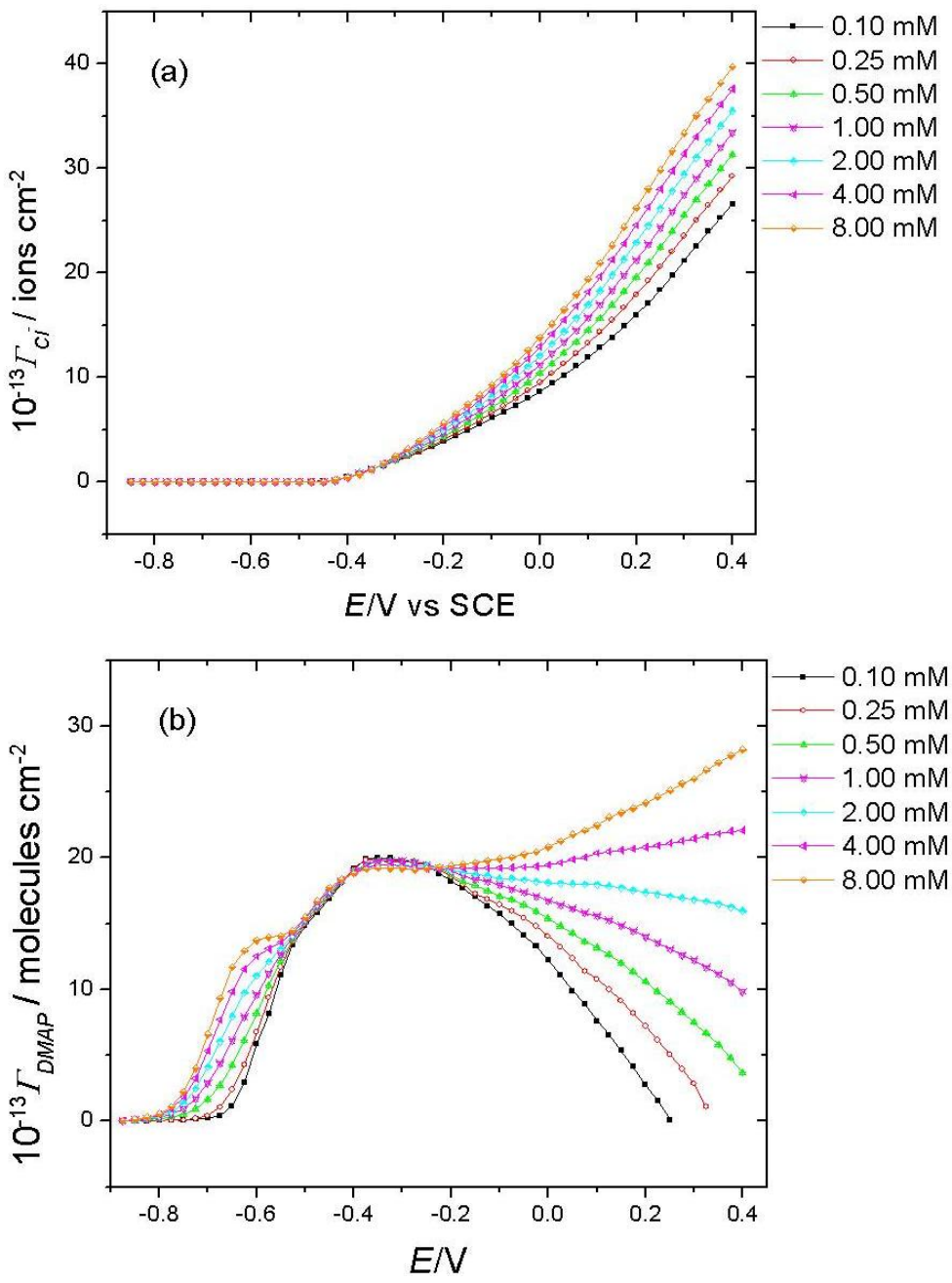

Fig. 3.7

Gibbs excess as a function of electrode potential for polycrystalline gold at pH 7.5:

(a) Variable chloride concentrations, viz. 0.1 mM(■), 0.25 mM(○), 0.5 mM(▲), 1 mM(⊠), 2 mM(◓), 4 mM(◀), 8 mM(◆).

(b) Variable DMAP concentrations, viz0.1 mM(■), 0.25 mM(○), 0.5 mM(▲), 1 mM(⊠), 2 mM(◓), 4 mM(◀), 8 mM(◆).

coverage at slightly negative potentials on both polycrystalline gold[35] and Au(111)[32] are only weakly observed in Figure 3.7a. This may indicate that the ΔG_{ads}^{o} for chloride and DMAP/DMAPH$^+$ are comparable at these potentials and this leads to a lower surface chloride concentration. Figure 3.7b shows the adsorption of DMAP/DMAPH$^+$ in the presence of 0.25 mM chloride. Low concentrations of the organic ligand lead to well-pronounced adsorption maxima at E ~ -0.35 V with the surface concentration dropping to zero at very positive and very negative potentials. Higher bulk concentrations of DMAPH$^+$ perturb the surface excess plots at positive potentials indicating that DMAP/DMAPH$^+$ begins to successfully compete with chloride for gold adsorption sites as its chemical potential in the electrolyte increases. The shoulder observed at ~ -0.6 V represents the transition from the flat-lying DMAPH$^+$ to vertically aligned DMAP.[15] The maximum adsorption at E ~ -0.35 V equals 3.3 x 10^{-10} moles cm^{-2}, which is 50-65% of the maximum surface concentration measured for vertically aligned DMAP in the absence of coadsorbates.[15] The lower maximum concentration evidently arises because chloride ions remain adsorbed on the Au surface preventing the formation of a well-packed DMAP monolayer.

The competitive nature of the chloride-DMAP system can be best illustrated by Figure 3.8. This graph plots the surface excesses of both DMAP and chloride on the same axis for an equimolar (0.25 mM) solution. Between -0.7V < E < -0.4V DMAP is exclusively adsorbed on the electrode surface and its surface excess increases with increasing potential. However, as the potential is increased positive of -0.4V, the DMAP surface concentration fails to increase to the limiting value expected for a complete, vertically-oriented monolayer. Instead Γ_{DMAP} begins to decrease and there is a

concomitant increase in Γ_{Cl}^{-}. At the most positive potentials studied, DMAP is completely removed from the surface and replaced with a relatively high (*ca.* one third of a full monolayer[32]) coverage chloride layer. Only in the range of potentials, -0.4V < *E* < 0.4V, do chloride and DMAP coexist on the electrode surface. The inset in Figure 3.8 plots Γ_{DMAP} *versus* Γ_{Cl}^{-} for this range of potentials and it is clearly evident that there is a linear correlation between chloride adsorption and the loss of DMAP species. The slope of the line corresponds to 1.25 chloride ions per DMAP which indicates that the adsorption of four chloride ions leads to a loss of five DMAP molecules from the gold surface.

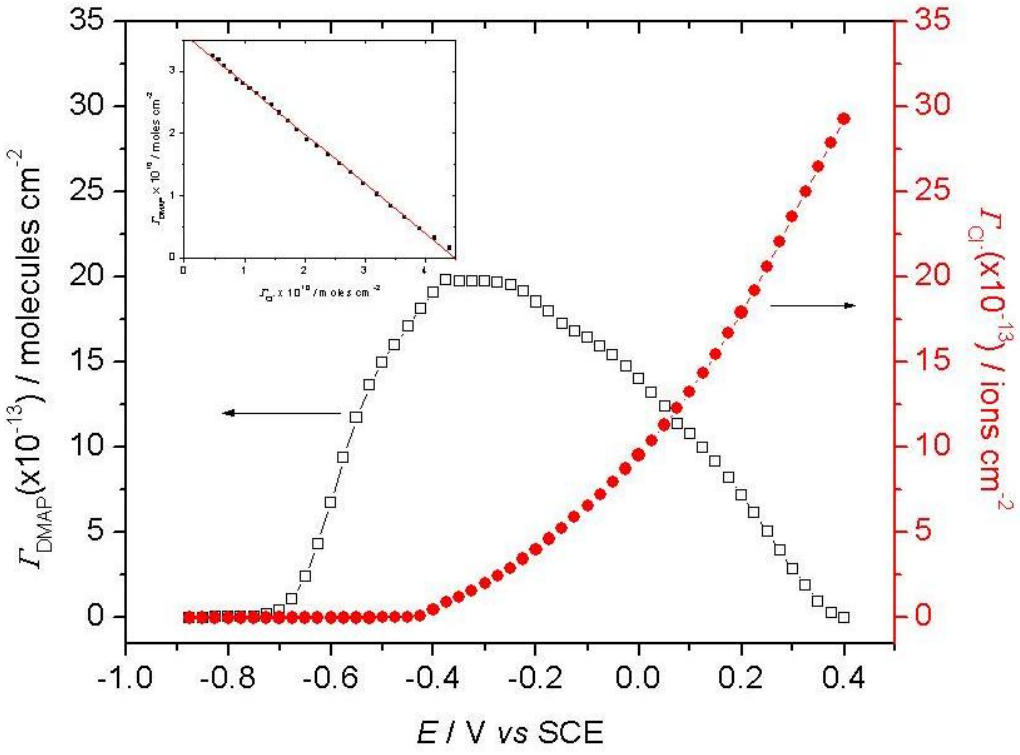

Fig. 3.8

Gibbs excess as a function of electrode potential for DMAP (□) and chloride (●) on polycrystalline gold at pH 7.5 for an equal formal concentration of DMAP and chloride (0.25 mM), Γ_{DMAP} *versus* Γ_{Cl}^{-} plot is shown in the inset.

3.3.6 Zeta potential measurements

The analysis of the electrochemical data described above leads to a quantitative picture of the displacement of DMAP from the gold electrode surface by the addition of sodium chloride. These results clearly show competitive adsorption behavior between chloride and DMAP which depends on i) pH ii) chloride concentration and iii) the electrical state of the gold surface (*i.e.* surface charge or potential). Direct comparison of the systems on 2D and 3D gold can readily be made with reference to the first two parameters, and indeed optical spectroscopy data on gold nanoparticles qualitatively agrees very well with the electrochemical studies on gold electrodes. To be able to relate the surface coverage data obtained using electrochemical techniques with the observed behaviour of DMAP-Au MPNs, an estimate of the nanoparticles' surface potential, ϕ_2 is required. The term surface potential has different connotations in colloid chemistry and electrochemistry. In the former, surface potential (usually denoted as ψ_o) is a measure of the electrostatic forces arising from the total charge, *q*, on the colloidal particle. In electrochemical terminology the congruent physical parameter is called the outer Helmholtz potential, ϕ_2. Given that $\phi_2 \equiv \psi_o$, the electrochemical symbolism is used here even when discussing the "surface potential" of the nanoparticles.

For a spherical particle, the surface potential is a function of the total charge *q*, the Debye length of the electrolyte (1/κ), and the particle radius *a*. Where

$$q = \sigma_m + nF\Gamma_{Cl^-} + nF\Gamma_{DMAPH^+} \qquad (3.10)$$

and,

$$\kappa = \left(\frac{2n^0 Z_i^2 e^2}{\varepsilon \varepsilon_0 kT} \right)^{1/2} \tag{3.11}$$

In Equation (3.11), k is the Boltzmann constant, ε is the dielectric of water, ε_o the permittivity of vacuum, n^o is the number concentration of electrolyte ions with valency Z_i and e is the fundamental charge. Deriving a relation between q and ϕ_2 requires solving the Poisson-Boltzmann equation which has been well-described for planar electrodes[37] but becomes more complicated for spherical surfaces. In such instances, the solution to the Poisson-Boltzmann equation is highly dependent on the radius of the particle in relation to the Debye length of the electrolyte.[38] Kimura et al.[39] have shown the qualitative applicability of an expression previously derived by Ohshima et al.[40,41] to spherical particles in 1:1 electrolytes over a wide range of values of κa

$$q = \left(\frac{2\varepsilon\varepsilon_o \kappa kT}{e} \right) \sinh\left(\frac{Y}{2} \right) \left[1 + \frac{1}{\kappa a} \left(\frac{2}{\cosh^2(Y/4)} \right) + \frac{1}{(\kappa a)^2} \left(\frac{8 \ln\left[\cosh(Y/4) \right]}{\sinh^2(2)} \right) \right]^{1/} \tag{3.12}$$

where $Y = e\phi_2 / kT$. If the particle radius is large compared to the double layer thickness (κa > ca. 5) then the double layer can be treated as flat, and Equation (3.12) simplifies to the more familiar form used for planar electrodes.[37]

If the surface potential can be experimentally measured then the value of the total charge on the colloid's surface can be evaluated using Equation (3.12). In turn, the corresponding value of σ_m, determined from charge density measurements, can then be used to relate the measured value of ϕ_2 to an electrode potential, E. This approach was followed by measuring the zeta potential of DMAP-Au MPNs at different pH and electrolyte compositions. The ζ (Zeta) potential is a measure of the potential at the so-

called “plane of shear” between the double layer of the colloid and the surrounding medium and is deduced from the electrophoretic mobility, which is the measured quantity in an electrokinetic experiment.[42] Although it does not perfectly coincide with the surface potential, it is often used as a very good estimate of ϕ_2 and with the assumption that $\phi_2 \approx \zeta$. Measured ζ potential for the six systems is shown in Table 3.1.

Electrolyte	**ζ potential / mV**	**q / μC cm^{-2}**
pH 9.5 ; 5 mM NaF	31±2	1.06±0.04
pH 9.5 ; 5 mM NaCl	31±2	1.06±0.04
pH 7.5 ; 5 mM NaF	31±2	1.06±0.04
pH 7.5 ; 5 mM NaCl	30±2	0.99±0.07
pH 5.5 ; 5 mM NaF	21±3	0.69±0.10

Table 3.1

Parameters obtained from Zeta Potential Measurements of DMAP-Au Nanoparticles in the presence of NaF and NaCl at pHs 9.5, 7.5 and 5.5.

As it is clear from the table, the ζ potential could be measured for all pHs for 5 mM NaF and at pH 7.5 and pH 9.5 for 5 mM NaCl. However, at pH 5.5, a stable ζ potential could not be obtained in the presence of chloride ions presumably due to extensive particle aggregation. At pH 9.5, the value of 31±2 mV is in excellent agreement with

values previously reported for DMAP-Au nanoparticles.[9,12]. In those studies, the observation of positive surface potentials led both sets of authors to propose that DMAP adsorbs on the gold surface in a zwitterionic, resonance structure. However, a monolayer of zwitterions is electrically net neutral and would be unable to generate a non-zero ζ potential. Given that the present electrochemical results, performed in the presence of NaCl, combined with previous reports on the adsorption of DMAP in the absence of halide[15] show that only the neutral form of DMAP adsorbs on Au at high pH, a more reasonable explanation is that the surface of the metal core is positively charged. Using Equation (3.12) and a particle radius of 5 nm, ζ = 31 mV corresponds to a total charge of 1.1 μC cm^{-2}. Therefore, in accordance with Equation 3.10, with $\Gamma_{Cl^-} = \Gamma_{DMAPH^+} = 0$, $q = \sigma_m = 1.1$ μC cm^{-2}. The charge data from DMAP adsorption on polycrystalline gold[15] was used to show that at high electrolyte concentrations of DMAP such a surface charge occurs at electrode potentials ~ -0.6V *versus* SCE where $\Gamma_{\mathrm{DMAP}} \approx 0.8\Gamma_{\mathrm{DMAP,max}}$. This relatively high coverage of DMAP provides sufficient steric stability to prevent particle aggregation. The fact that the ζ potential is unaltered in the presence of chloride ions at high pH further demonstrates that chloride does not adsorb on the gold surface under these conditions. In neutral (pH 7.5) solutions the ζ potential remains at 31±2 mV in both 5 mM NaCl and 5 mM NaF. In the presence of chloride ions, this again gives a value of q = 1.1 μC cm^{-2}. To equate this to surface charge density, chronocoulometry data shown in Figure 3.6c can be used, but the contribution to q from adsorbed chloride must be considered (i.e. in Equation 3.8, $nF\Gamma_{Cl^-} \neq 0$).

A plot of q versus σ_m for 5 mM NaCl in the presence of DMAP is shown in Figure 3.9 and shows a quasi-parabolic shape. In other words, there are two values of σ_m that equate to a total q = 1.1 μC cm^{-2}. The values are 1.0 μC cm^{-2} and 20.0 μC cm^{-2} and from Figure 3.6a these surface charge densities correspond to electrode potentials of ≈ -0.45V and ≈ -0.025V *versus* SCE. It can be seen from Figure 3.7a that the latter value equates to sizeable chloride adsorption coverages while the former resides just at the onset of chloride adsorption. While the possibility that the gold nanoparticle surface is very highly positively charged cannot be completely dismissed, the lower value for σ_m is more consistent with the ζ potential results obtained at higher pHs. Additionally, the fact that chloride ions are incipiently adsorbed when σ_m = 1.0 μC cm^{-2} at pH 7.5 and ≈ 5mM NaCl agrees very well with the slightly red-shifted surface plasmon resonance observed in the optical spectroscopy experiments (Figure 3.1, panel E) for nearly identical conditions.

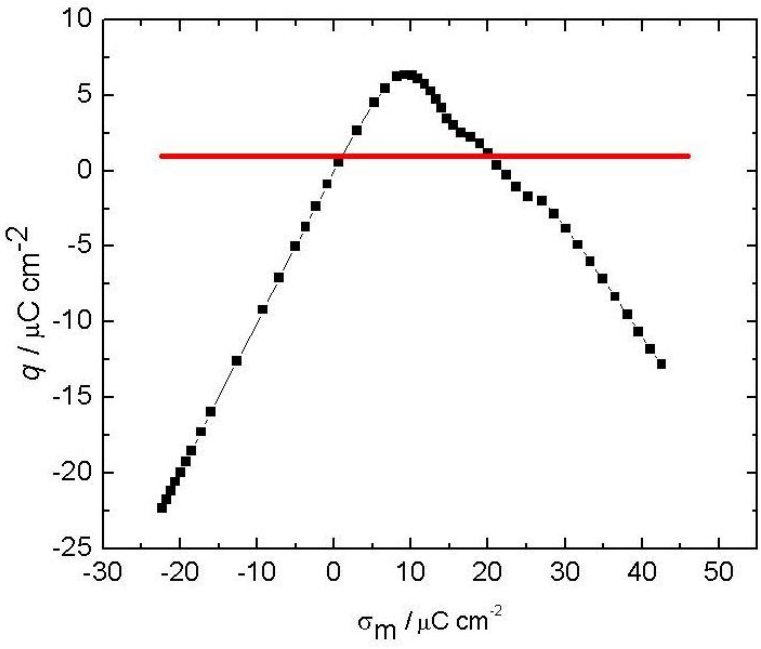

Fig. 3.9

A plot of q versus σ_m for 5 mM NaCl in the presence of DMAP.

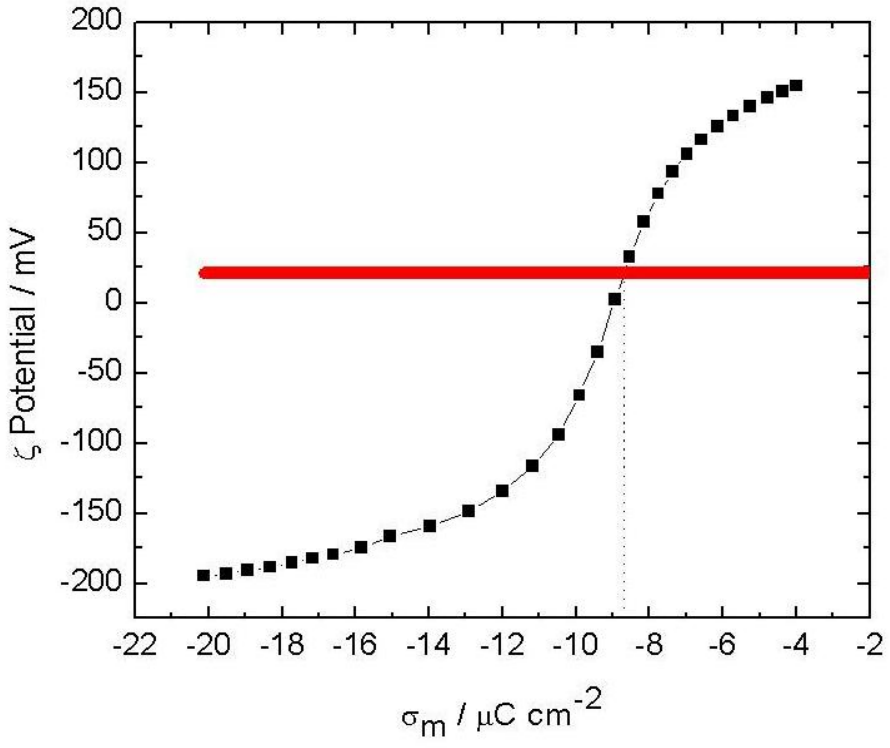

Fig. 3.10

A plot of ζ potential as a function of the metal charge density for DMAP adsorption on polycrystalline gold at pH 4.5.

Likewise, the decreased ζ potential in acidified 5 mM NaF solutions can also be explained. Based on the electrosorption studies on polycrystalline gold, DMAP adsorbs as its conjugate acid on negatively charged gold surfaces. If we take the values of Γ_{DMAPH^+} and σ_m obtained at pH 4.5,[15] again Equations (3.10)and (3.12) can be used to determine the total charge and the surface potential. Figure 3.10 is a plot of ζ (equivalent to ϕ_2) as a function of the metal charge density and shows that the positive charge arising from the adsorbed $DMAPH^+$ leads to positive ζ potentials even when the metal itself is

negatively charged. In Figure 3.10 a horizontal line that intersects the ordinate axis at 21 mV is shown, the value obtained from the ζ potential measurements at pH 5.5 NaF. Although the electrochemical results and the ζ potential measurements were made at slightly different pH (4.5 and 5.5, respectively), Figure 3.10 illustrates that the observation of a smaller surface potential in acidic solutions is consistent with the conversion of adsorbed DMAP to a low coverage layer of $DMAPH^+$.

3.4 Summary and Conclusions

Halide induced aggregation of DMAP stabilized gold MPNs has been studied using UV-Vis spectroscopy, transmission electron microscopy and Zeta potential measurements. It has been demonstrated that this effect is above and beyond the pH-induced destabilization previously noted by others.[12,15] In contrast to fluoride, strong chloride induced aggregation occurs at neutral as well as moderately acidic pHs. At high pH, the addition of chloride ions has no influence on the gold particles' surface plasmon but bromide and iodide ions have significantly red-shifted the surface plasmon even at high pH. This has been explained using differential capacity studies where it has been demonstrated that the displacement of $DMAP(H^+)$ by halide ions is highly dependent on pH and the identity of the halide ions, i.e. $DMAP(H^+)$ displacement by halides on the surface follows the order $I^- > Br^- > Cl^- > F^-$. Chloride induced aggregation at different pHs has been further investigated using chronocoulometric studies. Competitive adsorption in neutral (pH 7.5) solutions has been quantified where it has been shown that each adsorbing chloride ion replaces roughly one DMAP molecule. This ligand exchange is driven by positive metal charge densities. As the pH is lowered below ca. 6, there is increasingly less DMAP per unit area adsorbed on the gold surface. The presence

of chloride accelerates this decrease in the surface concentration of organic stabilizer through a competitive adsorption process. The electrochemical results performed on two-dimensional gold help explain the aggregation of gold nanoparticles which was followed with optical spectroscopy. The observed red-shifting in neutral to acidic solutions in the presence of chloride is a consequence of the particles losing their stability due to chloride replacing DMAP on the surface of the nanoparticles. Zeta potential measurements were used to bridge the studies on 2D and 3D gold. These experiments allow the determination of the electrical state of the nanoparticles. Zeta potential measurements indicate that in neutral to basic solutions, DMAP-Au nanoparticles are positively charged. It has been shown that this positive charge does not arise from formal charges or zwitterionic resonance structures of the DMAP monolayer but rather from a positive charge on the metal surface. The sign of this charge is reversed when the pH is lowered to the point where the surface DMAP becomes protonated.

These results can be used to offer insight into the role DMAP plays in stabilizing colloidal gold. In general, the kinetic stability of aqueous gold sols can be explained with DLVO theory[28] where the layer of surface charge on individual colloids (usually provided by potential determining ions) provides electrostatic repulsion between neighboring particles. This electrostatic repulsion gives rise to surface potentials comparable to the values observed for the DMAP-Au system. On the other hand, the stability of uncharged, monolayer protected metal nanoparticles (typically derived from thiol-gold chemistry) in non-polar, organic solvents is attributable to a steric effect created by the molecules in the protecting monolayer. Electrochemical measurements of this system indicate a well-packed DMAP monolayer that one might expect to provide

nearly equivalent steric stability. Upon initial consideration, it would therefore seem that DMAP-Au MPNs present a possible hybrid between the electrostatic and steric stability mechanisms. However, experiments with NaCl and NaF electrolytes at high pH indicate that this surface charge is not primarily responsible for the stability of the particles. Instead it is seen that it is the integrity of the DMAP monolayer that dictates the stability of DMAP-Au MPNs and only when the neutral, vertically bound DMAP molecules are displaced from the surface do the particles begin to aggregate. In this sense the aqueous DMAP-Au system behaves very much like thiol MPN systems and very differently from aqueous citrate-stabilized gold sols. This fact may affect the approach taken to further functionalize water-dispersible metal nanoparticles for application purposes. Additionally, this work demonstrates that the influence of salt solutions, especially those that contain chloride or other halides, on the aggregation of monolayer protected metal nanoparticles should not be ignored when designing nanoparticle assays based on colorimetry.

Reference List

1. Ackerson, C. J.; Jadzinsky, P. D.; Kornberg, R. D. Thiolate Ligands for Synthesis of Water-Soluble Gold Clusters. *Journal of the American Chemical Society* **2005,** *127* (18), 6550-6551.

2. Templeton, A. C.; Wuelfing, W. P.; Murray, R. W. Monolayer-Protected Cluster Molecules. *Accounts of Chemical Research* **1999,** *33* (1), 27-36.

3. Chen, S.; Kimura, K. Synthesis and Characterization of Carboxylate-Modified Gold Nanoparticle Powders Dispersible in Water. *Langmuir* **1999,** *15* (4), 1075-1082.

4. Shon, Y. S.; Wuelfing, W. P.; Murray, R. W. Water-Soluble, Sulfonic Acid-Functionalized, Monolayer-Protected Nanoparticles and an Ionically Conductive Molten Salt Containing Them. *Langmuir* **2001,** *17* (4), 1255-1261.

5. Cliffel, D. E.; Zamborini, F. P.; Gross, S. M.; Murray, R. W. Mercaptoammonium-Monolayer-Protected, Water-Soluble Gold, Silver, and Palladium Clusters. *Langmuir* **2000,** *16* (25), 9699-9702.

6. Turkevich, J.; Stevenson, P. C.; Hillier, J. A study of the nucleation and growth processes in the synthesis of colloidal gold. *Discuss. Faraday Soc.* **1951,** *11*, 55-75.

7. Faraday, M. The Bakerian Lecture: Experimental Relations of Gold (and Other Metals) to Light. *Philosophical Transactions of the Royal Society of London* **1857,** *147*, 145-181.

8. Gittins, D. I.; Susha, A. S.; Schoeler, B.; Caruso, F. Dense Nanoparticulate Thin Films via Gold Nanoparticle Self-Assembly. *Advanced Materials* **2002,** *14* (7), 508-512.

9. Gittins, D. I.; Caruso, F. Spontaneous Phase Transfer of Nanoparticulate Metals from Organic to Aqueous Media. *Angewandte Chemie International Edition* **2001,** *40* (16), 3001-3004.

10. Yu, A.; Liang, Z.; Cho, J.; Caruso, F. Nanostructured Electrochemical Sensor Based on Dense Gold Nanoparticle Films. *Nano Letters* **2003,** *3* (9), 1203-1207.

11. Larson, I.; Chan, D. Y. C.; Drummond, C. J.; Grieser, F. Use of Atomic Force Microscopy Force Measurements To Monitor Citrate Displacement by Amines on Gold in Aqueous Solution. *Langmuir* **1997,** *13* (9), 2429-2431.

12. Gandubert, V. r. J.; Lennox, R. B. Assessment of 4-(Dimethylamino)pyridine as a Capping Agent for Gold Nanoparticles. *Langmuir* **2005,** *21* (14), 6532-6539.

13. Gandubert, V. r. J.; Lennox, R. B. Surface Plasmon Resonance Spectroscopy Study of Electrostatically Adsorbed Layers. *Langmuir* **2006,** *22* (10), 4589-4593.

14. Kunze, J.; Burgess, I.; Nichols, R.; Buess-Herman, C.; Lipkowski, J. Electrochemical evaluation of citrate adsorption on Au(1á1á1) and the stability of citrate-reduced gold colloids. *Journal of Electroanalytical Chemistry* **2007,** *599* (2), 147-159.

15. Barlow, B. C.; Burgess, I. J. Electrochemical Evaluation of 4-(Dimethylamino)pyridine Adsorption on Polycrystalline Gold. *Langmuir* **2006,** *23* (3), 1555-1563.

16. Elghanian, R.; Storhoff, J. J.; Mucic, R. C.; Letsinger, R. L.; Mirkin, C. A. Selective Colorimetric Detection of Polynucleotides Based on the Distance-Dependent Optical Properties of Gold Nanoparticles. *Science* **1997,** *277* (5329), 1078-1081.

17. Storhoff, J. J.; Elghanian, R.; Mucic, R. C.; Mirkin, C. A.; Letsinger, R. L. One-Pot Colorimetric Differentiation of Polynucleotides with Single Base Imperfections Using Gold Nanoparticle Probes. *Journal of the American Chemical Society* **1998,** *120* (9), 1959-1964.

18. Rosi, N. L.; Mirkin, C. A. Nanostructures in Biodiagnostics. *Chemical Reviews* **2005,** *105* (4), 1547-1562.

19. Haes, A. J.; Van Duyne, R. P. A Nanoscale Optical Biosensor:ΓÇë Sensitivity and Selectivity of an Approach Based on the Localized Surface Plasmon Resonance Spectroscopy of Triangular Silver Nanoparticles. *Journal of the American Chemical Society* **2002,** *124* (35), 10596-10604.

20. Riboh, J. C.; Haes, A. J.; McFarland, A. D.; Ranjit Yonzon, C.; Van Duyne, R. P. A Nanoscale Optical Biosensor:ΓÇë Real-Time Immunoassay in Physiological Buffer Enabled by Improved Nanoparticle Adhesion. *The Journal of Physical Chemistry B* **2003,** *107* (8), 1772-1780.

21. Pergolese, B.; Muniz-Miranda, M.; Bigotto, A. Surface Enhanced Raman Scattering Investigation of the Halide Anion Effect on the Adsorption of 1,2,3-Triazole on Silver and Gold Colloidal Nanoparticles. *The Journal of Physical Chemistry B* **2005,** *109* (19), 9665-9671.

22. Pang, S.; Kondo, T.; Kawai, T. Formation of Dendrimer-like Gold Nanoparticle Assemblies. *Chemistry of Materials* **2005,** *17* (14), 3636-3641.

23. Rai, A.; Singh, A.; Ahmad, A.; Sastry, M. Role of Halide Ions and Temperature on the Morphology of Biologically Synthesized Gold Nanotriangles. *Langmuir* **2005,** *22* (2), 736-741.

24. Cheng, W.; Dong, S.; Wang, E. Synthesis and Self-Assembly of Cetyltrimethylammonium Bromide-Capped Gold Nanoparticles. *Langmuir* **2003,** *19* (22), 9434-9439.

25. Linnert, T.; Mulvaney, P.; Henglein, A. Surface chemistry of colloidal silver: surface plasmon damping by chemisorbed iodide, hydrosulfide (SH-), and phenylthiolate. *The Journal of Physical Chemistry* **1993,** *97* (3), 679-682.

26. Dasog, M.; Scott, R. W. J. Understanding the Oxidative Stability of Gold Monolayer-Protected Clusters in the Presence of Halide Ions under Ambient Conditions. *Langmuir* **2007,** *23* (6), 3381-3387.

27. Singh, S.; Pasricha, R.; Bhatta, U. M.; Satyam, P. V.; Sastry, M.; Prasad, B. L. V. Effect of halogen addition to monolayer protected gold nanoparticles. *Journal of Materials Chemistry* **2007,** *17* (16), 1614-1619.

28. Israelachvili, J. N. *Intermolecular and surface forces;* 2 ed.; Academic Press, London: 1992.pp. 341-385.

29. Weisbecker, C. S.; Merritt, M. V.; Whitesides, G. M. Molecular Self-Assembly of Aliphatic Thiols on Gold Colloids. *Langmuir* **1996,** *12* (16), 3763-3772.

30. Jacek Lipkowski 1998 Alcan Award LectureSurface electrochemistry - surface science with a joy stick. *Canadian Journal of Chemistry* **1999,** *77* (7), 1163-1176.

31. Damaskin, B.; Frumkin, A.; Chizhov, A. Generalized model of the surface layer for the case of adsorption of organic molecules on the electrode. *Journal of Electroanalytical Chemistry and Interfacial Electrochemistry* **1970,** *28* (1), 93-104.

32. Shi, Z.; Lipkowski, J. Chloride adsorption at the Au(111) electrode surface. *Journal of Electroanalytical Chemistry* **1996,** *403* (1-2), 225-239.

33. Dean, J. A. Handbook of Chemistry. 15 ed.; McGraw-Hill: New York, 1999.

34. Shi, Z.; Lipkowski, J. Coadsorption of Cu^{2+} and $SO4^{2-}$ at the Au(111) electrode. *Journal of Electroanalytical Chemistry* **1994,** *365* (1-2), 303-309.

35. Kolics, A.; Thomas, A. E.; Wieckowski, A. 36Cl labelling and electrochemical study of chloride adsorption on a gold electrode from perchloric acid media. *Journal of Chemical Society , Faraday Trans.* **1996,** *92* (20), 3727-3736.

36. Horanyi, G.; Rizmayer, E. M.; Joo, P. Radiotracer study of the adsorption of Cl^- and HSO^{4-} ions on a porous gold electrode and on underpotential deposited metals on gold. *Journal of Electroanalytical Chemistry and Interfacial Electrochemistry* **1983,** *152* (1-2), 211-222.

37. Mohilner, D. M. In *Electroanalytical chemistry: A series of advances*, Bard, A. J., Ed.; Dekker: New York, 1966; Vol. 1, p 242.

38. Klabunde, K. J. In *Nanoscale Materials in Chemistry*, Mulvaney, P., Ed.; John Wiley and Sons: New York, 2001.

39. Kimura, K.; Takashima, S.; Ohshima, H. Molecular Approach to the Surface Potential Estimate of Thiolate-Modified Gold Nanoparticles. *The Journal of Physical Chemistry B* **2002,** *106* (29), 7260-7266.

40. Ohshima, H.; Healy, T. W.; White, L. R. Accurate analytic expressions for the surface charge density/surface potential relationship and double-layer potential distribution for a spherical colloidal particle. *Journal of Colloid and Interface Science* **1982,** *90* (1), 17-26.

41. Ohshima, H. Surface Charge Density/Surface Potential Relationship for a Spherical Colloidal Particle in a Solution of General Electrolytes. *Journal of Colloid and Interface Science* **1995,** *171* (2), 525-527.

42. Adamson, A. W. In *Physical Chemistry of Surfaces*, Adamson, A. W., Ed.; Wiley: New York, 1990.

Chapter 4

Electrochemical Evaluation Dimethylaminopyridine Adsorption on Au(111)

4.1 Introduction

The adsorption of π-conjugated molecules on noble metal surfaces has been extensively studied in recent years. Well-studied aromatic molecules like pyridine[1-9], thiophene[10] and benzene[11] often serve as molecular building blocks for larger derivatives used in optoelectronics,[12,13] nanoparticle synthesis[14-16] and other guest-host networks[17]. Most frequently studied surfaces as hosts for pyridine and its derivatives are gold, silver and platinum. Pyridine is a classical example for molecules having different coordination sites: π-electrons of the aromatic ring as well as the nonbonding orbital of the heterocyclic nitrogen. Depending on the electrical state of the surface and binding sites, the orientation of the molecule on the surface varies. The adsorption of pyridine on polycrystalline as well as various low-index and high-index single crystal gold surfaces has been thoroughly studied by Lipkowski's group.[1,2,5,7] The difference in surface coverage and the loss of binding energy upon reorientation of the molecule with changes in the electrical state of the surface has been extensively discussed in the literature.[1,5,8,18]

Of the many derivatives of pyridine,[19,20] 4-(N,N-dimethylamino)pyridine (DMAP) has an additional importance as it is widely used as a stabilizer for gold nanoparticles.[14,21,22] An electrochemical evaluation of DMAP adsorption on polycrystalline gold electrodes has been previously reported by Barlow and Burgess.[23] The presence of the dimethylamino-substituent at the para-position makes the molecule a

stronger base (pK_a of conjugate acid ~ 9.7) and a stronger nucleophile in contrast to unsubstituted pyridine (pK_a of conjugate acid ~ 5.2). Lipkowski *et al.*'s work on pyridine adsorption indicates that pyridine can assume a vertical as well as a horizontal state on gold surfaces, the nature of which is dependent on the electrical potential as well as the crystallography of the surface.[1,3-6] Lipkowski et. al. proposed that pyridine undergoes reorientation from a horizontal to vertical configuration on polycrystalline, (111) and (100) gold surfaces[2,5] at positive potentials, while only the vertical adsorption is possible on (110) and high-index faces of gold.[4,6,9] Results of pH dependent DMAP adsorption studies on polycrystalline gold from the Burgess group have shown that, at high pH (pH ≥ 9.7), DMAP assumes only a vertical orientation even at negative potentials. Notably, the pH dependent adsorption of pyridine or its derivatives on gold surfaces has not been systematically studied as a function of pH. The limited available literature reports on pyridine adsorption on gold at low pH[24,25] concur with the adsorption behavior of DMAP on polycrystalline gold; at low pH, both DMAP and pyridine undergo reorientation from the horizontal to the vertical configuration as the potential is scanned from negative to positive values.

Based on all previous reports of pyridine and its derivatives, it can be rationalized that when the molecule is oriented vertically on the surface, it binds by its endocyclic nitrogen, and when the molecule is adsorbed horizontally on the surface, it is coordinated through the π electrons of the aromatic ring. Since almost all of the studies of pyridine adsorption on gold have been done in solution well above its conjugate acid's pK_a, the difference in adsorption due to the relative amounts of pyridine (deprotonated form) and pyridinium (protonated form) has not been a subject of investigation. Since the

coordination of the pyridine and pyridinium is through potentially different adsorption motifs, the relative amounts of these two species is a key aspect to consider. The relative amount of DMAP or $DMAPH^+$ at a particular fixed pH can be estimated according to equation:

$$\frac{[DMAP]}{[DMAPH^+]} = 10^{pH-pK_a} \qquad (4.1)$$

At pH 9.7, there is an equal concentration of both protonated and deprotonated forms of DMAP in solution. According to the previous quantitative analysis of DMAP adsorption on polycrystalline gold,[23] the deprotonated from of DMAP is vertically oriented on the gold surface through its endocyclic nitrogen at high pH. At pH 4.5, $[DMAPH^+]$ is about 5 orders of magnitude higher than [DMAP] which shifts the acid - base adsorption equilibrium in favor of adsorbed $DMAPH^+$. Experimentally, this has been observed only at negative potentials, at pH 4.5 on polycrystalline gold.[23] The protonated pyridinium moiety loses its ability to coordinate through its endocyclic nitrogen and hence is coordinated to the metal surface through the delocalized π electrons and adsorbs horizontally on the surface at negative potentials. As the applied potential becomes more positive, adsorbed $DMAPH^+$ loses its proton at the endocyclic nitrogen and reorients to coordinate through a vertical state of adsorption. This is consistent with Arvia and co-workers' study of pyridine (or pyridinium) adsorption on polycrystalline gold at low pH.[23] The major difference between pyridine adsorption and DMAP adsorption on polycrystalline gold was at high pH, where there has been no evidence for $DMAPH^+$ adsorption even at negative potentials on polycrystalline gold, whereas pyridinium ions were reported to adsorb in the horizontal fashion at negative potentials.

From these previous studies, it is apparent that unless protonated, the endocyclic nitrogen is the best coordination site for pyridine/DMAP molecule on gold surfaces. Protonated endocyclic nitrogen loses its properties as a coordination centre for pyridine and its derivatives on gold surfaces, whereas pyridinium derivatives are coordinated to gold by their π-electron system. The vertical adsorption through endocyclic nitrogen can be understood as the mixing of the nonbonding orbital of nitrogen with d, s and p_z states of the gold metal.[18,26] At negative potentials, particularly when the endocyclic nitrogen is protonated, the lone pair of the endocyclic nitrogen can only weakly coordinate to the metal and hence assumes back donation to the delocalized π-electrons of the pyridine ring. Equilibria between DMAP, H^+ and the gold electrode are schematically shown in Figure 4.1 for different electrical states of the metal. For completeness, it should be noted that though this scheme is potentially generally applicable for all pyridine derivatives, only the DMAP system has been thoroughly investigated as a function of pH.

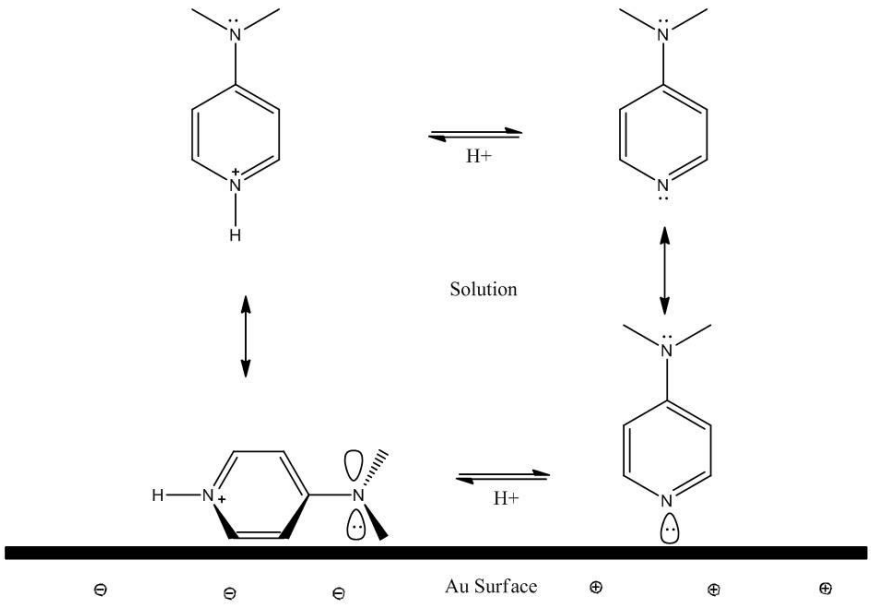

Fig. 4.1
Schematic showing equilibria between DMAP, protons and gold surface.

4.2 Experimental

In this chapter, the adsorption of DMAP on single crystal gold surfaces is described. A qualitative analysis of DMAP/DMAPH$^+$ adsorption on Au(111), Au(100) and polycrystalline gold surfaces is provided with differential capacity measurements, so as to explicate the potential dependent adsorption of DMAP/DMAPH$^+$. Electrochemical experiments to extract thermodynamic parameters that quantitatively characterize DMAP adsorption on Au(111) is discussed, in contrast to the previously reported studies of DMAP adsorption on polycrystalline gold[23] and pyridine adsorption on different gold surfaces[1,2,4,5]. Experimental methodologies for capacity measurements and chronocoulometry measurements have been already detailed in Chapter 2. More specific experimental details of the electrochemical setup and potential step sequences for DMAP adsorption on gold electrode is given in Chapter 3, Section 3.2.5. As in the previous chapter, the representation "DMAP" refers to the free base (neutral) form of the molecule and "DMAPH$^+$" represents the protonated form of the molecule. In instances where the species in question could be either the base or acid form, it is indicated as DMAP(H$^+$), and when the electrolyte contains an appreciable mixture of both DMAP and DMAPH$^+$ species, DMAP/DMAPH$^+$ is explicitly written.

4.3 Results and Discussions

4.3.1 Differential capacity

Differential capacity measurements were carried out to qualitatively characterize the electrochemical adsorption of DMAP(H$^+$) on gold. The measurements were done on Au(111), Au(100) and polycrystalline electrodes at two representative pH values, *viz.* pH 4.5 and pH 9.7. Figure 4.2a shows differential capacity curves for DMAP(H$^+$) adsorption

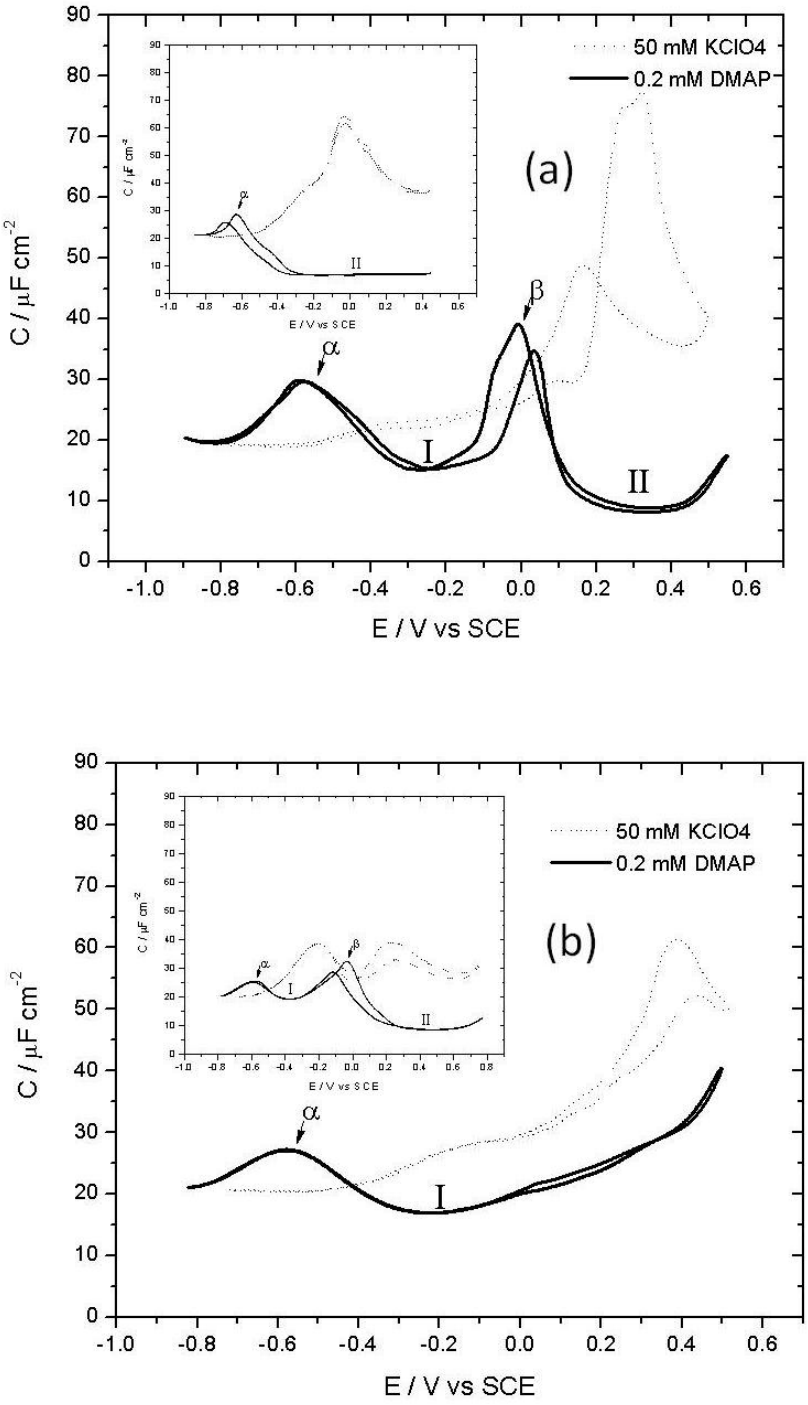

Fig.4.2

Differential capacity curves for Au(111) in 50 mM $KClO_4$ supporting electrolyte (·····) and in the presence of 0.2 mM formal concentration of DMAP (—) at (a) pH 9.7 and (b) pH 4.5.

The insets show corresponding differential capacity curves for polycrystalline gold under identical conditions.

at pH 9.7 on the Au(111) electrode and the adsorption behavior on polycrystalline gold under the same conditions is shown in the inset. At the most negative of potentials, the capacity curves for the solution containing DMAP(H^+) merge with the electrolyte curve, indicating that DMAP(H^+) is completely desorbed from the electrode's surface. On Au(111), as the potential is scanned in the positive direction, a somewhat broad, but featureless, pseudocapacitive peak (denoted α) centered at E ~ -0.6 V is observed. The α peak is shifted to E ~ -0.7 V for polycrystalline gold electrode (inset). Following this peak, the capacity drops to a pit region(C~15 μFcm^{-2}) and at further positive potentials a second, large, pseudocapacitive peak (denoted by β) is seen on Au(111). Following the β peak, the capacity drops to a second, but lower capacity pit region (C~7 μFcm^{-2}). This β peak is not observed for DMAP on polycrystalline gold (inset) at this pH.

Figure 4.2b shows differential capacity curves corresponding to DMAP(H^+) adsorption at pH 4.5 on the Au(111) electrode as well as the polycrystalline gold (inset). Due to hydrogen evolution, the electrolyte curve could not be scanned to sufficiently negative potentials to match the capacity curve for the solution containing DMAP(H^+), but the capacity at negative potentials for both the electrolyte and DMAP(H^+) curves match, indicating the desorption of DMAP(H^+) at negative potentials. Following the α peak, the capacity falls to a pit region (C~17 μFcm^{-2}) and slowly increases as the potential is scanned to further positive values. However, unlike the case at pH 9.7, there is no indication of a β peak for Au(111) at this pH. Apparently, the capacity increases at positive potentials even though there is no obvious phase transition peak. The increase in capacitance is commensurate with the rise in the electrolyte curve. Adsorption of anions at the interface may occur if the surface coverage of DMAP(H^+) is very low at these

potentials which would account for the observed increase in capacity. Alternatively, a partial desorption of the DMAP(H^+) from the surface may also result in an increase in the capacity. On polycrystalline gold at this lower pH, following the α peak and the capacity pit region, another pseudocapacitive peak (β) is observed, which then falls to a low capacity region (C ~ 7 μFcm^{-2}) at further positive potentials.

A qualitative evaluation of the electrochemical adsorption of DMAP(H^+) on Au(111) and polycrystalline gold suggests that there is a significant crystallography dependence on the adsorption behavior of DMAP(H^+) on gold surfaces. At high pH, two adsorption states are observed on Au(111), state I adsorption corresponds to a capacity of ~17 μFcm^{-2} and adsorption state II corresponds to C ~ 7 μFcm^{-2}. At this high pH, only adsorption state II is observed for the polycrystalline electrode. Conversely, at low pH, only adsorption state I is observed on Au(111), while states I and II, both are observed on the polycrystalline electrode.

If one once again neglects the contribution of the diffuse part of the double layer, the approximate fractional coverage, Θ, can be determined using Damaskin's theory of parallel capacitors[27]

$$C = C_{org}\Theta + C_0(1 - \Theta) \qquad (4.2)$$

where C is the measured capacity at a given pH, C_{org} is the capacity of a complete monolayer, and C_0 is the capacity of the bare electrode. The ratio of the fractional surface coverage in state I and state II can be calculated using the assumption that the value of C_{org} = 7.0 μF cm^{-2} (i.e., the lowest capacity measured).

The ratio of the fractional coverage of state I and state II is approximately 4. This semi-quantitative analysis indicates that state I is a low coverage DMAP(H^+) which can undergo a phase transition to form a high DMAP surface coverage at state II. The range of potentials for these adsorption states on gold surface has strong crystallography dependence as can be observed by comparing the differential capacity data obtained for the Au(111) and polycrystalline gold electrodes.

The general nature of the differential capacity plots described above is qualitatively comparable to the well-studied adsorption of pyridine on gold. Lipkowski and co-workers reported capacitive plots of pyridine adsorption on polycrystalline gold and Au(111) demonstrating the two-state adsorption behavior.[1,5] The pseudocapacitive peak between state I and state II adsorption states for pyridine adsorption on gold surfaces was attributed to the phase transition from horizontally adsorbed pyridine at negative potentials to a vertical orientation at positive potentials. The two state adsorption states with a pseudocapacitive transition peak between the two states of adsorption in the current system suggests a similar horizontal to vertical transition. The differential capacity plots for DMAP(H^+) adsorption on polycrystalline gold at low pH and Au(111) at high pH in Figure 4.2 show qualitatively similar capacity curves. More importantly, here only one adsorption state is seen for DMAP(H^+) on polycrystalline gold at high pH and on Au(111) at low pH. It is therefore apparent that the electrosorption of DMAP(H^+) on gold is very much dependent on the crystallographic orientation of the gold surface as well as the electrolyte pH.

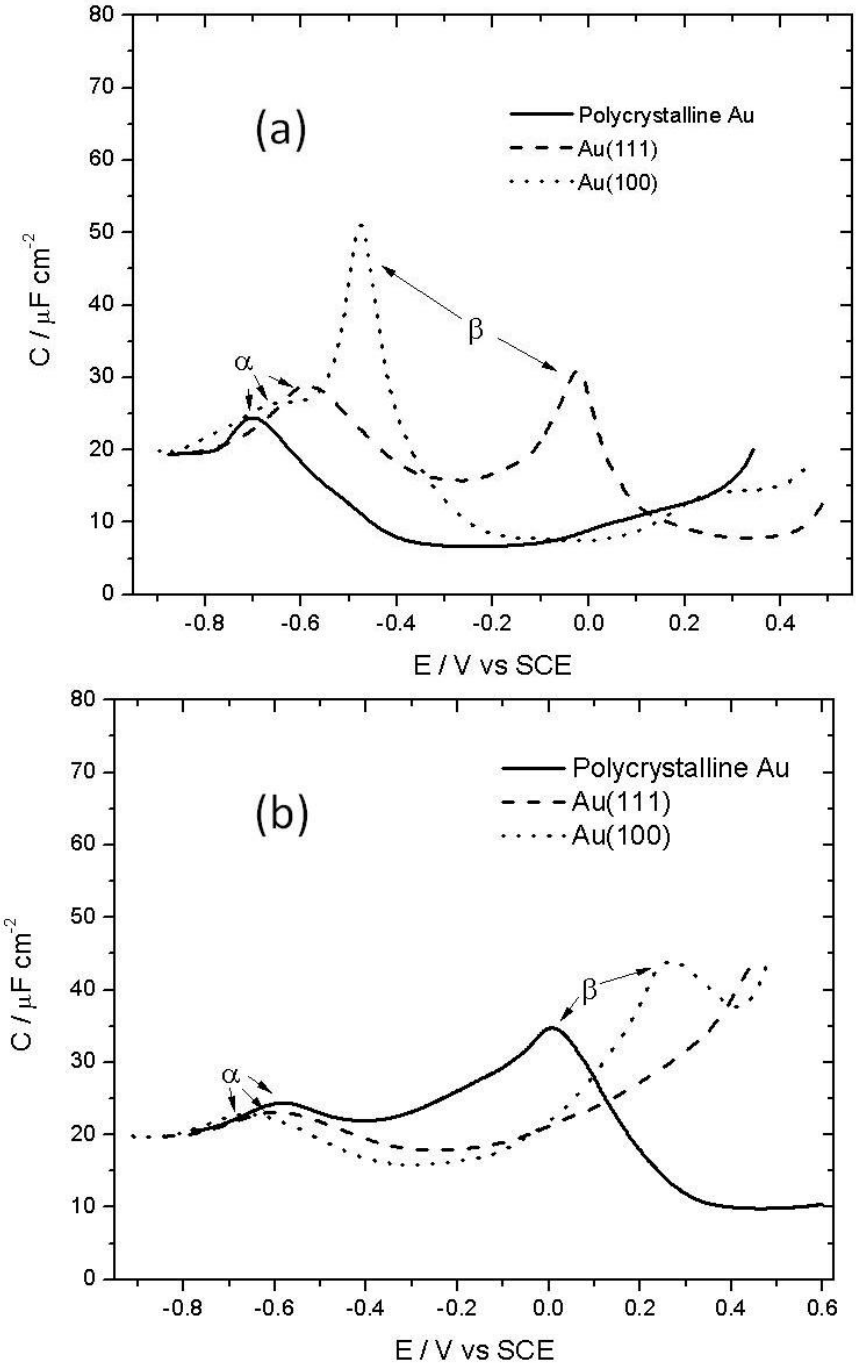

Fig. 4.3

Differential capacity curves for Au(111) (----), Au(100) (⋯⋯) and polycrystalline gold (—) in the presence of 0.1 mM formal concentration of DMAP at (a) pH 9.7 and (b) pH 4.5.

To further investigate the dependence of crystallography on the stability of these two adsorption states, the adsorption behavior of DMAP(H^+) on Au(100) was also studied. The adsorption behavior of DMAP(H^+) on Au(100) is compared with Au(111) and polycrystalline gold at the representative pHs (0.1 mM formal concentration of DMAP) in Figure 4.3 (for clarity, only the positive-going scans are shown). At pH 9.7 (Figure 4.3a), a sharp pseudocapacitive β-peak appears immediately after the α-peak, suggesting that DMAP adsorption in state I is present on Au(100) for only a very narrow range of potentials. At pH 9.7, there is no evidence of state I adsorption on polycrystalline gold, and it is only present on Au(100) for a very narrow range of potentials (-0.55 V to -0.60 V). On the other hand, state I is present for a wider range of potentials ((-0.45 V to -0.10 V) on Au(111) in basic solutions. At pH 4.5 (Figure 4.3b), the adsorption behavior on Au(100) is similar to Au(111), but a β-peak is clearly seen on Au(100) at *E* ~0.25V whereas it is entirely absent for the Au(111) electrode. The position of the Au(100) β-peak is shifted in the positive direction by approximately 0.25 V compared to polycrystalline gold. It appears that the stability of adsorption state I on Au(100) falls between that of A(111) and polycrystalline gold. At pH 4.5, there is no evidence of state II or a phase transition peak on Au(111), but a phase transition peak that is shifted to positive potentials can be seen on Au(100). This can be related to the adsorption behavior on polycrystalline gold where state II is stable for a wider range of positive potentials. Within the range of potentials investigated, the stability of state I adsorption (or equivalently, the instability of state II adsorption) of DMAP(H^+) follows the order Au(111) > Au(100) >Au(poly), at both pHs studied.

4.3.2 Chronocoulometry

Chronocoulometry studies of DMAP(H^+) adsorption on Au(111) has been performed and compared with previously reported studies on polycrystalline gold surfaces. Chronocoulometry studies were performed at different DMAP/$DMAPH^+$ concentrations at electrolytes of pH 4.5 and 9.7. Details of the chronocoulometry measurements and the determination of absolute charge density at a given potential have already been discussed in Chapter 2 and Chapter 3. The desorption potential was determined on the basis of differential capacity measurements, i.e. DMAP/$DMAPH^+$ desorbs from the electrode at potentials below -0.9 V on all gold surfaces at concentrations less than 2 mM.

The results of chronocoulometry measurements performed at pH 9.7 are shown in Figure 4.4a. The plots are divided into four sections. Region Ia corresponds to the most negative electrode polarizations where all the curves merge with the electrolyte curve, indicating complete desorption of DMAP/$DMAPH^+$ at these potentials. An inflection point is observed in the boundary between region Ia and region IIa that corresponds to the adsorption/desorption peaks observed in the differential capacity curves. In region IIa, the charge curves are quasi-linear at all the measured concentrations of DMAP/$DMAPH^+$, which is consistent with state I adsorption on Au(111) described in the Differential Capacity section. A more pronounced inflection point that follows a quasi-plateau region is observed in region IIIa. This inflection point and the quasi-plateau region is consistent with the phase transition peak and state II adsorption described in the Differential Capacity section. All the charge curves that correspond to different concentrations of DMAP/$DMAPH^+$ intersect the curve for the supporting electrolyte at E ~ 0.265 V, which

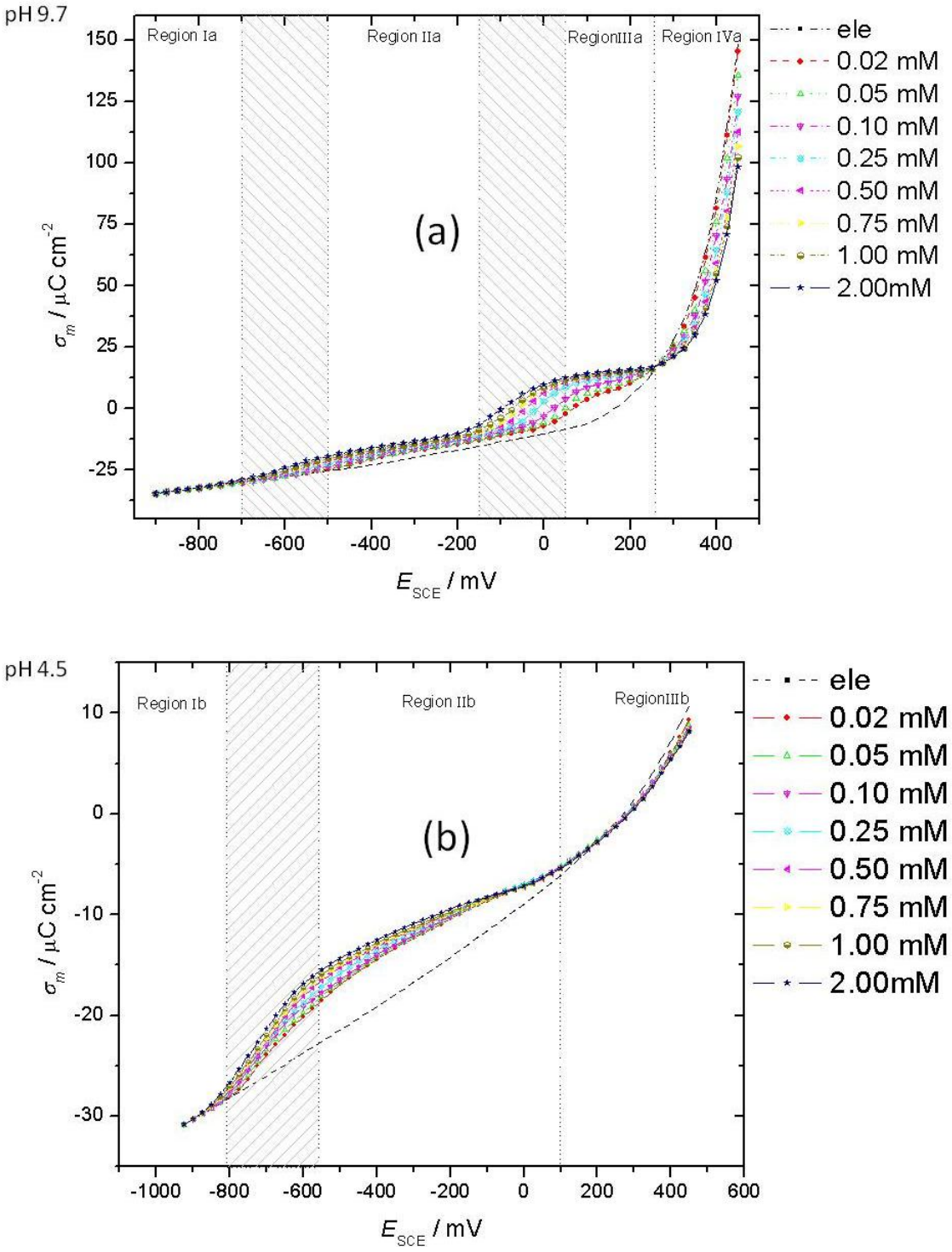

Fig.4.4

Charge density versus electrode potential curves for Au(111) in 50 mM $KClO_4$ supporting electrolyte (----) and following DMAP concentrations: 0.02 mM (●), 0.05 mM (△), 0.10 mM(▽), 0.25 mM(▩), 0.50 mM(◁), 0.75 mM(▷), 1.00 mM(⬙), 2.00 mM(★), at (a) pH 9.7 and (b) pH 4.5.

is close to the pzc of Au(111), indicating that this is the potential of maximum adsorption, E_{max}. In region IVa, the slopes of the charge density curves for the electrolyte and various DMAP/$DMAPH^+$ concentrations, both increase drastically, presumably due to hydroxide adsorption.

The shift in the potential of zero charge (ΔE_{pzc}) in the charge data due to the adsorption of DMAP/$DMAPH^+$ molecules on the surface provides insight into the nature of the adsorbed layer. The shift in pzc due to the displacement of surface water by a film of adsorbed molecules is described by[27]

$$\Delta E_{PZC} = \frac{\Gamma_m(\mu_{\mathrm{DMAP(H+)}} - n\mu_w)}{\varepsilon} \qquad (4.3)$$

where Γ_m is the maximum surface concentration of the surfactant, $\mu_{DMAP(H+)}$ and μ_w represents the average permanent dipole moment normal to the surface due to the adsorption of DMAP(H^+) and water molecules respectively, *n* is the number of water molecules displaced by a single DMAP(H^+) molecule and ε represents the permittivity of the inner layer. The shift in pzc is a measure of the internal dipoles created due to the adsorption of molecules on the metal surface and hence the magnitude of the pzc shift can be used as a measure of the orientation of adsorbed molecules/ions. A linear extrapolation of the charge density curve that corresponds to a particular state of adsorption to zero charge density ordinate was made to determine ΔE_{pzc} with respect to the electrolyte-only curve. ΔE_{pzc} corresponding to 1 mM bulk concentration of DMAP(H^+) on Au(111) at pH 9.7 was calculated at the two regions corresponding to different adsorption states identified from the equilibrium capacity curves. The extrapolation of the quasi linear part of the curve in region II gives a ΔE_{pzc} value ~ 0 V.

This would indicate that the molecule is lying flat on the surface in region II, which results no net dipole moment. Presumably, the endocyclic nitrogen of DMAP is protaned and ion-paired with perchlorate anion, in this region. On the other hand, the estimated ΔE_{pzc} for region III is ~ −1 V, which corresponds to a large negative net dipole.[28] This would indicate that a thickly packed vertical layer of DMAP is adsorbed on the surface in region III, with its endocyclic nitrogen facing towards the metal surface.

The charge density curves for pH 4.5 are presented in Figure 4.4b, where the curves are divided into three sections. In region Ib, charge density curves correspond to different concentrations of DMAP/$DMAPH^+$ merge with the electrolyte curve, indicating complete desorption of DMAP/$DMAPH^+$ from the surface. In the boundary between region Ib and region IIb, DMAP/$DMAPH^+$ charge curves are characterized by a pronounced inflection point that corresponds to adsorption/desorption peaks observed in the differential capacity measurements. This inflection point is followed by a quasi-plateau state in region IIb. Between region IIb and region IIIb, charge curves corresponding to all different concentrations of DMAP/$DMAPH^+$ merge, and intersect the charge curve for the electrolyte at potentials close to the E_{pzc}, which corresponds to the potential of maximum adsorption, E_{max}. In region IIIb, all of the charge curves are merged close to the electrolyte curve with no sign of inflection, indicating that there are no changes happening to the adsorbed layer in this region of potentials. At pH 4.5, only one state of adsorption is evident from the charge curves. The charge curve in region IIb was extrapolated to zero ordinate to determine the shift in the potential of zero charge. The ΔE_{pzc} value calculated for 1 mM bulk concentration of DMAP(H^+) on Au(111) at pH

4.5 was ~ +450 mV, which is again a large positive shift suggesting that $DMAPH^+$ is presumably lying flat on Au(111) surface at this pH.

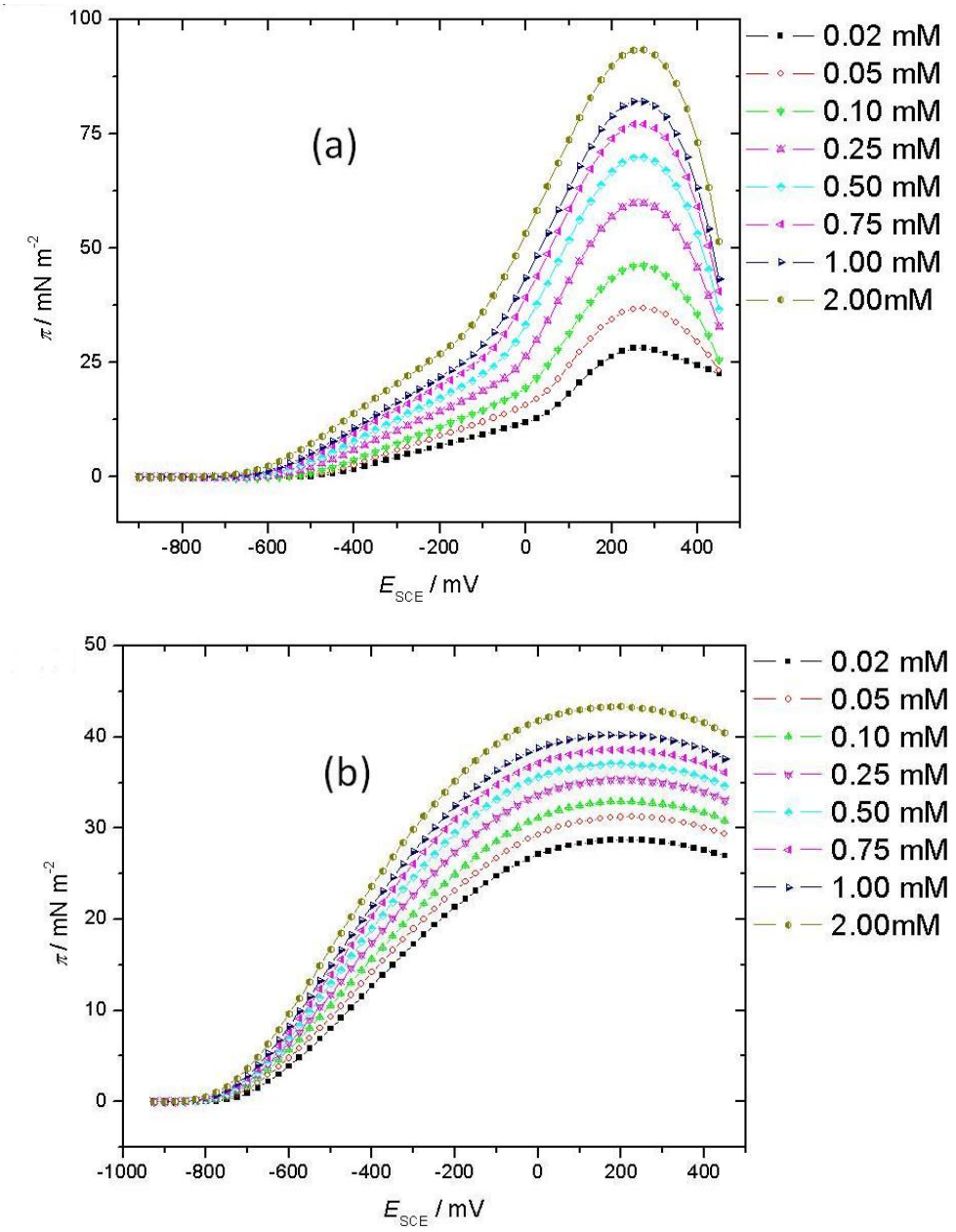

Fig. 4.5
Plots of the surface pressure of DMAP at the Au(111)/solution interface versus electrode potential for the following bulk DMAP concentrations: 0.02 mM (■), 0.05 mM (○), 0.10 mM(▽), 0.25 mM(⋇), 0.50 mM(◆), 0.75 mM(◀), 1.00 mM(▶), 2.00 mM(◐), at (a) pH 9.7 and (b) pH 4.5.

4.3.3 Surface pressures and Gibbs surface excesses

Apart from a qualitative description of the charge curves described above, chronocoulometry data can be used to quantify the adsorption of molecules at the interface. The analysis of the charge data follow a similar treatment described in Chapter 2 for DMAP/halide adsorption on polycrystalline gold.

Integration of the charge *versus* potential curves at any given concentration of the DMAP/DMAPH$^+$ species yields the surface pressure

$$\pi = \left(\int_{E_{des}}^{E_c} \sigma_m dE \right)_{c_x} - \left(\int_{E_{des}}^{E_c} \sigma_m dE \right)_{c_x=0} \qquad (4.4)$$

The surface pressure *versus* potential data for DMAP/DMAPH$^+$ adsorption on Au(111) calculated based on the chronocoulometry data, for the corresponding two pH systems studied are shown in Figure 4.5. At pH 9.7(Figure 4.5a), the surface pressure curves show a foot region at negative potentials that precedes a bell shaped region at positive potentials. These two regions once again suggest two different states of adsorption. Surface pressure data corresponding to pH 4.5 (Figure 4.5b) shows only one potential of maximum adsorption (at E ~ 0.1 V), suggesting one state of adsorption for DMAP/DMAPH$^+$ on Au(111) at this pH.

The Gibbs surface excess, Γ, can be calculated by differentiating surface pressure data with respect to the natural log of the formal DMAP/DMAPH$^+$ concentration at constant electrode potential:

$$\Gamma = \frac{1}{RT} \left[\frac{\delta \pi}{\delta ln c_{DMAP}} \right]_E \qquad (4.5)$$

For the pH 9.7 system, π *versus* ln c_{DMAP} were fitted to a third-order polynomial and the Gibbs excess was then calculated by differentiation of the fitted curves. Figure 4.6a shows Gibbs excess data corresponding to the pH 9.7 system, where the Γ versus E plot shows two limiting surface coverages. These two limiting surface coverages correspond to two different states of adsorption described in the Differential Capacity section. In state I, the largest coverage is 1.8×10^{-10} mol cm^{-2}, whereas the limiting coverage at state II is 7.0×10^{-10} mol cm^{-2}. The maximum surface coverage obtained here is equal to the maximum value obtained for DMAP adsorption on polycrystalline gold (7.0×10^{-10} mol cm^{-2})[23], but only one limiting surface coverage could be observed on polycrystalline gold at this pH. The value of maximum surface coverage obtained here is also comparable with the vertical adsorption of pyridine on Au(111) (6.7×10^{-10} mol cm^{-2})[5] and polycrystalline gold (7.0×10^{-10} mol cm^{-2}) reported by Stolberg et al.,[1] and the packing density of pyridine predicted based on van der Waal radii (7.6×10^{-10} mol cm^{-2}). The lower value of the limiting surface coverage obtained here (1.8×10^{-10} mol cm^{-2}) is comparable with surface concentration corresponding to flat-lying configuration of DMAP(H^+) on polycrystalline gold (1.5×10^{-10} mol cm^{-2}) at pH 4.5. Surface coverages of horizontally adsorbed pyridine (1.4×10^{-10} mol cm^{-2}) and 4-cyanopyridine (1.2×10^{-10} mol cm^{-2}) on Au(111) have been reported by Lipkowski and co-workers. Hence the two states of adsorption observed here can be understood as flate-lying (state I) and vertical (state II) orientation of DMAP on Au(111), which is different from polycrystalline gold where there was no evidence for state I adsorption of DMAP.

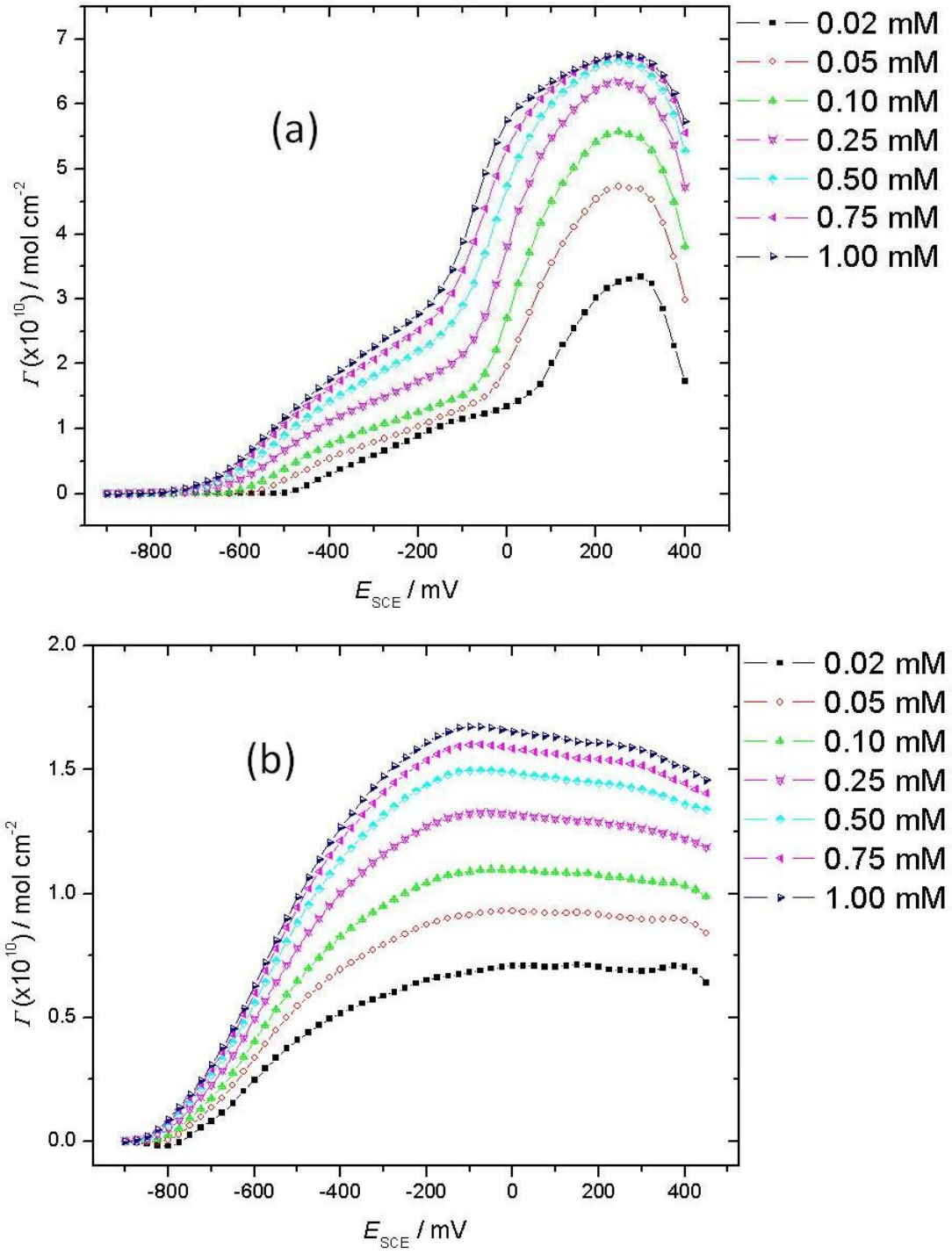

Fig. 4.6

Plots of the Gibbs excess of DMAP at the Au(111)/solution interface versus electrode potential for the following bulk DMAP concentrations: 0.02 mM (■), 0.05 mM (○), 0.10 mM(△), 0.25 mM(⋈), 0.50 mM(◇), 0.75 mM(◁), 1.00 mM(▷), at (a) pH 9.7 and (b) pH 4.5.

The Gibbs excess *versus* potential plot for DMAP(H^+) adsorption on Au(111) from the pH 4.5 electrolyte containing different bulk concentrations of the surfactant is shown in Figure 4.6b. At this pH only one state of adsorption was observed in the range of potentials studied. At very negative potentials, there is little surfactant adsorption on the surface, but with increasingly positive polarization, the surface concentration increases until reaching a plateau at the most positive potentials. The maximum value of surface coverage obtained here (1.8×10^{-10} mol cm^{-2}) matches the state I limiting surface coverage at pH 9.7, and once again corresponds to the flat-lying configuration of DMAP(H^+).

Comparing the Gibbs surface excesses of DMAP/DMAPH+ on Au(111) and polycrystalline gold helps to understand the difference in surface coverage on these surfaces. Gibbs surface excess for DMAP adsorption on polycrystalline and Au(111) electrodes corresponding to 1 mM bulk concentration at pH 9.7 is shown in Figure 4.7a. The limiting surface coverage of state II adsorption (vertically adsorbed molecule) is reached at E ~ -0.425 V on polycrystalline gold. On Au(111), state I (horizontally adsorbed molecule) levels of surface coverage is reached at E ~ -0.250 V and the surface coverage corresponding to state II adsorption (vertically adsorbed molecule) is reached at E ~ +0.050 V. In Figure 4.7b, Gibbs surface excess plots corresponding to 1 mM bulk concentration of DMAP(H^+) on Au(111) and polycrystalline gold are shown. On polycrystalline gold there is a clear evidence for two adsorption states: state I corresponds to horizontally adsorbed molecule at ~ -0.250 V and state II corresponds to vertically adsorbed molecules at ~ +0.050 V. On Au(111), the plot shows evidence for horizontal adsorption only, where the surface coverage corresponding to state I adsorption is

reached at ~-0.050 V and Gibbs surface excess remains more or less constant at positive potentials with no evidence for state II adsorption.

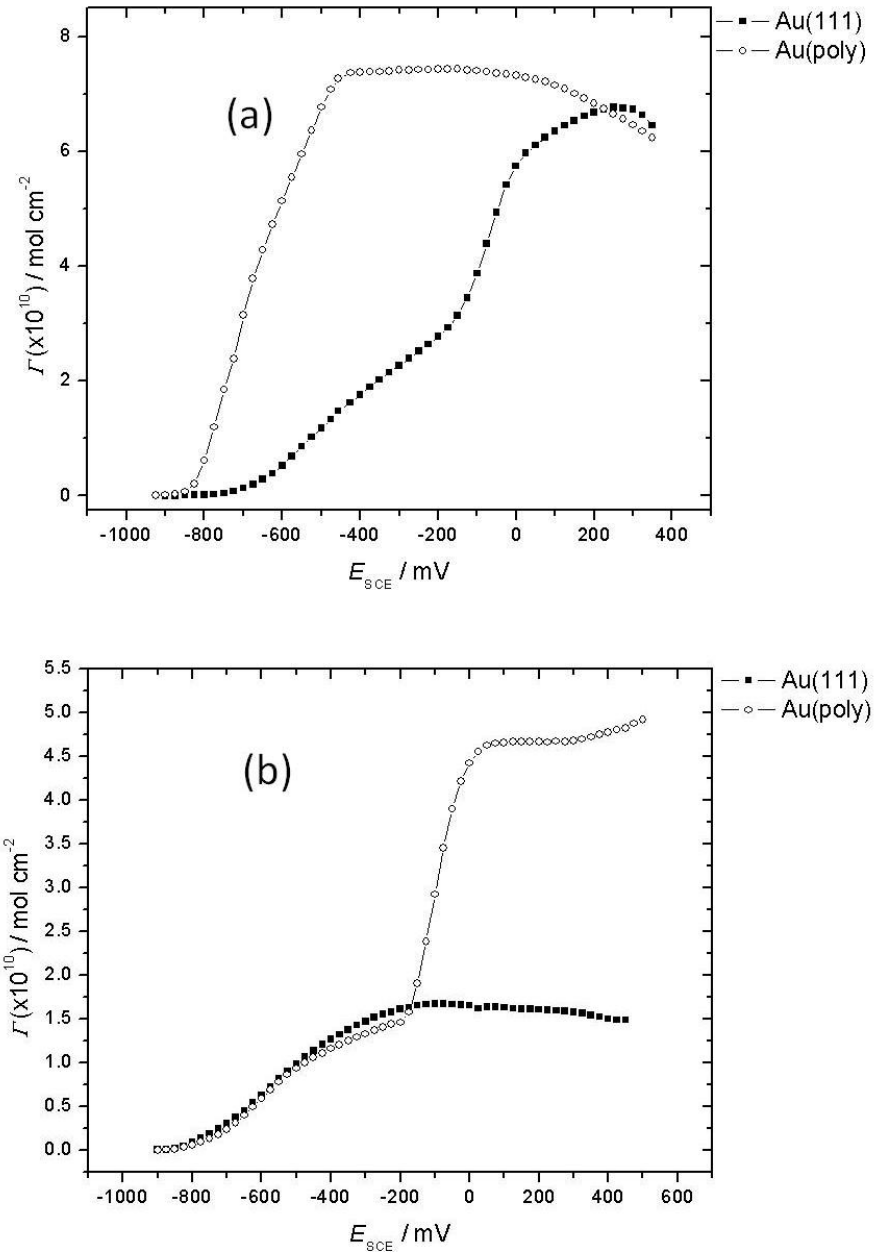

Fig. 4.7
Plots of the Gibbs excess of DMAP versus electrode potential at the Au(111)/solution interface (■), polycrystalline Au/solution interface (⊙) for the 1 mM bulk DMAP concentrations. (a) at pH 9.7, (b) at pH 4.5.

4.4 Summary and Conclusions

An electrochemical evaluation of the pH-dependent adsorption of 4-(dimethylamino)-pyridine on Au(111) has been provided and compared with Au(100) and polycrystalline gold surfaces. Differential capacity experiments and thermodynamic analyses of the chronocoulometry data suggest that DMAP(H^+) adsorption has a strong crystallographic dependence. On Au(111), even at high pH, $DMAPH^+$ is adsorbed on the surface at the negative end of the potentials studied, whereas there was no evidence of $DMAPH^+$ adsorption on polycrystalline gold at this pH. Both differential capacity measurements and thermodynamic analyses of the charge data suggest two states of adsorption on Au(111) at pH 9.7: A flat lying configuration of protonated DMAP molecules at negative potentials and vertically oriented DMAP molecules adsorbed through the endocyclic nitrogen at positive potentials. At pH 4.5, (well below the pK_a of $DMAPH^+$) only the protonated form of DMAP is adsorbed on Au(111), which is presumably adsorbed in a flat orientation, even at positive potentials. This again, is different from the adsorption behavior on polycrystalline gold, where horizontally adsorbed $DMAPH^+$ at negative potentials deprotonates and reorients to adsorb vertically at the positive end of the potentials. Clearly, $DMAPH^+$ adsorption is more favored on Au(111) in contrast to polycrystalline gold. Also, it has been observed that the stability of $DMAPH^+$ on the Au(100) surface falls between Au(111) and polycrystalline gold.

Recent literature report on DMAP stabilized gold nanoparticle synthesized in aqueous solution shows that the nanoparticle surface is polycrystalline with prominent (111), (200), (220) and (311) planes of face-centered cubic lattice being present on the surface of the metal core.[29] Based on the packing density of DMAP molecules on the

nanoparticle surface, Griffin and Fitzmaurice suggested the vertical orientation of DMAP is present on DMAP stabilized gold nanoparticles.[29] In the previous chapter, it has been made clear that the DMAP stabilized gold nanoparticle surface is positively charged. Also, the thermodynamic data provided herein suggests that the vertical adsorption of DMAP on Au(111) is possible only at high pH and at potentials more positive of its pzc. At pH 4.5, the adsorption of neutral DMAP is not favorable on Au(111) even at potentials above its pzc. DMAP stabilized gold nanoparticles are not very stable at pH $\leq$ 4.5. At this pH, only a low coverage (horizontal) adsorption of $DMAPH^+$ is observed on Au(111). At low pH, the differential capacity experiments on the (100) plane show no evidence for high coverage films even at potentials more positive of the pzc. On the contrary, even at low pH, the vertical adsorption of DMAP is observed on polycrystalline gold at potentials above its pzc. Since the vertical adsorption of DMAP is not favorable on Au(111) and Au(100) surfaces, this state of adsorption observed on polycrystalline gold at low pH must be resulting from the adsorption on some high-index planes on the polycrystalline gold electrode. Based on these observations, it can be concluded that, at low pHs, the vertical state of adsorption of DMAP is only stable on relatively higher order (hkl) planes. It appears that, both the solution pH and electrical state of the nanoparticle core, must favor the vertical state of adsorption of DMAP on the nanoparticle surface in order to provide stable colloidal dispersions.

Reference List

1. Stolberg, L.; Richer, J.; Lipkowski, J.; Irish, D. E. Adsorption of pyridine at the polycrystalline gold--solution interface. *Journal of Electroanalytical Chemistry and Interfacial Electrochemistry* **1986,** *207* (1-2), 213-234.

2. Stolberg, L.; Lipkowski, J.; Irish, D. E. Adsorption of pyridine at the Au (100)-solution interface. *Journal of Electroanalytical Chemistry and Interfacial Electrochemistry* **1987,** *238* (1-2), 333-353.

3. Stolberg, L.; Lipkowski, J.; Irish, D. E. Adsorption of pyridine at the Au (100)-solution interface. *Journal of Electroanalytical Chemistry and Interfacial Electrochemistry* **1987,** *238* (1-2), 333-353.

4. Stolberg, L.; Lipkowski, J.; Irish, D. E. Adsorption of pyridine at the Au(110)-solution interface. *Journal of Electroanalytical Chemistry and Interfacial Electrochemistry* **1990,** *296* (1), 171-189.

5. Stolberg, L.; Morin, S.; Lipkowski, J.; Irish, D. E. Adsorption of pyridine at the Au(111)-solution interface. *Journal of Electroanalytical Chemistry and Interfacial Electrochemistry* **1991,** *307* (1-2), 241-262.

6. Stolberg, L.; Lipkowski, J.; Irish, D. E. Adsorption of pyridine at the Au(311)--solution interface. *Journal of Electroanalytical Chemistry* **1992,** *322* (1-2), 357-372.

7. Stolberg, L.; Lipkowski, J.; Irish, D. E. Adsorption of pyridine at the Au(311)--solution interface. *Journal of Electroanalytical Chemistry* **1992,** *322* (1-2), 357-372.

8. Skoluda, P.; Holzle, M.; Lipkowski, J.; Kolb, D. M. Pyridine adsorption on reconstructed and unreconstructed Au(100). *Journal of Electroanalytical Chemistry* **1993,** *358* (1-2), 343-349.

9. Smith, C. I.; Maunder, A. J.; Lucas, C. A.; Nichols, R. J.; Weightman, P. Adsorption of Pyridine on Au(110) as Measured by Reflection Anisotropy Spectroscopy. *Journal of The Electrochemical Society* **2003,** *150* (4), E233-E236.

10. Sako, E. O.; Kondoh, H.; Nakai, I.; Nambu, A.; Nakamura, T.; Ohta, T. Reactive adsorption of thiophene on Au(1á1á1) from solution. *Chemical Physics Letters* **2005,** *413* (4-6), 267-271.

11. Bilic, A.; Reimers, J. R.; Hush, N. S.; Hoft, R. C.; Ford, M. J. Adsorption of Benzene on Copper, Silver, and Gold Surfaces. *Journal of Chemical Theory and Computation* **2006,** *2* (4), 1093-1105.

12. Ma, C. Q.; Mena-Osteritz, E.; Debaerdemaeker, T.; Wienk, M.; Janssen, R. G.; B+ñuerle, P. Functionalized 3D Oligothiophene Dendrons and DendrimersGÇö Novel Macromolecules for Organic Electronics. *Angewandte Chemie International Edition* **2007,** *46* (10), 1679-1683.

13. Wang, C.; Kilitziraki, M.; MacBride, J. A. H.; Bryce, M. R.; Horsburgh, L. E.; Sheridan, A. K.; Monkman, A. P.; Samuel, I. D. W. Tuning the Optoelectronic Properties of Pyridine-Containing Polymers for Light-Emitting Devices. *Advanced Materials* **2000,** *12* (3), 217-222.

14. Gittins, D. I.; Caruso, F. Spontaneous Phase Transfer of Nanoparticulate Metals from Organic to Aqueous Media. *Angewandte Chemie International Edition* **2001,** *40* (16), 3001-3004.

15. Meier, C.; Ziener, U.; Landfester, K.; Weihrich, P. Weak Hydrogen Bonds as a Structural Motif for Two-Dimensional Assemblies of Oligopyridines on Highly Oriented Pyrolytic Graphite:GÇë An STM Investigation. *The Journal of Physical Chemistry B* **2005,** *109* (44), 21015-21027.

16. Ziener, U. Self-Assembled Nanostructures of Oligopyridine Molecules. *The Journal of Physical Chemistry B* **2008,** *112* (47), 14698-14717.

17. Kunzel, D.; Markert, T.; German, s. l.; Benoit, D. M. Bis(terpyridine)-based surface template structures on graphite: a force field and DFT study. *Physical Cheistry Chemical Physics* **2009,** *11* (39), 8867-8878.

18. Lipkowski, J.; Stolberg, L.; Yang, D. F.; Pettinger, B.; Mirwald, S.; Henglein, F.; Kolb, D. M. Molecular adsorption at metal electrodes. *Electrochimica Acta* **1994,** *39* (8-9), 1045-1056.

19. Iannelli, A.; Richer, J.; Lipkowski, J. Adsorption of pyrazine at the polycrystalline gold-solution interface. *Langmuir* **1989,** *5* (2), 466-473.

20. Dretschkow, T.; Wandlowski, T. Structural studies of 2,2'-bipyridine on Au(100). *Journal of Electroanalytical Chemistry* **1999,** *467* (1-2), 207-216.

21. Gandubert, V. J.; Lennox, R. B. Assessment of 4-(Dimethylamino)pyridine as a Capping Agent for Gold Nanoparticles. *Langmuir* **2005,** *21* (14), 6532-6539.

22. Rucareanu, S.; Gandubert, V. J.; Lennox, R. B. 4-(N,N-Dimethylamino)pyridine-Protected Au Nanoparticles: Versatile Precursors for Water- and Organic-Soluble Gold Nanoparticles. *Chemistry of Materials* **2006,** *18* (19), 4674-4680.

23. Barlow, B. C.; Burgess, I. J. Electrochemical Evaluation of 4-(Dimethylamino)pyridine Adsorption on Polycrystalline Gold. *Langmuir* **2006,** *23* (3), 1555-1563.

24. Andreasen, G.; Vela, M. E.; Salvarezza, R. C.; Arvia, A. J. Dynamics of Pyridine Adsorption on Gold(111) Terraces in Acid Solution from in-Situ Scanning Tunneling Microscopy under Potentiostatic Control. *Langmuir* **1997,** *13* (25), 6814-6819.

25. Gomez, M. M.; Garcoa, M. P.; San Fabi+ín, J.; Vízquez, L.; Salvarezza, R. C.; Arvia, A. J. Influence of the Adsorbate Structure and Surface Barrier at Micropores. The Adsorption on Columnar-Structured Gold Electrodes of

Pyridine from Aqueous Perchlorate Ion-Containing Solutions. *Langmuir* **1997,** *13* (5), 1317-1326.

26. Jones, T. E.; Zuo, C.; Jagodzinski, P. W.; Eberhart, M. E. Molecular Orbital Model for Pyridine/Pyridyl Adsorption on Metal Surfaces. *The Journal of Physical Chemistry C* **2007,** *111* (14), 5493-5496.

27. Damaskin, B.; Frumkin, A.; Chizhov, A. Generalized model of the surface layer for the case of adsorption of inorganic molecules on the electrode. *Journal of Electroanalytical Chemistry* **1970,** *28* (1), 93-104.

28. Guidelli, R. Molecular Models of Organic Adsorption at Metal-Water Interfaces. In *Adsorption of Molecules at Metal Electrodes*, Lipkowski, J., Ross, P. N., Eds.; VCH Publishers, Inc.: New York, 1992.

29. Griffin, F.; Fitzmaurice, D. Preparation and Thermally Promoted Ripening of Water-Soluble Gold Nanoparticles Stabilized by Weakly Physisorbed Ligands. *Langmuir* **2007,** *23* (20), 10262-10271.

Chapter 5

Adsorption of a Quaternary Ammonium Surfactant on Au(100)

5.1 Introduction

In this chapter, a quantitative description of the adsorption of a cationic surfactant, N-octyl-N,N,N-trimethylammonium triflate (OTA-Tf), on both the reconstructed and unreconstructed surfaces of Au(100) is discussed. The scope of this work extends beyond the quantitative evaluation of a cationic surfactant adsorption on reconstructed and unreconstructed surfaces, and when combined with the results from Chapter 6 and Chapter 7 can be used to explain the growth mechanism of gold nanorods formed in the presence of quaternary ammonium bromide surfactants. There is speculation in the literature that nanoparticle anisotropy is caused by the differences in the surface concentrations of quaternary ammonium stabilizers on the low index faces. For example, it has been postulated that cetyltrimethylammonium bromide (CTA-Br) stabilized gold nanorods are formed due to the specific adsorption of CTA-Br on the Au(111) and Au(100) faces of gold nanoparticle seed crystals. Studies have suggested that the quaternary ammonium head group and the bromide anion are the key components inducing nanoparticle shape anisotropy.[1,2] More details of this aspect will be addressed in Chapter 6 and Chapter 7, whereas this chapter is dedicated to understanding the effect of surface reconstruction on the adsorption behavior of octyltrimethylammonium triflate on Au(100). Since a fully reconstructed Au(100) surface resembles an Au(111)-(1x1) surface, a preliminary understanding of the quaternary ammonium surfactant adsorption on Au(111) and Au(100) surfaces can be obtained from studies performed on reconstructed and unreconstructed Au(100) surfaces.

The use of a single crystal electrode is desirable for studying processes at electrified interfaces because a precise analysis is only possible if the structure of the electrode surface is known. Conversely, this is true only if the surface structure of a single crystal material can be derived directly from its bulk structure. In reality, the atoms at the surface often do not retain their bulk positions. For many single crystal surfaces, due to the break in translational symmetry at the surface, atoms at the surface experience different forces than bulk atoms and hence the atoms at the top layer rearrange with respect to the bulk structure. Rearrangement of surface atoms usually forms more densely packed structures at the surface because of increased electron density between the surface atom cores. This phenomenon, known as surface reconstruction, often involves local bond breaking and new bond formation, leading to a change in surface symmetry and the energetics of the surface.

It is well established from ultrahigh vacuum studies that surface reconstruction happens to all three low index faces of gold when they are subjected to heat treatment.[3,4] Accordingly, the face centered cubic crystal unit cell of bulk gold is reconstructed into a distorted hexagonal phase on the surface. Typical reconstruction of an Au(100) surface leads to a (5x20) reconstruction,[5,6] popularly known as the "hex" structure, while the (110) surface of gold typically reconstructs into (1x2) or (1x3),[4,7,8] popularly known as "missing row" reconstructions. In both these cases, the reconstruction leads to the formation of a periodic array of (111) microfacets on the surface. Though energetically stable, the Au(111) surface can also be thermally reconstructed into a compressed ($\sqrt{3}$x22) surface.[9,10] The overall change in surface structure resulting from this minor compression is relatively small. The effect of surface reconstruction on the adsorption

behavior of a quaternary ammonium surfactant on Au(100) surface is discussed in this chapter.

For an adsorbate-free single crystal surface, the Au(100)-hex is energetically more favorable, while the unreconstructed Au(100)-(1x1) state is generally more favored for an adsorbate covered surface.[11,12] Even though a reconstructed surface is thermodynamically more stable for adsorbate-free single crystals, a spontaneous reconstruction does not happen at room temperature. An activation energy barrier that corresponds to bond breaking and transport of atoms prevents a spontaneous reconstruction. Therefore reconstruction happens only when additional energy is supplied (generally in the form of heat) to overcome the activation energy barrier. Early observations of surface reconstruction phenomena on single crystal surfaces came from UHV studies whilst the reconstruction at the metal/electrolyte interface was under debate for a long time based on the assumption that reconstruction is only energetically favorable for a perfectly clean metal surface. The existence of surface reconstruction at the gold/electrolyte interface was first proposed by Hamelin[13] in order to explain certain features in the cyclic voltammograms of gold single crystal electrodes. Later, Yeager and coworkers obtained the first experimental evidence for reconstructed surfaces at the electrode/electrolyte interface with the help of their combined electrochemical and LEED study on Pt(110) surfaces.[14] In a series of contributions, a comprehensive description of the reconstruction phenomena of low index gold surface in electrochemical environments has been provided by Kolb and co-workers.[15]

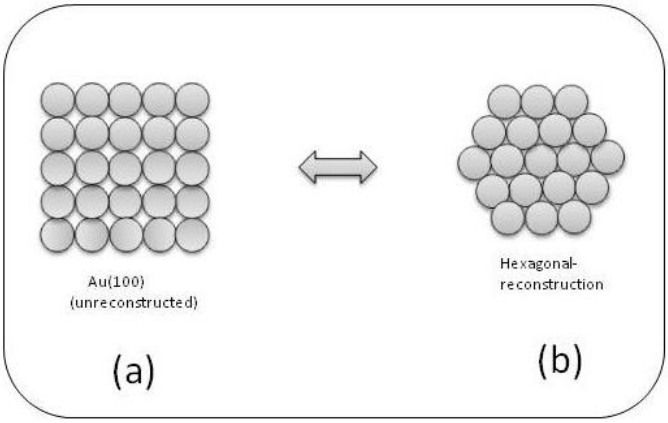

Fig. 5.1
The structure of (a) unreconstructed and (b) reconstructed Au(100) surfaces.

Of the three low-index faces of gold, metal surface reconstruction at the Au(100)/electrolyte is known to have the largest impact on the physical and electrochemical properties of the gold surface. The hexagonal close packed form of the reconstructed Au(100) (Figure 5.1b) contains about 24% more surface atoms than the unreconstructed square lattice(Figure 5.1a). The unreconstructed square Au(100) surface lattice undergoes a structural rearrangement into the hexagonal form when the crystal/electrode is subjected to flame annealing. On the other hand, reconstruction is often removed by the adsorption of molecules on the reconstructed surface. A good example of the adsorbate induced lifting of surface reconstruction is CO adsorbed Pt(100), where it has been explicitly shown that CO adsorbed on the unreconstructed (100) surface is thermodynamically more stable.[11,12] This issue has more relevance in an electrochemical system since both the electrical potential and the adsorption/desorption of species from the electrolyte on the surface have strong influence on the surface reconstruction phenomena. Research in this direction has been prominent in the past few decades.[15-18]

In electrochemical systems, the application of a potential bias to an electrode alters the surface charge density which in turn affects the surface structure of the crystal. At negative charge densities the reconstructed surface is energetically favored while a positive charge density yields the unreconstructed (1x1) surface. A well-prepared Au(100) electrode exhibits a nearly perfect 5x20 ("hex") reconstructed surface after careful thermal annealing for sufficiently long time (*ca.* 15 mins).[19] In electrochemical systems, the Au(100)-hex is stable at negative potential bias, but the surface reconstruction is lifted (i.e., transformed to unreconstructed form) when a sufficiently positive potential bias is applied to the electrode.[20] Thus a thermally reconstructed Au(100)-hex surface can be transformed to a Au(100)-(1x1) (i.e., the unreconstructed surface) by the application of sufficiently positive potential bias[16,19], and a partial restoration of the Au(100)-hex surface can be achieved by re-application of a sufficiently negative potential.[19,20] Further, these structural transitions with respect to the potential bias are altered by the adsorption of ionic or molecular species.[15] In general, a reconstructed Au(100) surface is energetically not stable in the presence of adsorbed anions and is stable in the presence of adsorbed cationic species.[15]

Octyltrimethylammonium triflate is a quaternary ammonium surfactant with trifluoromethanesulfonate (triflate) acting as a counter ion. Since triflate anions do not specifically adsorb on gold,[21] the electrochemical response of gold electrodes in the presence of this surfactant can be assumed to be resulting from the contribution of the cationic part. The influence of adsorbates on the stability of the reconstructed phase of Au(100) has been a subject of significant interest.[15,17,22] It is well known that specifically adsorbed inorganic anions such as Cl^-, Br^-, I^-, SO_4^{2-}, and OH^- drive the (hex) – (1x1)

transition whereas inorganic cations such as Cs^+ do not.[15] Based on literature data, the effect of neutral organic molecule adsorption can be divided into species that i) readily lift the reconstruction upon adsorption, such as adenine[22] and pyridazine[15] ii) molecules like pyridine that only lift the reconstruction upon a phase transition in the adsorbed layer,[23] and iii) molecules such as coumarin[24] and cyclohexanone[17] that actually retard the (hex) – 1x1 transition. Given the dichotomy between inorganic cations and neutral organic molecules, it is unclear what role an organic cation such as OTA^+ will have on the Au(100)-hex stability. The effect of the surface reconstruction on the adsorption behavior of a quaternary ammonium surfactant is discussed in this chapter.

5.2 Experimental

5.2.1 Synthesis of octyltrimethylammonium triflate

Octyltrimethylammonium triflate was synthesized by methylation of N,N-dimethyloctylamine (Aldrich) using methyl trifluoromethanesulfonate (Aldrich). Methyl trifluoromethanesulfonate was added dropwise to 20% excess dimethyloctylamine in distilled toluene, under stirring at 0 ^oC. The appearance of a white precipitate immediately after the addition of the methylating agent indicates the formation of tetra-alkylammonium triflate which is insoluble in toluene. The reaction was allowed to stand for another 12 hrs to achieve complete conversion. The white precipitate thus formed was filtered, washed with pentane and dried to remove any traces of the solvent. The dried ammonium triflate salt was then double recrystallized in hexane-ethyl acetate mixed solvent, then in water and dried under vacuum. The purity of the final product octyltrimethylammonium triflate was tested by ^1H NMR. The Kraft temperature (or critical micelle temperature) of this surfactant is ~16 ^oC and the surfactant stock solution

should be kept at a higher temperature because any minor amount of crystallization from the stock solution can act as nucleation sites leading to pre-micelle formation. Quaternary ammonium surfactants are known to make pre-micelles if nucleation sites are available and hence all these measurements were done after repeated recrystalliztion. Fresh solutions were made before each set of measurements, then incubated at 30 ^{o}C to avoid any possible pre-micelle formation. The critical micellar concentration of the surfactant was determined to be 8 mM (the details of Wilhelmy plate method to determine the critical micelle concentration is given in Chapter 7, section 7.1).

5.2.2 Electrochemical measurements

A detailed description of the electrochemical setup and experimental methodologies for cyclic voltammetry and chronocoulometry measurement are given in Chapter 2. All the electrochemical measurements were done in 0.1 M sodium fluoride electrolyte (pH ~ 8) under an argon atmosphere with a single crystal electrode in a hanging meniscus arrangement. The sodium fluoride (99.99%, Sigma-Aldrich) salt used for preparing the electrolyte solution was cleaned in a UV-ozone chamber (Spectronics Corporation, USA), in order to remove organic impurities. All solutions were prepared with Milli-Q ultrapure water (> 18.2 MΩ cm).

5.2.2.1 *Potential Step Sequence for the chronocoulometry measurements*

A general description of the potential step sequence is described in Chapter 2, Section 2.4. Two important variations of the basic potential step sequences needed for the chronocoulometry experiments described in this chapter are outlined below.

For the basic chronocoulometry method, the Au electrode was held at a base potential, E_b, for 30 s. The potential was then stepped to the variable value of interest, E_c, and held for a sufficient time to achieve adsorption equilibrium (between 60 to 180 s depending on the concentration of OTA). To desorb OTA from the electrode interface, a negative potential, E_{des} was applied for 200 ms and the current transient corresponding to desorption was measured. The potential was then stepped back to the base value and the cycle was repeated using a new value of E_c. Chronocoulometry measurements on reconstructed Au(100) followed this procedure with values of E_b and E_{des} being -0.45 V and –0.90 V, respectively. The procedure was modified for the chronocoulometry measurements on unreconstructed Au(100) electrode, in order to minimize the reconstruction effects at potentials further negative of -0.20 V. An additional potential step was introduced ($E_{c'}$ = -0.20 V for 55 to 175 s depending on the concentration of OTA) before stepping to a variable potential E_c, where it was held for only 10 s. The values of E_b and E_{des} for the unreconstructed Au(100) were 0.00 V and -0.95 V, respectively. The variable potential E_c was incremented from a positive potential to more negative values for experiments performed with an unreconstructed Au(100) whereas it followed the classical procedure (an initial negative potential for E_c which is incremented in positive steps) for reconstructed Au(100). A similar potential step routine for unreconstructed surface has recently been employed by Feliu for studying the adsorption of adenine on Au(100).[22] Potential step sequences used for the chronocoulometry experiments described in this chapter, for reconstructed and unreconstructed surfaces are schematically shown in Figure 5.2.

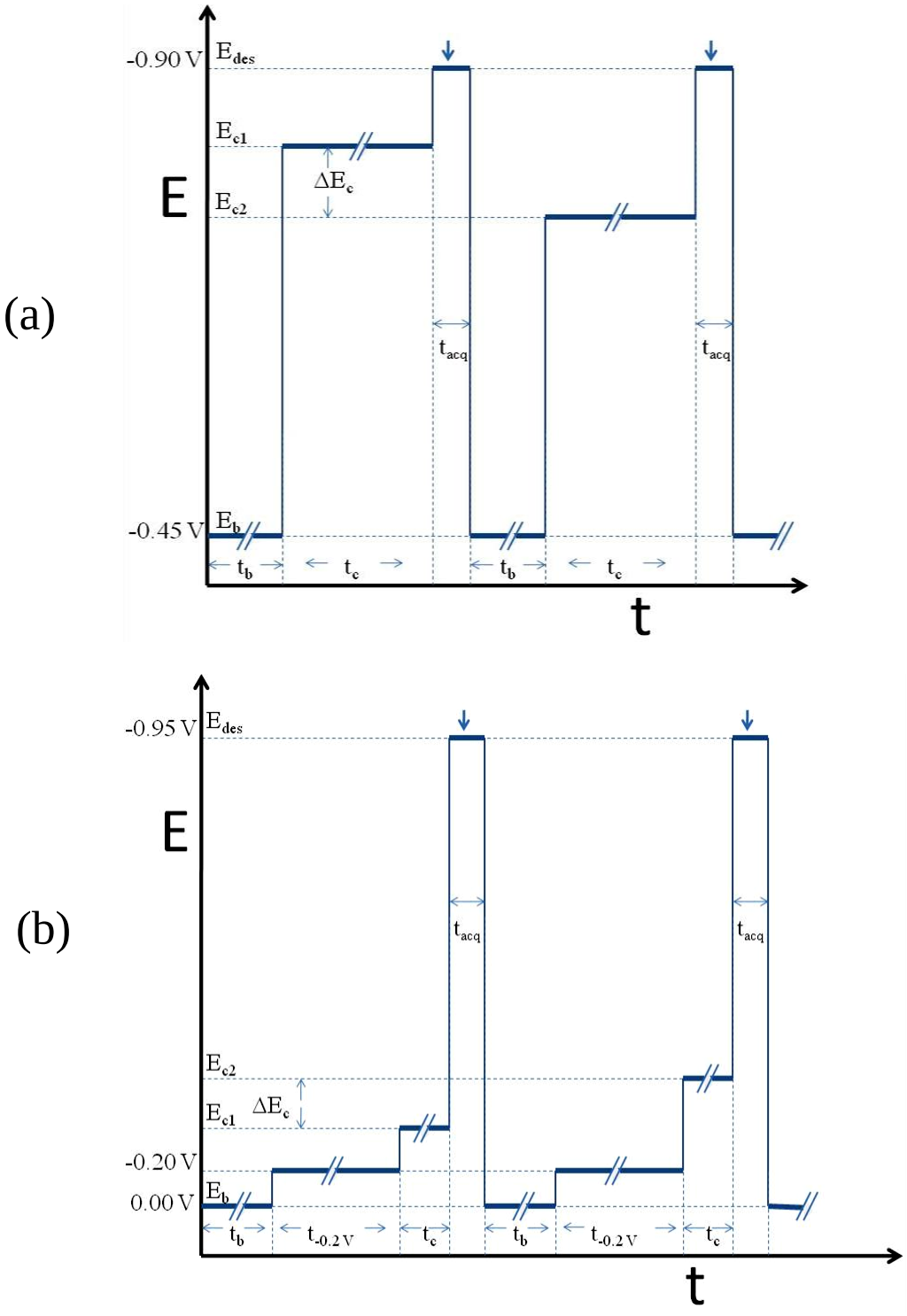

Fig. 5.2

A schematic showing step sequences for (a) reconstructed Au(100) and (b) unreconstructed Au(100).

5.3 Results and Discussion

5.3.1 Cyclic voltammetry

Figure 5.3 shows cyclic voltammograms of the Au(100) electrode in 50 mM NaF electrolyte. The electrode was introduced to the electrochemical cell after annealing in a hydrogen flame for about 5 mins to generate a thermally reconstructed surface. The reconstructed surface may be lifted either on quenching the electrode or on scanning the electrode to potentials positive of the pzc. In order to retain the reconstructed surface while introducing the electrode to the electrolyte surface, the electrode was first allowed to cool in the argon atmosphere of the cell and a hanging meniscus was formed while maintaining a potential bias of -0.8 V.

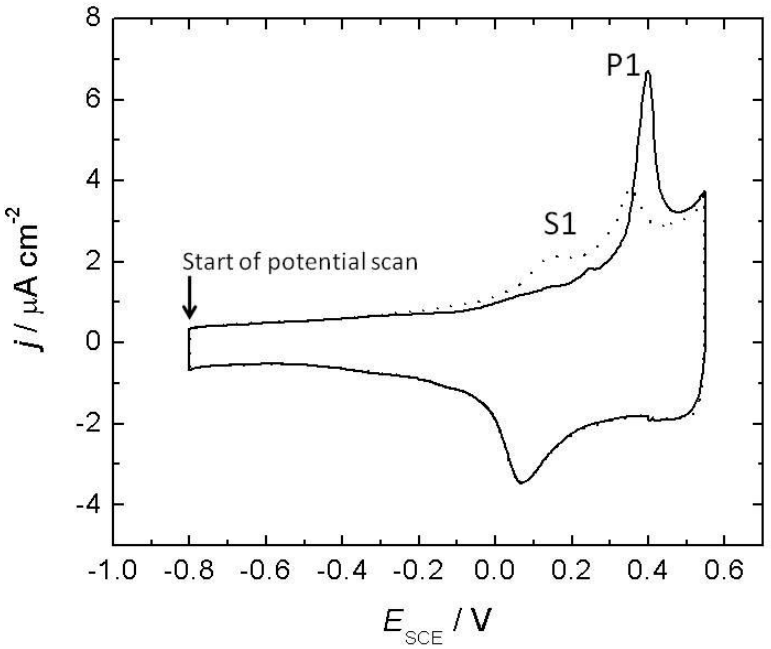

Fig. 5.3
First (solid line) and second cycle (dotted line) voltammograms of a thermally annealed Au(100) electrode in 0.1 M NaF, at scan rate 20 mV/s.

The reconstructed surface is known to be very stable at this potential.[20] The solid line in Figure 5.3 corresponds to the first scan, starting with an anodic (positive-going) potential sweep starting from -0.8 V. At potentials negative of the pzc of Au(100), +0.06 V, the cyclic voltammogram resembles the typical double layer region of a gold electrode, but is dominated by a sharp peak at 0.40 V which is labeled P1. For an Au(100) electrode, the lifting of reconstruction can be detected as the appearance of a sharp current peak in the cyclic voltammogram due to the changes of the potential of zero charges of (hex) and (1x1) surfaces, and the amount of adsorbed anions or organics between the reconstructed and unreconstructed surfaces. This peak potential is used as a convenient indicator of the stability of the reconstructed phase. The transition is driven by the specific adsorption of inorganic species, in this case OH^- ions and the position of P1 is in close agreement with Kolb's work at comparable pH[15]. By reversing the potential sweep after the observation of the P1 peak, the resulting cathodic half CV (Figure 5.3) correlates with an unreconstructed surface. At negative potentials, a partial, charge-induced reformation of the surface reconstruction (electrochemical surface reconstruction) of the Au(100)-1x1 surface can occur.[20] This is evidenced in the second cyclic voltammogram in Figure 5.3 (dotted line) which shows the appearance of P1 albeit shifted by ~ 50 mV in the negative direction and attenuated by roughly a factor of two. In previous studies on Au(100) and its surface reconstruction, the peak attenuation and the negative shift have been attributed to differences in the average domain size of the charge-induced reconstruction compared to the thermally generated reconstruction.[15] The second cycle in Figure 5.3 also shows the appearance of a new shoulder (labeled S1) at ca. 0.15 V, which is assigned to the adsorption of OH^- ions on unreconstructed Au(100). At 20 mV/s the

voltammogram remains essentially invariant after the second cycle indicating a steady-state toggling of the (hex) – (1x1) transition. However scanning at slower rates or holding at negative potentials enhances the P1 peak intensity resulting from the charge induced reconstruction of the surface at negative potentials.

In Figure 5.4, it is demonstrated that the P1 peak can be restored to some extent in the second cycle (shown as P1' in Figure 5.4) by holding at a sufficiently negative potential (-0.75 V) for 3 mins. It should be noted that P1 can never be restored to the same amplitude of the thermally annealed surface by electrochemical annealing even after very long durations of negative potential biasing (~1 hr).

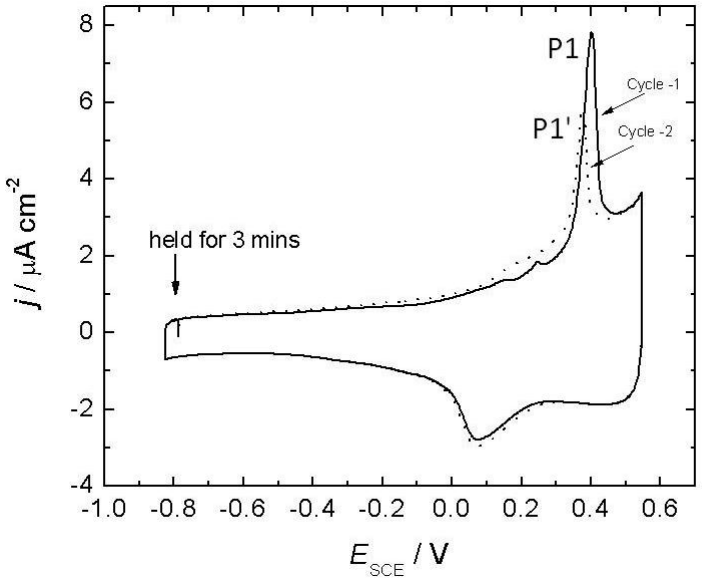

Fig. 5.4
Voltammograms of a thermally annealed Au(100) (solid line) and an electrochemically annealed Au(100) (achieved by holding at -0.75 V for 3 mins) before the second cycle (dotted line). Scan rate was 20 mV/s.

The next step was to attempt to determine whether or not the adsorption of OTA-Tf, which possesses an ionic headgroup and an organic tail group, would increase or decrease the stability of the thermally reconstructed Au(100)-hex surface compared to the Au(100)-(1x1) surface. Cyclic voltammograms of Au(100) in 50 mM NaF electrolyte containing 1 mM octyltrimethyl-ammonium triflate are shown in Figure 5.5. Analogous to Figures 5.3 and 5.4, the solid line corresponds to the current response for a thermally reconstructed surface and the dotted line corresponds to the second cycle that corresponds to a surface after the thermal reconstruction has been lifted. A peak at -0.65 V which is labeled P2, is caused by the onset of surfactant adsorption on the Au(100)-hex surface. The adsorption of the surfactant clearly does not lift the thermally induced reconstruction because the P1 peak is also observed at +0.50 V, which in fact is slightly positive shifted compared to the position of P1 in Figure 5.3. The positive potential shift in P1 compared to Figure 5.3 implies that the presence of adsorbed OTA-Tf suppresses the lifting of the reconstruction. As pointed out by Kolb[15] and Skołuda[17], this results from the fact that the adsorbed organic ions hinder the specific adsorption of inorganic ions (OH^- in this particular case) that lift the reconstruction. Peak P2' is observed at ~ -0.75 V on the negative scan and is caused by OTA-Tf desorption. If the potential excursion in the positive direction exceeds the transition potential (i.e the potential is scanned positive of peak P1), then peak P2' must arise from desorption of surfactant species from the unreconstructed Au(100) surface. However, as shown by the upper voltammogram in Figure 5.5 (bold line), if the potential is kept negative enough such that the thermally induced reconstruction is not lifted, then both peaks P2 and P2' correspond to surfactant

adsorption (desorption) from the Au(100)-hex surface. The dependence of the P2' peak position indicates that the interaction between the surfactant and the metal differs for the reconstructed and unreconstructed Au(100) surfaces.

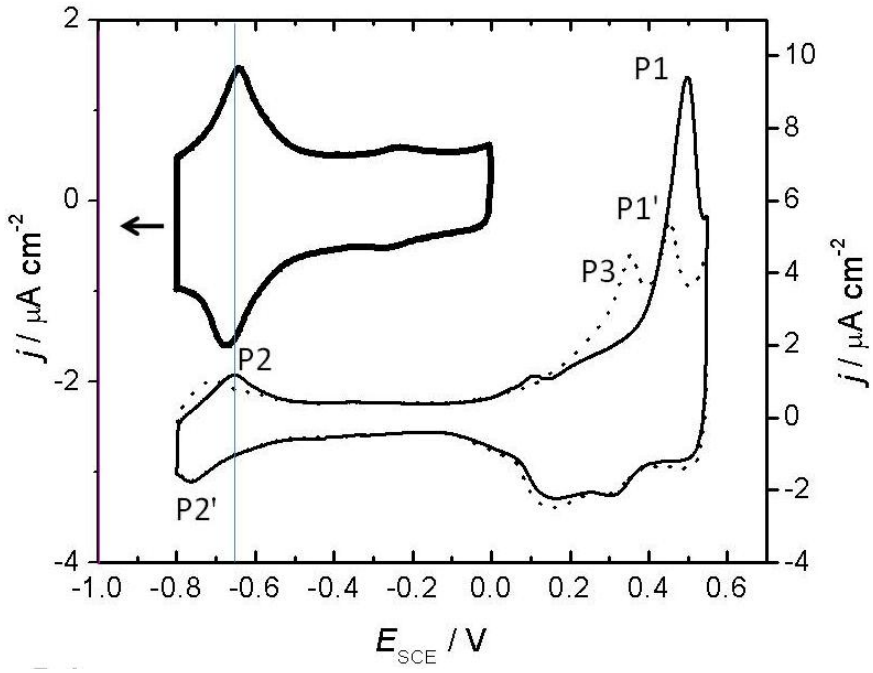

Fig. 5.5
Cyclic voltammograms of a thermally reconstructed Au(100) electrode in 0.1 M NaF plus 1mM OTA-Tf. The electrode was introduced to the electrolyte at -0.8V and the first voltammogram is shown as the thin solid line. The second cycle is shown as a dotted line. The ordinate for these two voltammograms is the right vertical axis. The inset voltammogram shows the results from scanning a thermally reconstructed Au(100) electrode between -0.8V and 0.0V. The ordinate for this CV is the left vertical axis.

In potential cycles subsequent to the first one, a distinct new peak, P3, is observed at +0.35 V (dotted line in Figure 5.5). Skołuda has attributed the appearance of splitting in the transition peak to differences in the nucleation origins of thermally prepared and charge-induced reconstructions[17]. It is possible that this might explain the appearance of

P3 in the second and following potential cycles in this system. To test this hypothesis two potential holding experiments were performed on an Au(100) electrode whose initial thermal reconstruction had been lifted by extensive potential cycling. As shown by the solid line in Figure 5.6, if the potential is held at -0.63 V for 5 mins and then scanned in the positive direction, P3 only appears as a very weak shoulder whereas the primary transition peak (P1) is strongly pronounced at 0.45 V. If the potential is held at -0.20V for 5 minutes the surface remains unreconstructed (i.e., Au(100)-(1x1)) and the following positive sweep shows a strong P3 peak at the complete expense of P1. Figure 5.6 demonstrates that P3 cannot be associated with lifting of the reconstruction. The increased intensity of P3 on unreconstructed compared to reconstructed surfaces, combined with its absence in surfactant-free electrolytes, implies that this peak may be associated with a phase transition of the surfactant, which is unique to the Au(100)-(1x1) surface.

A qualitative evaluation of octyltrimethylammonium triflate adsorption on the reconstructed surface of Au(100) using cyclic voltammetry demonstrates that the adsorption of this surfactant does not lift the reconstructed surface. It is only upon sweeping the potential to positive values that the reconstruction can be lifted. The presence of adsorbed OTA^+ ions hinders this process relative to a bare gold surface. The presence of adsorbed OTA^+ on a reconstructed surface is significantly different from its adsorption on an unreconstructed surface as can be inferred from the position of the P2/P2' adsorption/desorption peaks.

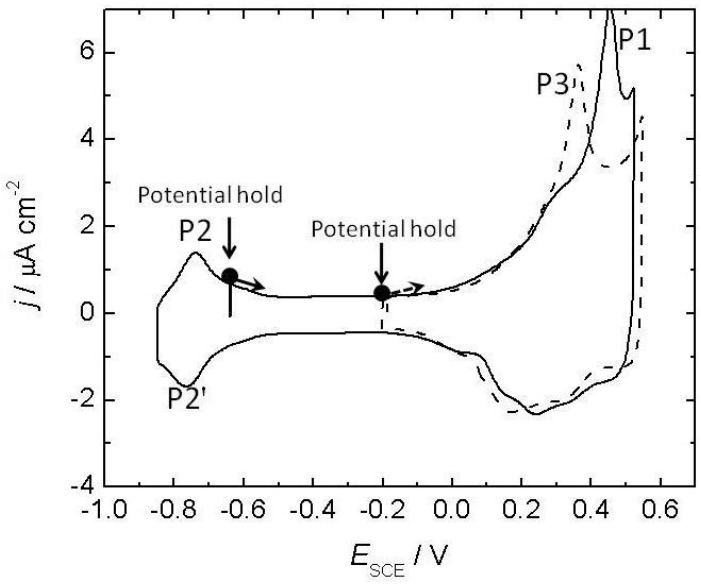

Fig. 5.6
Cyclic voltammograms (20 mV/s) of an unreconstructed Au(100) electrode in 0.1 M NaF plus 1mM OTA-Tf. The solid black line is the CV after the potential was held at -0.6V for 5 minutes (the initial scan direction was in the positive direction as indicated by the arrow). The dashed line is the equivalent experiment but the initial potential was held at -0.2V for 5 minutes.

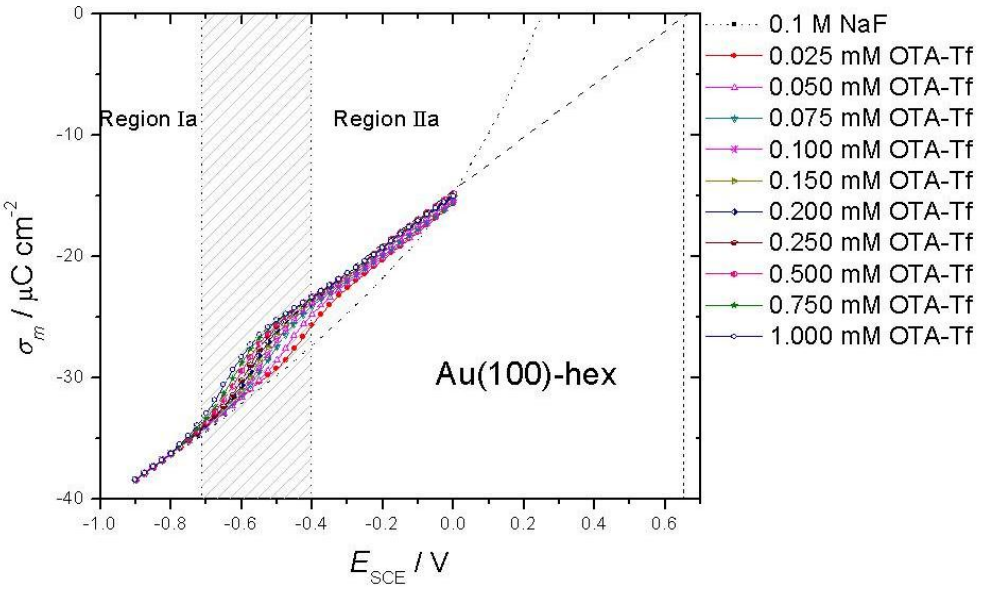

Fig. 5.7
Charge density versus potential curves for the reconstructed Au(100) electrode in contact with the 0.1 M NaF supporting electrolyte (dashed line) and the following concentrations of OTA-Tf. 0.025 mM (●), 0.05 mM (△), 0.075 mM (▽), 0.10 mM (⊠), 0.15 mM (▶), 0.20 mM (◆), 0.25 mM (⬟), 0.50 mM (◐), 0.75 mM (★), 1.0 mM (⊙).

5.3.2 Chronocoulometry measurements

5.3.2.1 Reconstructed Au(100)

As in the previous chapters, the experimental and theoretical framework developed by Richer and Lipkowski[25] for applying chronocoulometry to the study the adsorption of molecules/ions on ideally polarized electrodes has been used in this chapter as well. As described in Chapter 2, section 2.4, this technique requires the measurement of the capacitive charging currents associated with stepping the electrode's potential from a value where the organic molecules are adsorbed, E_c, to one where they are completely desorbed, E_{des}. A transition between reconstructed and unreconstructed Au(100) surfaces during the potential step also contributes to the measured current and would invalidate the data obtained from chronocoulometry. Thus, to ensure that the gold surface remained in its reconstructed state throughout the course of the chronocoulometry experiments, the adsorption potentials was limited to $E_c \leq 0.0$ V. In separate experiments the stability of the reconstruction has been verified by monitoring the position of the OTA-Tf adsorption/desorption peaks in the CV after prolonged potential stepping. For all concentrations of surfactant studied, the voltammetric peak position was stable as long as E_c did not exceed 0.00 V. The potential step sequence was used for these measurements is illustrated in Figure 5.2a. A series of σ_m-E curves obtained for OTA-Tf concentrations ranging from 0.025 mM to 1.0 mM is presented in Figure 5.7. The plots reveal two regions (labeled with Roman numerals in Figure 5.7) where the measured charge density varies linearly with the electrode's potential. Region Ia maps to very negative potentials where the curves all merge with the data for the electrolyte, confirming the complete desorption of OTA-Tf at these polarizations. Following a pronounced inflection (the

onset of which moves toward negative potentials with increasing surfactant concentrations) region IIa is observed which marks a state of surfactant adsorption. At *E* ~ -0.2V there is a very subtle difference in slope defining a possible change in the state of adsorption, which is consistent with the pseudo capacitive peak observed in the differential capacity curve (*vide infra*).

5.3.2.2 Unreconstructed Au(100)

As discussed in the previous section, an unreconstructed surface in the presence of OTA-Tf is stable at moderate potentials (*E* > *ca.* -0.20V). For the charge measurements on Au(100)-1x1 surface, a modified potential step routine was used as described in the experimental section (Figure 5.2b). The results for the chronocoulometry experiments for variable OTA-Tf concentrations are shown in Figure 5.8.

Qualitatively, the plots look quite similar to the experiments with the reconstructed Au(100) surface. Once again the curve can be divided into linear regions corresponding to the bare electrode surface (region Ib) and adsorbed surfactant (region IIb). The principal differences between Figures 5.7 and 5.8 seems to only be the values of the adsorption onset potentials for any given concentration of OTA-Tf which are shifted cathodically for Au(100)-1x1. The σ_m-*E* curves can also be used to assess the shift in the electrode's potential of zero charge, ΔE_{pzc}, upon adsorption of organic species. This requires extrapolation of the linear portion of the charge density plots to the ordinate axis intercept. The results of the extrapolation vary very weakly with OTA-Tf concentration, but the value of ΔE_{pzc} corresponding to the highest concentration was obtained for both reconstructed and unreconstructed surfaces. The ΔE_{pzc} for the reconstructed Au(100) surface is +0.25V and + 0.23V for unreconstructed Au(100).

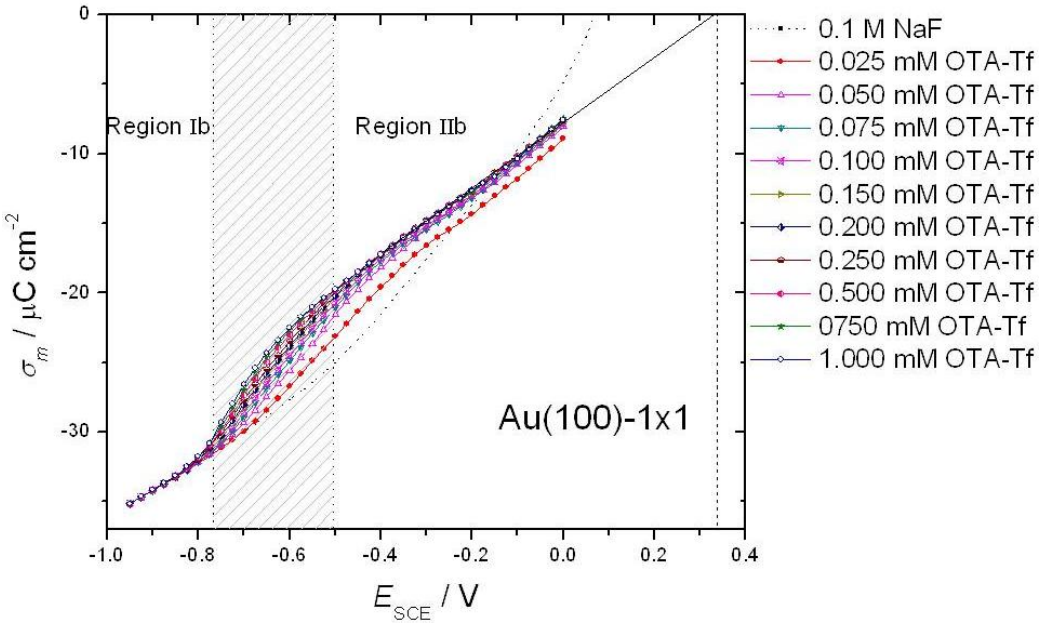

Fig. 5.8
Charge density versus potential curves for the unreconstructed Au(100) electrode in contact with the 0.1 M NaF supporting electrolyte (dashed line) and the following concentrations of OTA-Tf. 0.025 mM (●), 0.05 mM (△), 0.075 mM (▽), 0.10 mM (⊠), 0.15 mM (▶), 0.20 mM (◆), 0.25 mM (⬟), 0.50 mM (◐), 0.75 mM (★), 1.0 mM (⊙).

5.3.3 Differential capacity plots

From the cyclic voltammetry studies, it is clear that the thermally reconstructed Au(100)-hex surface is very stable at negative potentials in the presence of adsorbed OTA-Tf. In addition, if the unreconstructed surface is formed by positive electrode polarizations, the reformation of the Au(100)-hex surface is kinetically slow at negative potentials. Hence it should be possible to study the adsorption behavior of the surfactant at potentials below 0 V on both reconstructed and unreconstructed surfaces. Information about the adsorbate layer at the interface is better illustrated in the differential capacity plot that was generated by differentiation of the charge density. Differential capacity curves corresponding to OTA-Tf adsorption on reconstructed as well as unreconstructed

surfaces are shown in Figure 5.9. The dotted lines correspond to electrolyte-only, (i.e. 100 mM NaF), and the solid lines correspond to the electrolyte with the addition of 1 mM surfactant bulk concentration.

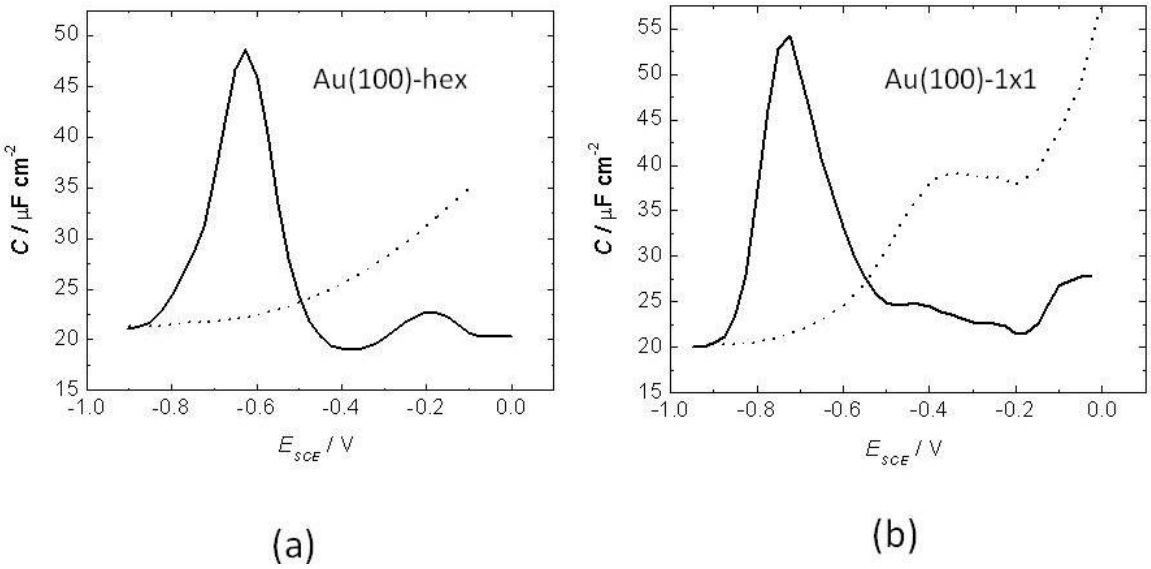

Fig. 5.9
Differential capacity curves obtained from differentiation of the charge data for the electrolyte only (dotted line) and the 1.0 mM OTA-Tf charge curves (solid line) for (a) reconstructed Au(100) (b) unreconstructed Au(100)

In Figure 5.9a, (i.e., data for reconstructed Au(100)), after the adsorption peak at E = -0.62 V, the capacity falls below the level of the electrolyte, indicative of surfactant adsorption. At the positive end of the potentials, a shallow capacity minimum is observed at E = -0.40 V and a weak pseudo-capacitance peak is observed at E = -0.2 V. Though weak, the observed pseudo-capacitance peak implies a transition in the state of the adsorbed organic film. However, the differences between the limiting capacities on either side of this peak are negligibly small and imply that the organic ion coverages must be similar on either side of the peak. The limiting capacity in this region is 20±2 μF cm^{-2}

which is virtually the same value reported for similar ionic surfactant systems adsorbed on Au(111) electrodes.[26,27]

The differential capacity curve corresponding to OTA-Tf adsorption on an unreconstructed Au(100) surface is shown in Figure 5.9b. Qualitatively, the differential capacity curves for OTA-Tf adsorption on reconstructed and unreconstructed surfaces look similar, the only striking difference being the position of the adsorption/desorption peak. A minor difference is that the capacity of the interface upon surfactant adsorption on unreconstructed Au(100) is 23 ± 2 μF cm^{-2}, which is approximately 15% higher than that for the reconstructed Au(100) surface. This difference implies that the nature of OTA-Tf adsorption slightly differs for the unreconstructed surface compared to the reconstructed surface. These differences could be related to the amount of OTA^+ adsorbed, the orientation of the adsorbed surfactant, or the presence of co-adsorbed triflate anions. Rather than studying the qualitative/structural difference of the adsorbate at the interface, the major focus of this chapter is to provide a quantitative evaluation of the surfactant adsorption on reconstructed and unreconstructed phases of the Au(100) surface.

5.3.4 Gibbs surface excesses

The chronocoulometry results provide data that can be used to determine the Gibbs surface excess of surfactant (details given in Chapter 2, section 2.5). From the electrocapillary equation, integration of the σ_m-E curves at any given concentration of OTA-Tf yields the surface pressure.

$$\pi = \left(\int_{E_{des}}^{E_c} \sigma_m dE \right)_{C_{OTATf}} - \left(\int_{E_{des}}^{E_c} \sigma_m dE \right)_{C_{OTATf}=0} \qquad (5.1)$$

The Gibbs surface excess, Γ, can be calculated from the film pressure data by differentiation with respect to the natural log of OTA-Tf concentration at constant electrode potential.

$$\Gamma = \frac{1}{RT} \left(\frac{\partial \pi}{\partial \ln C_{OTATf}} \right)_{T,P,E} \qquad (5.2)$$

The surface pressures for OTA-Tf adsorption on reconstructed and unreconstructed Au(100) was calculated using the charge data. In both cases, the surface pressure was almost linearly dependent on the logarithm of the surfactant concentration which implies very weak concentration dependence on the Gibbs excess. A linear fitting algorithm was used to determine Γ which essentially provides an average value of the Gibbs excess over the range of concentrations studied (0.025mM – 1.0 mM). Comparison of the Gibbs surface excess data between reconstructed and unreconstructed electrodes was done on a rational potential scale, which accounts for the differences in the pzc of the reconstructed and unreconstructed Au(100) surfaces. i.e. $E_{rational} = E_{SCE} - E_{pzc}$. The plots of Γ versus rational potential for the two Au(100) surfaces are shown in Figure 5.10. Both curves have the same shape and indicate the surface concentration of surfactant increases with potential. In region II potentials (points in Figure 5.10) the Gibbs excesses range from 1.5-2.2 x 10^{-10} moles cm^{-2}. Given the approximately 10% error in the data analysis technique[28] these values are in close agreement with the limiting Gibbs excesses reported for N-Decyl-N,N,N-trimethylammonium triflate (DeTATf) adsorption on Au(111)[21]. For further comparison, the measured Gibbs excess for the formation of hemimicelles is ~4 x 10^{-10} moles cm^{-2} for sodium dodecyl sulfate (SDS)[27] and ~5 x 10^{-10} moles cm^{-2} for N-

Dodecyl-N,N-dimethyl-3-ammonio-1-propanesulfonate (DDAPS)[26]. The lower Gibbs excess measured for OTA-Tf adsorption on Au(100) suggests the absence of micellar aggregation. The Gibbs excess plots for the two Au(100) crystal surfaces also indicate that at common rational potentials, slightly more surfactant is adsorbed on a reconstructed substrate compared to its unreconstructed analogue. This implies that there is a greater specific interaction between the surfactant and the Au(100)-hex surface. This agrees with the earlier comments on the small differences in the differential capacities and shifts in E_{pzc}. However, the differences in the state of the adsorbed organic film do not lead to appreciable differences in the Gibbs excesses.

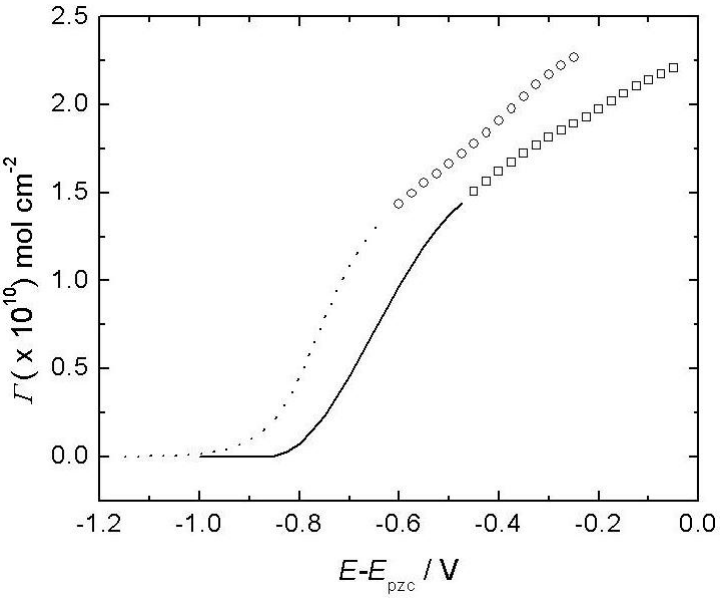

Fig. 5.10
Relative Gibbs surface excesses plotted on a rational potential scale. The solid black line and squares are for the unreconstructed Au(100) electrode. The dotted line and circles are for the reconstructed Au(100) electrode. Symbols are used to emphasize Gibbs excess data corresponding to state II potentials defined in Figures 5.7 and 5.8.

5.4 Summary and Conclusions

The adsorption of a quaternary ammonium surfactant on both the reconstructed (Au(100)-hex) and unreconstructed (Au(100)-1x1) surfaces of a Au(100) electrode has been evaluated. Using cyclic voltammetry studies it has been demonstrated that the adsorption of surfactant does not lift the "hex" reconstruction formed by thermal annealing of a Au(100) electrode. Instead, the presence of the surfactant hinders the adsorption of more strongly adsorbed hydroxide ions and extends the stability range of the Au(100)-hex surface. The CVs and capacity curves for Au(100)-hex and Au(100)-1x1 are qualitatively very similar. Both are characterized by a single-state of adsorption, which is preceded by an adsorption peak. This study is limited to polarizations where the electrode's surface is considerably negatively charged. The Gibbs excess of OTA-Tf is relatively lower compared to the values typical of surfactant hemimicelle formation. On a rational potential scale, the surfactant adsorbs on the Au(100)-hex surface at more negative potentials compared to the unreconstructed surface. This indicates that there is a stronger specific interaction between the aliphatic quaternary ion and the reconstructed substrate. However, this study has shown that the difference in the strength of the specific interaction is rather small and, furthermore, the adsorption of a quaternary ammonium surfactant on either surface of Au(100) is qualitatively very similar to the adsorption on Au(111). The very weak dependence of cationic surfactant adsorption on different gold surfaces implies that the role of halide co-adsorption may be very significant in the mechanism of anisotropic nanocrystal growth.

Reference List

1. Smith, D. K.; Korgel, B. A. The Importance of the CTAB Surfactant on the Colloidal Seed-Mediated Synthesis of Gold Nanorods. *Langmuir* **2008,** *24* (3), 644-649.

2. Garg, N.; Scholl, C.; Mohanty, A.; Jin, R. The Role of Bromide Ions in Seeding Growth of Au Nanorods. *Langmuir* **2010,** *26* (12), 10271-10276.

3. Somorjai, G. A.; Van Hove, M. A. Adsorbate-induced restructuring of surfaces. *Progress in Surface Science* **1989,** *30* (3-4), 201-231.

4. Binnig, G.; Rohrer, H.; Gerber, C.; Weibel, E. (111) facets as the origin of reconstructed Au(110) surfaces. *Surface Science* **1983,** *131* (1), L379-L384.

5. Van Hove, M. A.; Koestner, R. J.; Stair, P. C.; Bibqrian, J. P.; Kesmodel, L. L.; Bartos, I.; Somorjai, G. A. The surface reconstructions of the (100) crystal faces of iridium, platinum and gold: II. Structural determination by LEED intensity analysis. *Surface Science* **1981,** *103* (1), 218-238.

6. Binnig, O. K.; Rohrer, H.; Gerber, C.; Stoll, E. Real-space observation of the reconstruction of Au(100). *Surface Science* **1984,** *144* (2-3), 321-335.

7. Moritz, W.; Wolf, D. Multilayer distortion in the reconstructed (110) surface of Au. *Surface Science* **1985,** *163* (1), L655-L665.

8. Moller, J.; Niehus, H.; Heiland, W. Direct measurement of Au(110) surface structural parameters by low energy ion backscattering. *Surface Science* **1986,** *166* (1), L111-L114.

9. Harten, U.; Lahee, A. M.; Toennies, J. P.; ll, C. Observation of a Soliton Reconstruction of Au(111) by High-Resolution Helium-Atom Diffraction. *Physical Review Letters* **1985,** *54* (24), 2619.

10. Barth, J. V.; Brune, H.; Ertl, G.; Behm, R. J. Scanning tunneling microscopy observations on the reconstructed Au(111) surface: Atomic structure, long-range superstructure, rotational domains, and surface defects. *Physical Review. B* **1990,** *42* (15), 9307.

11. Heinz, K.; Lang, E.; Strauss, K.; Mnller, K. Observation of the structural transition Pt(100) (1 x 1) - hex by LEED intensities. *Applications of Surface Science* **1982,** *11-12*, 611-624.

12. Ertl, G. Catalysis and surface phase transformation. *Surface Science* **1985,** *152-153* (Part 1), 328-337.

13. Hamelin, A. The crystallographic orientation of gold surfaces at the gold-aqueous solution interphases. *Journal of Electroanalytical Chemistry* **1982,** *142* (1-2), 299-316.

14. Homa, A. S.; Yeager, E.; Cahna, B. D. Leed-aes thin-layer electrochemical studies of hydrogen adsorption on platinum single crystals. *Journal of Electroanalytical Chemistry* **1983,** *150* (1-2), 181-192.

15. Kolb, D. M. Reconstruction phenomena at metal-electrolyte interfaces. *Progress in Surface Science* **1996,** *51* (2), 109-173.

16. Ross, P. N.; D'Agostino, A. T. The effect of surface reconstruction on the capacitance of Au(100) surfaces. *Electrochimica Acta* **1992,** *37* (4), 615-623.

17. Skoluda, P. Extension of the stability range of the reconstructed Au(100) surface in the presence of organic molecules. *Electrochemistry Communications* **2003,** *5* (2), 142-145.

18. Titmuss, S.; Wander, A.; King, D. A. Reconstruction of Clean and Adsorbate-Covered Metal Surfaces. *Chemical Reviews* **1996,** *96* (4), 1291-1306.

19. Kolb, D. M.; Schneider, J. Surface reconstruction in electrochemistry: Au(100-(5 x 20), Au(111)-(1 x 23) and Au(110)-(1 x 2). *Electrochimica Acta* **1986,** *31* (8), 929-936.

20. Schneider, J.; Kolb, D. M. Potential-induced surface reconstruction of Au(100). *Surface Science* **1988,** *193* (3), 579-592.

21. Brosseau, C. L.; Sheepwash, E.; Burgess, I. J.; Cholewa, E.; Roscoe, S. G.; Lipkowski, J. Adsorption of N-Decyl-N,N,N-trimethylammonium Triflate (DeTATf), a Cationic Surfactant, on the Au(111) Electrode Surface. *Langmuir* **2006,** *23* (4), 1784-1791.

22. Prado, C.; Prieto, F.; Rueda, M.; Feliu, J.; Aldaz, A. Adenine adsorption on Au(111) and Au(1á0á0) electrodes: Characterisation, surface reconstruction effects and thermodynamic study. *Electrochimica Acta* **2007,** *52* (9), 3168-3180.

23. Stolberg, L.; Lipkowski, J.; Irish, D. E. Adsorption of pyridine at the Au (100)-solution interface. *Journal of Electroanalytical Chemistry and Interfacial Electrochemistry* **1987,** *238* (1-2), 333-353.

24. Skoluda, P.; Hanun, U. W.; Kolb, D. M. On the stabilization of reconstructed Au(100) surfaces by coumarin. *Journal of Electroanalytical Chemistry* **1993,** *354* (1-2), 289-294.

25. Richer, J.; Lipkowski, J. Measurement of Physical Adsorption of Neutral Organic Species at Solid Electrodes. *Journal of The Electrochemical Society* **1986,** *133* (1), 121-128.

26. Cholewa, E.; Burgess, I.; Kunze, J.; Lipkowski, J. Adsorption of dimethyl-3-ammonio-1-propanesulfonate (DDAPS), a model zwitterionic surfactant, on the Au(111) electrode surface. *Journal of Solid State Electrochemistry* **2004,** *8* (10), 693-705.

27. Burgess, I.; Zamlynny, V.; Szymanski, G.; Lipkowski, J.; Majewski, J.; Smith, G.; Satija, S.; Ivkov, R. Electrochemical and Neutron Reflectivity Characterization of Dodecyl Sulfate Adsorption and Aggregation at the GoldGêÆWater Interface. *Langmuir* **2001,** *17* (11), 3355-3367.

28. Lipkowski, J. In *Adsorption of molecules at metal electrodes*, Lipkoski, J., Ross, P. N., Eds.; VCH: New York, 1992; pp 171-238.

Chapter 6

Potential Induced Restructuring of N-Octyl-N,N,N-trimethylammonium Triflate Aggregates on Au (111)

6.1 Introduction

In aqueous solutions, surfactants self-assemble into aggregates when the repulsive interactions between the polar head groups and solvent are dominated by the attractive interactions of the hydrophobic tails of the surfactant. The curvature and geometry of these aggregates are determined by the molecular structure of the surfactant and the presence of other molecular or ionic species in the solution. Surfactant aggregates formed in solution (micelles) exhibit a rich array of different shapes such as spheres, cylinders and bilayers.[1] Reasonable predictions of aggregate shapes can be made on the basis of the forces acting on the surfactant monomer, and structural transitions can be understood in terms of the changes in the intermolecular forces between the surfactants. For instance, an increase in electrolyte concentration reduces the electrostatic repulsion between the ionic headgroups of the surfactants, thus lowering the curvature of the aggregates, and manifesting in a sphere-to-rod transition in certain cases.[2] These structural transitions can be summarised in terms of packing parameters: the ratio of the hydrocarbon volume to the product of the area occupied by the headgroup and length of the hydrocarbon chain.[1]

Surfactants adsorbed at the interface, especially at the solid/liquid interface, also self-assemble into aggregate structures in a manner analogous to the bulk phase micellization, but the aggregate structures at the solid/liquid interface are influenced by additional factors that result primarily from the interactions with the adsorbent. Because

of these differences in the interaction parameters, surface aggregates can differ significantly in size and shape from the micelles that form in the bulk. While aggregates formed in solution can be studied using various spectroscopic techniques, a precise evaluation of the aggregate structures at the solid/liquid interface is rather challenging. Scanning probe techniques such as atomic force microscopy (AFM) and scanning tunnelling microscopy (STM) have been widely used for this purpose because of their ability to provide direct visualization of the aggregate structures on a variety of solid surfaces and under various solution conditions.[3,4] While the major attraction of the scanning probe based techniques is the direct visualization of the aggregate structures, interactions of the scanning probe with the aggregate molecules can be of serious concern. Weakly adhered adsorbates can be affected[5] or even scraped away by the scanning tip[6] or the protruding headgroups may make the underlying structure fuzzy and unresolvable.[7]

Another important aspect is that the structure of the aggregates at the solid/liquid interface also depends on the electrical state of the adsorbent, and hence aggregate structures of the amphiphilic molecule could be significantly different on surfaces having different surface charges.[2] Furthermore, the charge/electrical state of the surface can be controlled by applying an electrical potential, thus influencing the structure of the surface aggregates. In an electrochemical experiment, the charge flowing to the electrode as a result of the surfactant adsorption can be measured to provide information about the adsorbate. One essential criterion for an in-depth investigation of the processes happening at the interface is that the electrode/electrolyte interface should behave as an ideal capacitor over a wide range of potentials. In reality, only very few electrode materials

satisfy this prerequisite over a satisfactorily wide range of potentials. In the past two decades, there have been considerable efforts in this direction by various groups. For example, the structural and kinetic aspects of aggregate formation were studied as a function of the applied potential at the mercury/electrolyte interface using differential capacity measurements.[8-14] In a series of contributions, Lipkowski and coworkers have investigated potential dependent adsorption of various surfactants on single crystal electrodes to provide quantitative information about the adsorbate at the interface.[15,16] In recent years, combining high resolution scanning probe microscopy and electrochemical studies, Lipkowski's group were able to provide both quantitative and structural information about the surfactant aggregates at the electrode/electrolyte interface.[17,18]

This chapter is dedicated to a quantitative evaluation of the potential dependent structural transformations of octyltrimethylammonium triflate (OTA-Tf) at the Au(111)/electrolyte interface. The electrochemical evaluation of OTA-Tf adsorption on Au(100) discussed in the previous chapter is extended to Au(111) in this chapter. In the previous chapter, the focus was given to the surface reconstruction of the electrode, and an evaluation of the surfactant adsorption on both reconstructed and unreconstructed surfaces has been provided. A detailed analysis of the surfactant aggregate structure was avoided largely because of the difficulties arising from the potential induced surface restructuring of the Au(100) electrode. The advantage of an Au(111) surface in contrast to the Au(100) is that its surface is more stable without major restructuring for a wider range of potentials and hence it behaves as a finer ideally polarized surface. Furthermore, a reconstructed Au(111) surface is not structurally very different from an unreconstructed Au(111) surface: A fully reconstructed Au(111) has only 4.4% more atoms on the surface

than an unreconstructed surface, whereas a reconstructed Au(100) surface has 24% more atoms than an unreconstructed surface. Hence, subtle reconstruction effects during electrochemical experiments should not hamper a detailed analysis of the surfactant structure on an Au(111)/electrolyte interface. In this chapter, the focus is given to a detailed evaluation of the structural aspects of the adsorbed surfactant. A qualitative description of the OTA-Tf aggregate structure on Au(111) electrode is given based on equilibrium capacity measurements and a more detailed quantitative description will be given using interfacial charge measurements.

6.2 Experimental

6.2.1 Wilhelmy plate method

The surface pressure at the air/solution interface was measured using the Wilhemy plate method. The Wilhelmy plate was a thin sandblasted platinum plate (19.6 mm long x 10 mm wide) connected to a microbalance (KSV-instruments). The plate was thoroughly cleaned by flame annealing and oriented perpendicular to the air/solution interface. The surface pressure, $\pi = (\gamma_0 - \gamma_c)$, was determined, where γ_0 is the surface tension in the absence of OTA-Tf in the bulk solution and γ_c is the surface tension at a given concentration of OTA-Tf in the bulk.[19]

6.2.2 Electrochemical measurements

A detailed description of the electrochemical setup and experimental methods for cyclic voltammetry, differential capacity and chronocoulometry is given in Chapter 2. All the electrochemical measurements were done in 0.1 M sodium fluoride electrolyte (pH ~ 8) in an argon atmosphere (pump purge) with the single crystal electrode in a hanging

meniscus arrangement (Chapter 2, Figure 2.1). The electrolyte, sodium fluoride (99.99%, Sigma-Aldrich) was cleaned in a UV-ozone chamber (Spectronics corporation, USA). Octyltrimethylammonium triflate was synthesized and purified in the lab (the details are given in Chapter 5, Section 5.2.1). All solutions were prepared with Milli-Q ultrapure water (> 18.2 MΩ cm).

6.3 Results and Discussions

6.3.1 Adsorption of octyltrimethylammonium triflate at the air/water interface

Adsorption of OTA-Tf at the air/water interface was determined by measuring the surface pressure as a function of the concentration of the surfactant using the Wilhelmy plate method. A plot of surface pressure as a function of the logarithm of the surfactant concentration in 0.1 M aqueous NaF electrolyte is shown in Figure 6.1.

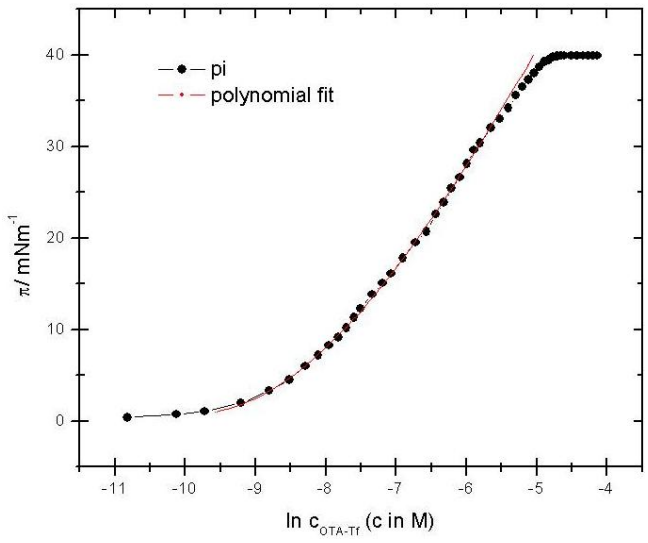

Fig. 6.1

Plot of the surface pressure at the air/solution interface *versus* the logarithm of the bulk concentration of OTA-Tf. A polynomial fit for data below the cmc is shown as a solid line.

The critical micelle concentration (cmc) is the point at which the surface pressure plateaus. The cmc of OTA-Tf was determined from the point of intersection of straight fits of the plateau region to the initial rise in surface pressure; the cmc value thus determined was 8 mM. Gibbs excess of OTA-Tf at the air/liquid interface can be obtained from surface pressure (π) *versus* $\ln c_{\text{OTA-Tf}}$ plot using the Gibbs equation.

$$\Gamma = \frac{\delta\pi}{RT\delta lnc_{OTA-Tf}} \qquad (6.1)$$

The Gibbs excess at the air/solution interface was determined from the derivative of the polynomial fit to the surface pressure data below the cmc and is plotted as a function of the logarithm of concentration in Figure 6.2. It is worth noting that the maximum value of the Gibbs excess obtained here is ~ 5.25 x 10^{-10} mols/cm^2, which is almost double compared to the Gibbs excess that is estimated (~3 x 10^{-10} mols/cm^2) based on the surfactant headgroup area[20] for a full monolayer at the interface. According to the classical theory of surfactant aggregation, only a monolayer of the surfactant can be formed at the air/water interface. Interestingly, a survey of the recent literature on similar tetraalkylammonium surfactants reveals that all the reported surface excess values (~ 4 x 10^{-10} mols/cm^2 to ~ 5.5 x 10^{-10} mols/cm^2)[16,21,22] correspond to more than a monolayer (ca. twofold) estimated based on the surfactant head group. Even though a detailed analysis of the surfactant structure at the air/water interface is beyond the scope of this thesis, this observation is interesting as some of the very recent literature reports provide clear evidences for bilayers at the air/solution interface for certain surfactants.[23]

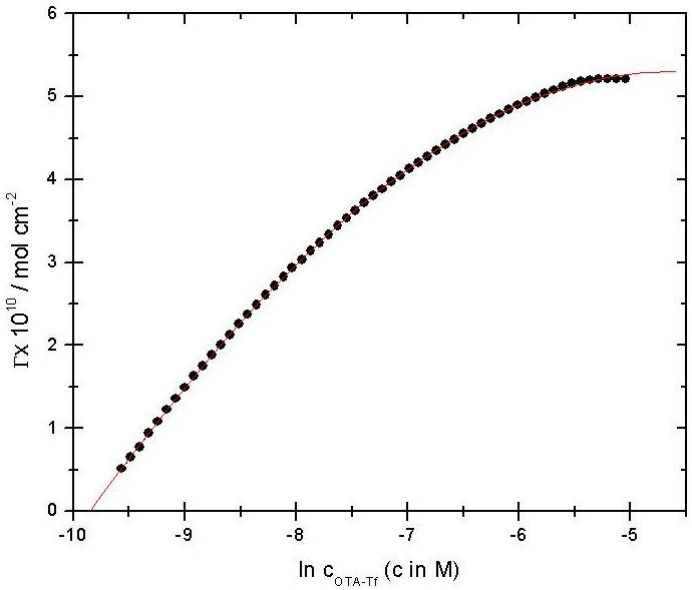

Fig. 6.2

Relative Gibbs excess of OTA-Tf at the air/solution interface plotted versus the logarithm of the bulk concentrations.

6.3.2 Cyclic voltammetry

As an initial survey of the adsorption behaviour of OTA-Tf on Au(111), cyclic voltammetry measurements were performed. Figure 6.3 shows the cyclic voltammograms corresponding to variable OTA-Tf bulk concentrations recorded at 20 mV/s scan rate in the double layer region of Au(111), in 0.1 M NaF supporting electrolyte. Large reversible peaks seen at the negative potentials (region I, Figure 6.3) correspond to the adsorption/desorption of OTA-Tf at the Au(111) interface. Increasing relative intensities and negative shifts of the peak positions with increasing bulk concentration suggest that the adsorption is thermodynamically favoured at higher bulk concentrations of OTA-Tf. Following the adsorption peak, the current gradually falls below the electrolyte curve (region II, Figure 6.3), indicating the formation of a surfactant layer at the interface. An elevated current plateau in region III (Figure 6.3), could be observed only at higher bulk

concentrations (> 0.25 mM). Such a high current plateau region could be associated with the kinetics of structural transformation of surface aggregates formed at higher bulk concentrations. At further positive potentials (region IV, Figure 6.3), a steep increase in the current is observed suggesting surfactant desorption, a phase transition in the adsorbed layer or both happening at the onset of pre-oxidation of the gold surface.

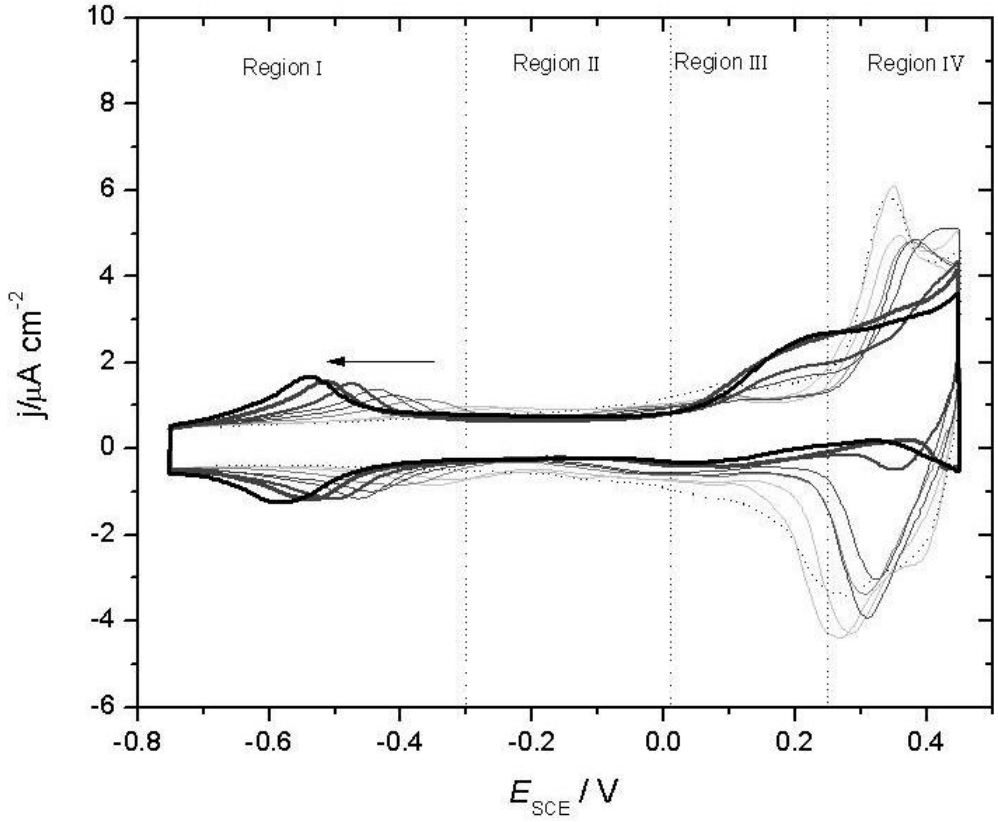

Fig. 6.3

Cyclic voltammetry curves recorded for the Au(111) electrode in 0.1 M NaF without OTA-Tf (dotted line) and with variable concentrations of OTA-Tf starting from 0.02 mM (light gray line) to 2 mM (thick black line).

6.3.3 Capacity measurements

Interfacial capacitance can be used as a measure of the extent of surfactant adsorption at the interface. In simplistic terms, and by neglecting the capacitive contribution of the diffusion layer, adsorption at the interface can be described by Helmholtz capacity,

$$C_H = {}^{\varepsilon}/_{x} \qquad (6.2)$$

where ε is the permittivity and x is the thickness of the adsorbed layer. Adsorption of surfactant causes an increase in the double layer thickness. Additionally, hydrocarbons have low ε values, and thus lower the interfacial capacity as the surfactant replaces adsorbed ions and water molecules from the inner layer. As the concentration of the surfactant in the bulk is increased, the interfacial concentration also increases and a further decrease in the measured capacity is observed. At moderately higher concentrations (yet still below the cmc), these surfactants can form surface aggregates,[24-27] the structure of which changes with adsorbate concentration and/or the electric state of the substrate. Such structural variations effectively change the fractional surface coverage and hence the measured capacity. Thus measurement of interfacial capacity provides useful information about the aggregate structure at the interface.

Qualitative aspects of the surfactant modified interface can be obtained using differential capacity measurements. In the differential capacity technique, a linear voltage sweep (5 mV/s) is applied to the surface. Hence the capacity values obtained here does not correspond to equilibrium measurements. If the structure of the surfactant aggregates at the interface changes with potential, a phase transition peak is expected within the

capacity pit region where the surfactant is predominantly adsorbed. As per the thermodynamic analysis of a first order phase transition at a charged interface, the criterion for a reversible surface phase transition is[28]

$$\left(\frac{\partial E}{\partial \sigma_m}\right)_{T,P,\mu} = 0$$

or $$\left(\frac{\partial C}{\partial E}\right)_{T,P,\mu} \rightarrow \infty \qquad (6.3)$$

i.e., the electrode potential remains constant while the charge density changes due to the phase transition, resulting in an abrupt change of the differential capacity with electrode potential. A phase change leading to the formation/deformation of surface micelles usually occurs in a less abrupt manner resulting in a finite value of change in capacity with respect to electrode potential, and a pseudocapacitive peak is expected for a phase transition between surface micelles.[28] However, if the structural transitions of surface aggregates with change in potential are so slow (*vide infra*) that the interface does not have sufficient time to relax during the voltage sweep, then a pseudocapacitive peak may not be seen. Alternatively, capacity values obtained by waiting at each potential for sufficiently long time so as to reach adsorption equilibrium (i.e., equilibrium capacity curves), would reveal capacity changes associated with structural transitions occurring over relatively longer time scales.

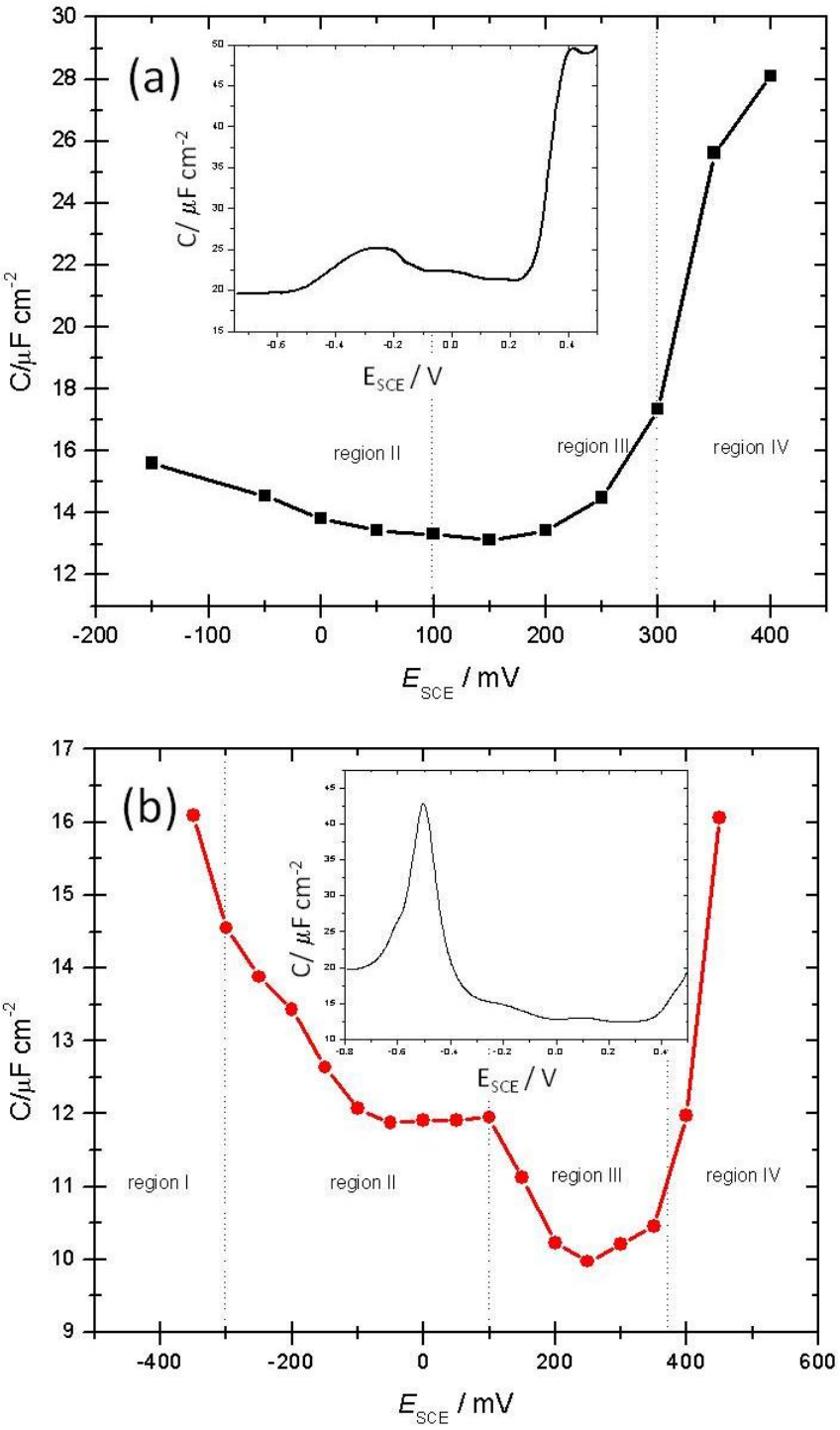

Fig. 6.4

Equilibrium capacity for 0.025 mM (a) and 1 mM (b) bulk concentrations of OTA-Tf on Au (111). Inset shows corresponding differential capacity curves at 5 mV/s scan rate.

In Figure 6.4, equilibrium capacity curves (600 s hold time) and corresponding differential capacity curves (inset) for two representative concentrations (0.025 mM and 1 mM) are shown. A general feature of the interfacial capacity for the entire double layer region can be obtained using the differential capacity curves shown in the inset: After the adsorption peak at negative potentials, a low capacity region is observed at intermediate potentials indicating the adsorption of the surfactant. A steep increase in the capacity seen at extreme positive potentials suggests possible desorption of the surfactant at positive potentials. At higher bulk concentrations of the surfactant, the capacity pit region is further deepened, suggesting an increase in the surface concentration resulting in a more compact adsorbate layer of the surfactant at higher bulk concentrations. For the current system, though voltammetric curves hinted the possibility of aggregate structures at higher concentrations, no explicit phase transition peaks could be observed in the differential capacity plot. To investigate the possibility of any slowly proceeding structural transitions, equilibrium capacity curves were obtained for the two representative concentrations. At lower bulk concentration of the surfactant (Figure 6.4 a), the equilibrium capacity curve is qualitatively very similar to the corresponding potential region of the differential capacity curve shown in the inset. But at higher bulk concentration of the surfactant (Figure 6.4b), two explicit capacity states can be seen between -100 mV and +350 mV in the equilibrium capacity curve, which is not evident in the differential capacity curve shown in the inset. These two different capacity states suggest the effective thickness of the adsorption layer within this potential range changes, presumably due to a transition in the structure of the aggregates and a possible change in surfactant surface coverage.

In order to study the kinetics of surfactant adsorption at the interface, capacity was measured as a function of time, which is discussed in the following section. Capacitance transients can reveal time-dependent changes in the double layer structure. Typical diffusion controlled adsorption processes exhibiting a decrease in the double layer capacity with time can be well described by the Delahay-Trachtenberg law,[29] but in certain cases the double layer capacity actually increases with time (usually on a relatively longer time scale). This later observation remained unexplained for a long time and was often (erroneously) attributed to the effects of surfactant impurities. In 1999, Retter et. al. elucidated the kinetics of surfactant adsorption at the mercury/electrolyte interface with the help of capacity transients, and clarified the nature of long-term capacity curves.[10] Their work showed that an increase in capacity is related to the formation of three dimensional surface aggregates from an initial condensed layer. In the present work, the Au(111) electrode also behaves as an ideal capacitor at least in the range of potentials where the surfactant is predominantly adsorbed, and hence a similar approach would reveal any slowly proceeding structural transitions.

The kinetics of slowly proceeding phase changes of OTA-Tf on an ideally polarized Au(111) electrode was examined using capacity transient measurements. Capacity transients were measured for two representative concentrations *viz.* 0.025 mM (represents low bulk concentrations) and 1 mM (represents the bulk concentrations where surface aggregates are suspected based on cyclic voltammogram data). Capacity transients were obtained by stepping from the desorption potential to a potential of interest and then waiting there long enough (200 s to 600 s, please see Figure 6.5) until an equilibrium capacity is reached. Before each capacity step, any adsorbed species was

desorbed from the surface by stepping to -800 mV where OTA-Tf is completely desorbed from the surface. Each capacity transient obtained this way represents the adsorption of surfactant from the bulk on a clean, adsorbate free surface upon which surfactant molecules nucleate and grow to form a stable surface layer.

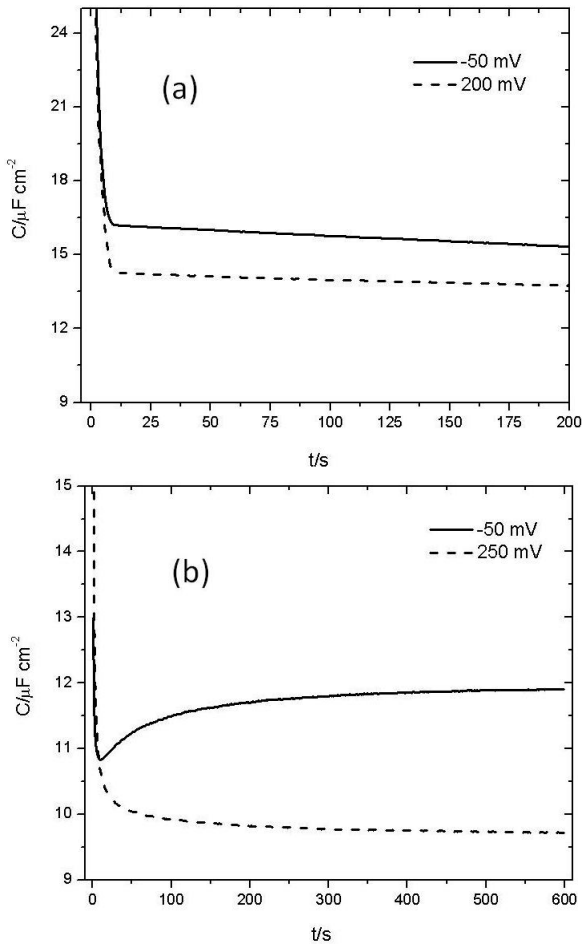

Fig. 6.5

Representative capacity transients for region II (solid line) and region III (dashed line) potentials at (a) 0.025 mM and (b) 1 mM bulk concentrations of OTA-Tf.

Capacity transients corresponding to 0.025 mM bulk concentration (Figure 6.5a) of the surfactant show a typical diffusion controlled adsorption process for the two representative potentials. Conversely, for 1 mM OTA-Tf bulk concentration (Figure 6.5b)

the shape of the capacity transients is significantly different for the two representative potentials. The representative transients within region III (+200 mV for 0.025 mM bulk concentration and +250 mV for 1 mM bulk concentration) follow a typical two-dimensional nucleation and growth model, where the capacity decreases monotonically and approaches a capacity asymptote, suggesting the slow formation of a single structure of adsorbed surfactants at these potentials. But the shape of the transients at -50 mV (within region II) indicates more complex adsorption behavior at 1 mM bulk concentration (Figure 6.5b). Initially the transient reaches a minimum value then increases to attain equilibrium capacity in about 3 mins (Figure 6.5b). Similar capacity transients were reported by various groups at the mercury/electrolyte interface.[8,9,13] According to these studies, the processes happening at the interface can be described as follows: the initial capacity drop corresponds to the adsorption of the surfactant molecules and subsequent formation of a compact monolayer; this compact layer of surfactant molecules is only metastable at this potential and converts to a less densely packed layer of three dimensional surface aggregates at larger time scales. The formation of surface aggregates in general, is thought to be realized by the initial formation of stable nuclei and their subsequent growth until they coalesce to form a macroscopic phase. The initial capacity minimum observed in the capacity transient corresponds to a compact vertical layer of surfactant molecules, and the increasing capacity at longer time scales corresponds to a slowly proceeding phase transition from a condensed layer to a film of three dimensional surface aggregates having an overall lower surface coverage. Consistent with Retter's formalism, the transient obtained in region II (Figure 6.5b, -50 mV) describes the formation of a kinetically favoured arrangement of a monolayer of

compact, vertical oriented surfactant molecules which then transforms to a more thermodynamically favourable structure of surfactant aggregates by means of maximizing the hydrophobic interaction of the surfactant tail group with the electrode surface. Since the diffusion and adsorption rates of the surfactant molecules are faster than the rate of formation of the thermodynamically stable surfactant arrangement, a compact layer of perpendicular surfactant molecules is initially formed, resulting in the observed capacity minimum. This compact monolayer then undergoes a slower transition into a more open, aggregated structure of higher interfacial capacitance. The model provided above is based entirely based on the qualitative similarities between the OTA-Tf –Au(111) system and similar systems studied by Retter. It should be stated that alternative surfactant geometries could also provide similar C(t) transients and scanning probe microscopy would be required to conclusively determine which model is actually operative.

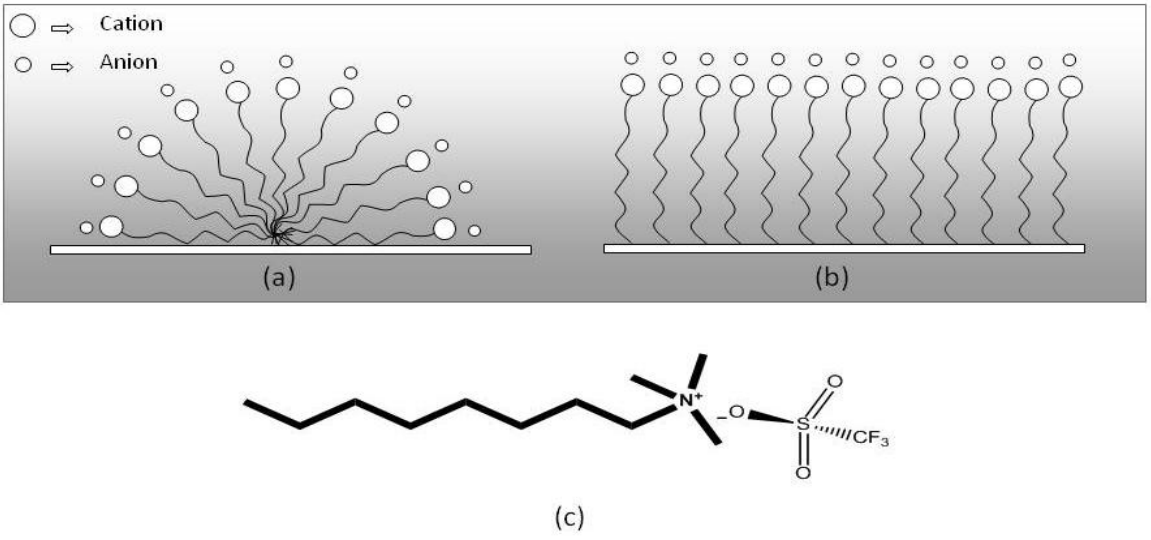

Fig. 6.6

Schematic showing cross-sections of (a) hemicylindrical as wells as (b) perpendicular aggregates of OTA-Tf on a surface.

(c) Schematic structure of N-octyl-N,N,N-trimethylammonium triflate (OTA-Tf).

At region III potentials, the charge on the surface is minimal (i.e., potentials close to the pzc, please see Figure 6.7). It is well known that the adsorption energy of organic molecules is most favorable at the pzc[30,31] hence it is likely that the hydrocarbon tail prefers to interact with the surface in region III in such a way to maximize the interfacial number density of hydrocarbon groups. This drives the formation of a vertical surfactant layer with the hydrophilic head groups oriented towards solution. Potential dependent structural transitions of aggregate structures on mercury/electrolyte interfaces have been investigated by Retter and co-workers, who developed a model based on electrochemical measurements that relates interfacial capacitance to structural transitions at the interface. According to Retter's formalism,[12] if a compact layer of perpendicularly adsorbed surfactant molecules of length *r*, transform into hemicylindrical aggregates with a cross-section radius *r*, then the change in effective thickness of the adsorption layer can be obtained as

$$d_{vertical} \Big/ d_{hemicylindrical} = 2r^2 \Big/ (\pi r^2/2) = 1.273 \qquad (6.4)$$

It implies that the effective thickness of the adsorption layer is decreased by a factor of 1.273 when a complete monolayer of perpendicularly adsorbed molecules changes to a densely packed array of hemicylindrical surface micelles (Figure 6.6). Since the capacity is inversely proportional to thickness, the transition from a layer of perpendicularly adsorbed molecules to hemicylindrical aggregates would lead to a relative increase in capacity by a factor of 1.273. A similar geometric consideration can be applied for a transition from perpendicularly adsorbed layer to a hemi*spherical* aggregate to show a relative increase in capacity by a factor of 1.654.[12]

From Figure 6.4b, if the capacity minimum in region III is compared to the capacity plateau in region II, the increase in effective capacity can be calculated as C/C` = $11.90\ \mu F\ cm^{-2} / 9.75\ \mu F\ cm^{-2} \approx 1.22$. This value is very close to the change in effective capacitance expected for a vertical layer of surfactant evolving into a layer of hemicylindrical aggregates and suggests the formation of a vertical layer corresponding to capacity minimum in region III and hemicylindrical aggregates at the capacity plateau in region II.

6.3.4 Chronocoulometry

Chronocoulometry measurements were carried out to gather further quantitative information about OTA-Tf adsorption on Au(111), which can also be used to confirm the structural transformations discussed in the previous section based on equilibrium capacity measurements. From the cyclic voltammetry and differential capacity measurements, it has been verified that at potentials more negative of -750 mV, there is no OTA-Tf adsorbed on the surface in the range of concentrations (10μM to 1.5 mM) used in this study and hence -950 mV was chosen as the desorption potential for chronocoulometry measurements. The following potential step sequence was used in the chronocoulometry experiment: the Au(111) electrode was initially maintained at a base potential E_b = +150 mV for 30 s and then stepped to a potential of interest, E_c , for 200 s to establish adsorption equilibrium, then the potential was stepped to the desorption potential, E_{des} = -950 mV for 200 ms and the resulting current transient due to the desorption of the surfactant molecules and charging of the double layer was measured. To enhance the mass transport of the surfactant, the solution was stirred throughout the step sequences

except for a 10 s period prior to the desorption step. The current transients obtained at the desorption potential were then integrated to obtain the difference in charge densities between E_c and E_{des}. The absolute values of charge densities were then determined by using the potential of zero charge determined from the position of diffuse layer minimum obtained from a separate differential capacity experiment done in 10 mM NaF electrolyte. For an Au(111) electrode having a predominantly unreconstructed surface in a slightly basic electrolyte, the pzc was found to be 270 mV. Since 0.1 M NaF (pH~8) was used as the supporting electrolyte, the same pH was maintained in all these measurements. Before the measurements, the electrode was cycled through the full oxidation region for a number of times to reduce any effect due to thermal reconstruction and hence all these electrochemical measurements were done on a largely unreconstructed surface.

The charge density versus potential plot for various concentrations of OTA-Tf, ranging from 10 μM to 1.5 mM (all below the cmc of OTA-Tf) is shown in Fig 6.7. The charge curves that correspond to different concentrations of OTA-Tf are indistinguishable from the electrolyte curve at potentials negative of -700 mV (region I) suggesting no surfactant adsorption at those potentials. In the shaded section between region I and region II, the charge density steeply increases with increasing potential and this represents the negative potential limit where surfactants start adhering to the surface. The extent of adsorption and the position of the onset of surfactant adsorption depend on the bulk concentration. In region II, the charge curves are quasi-linear, and with increasing surfactant bulk concentration, the absolute value of the charge also increases, indicating an increasing surface concentration. In region III, the slope of the charge curves is significantly different from region II indicating a phase transition of the adsorbed

surfactant layer. In this region, at higher concentrations, the charge density curves show only very weak potential dependence suggesting a stable compact layer of surfactant at the interface. In region IV, the charge curves show steep increases with potential and tend to merge with the electrolyte curve at more positive potentials. This indicates probable desorption of the surfactants.

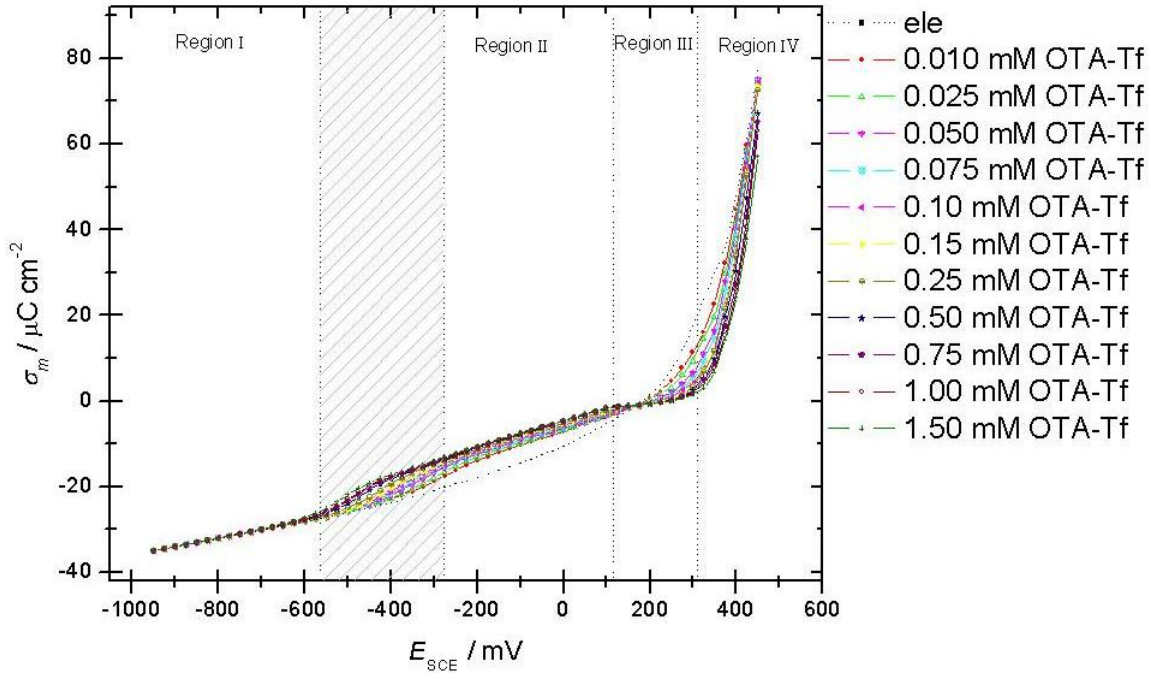

Fig. 6.7

Charge density versus electrode potential curves for Au(111) in 0.1 M NaF supporting electrolyte (----) and following OTA-Tf concentrations: 0.01 mM (●), 0.025 mM (△), 0.05 mM(⏚), 0.075 mM(⊠), 0.10 mM(◀), 0.15 mM(▶), 0.25 mM(◒), 0.5 mM(★), 0.75 mM(⬟), 1 mM(⊙), 1.5 mM(+).

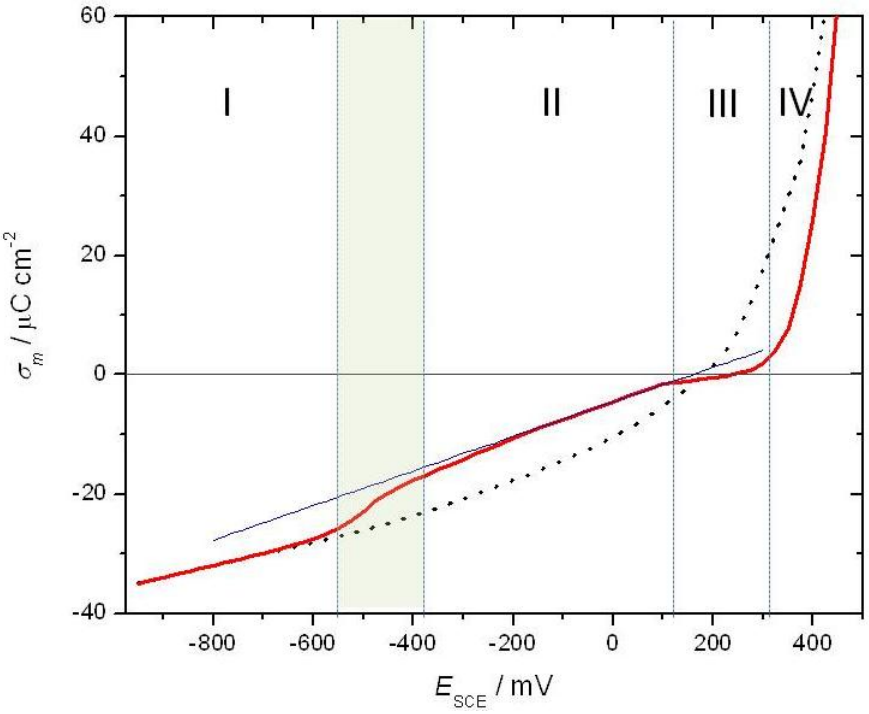

Fig. 6.8

Charge density curves for the Au (111) electrode in contact with 0.1 M NaF electrolyte solution (dotted line) and 1mM bulk concentrations of OTA-Tf (solid line) showing the extrapolation to determine pzc.

The shift in the potential of zero charge (ΔE_{pzc}) due to the adsorption of surfactant determined from the charge curves shows significant difference in the ΔE_{pzc} values at the potentials corresponding to two different adsorption states. The shift in pzc due to the displacement of surface water by a film of adsorbed molecules is described by[32]

$$\Delta E_{PZC} = \frac{\Gamma_m(\mu_{OTA} - n\mu_w)}{\varepsilon} \qquad (6.5)$$

where Γ_m is the maximum surface concentration of the surfactant, μ_{OTA} and μ_w represents the average permanent dipole moment normal to the surface due to the adsorption of OTA and water molecules respectively, n is the number of water molecules displaced by an adsorbed OTA molecule and ε represents the permittivity of the inner layer. ΔE_{pzc}

corresponding to 1 mM bulk concentration of OTA-Tf was determined at the two regions corresponding to different adsorption states identified from the equilibrium capacity curves (Figure 6.8). In region III, ΔE_{pzc} can be directly determined as the OTA-Tf charge curves intersect with the zero charge density ordinate in this region. In region II, a linear extrapolation of the OTA-Tf charge density curve to zero charge density ordinate was made, in order to determine ΔE_{pzc} with respect to the electrolyte-only curve. The values of ΔEpzc determined in both regions were close to 0 mV; a very plausible explanation is that the molecule is adsorbed as a zwitterion. Support for a model based on the first layer of molecules adsorbed flat on the electrode surface comes from the EC-STM studies by Lipkowski and co-workers on a similar quaternary ammonium triflate system which showed such an orientation at low surfactant concentrations and in a similar regions of potentials.[33]

Surface pressure is a measure of the energetics of surfactant adsorption, which can be calculated by integrating the charge versus potential curves at any given concentration.

$$\pi = \left(\int_{E_{des}}^{E_c} \sigma_m dE \right)_{C_{OTATf}} - \left(\int_{E_{des}}^{E_c} \sigma_m dE \right)_{C_{OTATf}=0} \qquad (6.6)$$

Surface pressure for the adsorption of OTA-Tf on Au(111) was calculated using this equation and the plot is shown in Figure 6.9. The surface pressure plot contains bell shaped curves with maxima (E_{max}) at ~ +200 mV. This potential corresponds to the intersection points of the charge density curve of the surfactant with the electrolyte curve. The potential of maximum adsorption is confined in adsorption region III and there is a

slight positive shift in E_{max} (ΔE_{max} ~ +25 mV) over the full concentration range, indicating concentration induced film reorganization. [16,18] At higher concentrations, the surface pressure versus electrode potential curves deviate from the typical quasi-Gaussian shape expected for organic molecules having a single state of adsorption, further indicating multiple states of adsorption at higher concentrations. At more positive potentials (region IV) the surface pressure approaches zero, which is again consistent with surfactant desorption at positively polarized electrodes.

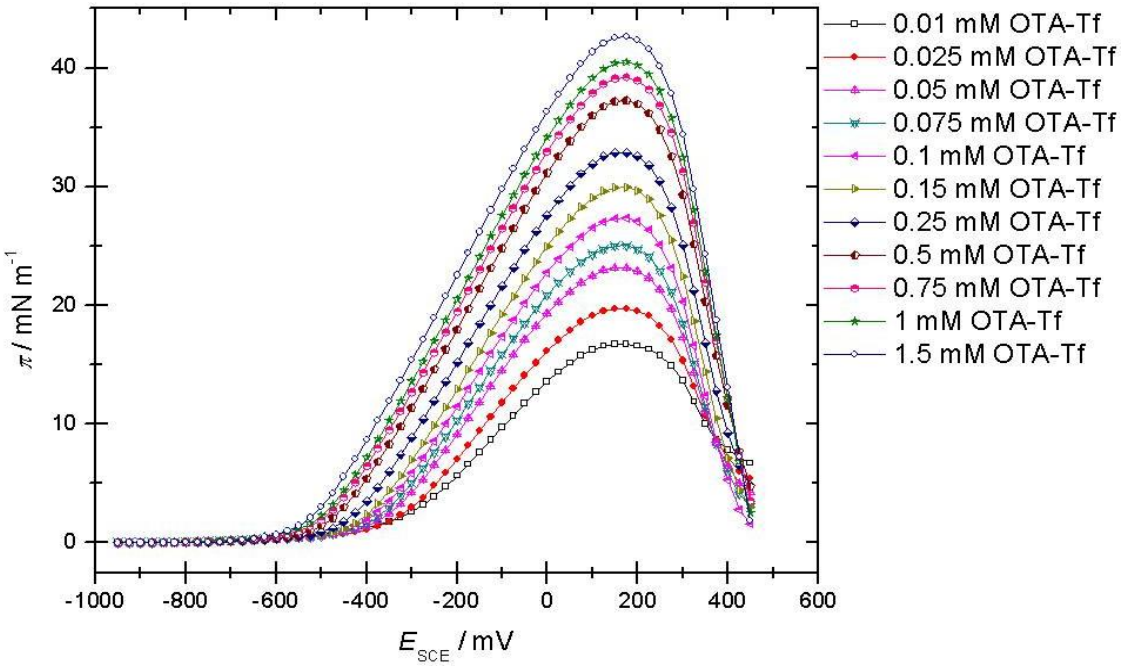

Fig. 6.9

Surface pressure *versus* electrode potential plot at the Au(111)/ electrolyte interface for various OTA-Tf concentrations: 0.01 mM (■), 0.025 mM (●), 0.05 mM(▲), 0.075 mM(▼), 0.10 mM(◀), 0.15 mM(▶), 0.25 mM(◆), 0.5 mM(⬟), 0.75 mM(⬬), 1 mM(★), 1.5 mM(○).

6.3.5 Gibbs surface excess

The Gibbs surface excess (Γ) can be calculated from the electrocapillary equation by differentiating the surface pressure versus natural logarithm of the bulk OTA-Tf concentration at constant electrode potential.

$$\Gamma = \frac{1}{RT}\left(\frac{\partial \pi}{\partial \ln C_{OTATf}}\right)_{T,P,E} \qquad (6.7)$$

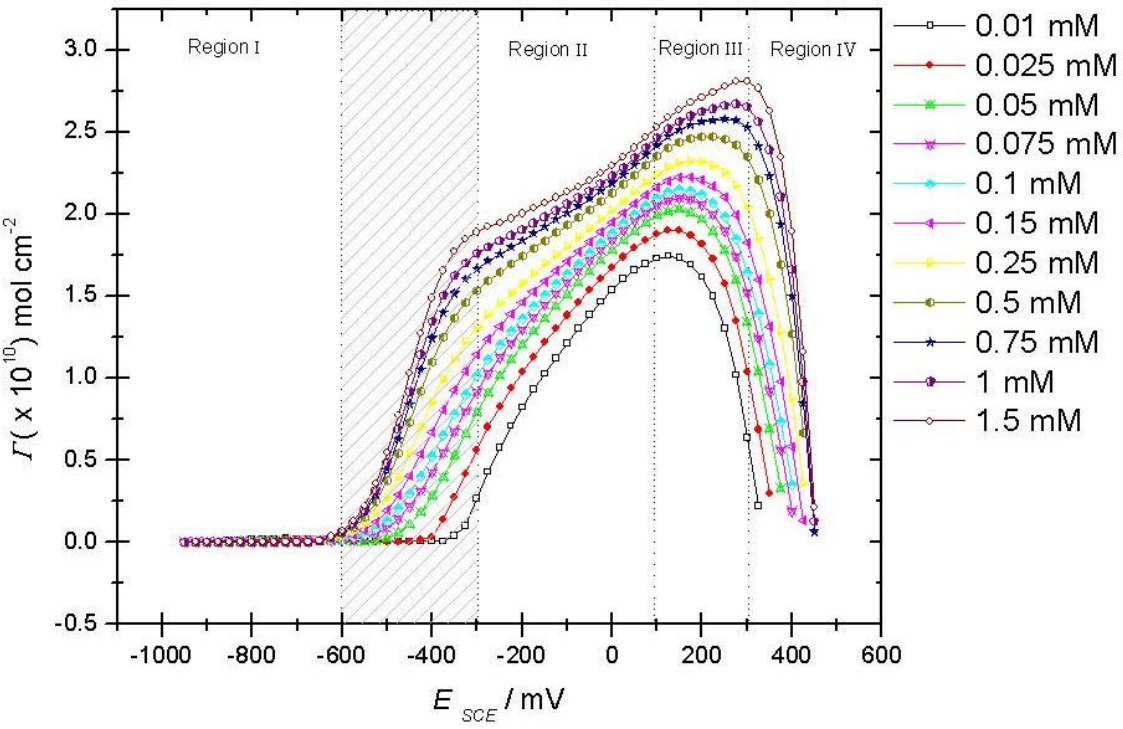

Fig. 6.10

Plots of the Gibbs surface excess of OTA-Tf at the Au(111)/solution interface versus electrode potential for the following bulk OTA-Tf concentrations: 0.01 mM (■), 0.025 mM (●), 0.050 mM(▲), 0.075 mM(▼), 0.10 mM(◆), 0.15 mM(◀), 0.25 mM(▶), 0.50 mM(◐), 0.75 mM(★), 1 mM(◗), 1.5 mM(○).

Gibbs excesses as a function of the electrode potential for different bulk concentrations of the surfactant ranging from 10 μM to 1.5 mM is plotted in Figure 6.10. Consistent with the previous discussions, the Gibbs excess *versus* potential plot is also divided into four regions for preliminary qualitative evaluation. Region I represents the potentials where surfactants are not adsorbed on the surface, and the shaded region corresponds to potential where surfactants begin to adsorb on the surface; a significant increase in surface excess can be seen after -600 mV in this region. The surface excess continues to rise in region II, albeit at a reduced rate. At higher concentrations surface excess reaches toward a quasi-potential independent level suggesting the formation of relatively stable surface aggregates at higher concentrations. In region III, the surface excess shows very strong concentration dependence. At lower bulk concentrations the surfactants begin to desorb from the surface in this region whereas at larger bulk concentrations the surface excess is high in comparison to region II. In region IV, the surfactant starts to desorb from the surface as is evident from the Gibb excess values tending to zero. Quantitative aspects of the Gibbs excess plot with a more detailed discussion of surface aggregates in regions II and III, combined with information regarding structural transformations obtained from capacity measurements discussed in the previous section is given below.

At 0.025 mM bulk concentration, surfactants do not form aggregates on the surface as evidenced by the observation of a single adsorption state in the Gibbs excess plot and the equilibrium capacity plot. The maximum surface excess (~ 1.9 $x10^{-10}$ mols cm^{-2}, E = +125 mV) obtained at lower concentrations is significantly less than that expected for a complete monolayer on the surface. The maximum surface concentration of a close packed vertical monolayer of OTA-Tf molecules estimated from the cross

sectional area of the headgroup is ~3 x 10^{-10} mol cm^{-2}. The two-state adsorption behaviour suggested by equilibrium capacity measurement at higher bulk concentration is supported by the quantitative data from the Gibbs excess plot. For instance, the Gibbs excess curve for 1 mM bulk OTA-Tf concentration attains a maximum value ~ 2.7x10^{-10} mol cm^{-2} at E ~ +250 mV, which is very close to the maximum surface concentration estimated for a close packed vertical monolayer of OTA-Tf molecules, suggesting a vertical monolayer of adsorbed OTA-Tf in region III. Clearly the discussion made in the previous section based on capacity transients also suggested a vertical monolayer of the surfactant at ~+250 mV. The appearance of a shoulder plateau at higher concentrations in region II suggests the formation of stable surface aggregates in this region. Using Retter's equivalent thickness model,[13] the difference in the surface concentration ($\Delta\Gamma$) for a vertical layer to hemicylindrical aggregate can be calculated from the limiting surface coverage data, i.e., $\Delta\Gamma$ = 2.7 x 10^{-10} x (1- 1/1.27) = 0.21 x 2.7 x 10^{-10} mol cm^{-2} = 0.45 x 10^{-10} mol cm^{-2}. Hence the surface excess corresponding to a hemicylindrical aggregate of OTA-Tf on the surface is calculated as 2.7 x 10^{-10} mol cm^{-2} – 0.45 x 10^{-10} mol cm^{-2} = 2.25 x 10^{-10} mol cm^{-2}. From the Gibbs excess plot, this value of Gibbs surface excess is attained at ~0 mV, i.e. in region II. This region corresponds to the equilibrium capacity plateau where the aggregate structure determined from the equilibrium capacity curve using Retter's formalism was hemicylindrical. Hence both the Gibbs excess data and the equilibrium capacity data suggest the formation of hemicylindrical aggregates in region II and a vertical layer in region III.

The dissimilarity between the capacity transients at region II and region III potentials (Figure 6.5b) can be elucidated at this point. Notably, both the curves show

similar behavior in the initial stages; the capacity drops within the first two seconds indicating the initial nucleation and subsequent growth processes forming a vertical layer at the interface (as the capacity drops to ~10.8 μF cm^{-2} in the first two seconds). After this point, the capacity transients are entirely different at these two representative potentials. The transient for +250 mV shows a slow drop in capacity to reach a value of ~ 9.7 μF cm^{-2}. This corresponds to a slow growth process that leads to a more compact layer (i.e. vertical layer). The transient corresponds to -50 mV shows a progressively increasing capacity that levels at a capacity value of ~12 μF cm^{-2}. This indicates a growth process that leads to a less compact adlayer (i.e. hemicylindrical aggregates).

The reversibility of this process was tested by stepping the potential from a value corresponding to the vertical layer to a value corresponding to the hemicylindrical aggregates and again stepped back to the potential where it forms a vertical layer, without applying a desorption potential in between (Figure 6.11). Initially, the capacity transient obtained for the step from the desorption potential to +250 mV shows the monotonic drop as previously described for the nucleation and growth process leading to a compact vertical layer. In the next stage, the potential was stepped to +50 mV without applying a desorption potential. The resulting capacity curve obtained here does not represent aggregate formation by means of a nucleation-growth procedure; instead it follows the direct structural transition from the vertical layer to the hemicylindrical aggregates. In the third stage, the potential was shifted back to +250 mV from +50 mV, which corresponds to the reverse process. In Figure 6.11, it can be seen that upon switching the potential from +250 mV to +50 mV, the capacity increases as expected for a transition from a compact film to a film of hemicylindrical aggregates. Upon the return step to +50 mV,

the capacity drops but does not match very well to the capacity minimum of a vertical layer obtained initially by the nucleation-growth process. This suggests that a compact layer cannot be fully reformed within the time scale of the experiment when the aggregate structure is directly switched from a potential corresponding to hemicylindrical aggregates to a potential corresponding to a vertical layer. This further explains why a phase transition peak was not observed in the differential capacity experiments involving a slower potential scan.

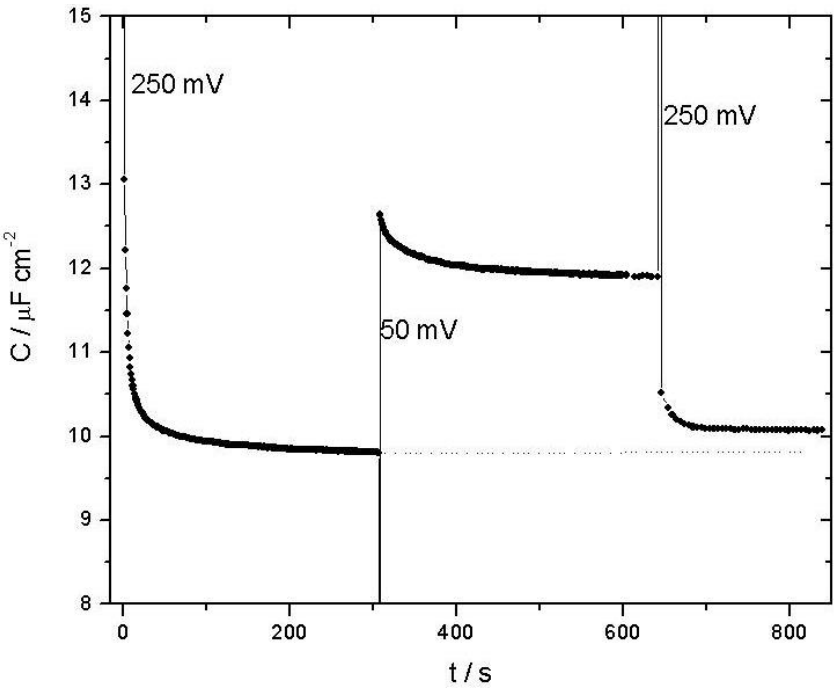

Fig. 6.11

Capacity transients demonstrating the reversibility of aggregate structural transitions at Au(111)/electrolyte interface for 1 mM OTA-Tf bulk concentration. +250 mV corresponds to potential where vertical layer of aggregate is formed. 50 mV corresponds to potential where hemicylindircal aggregate of OTA-Tf is formed.

6.3.6 Adsorption isotherms and Gibbs energies of adsorption

With the estimated value of Γ_{max} , the Frumkin isotherm has been tested by determining the fractional surface coverage (Θ) and then plotting $\ln\left[\frac{\Theta}{(1-\Theta)C/55.5}\right]$ against θ at constant potential according to the following relationship[30]

$$\frac{\theta}{(1-\theta)\,C/55.5} = \beta e^{2a\theta} \qquad (6.8)$$

where β is the adsorption coefficient related to the standard Gibbs energy of adsorption and *a* is the Frumkin interaction parameter.

$$\beta = e^{-\frac{\Delta G}{RT}} \qquad (6.9)$$

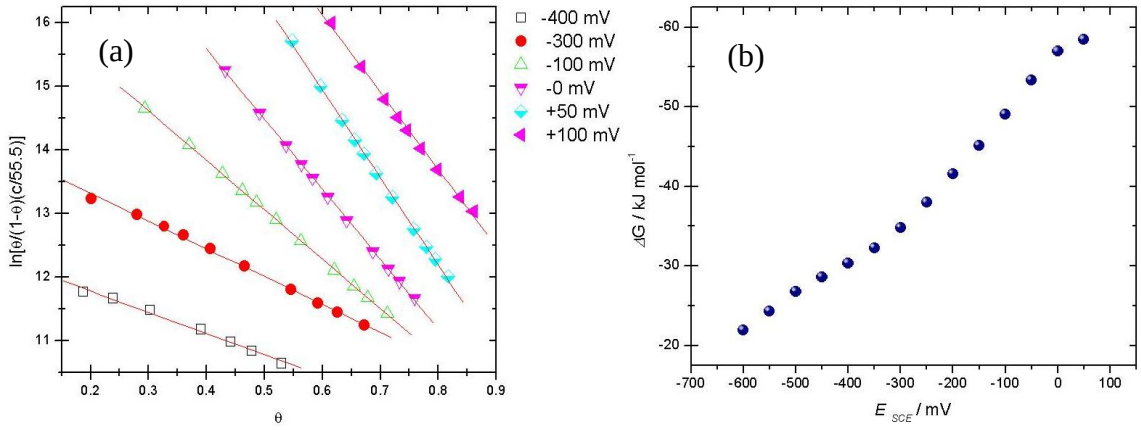

Fig. 6.12

(a) Representative Frumkin curves obtained at -400 mV(■), -300mV(●), -100 mV(△), 0 mV(▲), 50 mV(◆) and 100 mV (◀). The lines represent the linear regressions to the curves.

(b) Gibbs energies of adsorption plotted as a function of the electrode potential.

A good linear relationship was observed with a negative slope for regions I and II (Figure 6.12a), more complex isotherms are required at more positive potentials where it deviates from the Frumkin isotherm since the surfactant is in a different adsorption state. The standard Gibbs energy of adsorption was determined and plotted as a function of electrode potential in Figure 6.12b. The Frumkin interaction parameter has a negative value indicating repulsion between the adsorbed surfactant molecules. The plot shows that the free energy of adsorption increases with potential and reaches a maximum value at the potential that corresponds to saturation of the first state of adsorption.

6.4 Summary and Conclusions

The adsorption of a cationic surfactant on Au(111) surface has been studied with the help of interfacial capacity measurements and by using the thermodynamic analysis of the charge data. Measurements of the interfacial capacity provided important information about the aggregate structures and phase transition. The charge density data was used to extract quantitative information, *viz.* relative Gibbs surface excess and zero coverage Gibbs energies of adsorption, as a function of the electrode potential. Furthermore, by combining the surface concentration data with the equilibrium capacity data, the potential induced structural changes of OTA-Tf at the Au(111)/electrolyte interface has been studied. These studies demonstrate that there is a clear indication of the potential induced structural transformation of OTA-Tf aggregates on Au(111) surface. Combining chronocoulometry and capacity transient measurements, *plausible geometries* of the OTA-Tf aggregates as a function of the electrical state of the surface has been elucidated. Capacity plots and the Gibbs surface excess data suggest that the surfactant aggregates *plausibly* possess hemicylindrical geometry at negative

polarizations. According to the proposed model, the formation of surface aggregates at negative polarizations is a relatively slow process; a more compact adlayer is formed in the initial stages that slowly transforms (in ~ 2 mins) to an aggregate structure with lower surface coverage (a hemicylindrical structure according to the proposed model). At more positive potentials (E > +0.1 V), a stable, compact perpendicular surface layer is formed. Both capacity measurements and thermodynamic analysis of the charge data indicate desorption of the surfactant at E > +0.3 V.

Reference List

1. Israelachvili, J. N. *Intermolecular and surface forces;* 2 ed.; Academic Press, London: 1992.pp. 341-385.

2. Nguyen, D.; Bertrand, G. L. Calorimetric observations of the sphere-rod transition of tetradecyltrimethylammonium bromide and sodium dodecyl sulfate: Effects of electrolytes and nonelectrolytes at 25 and 45¦c. *Journal of Colloid and Interface Science* **1992,** *150* (1), 143-157.

3. Manne, S.; Gaub, H. E. Molecular Organization of Surfactants at Solid-Liquid Interfaces. *Science* **1995,** *270* (5241), 1480-1482.

4. Petri, M.; Kolb, D. M. Nanostructuring of a sodium dodecyl sulfate-covered Au(111) electrode. *Physical Chemistry Chemical Physics* **2002,** *4* (7), 1211-1216.

5. Schniepp, H. C.; Saville, D. A.; Aksay, I. A. Tip-Induced Orientational Order of Surfactant Micelles on Gold. *Langmuir* **2008,** *24* (3), 626-631.

6. Grant, L. M.; Ederth, T.; Tiberg, F. Influence of Surface Hydrophobicity on the Layer Properties of Adsorbed Nonionic Surfactants. *Langmuir* **2000,** *16* (5), 2285-2291.

7. Patrick, H. N.; Warr, G. G.; Manne, S.; Aksay, I. A. Self-Assembly Structures of Nonionic Surfactants at Graphite/Solution Interfaces. *Langmuir* **1997,** *13* (16), 4349-4356.

8. Sotiropoulos, S.; Avranas, A.; Papadopoulos, N. Study of Oleate Adsorption at the Mercury/Electrolyte Solution Interface as a Function of Electrode Potential and Time. *Langmuir* **1997,** *13* (26), 7230-7238.

9. Wandlowski, T.; Hromadova, M.; de Levie, R. On the Kinetics of Adsorption of Dodecyl Sulfate at the Mercury-Water Interface. *Langmuir* **1997,** *13* (10), 2766-2772.

10. Retter, U.; Avranas, A.; Lohse, H.; Siegler, K.; Lunkenheimer, K. On the Adsorption Kinetics of Octanoic Acid at the Mercury/Electrolyte Interface. *Langmuir* **1999,** *15* (10), 3661-3665.

11. Retter, U. One-Dimensional Nucleation-Growth-Collision in the Formation of Surface Hemimicelles of Amphiphiles. *Langmuir* **2000,** *16* (20), 7752-7756.

12. Retter, U.; Avranas, A. On Anion-Induced Formation of Hemicylindrical and Hemispherical Surface Micelles of Amphiphiles at the Metal/Electrolyte Interface. *Langmuir* **2001,** *17* (16), 5039-5044.

13. Retter, U.; Tchachnikova, M. On the formation of surface micelles at the metalá|áelectrolyte interface. *Journal of Electroanalytical Chemistry* **2003,** *550-551*, 201-208.

14. Avranas, A.; Papadopoulos, N. Adsorption of surfactants: differential capacitance studies using phase-sensitive alternating current voltammetry. *Langmuir* **1992,** *8* (11), 2804-2809.

15. Jacek Lipkowski 1998 Alcan Award LectureSurface electrochemistry - surface science with a joy stick. *Canadian Journal of Chemistry* **1999,** *77* (7), 1163-1176.

16. Brosseau, C. L.; Sheepwash, E.; Burgess, I. J.; Cholewa, E.; Roscoe, S. G.; Lipkowski, J. Adsorption of N-Decyl-N,N,N-trimethylammonium Triflate (DeTATf), a Cationic Surfactant, on the Au(111) Electrode Surface. *Langmuir* **2006,** *23* (4), 1784-1791.

17. Burgess, I.; Jeffrey, C. A.; Cai, X.; Szymanski, G.; Galus, Z.; Lipkowski, J. Direct Visualization of the Potential-Controlled Transformation of Hemimicellar

Aggregates of Dodecyl Sulfate into a Condensed Monolayer at the Au(111) Electrode Surface. *Langmuir* **1999,** *15* (8), 2607-2616.

18. Xu, S.; Chen, M.; Cholewa, E.; Szymanski, G.; Lipkowski, J. Electric-Field-Driven Surface Aggregation of a Model Zwitterionic Surfactant. *Langmuir* **2007,** *23* (13), 6937-6946.

19. Shaw, D. J. In *Colloid and Surface Chemistry*, 4 ed.; Butterworth-Heinemann: Oxford, UK, 1992.

20. Okano, L. T.; Quina, F. H.; El Seoud, O. A. Fluorescence and Light-Scattering Studies of the Aggregation of Cationic Surfactants in Aqueous Solution:GÇë Effects of Headgroup Structure. *Langmuir* **2000,** *16* (7), 3119-3123.

21. Cholewa, E.; Burgess, I.; Kunze, J.; Lipkowski, J. Adsorption of dimethyl-3-ammonio-1-propanesulfonate (DDAPS), a model zwitterionic surfactant, on the Au(111) electrode surface. *Journal of Solid State Electrochemistry* **2004,** *8* (10), 693-705.

22. Cholewa, E.; Burgess, I.; Kunze, J.; Lipkowski, J. Adsorption of dimethyl-3-ammonio-1-propanesulfonate (DDAPS), a model zwitterionic surfactant, on the Au(111) electrode surface. *Journal of Solid State Electrochemistry* **2004,** *8* (10), 693-705.

23. Moroi, Y.; Rusdi, M.; Kubo, I. Difference in Surface Properties between Insoluble Monolayer and Adsorbed Film from Kinetics of Water Evaporation and BAM Image. *The Journal of Physical Chemistry B* **2004,** *108* (20), 6351-6358.

24. Papadopoulos, N.; Sotiropoulos, S.; Nikitas, P. Equilibrium and kinetic properties of cetyl-dimethyl-benzyl-ammonium chloride at the mercury/electrolytic solution interface by means of phase sensitive three-dimensional AC

voltammetry. *Journal of Colloid and Interface Science* **1992,** *151* (2), 523-533.

25. Sotiropoulos, S.; Nikitas, P.; Papadopoulos, N. Adsorption of sodium dodecylsulphate on mercury as an example of micellization within a multilayer interphase. *Journal of Electroanalytical Chemistry* **1993,** *356* (1-2), 201-223.

26. Sotiropoulos, S.; Nikitas, P.; Papadopoulos, N. Interfacial micellization of cetyl-dimethyl-benzylammonium chloride and Tween-80R at the Hg/electrolyte solution interphase. *Journal of Electroanalytical Chemistry* **1993,** *356* (1-2), 225-243.

27. Avranas, A.; Papadopoulos, N.; Sotiropoulos, S. Adsorption behavior of bis (2-ethylhexyl) sodium sulfosuccinate (AOT) at the mercury-electrolyte solution interface as a function of electrode potential and time. *Colloid & Polymer Science* **1994,** *272* (10), 1252-1258.

28. Nikitas, P. Different types of phase transitions at charged interfaces: A thermodynamic analysis. *Journal of Electroanalytical Chemistry and Interfacial Electrochemistry* **1991,** *300* (1-2), 607-628.

29. Delahay, P.; Trachtenberg, I. Adsorption Kinetics and Electrode Processes. *Journal of the American Chemical Society* **1957,** *79* (10), 2355-2362.

30. Frumkin, A.; Obrutshewa, A. Influence of Electrical Field on the Adsorption of Neutral Molecules. *Nature* **1926,** *117*, 790.

31. Becucci, L.; Moncelli, M. R.; Guidelli, R. Ion Carriers and Channels in Metal-Supported Lipid Bilayers as Probes of Transmembrane and Dipole Potentials. *Langmuir* **2003,** *19* (8), 3386-3392.

32. Damaskin, B.; Frumkin, A.; Chizhov, A. Generalized model of the surface layer for the case of adsorption of inorganic molecules on the electrode. *Journal of Electroanalytical Chemistry* **1970,** *28* (1), 93-104.

33. Sek, S.; Chen, M.; Brosseau, C. L.; Lipkowski, J. In Situ STM Study of Potential-Driven Transitions in the Film of a Cationic Surfactant Adsorbed on a Au(111) Electrode Surface. *Langmuir* **2007,** *23* (25), 12529-12534.

Chapter 7

Influence of Bromide Ions on the Adsorption Behavior of a Quaternary Ammonium Surfactant on Au(111) and Au(100)

7.1 Introduction

The adsorption of octyltrimethylammonium triflate on Au(100) and Au(111) surfaces has already been discussed in Chapters 5 and 6, respectively. Since the triflate anion exhibits no significant specific adsorption on gold, it can easily be replaced by a specifically adsorbing anion on the surface.[1] The adsorption behavior of the quaternary ammonium cation is expected to be largely influenced by bromide anions because of strong specific adsorption of bromide on gold surfaces.[2-4] In this chapter, the adsorption of a quaternary ammonium surfactant in the presence of bromide will be discussed. Since halide salts of quaternary ammonium ions are extensively found in the literature as common stabilizing ligands for gold nanoparticles, the scope of this study extends beyond a fundamental interest in surfactant adsorption at the metal-solution interface. A very popular member of the cationic surfactant stabilizer family is cetyltrimethylammonium bromide (CTA-Br) and the stability of CTA-Br stabilized gold nanoparticles is often attributed to the strong binding affinity of bromide to gold, which in turn is believed to help the cationic surfactant strongly adhere to the metal surface[5]. More importantly, CTA-Br is the most popular ligand for the seed mediated synthesis of gold nanorods in aqueous solution.[6-10] In a typical synthetic protocol for gold nanorods synthesis by this route, the reaction mixture contains Au^{3+} ions ($HAuCl_4$), quaternary ammonium bromide surfactant (CTA-Br), a mild reducing agent (ascorbic acid) and

nanoparticle seeds (citrate/CTA-Br stabilized gold) dispersed/dissolved in an aqueous medium. Over the course of the past several years, it has been demonstrated that gold nanorods can be synthesized even by varying the parameters such as the source of gold ions,[11] nanoparticle seed,[12,12-14] reducing agent,[11] pH[15] or the chain length of the quaternary ammonium surfactant,[16] but the presence of bromide ions is found to be crucial for the formation of nanorods.[17-20] At present, the role of quaternary ammonium bromide surfactants on the formation of gold nanorods is a subject of debate in the literature[21]. Initially, the popular perception was that the rod-like micelles of CTA-Br act as soft templates,[8,13,22-25] but later it was demonstrated that gold nanorods can be synthesized even at concentrations below the cmc of CTA-Br,[26] which disproves this postulate. Currently, the most popular perception is that nanorod growth is promoted by the preferential adsorption of the quaternary ammonium surfactant on different facets of a single crystalline or twinned embryonic seed crystal.[13,26] The postulation of crystallography specific surfactant adsorption is attributed to crystallography specific bromide adsorption; bromide supposedly acts as a bridging centre between the nanorod surface and the quaternary ammonium headgroup of the surfactant[5,23]. Using selective area electron diffraction (SAED) and high resolution transmission electron microscopy (HRTEM) studies, it has been demonstrated by various groups that gold nanorods synthesized by the reduction of gold chloride using ascorbic acid in the presence of CTA-Br and single crystal gold seed crystals, are of pentagonal cross-section with (100) side facets and (111) end facets.[13] The crystallographic analysis of gold nanorods lead to the speculation that the preferential adsorption of the surfactant on (100) facets over (111) facets of the nanoparticle during the growth process leads to nanorod formation.[25,27]

Since the presence of bromide ions is crucial for the formation of nanorods,[26,28] it has been envisaged that the preferential adsorption of bromide ions on Au(100) facets brings more counter ion surfactant species to that facet making Au(111) facets more accessible for further growth. Preferential bromide adsorption on a (100) facet can be explained by the lower Au atom packing density on the more open (100) surface compared to a (111) surface. While this simple model is often used in the literature to explain nanorod growth, there has been no direct experimental evidence that supports this idea, which is perhaps due to the difficulty in studying the interface of the single crystal gold seed during the growth process. Though a direct investigation of the growth process is hampered by the experimental difficulties, indirect methods may be used to inspect the postulated mechanism. Although nanoparticles in aqueous solution undoubtedly carry a net surface charge, it is extremely difficult to determine the electrical state of a single crystal nanoparticle during the growth process. A useful first step could be the use of a model charged interface whose surface charge can be controlled. Such an interface is that between the interface of a gold electrode and an electrolyte solution.

Before going further into the details of the strategy used to address the nanorod growth mechanism, it has to be noted that a slight variation of the original synthetic route, in which a small amount of silver ions is used in order to improve the yield of the nanorods, is also popular in the current literature.[7,23] The crystallographic faces of a nanorod formed in the presence of Ag^+ ions is different from that formed in the absence of Ag^+ ions[29]. Further, the effect of silver on the crystallography of a gold nanorod is another contentious subject in the literature. Since the presence of Ag^+ is not essential for the formation of nanorods[12], the growth mechanism of nanorods being addressed in this

chapter considers the synthetic route for gold nanorod *without* the assistance of silver ions.

One major difference between a cationic surfactant and bromide ions is that cationic surfactants spontaneously aggregate in the bulk of solution whereas bromide ions cannot form aggregates in solution. Octyltrimethylammonium ions have a relatively weak interaction with the gold surface (ΔG_{ads} ~ -60 kJ/mol, discussed in the previous chapter) while bromide is known to have significantly stronger affinity with gold surfaces (ΔG_{ads} ~ -180 kJ/mol)[2]. Hence one may assume that bromide anions would bring more of its cationic surfactant counterpart to the interface provided the potential range is in favour of bromide adsorption. In this context, it is important to understand the adsorption behavior of both as a function of charge/potential of the surface. A systematic study of the adsorption of an alkyl trimethylammonium surfactant and bromide anion on Au(111) and Au(100) surfaces is discussed in this chapter. Two issues of fundamental interest are addressed: (1) the effect of bromide on the adsorption behavior of quaternary ammonium surfactant on gold, (2) the relative adsorption of quaternary ammonium bromide on (111) and (100) gold crystals. The results of these studies provide quantitative information that can help to confirm or contradict existing explanations concerning the formation of gold nanorods.

A convenient experimental strategy is to use an alkyl trimethylammonium surfactant with a non-specifically adsorbing anion and an independent source of bromide ions. The cationic surfactant chosen was octyltrimethylammonium with a triflate counter ion, and sodium bromide was used as the source of bromide ions; since sodium and triflate ions do not specifically adsorb on gold, in effect we have separate sources of the cationic

surfactant and the bromide anion. A shorter alkyl chain surfactant in comparison to CTA-Br was chosen because it provides a wider range of concentrations below the cmc and a shorter hydrocarbon chain can easily be desorbed from the electrode surface (details in chronocoulometry section).

7.2 Experimental

Experimental setup and methodologies are the same as those described in Chapters 5 and 6. Cyclic voltammetry, differential capacity and chronocoulometry analyses of OTA^+/Br^- were carried out on Au(111) and Au(100) surfaces. An additional reagent used for the experiments in this chapter, sodium bromide (≥ 99.99%), was purchased from Sigma-Aldrich.

A discussion of OTA^+/Br^- adsorption on Au(111) is provided in Section 7.3, where the effect of bromide on the adsorption behaviour of OTA-Tf is discussed. OTA^+/Br^- adsorption on Au(100) is discussed in Section 7.4. A comparison of the relative Gibbs surface excesses of OTA^+/Br^- on Au(111) and Au(100) surfaces is presented in Section 7.5.

7.3 Adsorption of OTA^+/Br^- on Au(111)

7.3.1 Cyclic voltammetry

Cyclic voltammograms in Figure 7.1 present a qualitative picture of the bromide and OTA-Tf adsorption at the Au (111)/electrolyte interface. Cyclic voltammogram of 1 mM bromide (dashed line) in 0.1 M NaF supporting electrolyte shows a low coverage adsorption of bromide in the potential range between -450 mV and -150 mV (region II), followed by a steep increase in current at ~ -100 mV leading to a sharp irreversible peak

corresponding to the lifting of (1x23) reconstruction of Au(111) surface and consequent formation of a condensed layer of bromide.[2] The experimental voltammogram is in excellent agreement with previous literature reports of the Au(111)/Br^- interface.[2] The adsorption behavior of OTA-Tf on Au(111) has already been discussed in Chapter 6 and is presented again here solely for comparison purposes (1 mM OTA-Tf, thin solid line). In the bulk of solution, the triflate anion will completely dissociate from any non-aggregated surfactant ions and the OTA-Tf can be considered to exist as discrete OTA^+ cations and Tf^- anions. Ion-pairing of the quaternary ammonium surfactant with an anionic species can occur at the metal/solution interface,[1,30] and within surfactant aggregates formed above the critical micelle concentration.[31,32] However, in the presence of a specifically adsorbing anion like bromide, the triflate counter ion is expected to be readily replaced on the surface and hence the adsorbed surfactant will be treated as a discrete cation (OTA^+) . The bold solid line in Figure 7.1 corresponds to a 1:1 mixture of both OTA^+ and Br^- (1 mM) in solution. The peak at ~-500 mV which corresponds to the adsorption of surfactant has broadened in the presence of bromide. This is caused by the overlap of the bromide adsorption and OTA^+ adsorption. A small, but highly reproducible, spike appears at ~ -400 mV, and indicates a possible phase transition of the adsorbed layer following the formation of an ordered layer of adsorbates. A sharp peak that corresponds to the lifting of reconstruction at ~ -25 mV due to bromide adsorption (dashed line) is shifted to more positive potentials (bold solid line) in the presence of OTA^+ and is considerably dampened in amplitude. A qualitative analysis of the cyclic voltammograms indicates potential regions where coadsorption of both Br^- and OTA^+ ions on the Au(111) surface is highly likely.

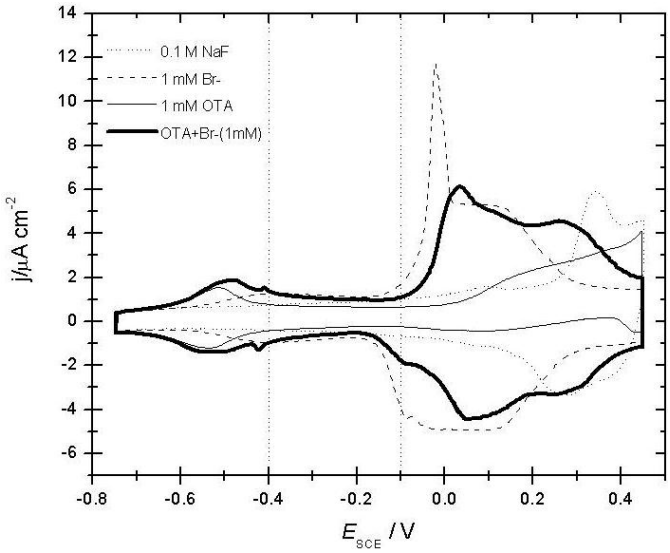

Fig. 7.1

Cyclic voltammograms for Au(111) in 0.1 M NaF electrolyte (dotted line), 1 mM Br- (dashed line), 1 mM OTA (thin solid line) and 1 mM OTA^+/Br^- (bold solid line).

7.3.2 Differential capacity

Differential capacity (DC) curves in Figure 7.2 show the adsorption behavior of OTA^+ in pure NaF electrolyte (thin solid line) and in the presence of bromide ions (bold solid line). The DC plots show an increase in the adsorption peak intensity (E ~ -500 mV) in the presence of bromide which then follows a capacity spike, all consistent with the corresponding portions in the cyclic voltammogram. Due to the presence of bromide ions at the interface, the capacity is consistently above the curve for 1 mM OTA^+ in pure electrolyte. After the pronounced capacitive feature at ~ 0 mV corresponding to the lifting of reconstruction due to the presence of bromide, a capacity plateau can be seen. This could indicate the formation of stable surface aggregates in this region of potentials (E ~ 200mV). Both cyclic voltammograms and differential capacity curves can only be considered as preliminary observations, primarily for the reason that these measurements do not correspond to a state of adsorption equilibrium.

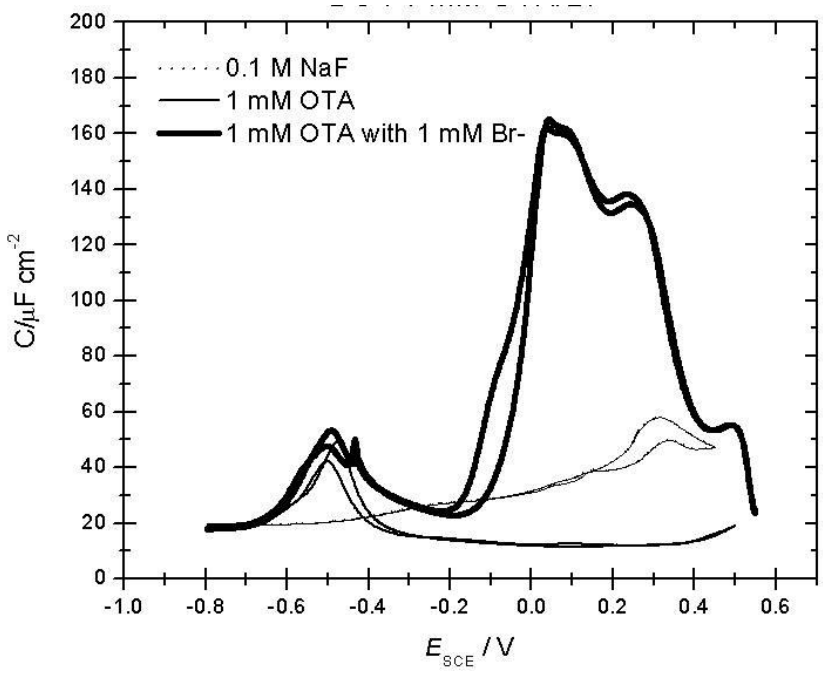

Fig. 7.2

Differential capacity curves of Au(111) in 0.1 M NaF electrolyte (dotted line) , 1 mM OTA^+ (thin solid line) and 1 mM OTA^+ + Br-(bold solid line).

7.3.3 Determination of OTA^+Br^- surface concentration

Quantitative information of the Br^- and OTA^+ surface concentration can be obtained using chronocoulometry in which the electrode's surface charge density due to adsorbed species at an equilibrated interface is measured. In order to get insight into the adsorption behavior of OTA^+ on the Au(111) surface in the presence of Br^- ions, two sets of electrochemical measurements were carried out; 1) by varying the concentration of quaternary ammonium surfactant at constant bromide concentration and 2) *vice-versa*, i.e. variable bromide concentration at constant surfactant concentration.

The electrocapillary equation for the gold/solution interface having a mixture of OTA-Tf surfactant and NaBr in NaF supporting electrolyte can be written as:

$$-d\gamma = \sigma_m dE + \Gamma_{OTA^+} d\mu_{OTA^+} + \Gamma_{Br^-} d\mu_{Br^-} \Gamma_{Na^+} d\mu_{Na^+} + \Gamma_{F^-} d\mu_{F^-} + \Gamma_{Tf^-} d\mu_{Tf^-} \quad (7.1)$$

where γ is the interfacial tension, σ_m is the metal charge density, E is the electrode potential, Γ is the Gibbs excess of the adsorbed species and μ is the chemical potential.

As the experiments are performed at constant supporting electrolyte concentration, $d\mu_{Na^+} = d\mu_{F^-} = 0$. The last term can be considered to be equal to zero as triflate shows no specific adsorption. Thus the equation 7.1 can be simplified to the following form

$$-d\gamma = \sigma_m dE + \Gamma_{OTA^+} d\mu_{OTA^+} + \Gamma_{Br^-} d\mu_{Br^-} \quad (7.2)$$

In order to extract the Gibbs excess of OTA^+ and Br^-, two sets of experiments performed in which the concentration of either of the species is kept constant while varying the concentration of the other species.

At constant Br^- concentration,

$$-d\gamma = \sigma_m dE + \Gamma_{OTA^+} d\mu_{OTA^+} = \sigma_m dE + \Gamma_{OTA^+} RT d\ln C_{OTA^+} \quad (7.3)$$

At constant OTA^+ concentration,

$$-d\gamma = \sigma_m dE + \Gamma_{Br^-} d\mu_{Br^-} = \sigma_m dE + \Gamma_{Br^-} RT d\ln C_{Br^-} \quad (7.4)$$

where C_{OTA^+} and C_{Br^-} are the concentrations of OTA^+ and Br^-, respectively.

In a chronocoulometry experiment, σ_m values were obtained by desorbing both OTA^+ and Br^- from the electrode surface. Hence charge data obtained for each set of experiments can be used to calculate the surface pressure (π) by employing the back integration procedure.

$$\pi = -d\gamma = \int_{E_{des}}^{E_c} (\sigma_m)_{(\Theta)} dE - \int_{E_{des}}^{E_c} (\sigma_m)_{(\Theta=0)} dE \quad (7.5)$$

where $(\sigma_m)_{(\Theta)}$and $(\sigma_m)_{(\Theta=0)}$denote the metal charge density measured in the presence and absence of the adsorbing species (either OTA^+ or Br^-).

The Gibbs surface excess, Γ, can be calculated from the surface pressure data by differentiation of the corresponding electrocapillary equation (equations (7.3) and (7.4)) with respect to the natural log of the adsorbate concentration at constant electrode potential.

$$\Gamma_{OTA^+} = \frac{1}{RT}\left(\frac{\delta\pi}{\delta ln c_{OTA^+}}\right)_{T,P,E} \quad (7.6)$$

$$\Gamma_{Br^-} = \frac{1}{RT}\left(\frac{\delta\pi}{\delta ln c_{Br^-}}\right)_{T,P,E} \quad (7.7)$$

In the following sections, the two sets of experiments mentioned above will be discussed in detail.

7.3.4 Variable [OTA^+] at constant [Br^-]

7.3.4.1 Cyclic voltammetry

Preliminary analyses were done using cyclic voltammetry. Figure 7.3 shows cyclic voltammograms for variable OTA^+ concentrations in the presence of 1 mM Br^- bulk concentration. Consistent with the previous discussion of surfactant adsorption on Au(111), the adsorption peaks at negative potentials shift further negative with increasing surfactant concentration. In the presence of bromide, the adsorption peak feature has an additional contribution from bromide adsorption and the small current spike previously noted is seen at higher concentrations of OTA (1 mM & 1.5 mM). The concentration dependence of this spike stems from the fact that only at higher surfactant concentrations does the OTA^+ adsorption occur at potentials more negative of bromide adsorption. This spike appearance may indicate a phase transition leading to an ordered arrangement of

the adsorbed layer due to inclusion of bromide into the surfactant adlayer. Such an anion induced phase transition of organic molecules adsorbed on the surface is reported in the literature.[33] In Figure 7.3, between -400 mV < *E* < -100 mV the curve is essentially parallel to the potential axis indicating no major structural changes of the adsorbed species in this region. The adsorbed layer of bromide and OTA^+ further experiences a major change upon the lifting of reconstruction and the simultaneous formation of a condensed layer of bromide (*E* > -50 mV). The sharp peak corresponding to the lifting of the reconstruction becomes less sharp and shifts to more positive potentials with increasing surfactant concentration. After the lifting peak, a quasi-plateau region of current can be seen, the width of which increases with bulk concentration of OTA^+. This region corresponds to co-adsorption of a condensed layer of bromide and the surfactant.

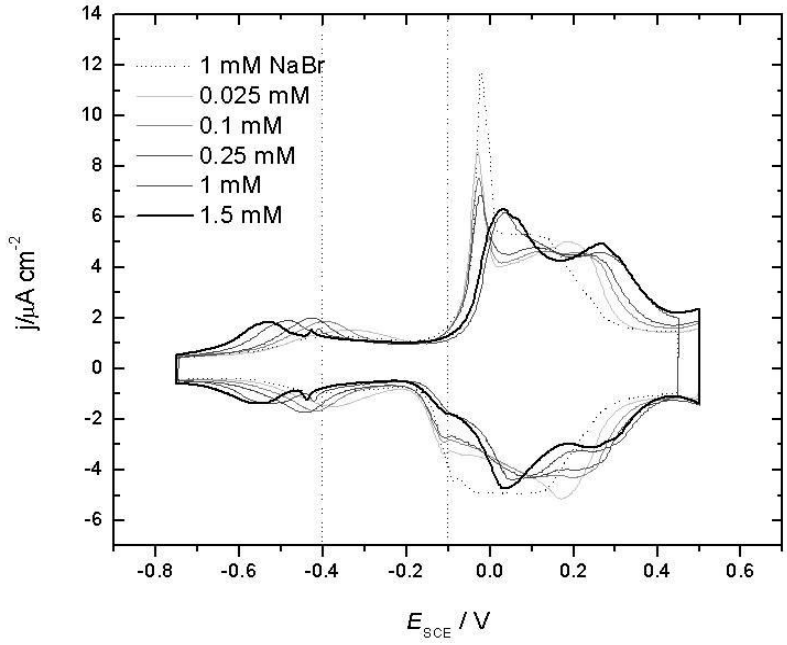

Fig. 7.3

Cyclic voltammograms of 1 mM Br^- (dotted line) and 1 mM Br^- with variable concentrations of OTA^+ from 0.025 mM (light gray line) to 1.5 mM (bold black line) at Au(111)/0.1 M NaF interface.

7.3.4.2 Chronocoulometry

Equilibrium charge density versus electrode potential data for series A chronocoulometry measurements (variable surfactant concentration in the presence of 1 mM Br^-) is shown in Figure 7.4. The charge density data for the supporting electrolyte (0.1 M NaF) in the absence of bromide and OTA^+ is shown as a dotted line. The charge density curve for 1 mM bromide is consistent with that reported in the literature.[2] This curve is composed of sections having different slopes; each corresponds to different states of halide species adsorption. Though a detailed description of the charge curve for adsorption of bromide on Au(111) is already available in the literature,[2] a brief description is provided here as it is helpful for the ensuing discussion. The initial foot at ~ -600 mV corresponds to a low coverage bromide adsorption which then follows a steep increase in charge (correlates with the sharp peak in the cyclic voltammogram) and the consequent adsorption of a condensed layer of bromide, which as a result leads to a large amount of positive charge flowing to the metal side of the interface. After 0 mV, the slope becomes smaller and this region correlates with the plateau region in the voltammogram where there is significant amount of bromide adsorbed on the surface. The slope significantly decreases after 300 mV where an ordered layer of bromide is formed. All charge curves (Figure 7.4) merge with the electrolyte curve at the negative end of the potential domain, confirming that both surfactant molecules and bromide ions are completely desorbed from the surface at very negative electrode polarizations. The charge curves corresponding to variable concentrations of OTA^+ are consistently above the bromide curve for the potentials -600 mV < E < -50 mV, suggesting co-adsorption of Br^- and OTA^+ in this potential range. From the previous studies (Chapter 6) it has been shown that this region corresponds to hemicylindrical aggregates of the surfactant in the

absence of a specifically adsorbing anion. Even though a comment on the co-adsorbed OTA^+/Br^- aggregate structure cannot be made at this point, it is apparent that a significant amount of OTA^+ is present even in the presence of bromide ions, in this region of potentials. For $E > -50$ mV, the metal charge density becomes less positive with the addition of OTA^+, which is an expected change for the adsorption of cationic species based on simple electrostatic considerations. At the most positive potentials studied, the OTA^+ curves are almost indistinguishable from the bromide curve suggesting that the adlayer of bromide is not affected by the cationic surfactant. A detailed thermodynamic analysis of the charge curves to extract quantitative information about the surface concentration of the adsorbates at the interface will be discussed in Section 7.3.6.

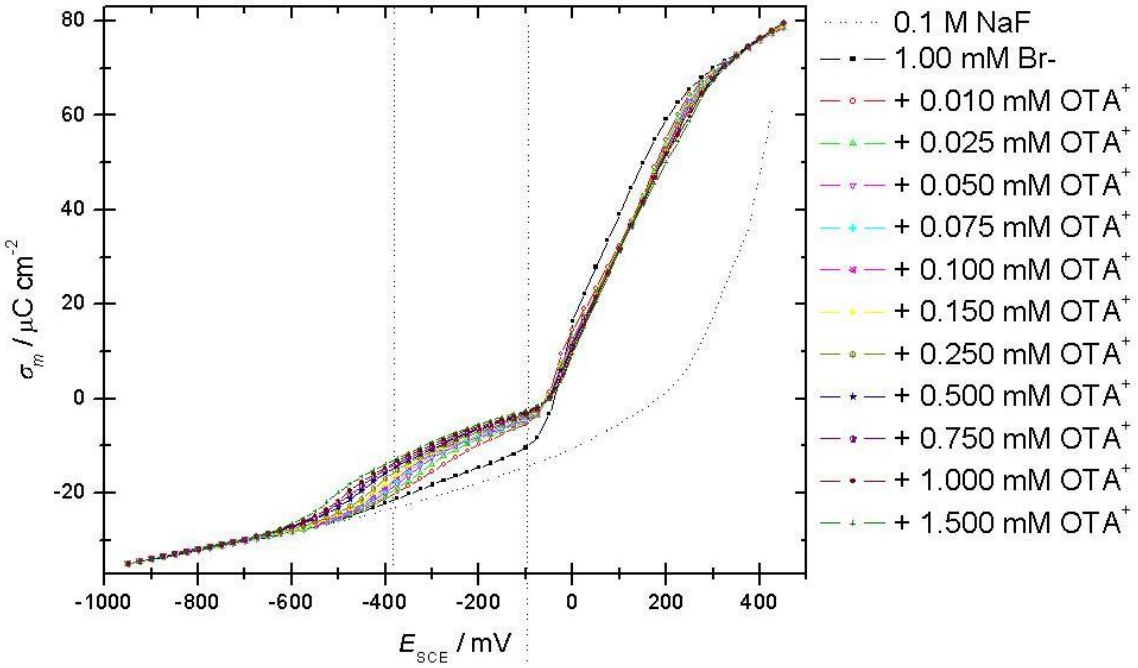

Fig. 7.4

Charge density versus electrode potential curves for Au(111) in 0.1 M NaF supporting electrolyte (----), 1 mM NaBr (■) and following OTA+ concentrations: 0.01 mM (○), 0.025 mM (△), 0.05 mM(▽), 0.075 mM(◈), 0.10 mM(⊠), 0.15 mM(▷), 0.25 mM(⬡), 0.5 mM(★), 0.75 mM(⬟), 1 mM(●), 1.5 mM(+).

7.3.5 Variable [Br^-] at constant [OTA^+]

7.3.5.1 Cyclic voltammetry

As before, cyclic voltammetry provides a qualitative description of the interface. Figure 7.5 shows cyclic voltammograms corresponding to series B measurements where the concentration of bromide is varied at constant OTA^+ concentration (1 mM). The voltammograms corresponding to 1mM OTA^+ only and with variable concentrations of bromide are shown as the dotted line and lines with different shades of gray respectively. With increase in bromide concentration, the OTA^+ adsorption and desorption peaks broaden as they overlap with the onset of bromide adsorption/desorption. Once again, the current spike is seen after the OTA^+ adsorption peak which shifts to more negative potentials with an increase in bromide concentration. This further clarifies that the spike is associated with the adsorption of bromide on a surface that already contains a film of OTA^+ ions. As discussed previously, between -400 mV < *E* < +400 mV both OTA^+ and Br^- are co-adsorbed on the surface. The steep increase in current due to the lifting of surface reconstruction is shifted to negative potentials with increase in bromide concentration, and the formation of a condensed layer of bromide co-adsorbed with OTA^+ follows at further positive potentials.

7.3.5.2 Chronocoulometry

Figure 7.6 shows charge curves corresponding to variable bromide concentration in the presence of 1 mM OTA^+ (series B chronocoulometry measurements). At negative potentials, all the curves are indistinguishable from the electrolyte curve, indicating complete desorption of OTA^+/Br^- from the surface. Between -500 mV < *E* < -50 mV, there is a slight increase in charge density which corresponds to low coverage adsorption

of bromide. After sweeping the potential beyond the lifting of the surface reconstruction, an abrupt increase in metal charge density is observed which corresponds to significant adsorption of bromide at more positive potentials.

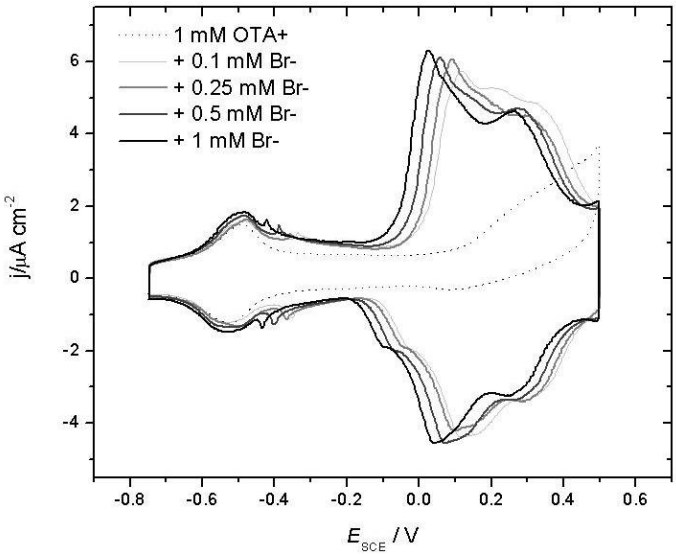

Fig. 7.5

Cyclic voltammograms of 1 mM OTA^+ (dotted line) and variable concentrations of Br^- from 0.1 mM (light gray line) to 1 mM (thick line) at the Au(111)/0.1M NaF interface.

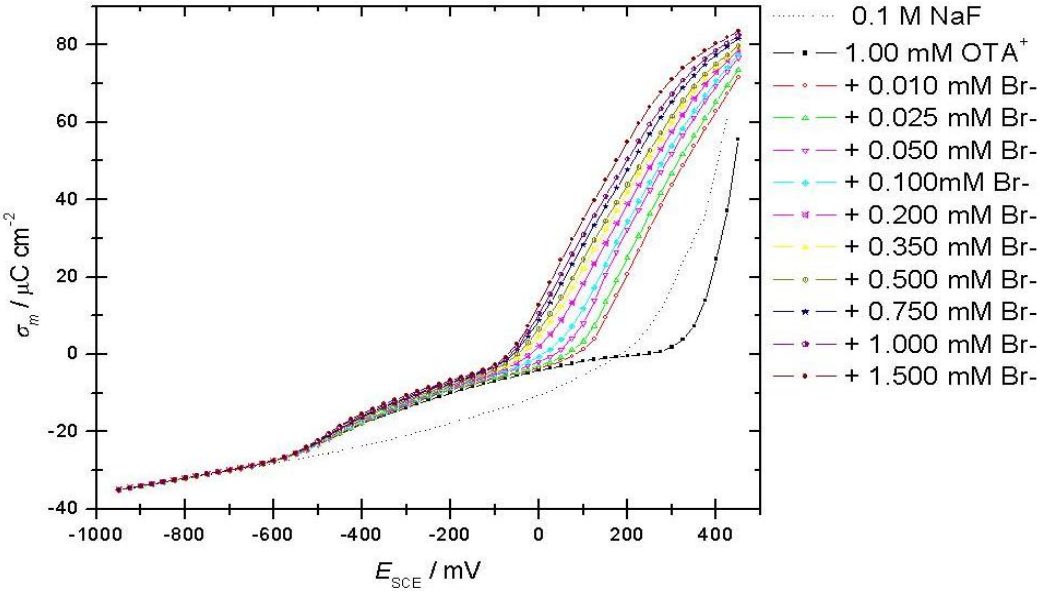

Fig. 7.6

Charge density versus electrode potential curves for Au(111) in 0.1 M NaF supporting electrolyte (----), 1 mM OTA (■) and following NaBr concentrations: 0.01 mM (○), 0.025 mM (△), 0.05 mM(▽), 0.10 mM(◈), 0.20 mM(⋇), 0.35 mM(▷), 0.50 mM(⬡), 0.75 mM(★), 1.0 mM(◑), 1.5 mM(●).

7.3.6 Gibbs surface excesses for OTA^+Br^- on Au(111)

Using the thermodynamics of ideally polarized electrodes, the surface concentrations of OTA^+, Γ_{OTA+}, at constant Br^- concentration in the bulk solution, and the surface concentrations for Br^- , Γ_{Br^-}, at constant OTA^+ concentration in the bulk of solution were calculated using the appropriate series of charge data. The Gibbs surface excesses (surface concentrations) were calculated from the charge data using the same methodology discussed in Chapter 3. Figure 7.7a shows Gibbs excess data for OTA^+ in the presence of 1 mM bromide. OTA^+ starts adsorbing at ~ -600 mV and the maximum surface concentration is attained at the onset of the potential corresponding to the lifting of the reconstruction due to bromide adsorption (~ -50 mV). The Gibbs excess decreases at more positive potentials and plateaus around +100 mV at higher bulk concentrations of OTA^+. In comparison to adsorption in the absence of Br^- (see Figure 7.8), here the Gibbs excess of OTA^+ is significantly high at the most positive potentials. The Gibbs excess versus potential plot of bromide in the presence of 1 mM OTA^+ is shown in Figure 7.7b. Consistent with the Gibbs excess of pure bromide reported in the literature,[2] only a very minor amount of Br^- is adsorbed at potentials between -500 mV and -50 mV($\Gamma \sim 10^{-10}$ mols cm^{-2}) even in the presence of OTA^+. These low surface coverages correspond to the gas phase low coverage adsorption of bromide on Au(111).[2] After the lifting of the reconstructed surface, a condensed layer of bromide is adsorbed on the surface and hence large values of Gibbs excess are seen at positive potentials. The Gibbs excess values obtained herein for bromide on Au(111) in the presence of OTA^+ is slightly above the reported Gibbs excess of bromide on bare Au(111) electrode in the absence of any other specifically adsorbing species.[2] This slight increase in the Gibbs excess of bromide in the

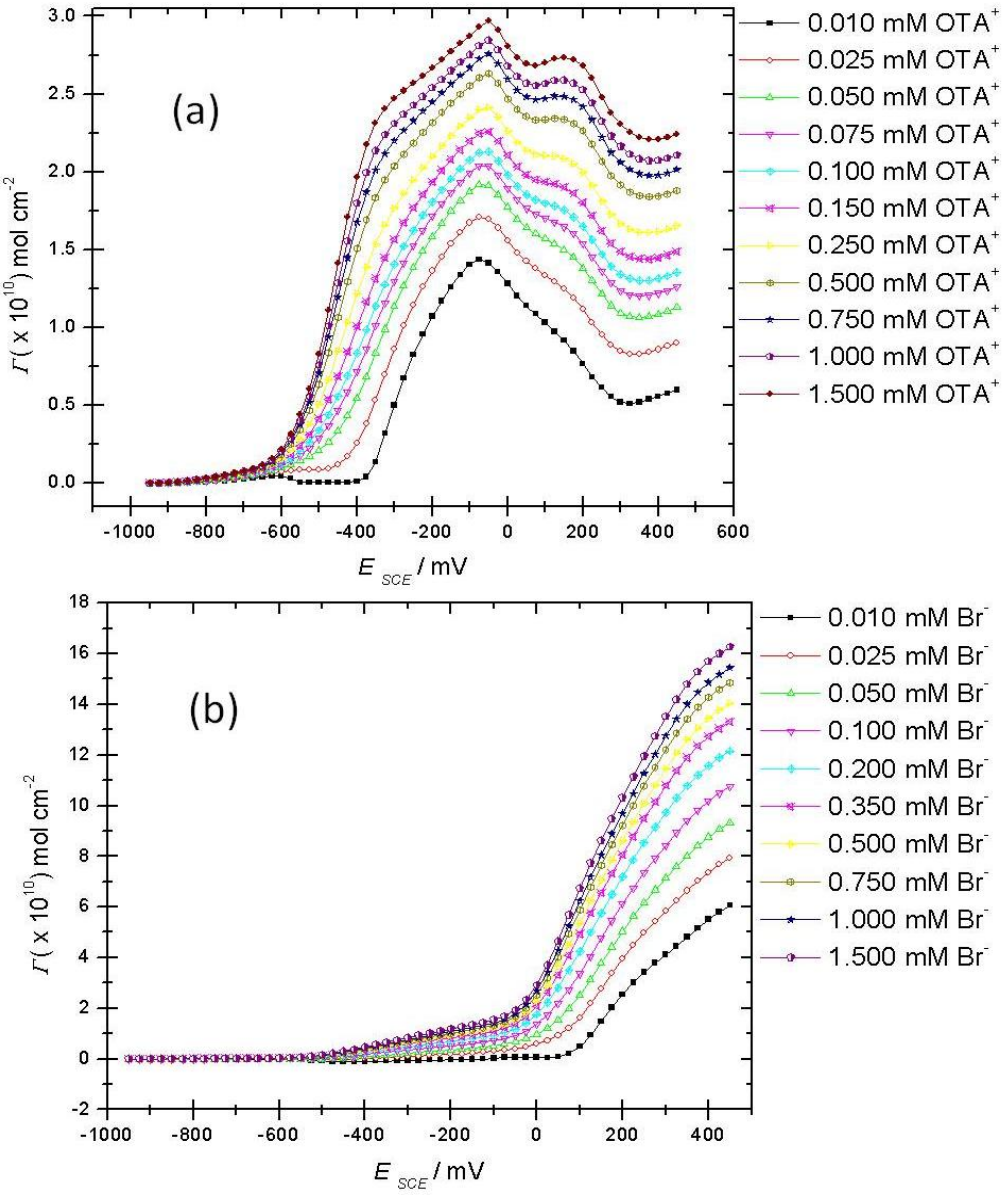

Fig. 7.7

(a) Plots of the Gibbs surface excess of OTA^+ in the presence of 1 mM NaBr bulk concentration at the Au(111)/solution interface versus electrode potential for the following bulk OTA^+ concentrations: 0.01 mM (■), 0.025 mM (○), 0.050 mM(△), 0.075 mM(▽), 0.10 mM(◈), 0.15 mM(⋇), 0.25 mM(▷), 0.50 mM(⬡), 0.75 mM(★), 1 mM(◑), 1.5 mM(●).

(b) Plots of the Gibbs surface excess of Br^- in the presence of OTA^+ at the Au(111)/solution interface versus electrode potential for the following bulk Br^- concentrations: 0.01 mM (■), 0.025 mM (○), 0.050 mM(△), 0.10 mM(▽), 0.20 mM(◈), 0.35 mM(⋇), 0.50 mM(▷), 0.75 mM(⬡), 1.00 mM(★), 1.5 mM(◑).

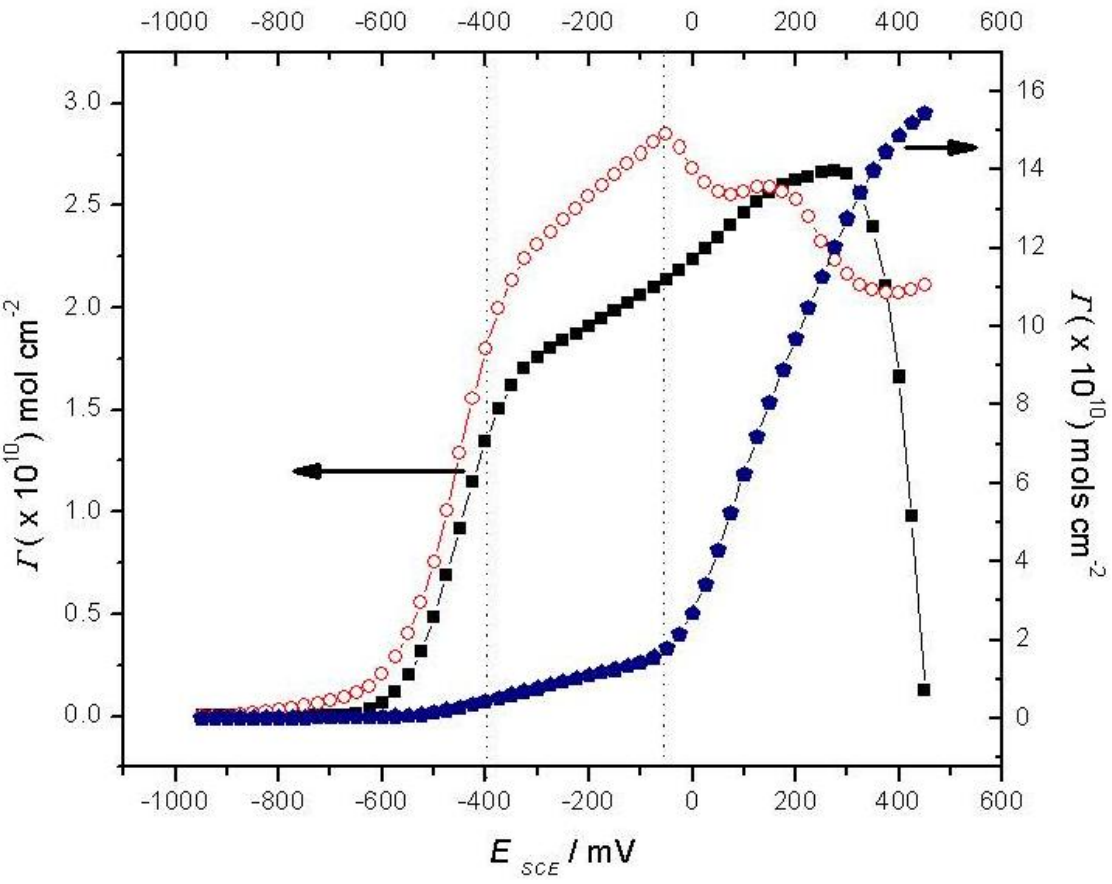

Fig. 7.8
Gibbs surface excess vs electrode potential plots for bulk concentrations of 1 mM OTA (■), 1 mM Br- in the presence of OTA^+(⬟) and 1 mM OTA+ in the presence of bromide (○) at the Au (111)/0.1 M NaF electrolyte interface.

presence of OTA^+ could be caused by the additional bromide anions carried by adsorbed cationic OTA^+ ions. Most importantly, it implies that OTA^+ ions do not competitively replace Br^- ions on the Au(111) surface. For a clearer picture of the influence of bromide on the adsorption behaviour of the cationic surfactant on Au(111), the Gibbs excess curve for OTA-Tf in pure supporting electrolyte (from the previous chapter) can be compared with the Gibbs excess of OTA^+ in the presence of bromide. Figure 7.8 shows the Gibbs excess versus potential curves for 1 mM OTA^+-only, 1 mM OTA^+ in the presence of 1

mM Br^- and 1 mM Br^- in the presence of 1 mM OTA^+. It can be inferred that in the presence of bromide ions, there is more OTA^+ adsorbed at potentials where relatively low levels of bromide are co-adsorbed on the electrode surface. After the lifting of reconstruction (E > -50 mV) the Gibbs excess curve of OTA^+ in the presence of bromide shows two plateau regions at positive potentials. The plateau regions with lower Gibbs excesses for OTA^+ in the presence of Br^- suggests a stable but less compact layer of OTA^+ at those potentials. These plateau regions can also be noticed qualitatively in the differential capacity curve shown in Figure 7.2. It should be noted that even though there is a decrease in the Gibbs excess of OTA^+ after lifting of the reconstruction due to bromide adsorption, it is still relatively high ($\Gamma \sim 2 \times 10^{-10}$ mols cm^{-2}), whereas in the absence of bromide, the surfactant tends towards complete desorption at the most positive potentials ($\Gamma \sim 0$ mols cm^{-2}). At potentials where OTA-triflate zwitterions form hemicylindrical aggregate in the absence of bromide ions (-400 mV < E < -100 mV), there is an approximately 25% increase in surface coverage in the presence of bromide ions. Numerically, such an increase is consistent with a transition from hemicylindrical aggregates to a monolayer film of vertical surfactants. While an unambiguous statement cannot be made about the structure of surfactant from surface excess plots alone, a more compact structure of the surfactant in the presence of bromide is evident in these regions of potentials. Presumably when bromide anions are present at the interface, the cationic head group of the OTA^+ can orient towards the bromide adlayer hence favoring the formation of a perpendicular layer of surfactant species.

A comparison of the surfactant adsorption with reference to an applied potential is often inconvenient as it is, of course, determined by the choice of reference electrode.

For instance, at the same applied potential, surface charge (or surface potential) of electrodes having different crystallographic orientations will be different. Parsons has advocated the use of electrode charge as the preferred electrical variable,[34] although this remains a somewhat contentious issue. Irrespective of these arguments, the Gibbs excess data determined in this study can be readily transformed and plotted against the metal charge density. The data is plotted against charge density because it is plausible that metal charge density rather than potential might be a more accessible evaluation of the electrical state of colloids. Gibbs excess plots for (a) OTA^+ in the presence of 1 mM bromide and (b) bromide in the presence of 1 mM OTA^+ are plotted against the metal charge density in Figure 7.9. Gibbs excess plots for OTA^+ in the presence of bromide shows maximum adsorption of surfactant at -10 $\mu C\ cm^{-2}$ (Figure 7.9a) but there is a significant amount of OTA^+ adsorbed even at positive surface charge densities where there is also a significant amount of bromide adsorbed (Figure 7.9b). Figure 7.9b also clearly demonstrates that bromide ions adsorb on the Au(111) surface from -30 $\mu C\ cm^{-2}$ to more positive charge densities. A comparison of the Gibbs excess of OTA^+ as a function of metal charge density with and without bromide in the electrolyte is shown in Figure 7.10. In the presence of bromide, there is a noticeable increase in the Gibbs excess of OTA^+ from charge densities where bromide starts to adsorb on the

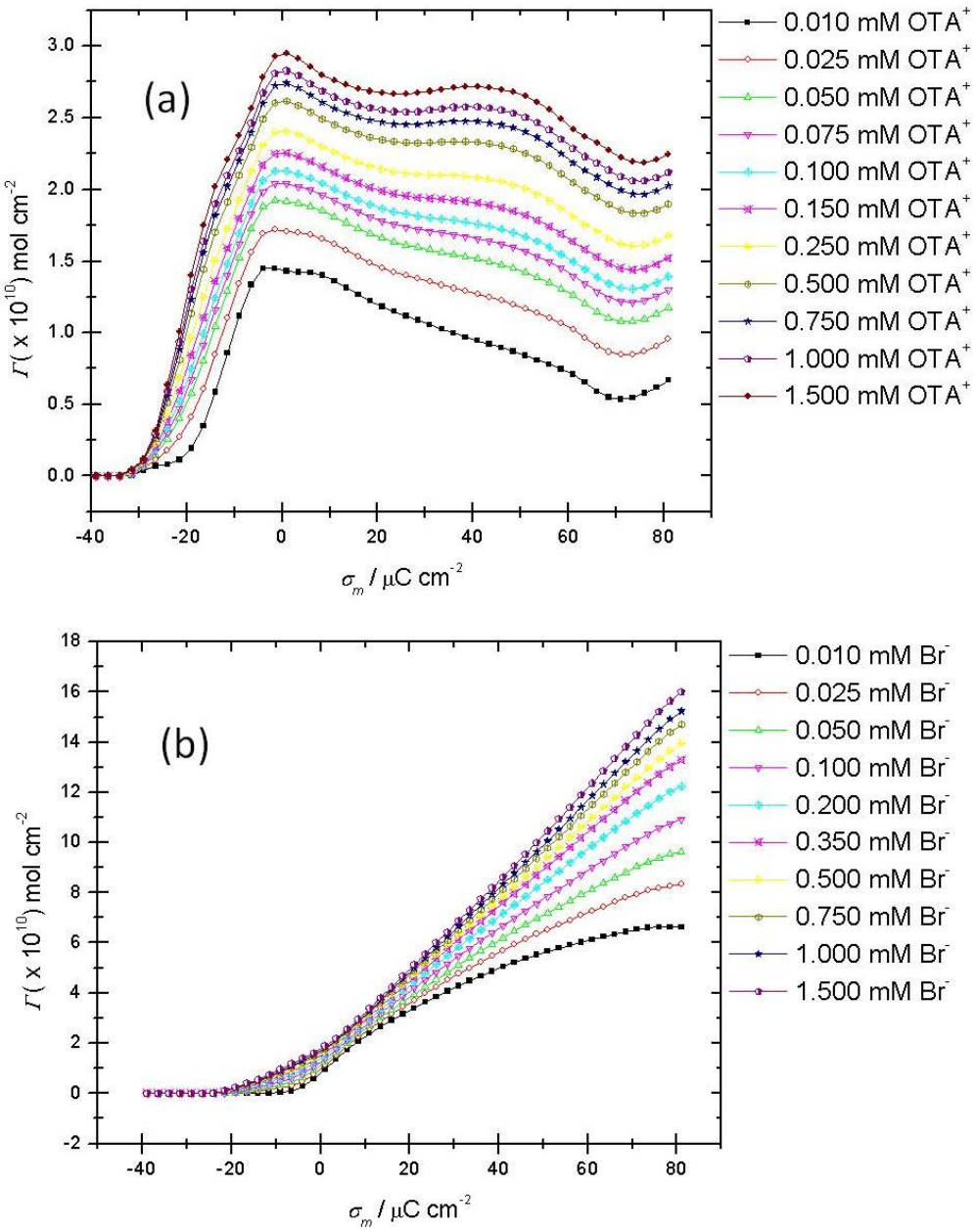

Fig. 7.9

(a) Plots of the Gibbs surface excess of OTA^+ in the presence of 1 mM NaBr bulk concentration at the Au(111)/solution interface versus metal charge density for the following bulk OTA^+ concentrations: 0.01 mM (■), 0.025 mM (○), 0.050 mM(△), 0.075 mM(▽), 0.10 mM(◈), 0.15 mM(⊠), 0.25 mM(▷), 0.50 mM(◐), 0.75 mM(★), 1 mM(◑), 1.5 mM(●).

(b) Plots of the Gibbs surface excess of Br^- in the presence of OTA^+ at the Au(111)/solution interface versus metal charge density for the following bulk Br^- concentrations: 0.01 mM (■), 0.025 mM (○), 0.050 mM(△), 0.10 mM(▽), 0.20 mM(◈), 0.35 mM(⊠), 0.50 mM(▷), 0.75 mM(◐), 1.00 mM(★), 1.5 mM(◑).

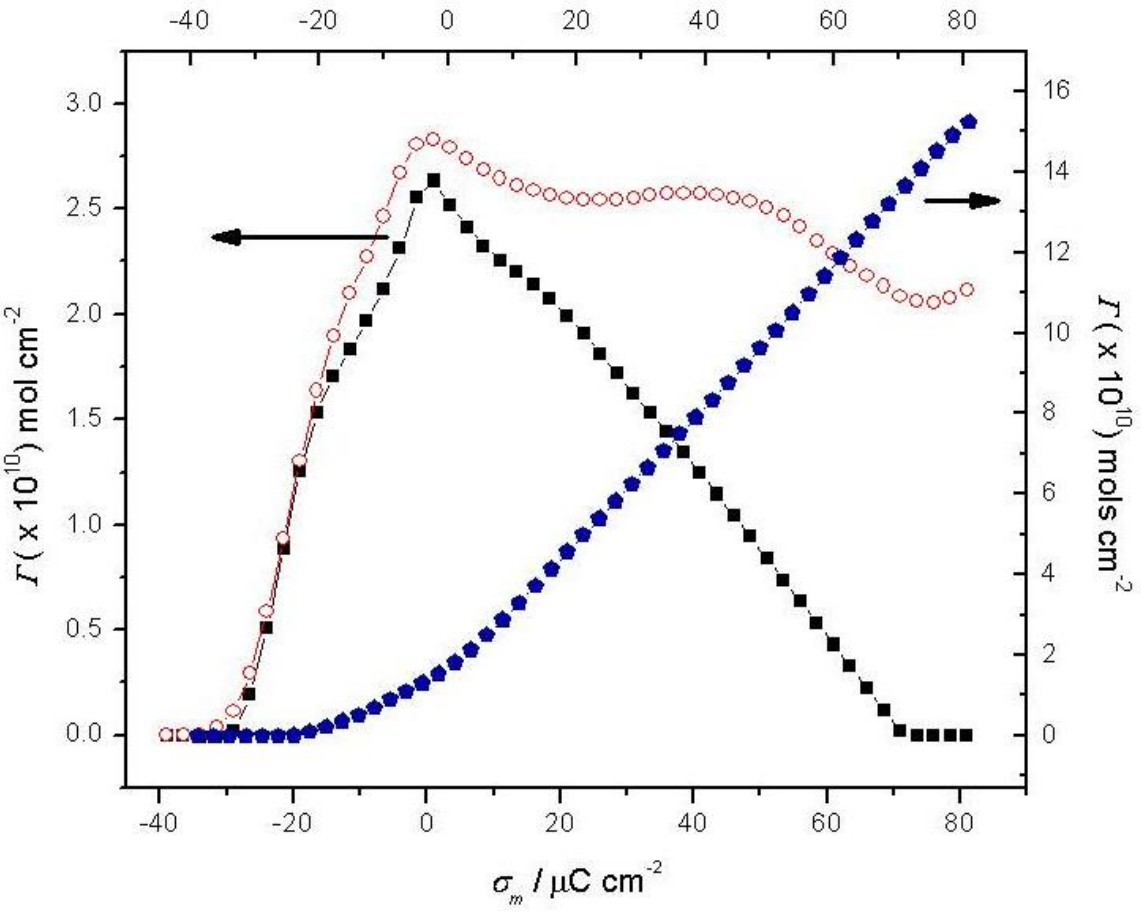

Fig. 7.10

Gibbs surface excess vs electrode potential plots for bulk concentrations of 1 mM OTA (■), 1 mM Br- in the presence of OTA+(⬟) and 1 mM OTA+ in the presence of bromide (○) at the Au (111)/0.1 M NaF electrolyte interface.

surface. Higher Gibbs excess values in this region show that the surfactant coverage corresponds to more than that of hemicylindrical aggregates (presumably a vertical layer), which could be due to the interaction of the cationic headgroup with the bromide adlayer. More importantly, the presence of bromide ions increases the level of OTA^+ adsorption at highly positively charged surfaces. In the absence of bromide, OTA^+ desorbs from the surface at the most positive polarizations while in the presence of

bromide there is still a significant amount of OTA^+ ($\Gamma \sim 2.2x10^{-10}$ mols cm^{-2}) on the surface even though the metal's surface charge exceeds +60 μC cm^{-2}.

7.4 Adsorption of OTA^+Br^- on Au(100)

In Chapter 5, it was demonstrated that there is little difference in the surface concentration of OTA-Tf between reconstructed and unreconstructed surfaces of Au(100), on a rational potential scale. It appears that there is no significant difference in the surface concentration of OTA-Tf between Au(111) and Au(100) surfaces, for the reason that reconstructed Au(100) surface is nearly identical to the unreconstructed Au(111) surface. However, bromide adsorption on Au(100) is significantly different from Au(111). Figure 7.11 shows a qualitative comparison using cyclic voltammetry. Here it appears that the adsorption and phase transitions of bromide on both crystals are significantly different. Adsorption of bromide on Au(111) and Au(100) were studied in depth by various groups[2,3] and a detailed analysis of bromide adsorption on these crystals has been previously reported. However, it is unclear how significant co-adsorption affects will be for the OTA^+/Br^- system for these low index crystallographic surfaces. Having already discussed the adsorption behaviour OTA^+/Br^- on Au(111) in the previous sections of this chapter, the adsorption behaviour of OTA^+/Br^- on Au(100) will be discussed in the following section which will allow for quantitative evaluation of the relative adsorption on these two surfaces.

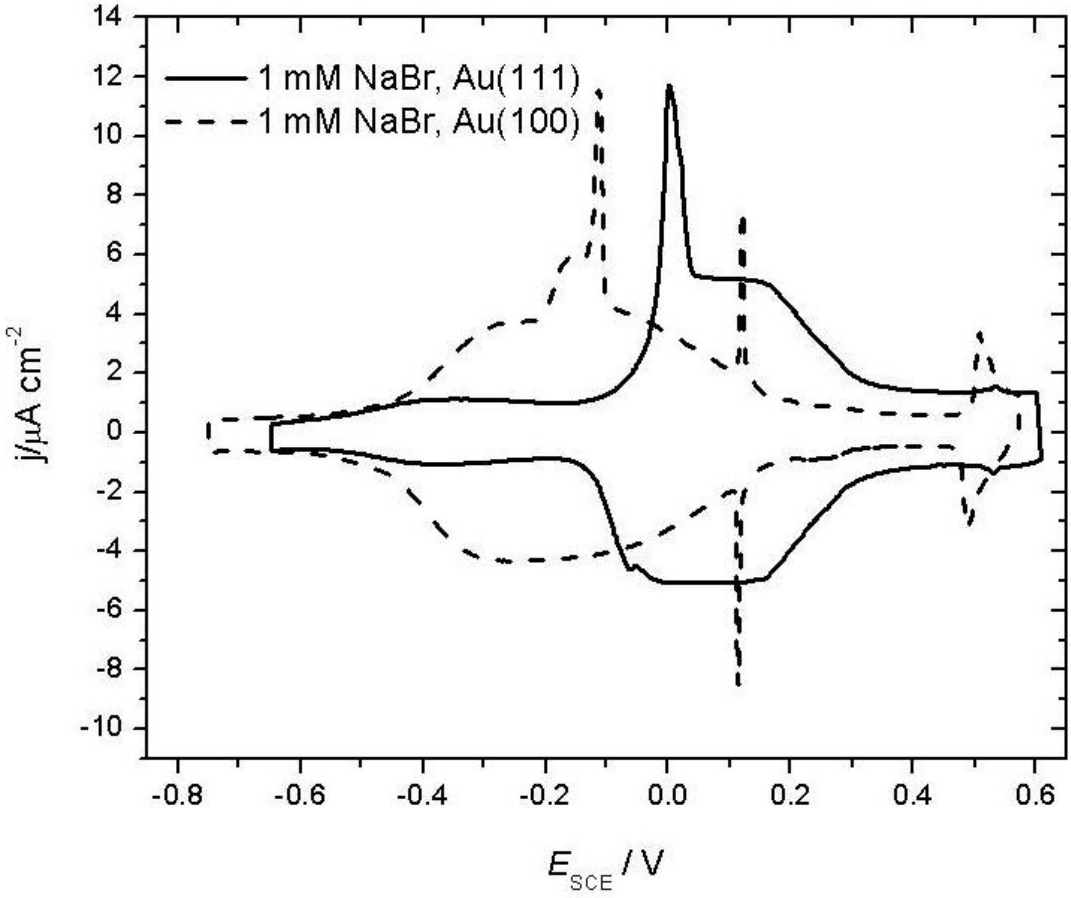

Fig. 7.11

Cyclic voltammograms of 1 mM Br^- at Au(111)/0.1 M NaF interface (solid line) and Au(100)/0.1 M NaF interface (dashed line).

Treatment of the Au(100) crystal prior to the electrochemical measurements to reduce reconstruction effects discussed in Chapter 5 has been repeated here again. Furthermore the adsorption of bromide lifts the surface reconstruction and hence the errors due to reconstruction are minimal in the presence of bromide ions. A modified chronocoulometry step sequence that further reduces the risk of reconstruction effects was used for these measurements (details provided in Chapter 5). For this work the Au electrode was held at a base potential, E_{base}= +150 mV, for 30 s. Then the potential was

stepped to a variable value of interest, E_C (E_{C1}=+450 mV), and held for about 180 s to achieve adsorption equilibrium. To desorb OTA^+/Br^- from the electrode surface, a negative potential, E_{des} (-1000 mV) was applied for 200 ms and the current transient corresponding to desorption was measured. The potential was then stepped back to the base value and the cycle was repeated using a new value of E_C ($E_{C2} = E_{C1}$ -25 mV). The electrolyte solution was stirred when the electrode potential was at E_C and E_{base}, but the stirring was stopped 10 s before applying desorption potential, E_{des}.

7.4.1 Cyclic voltammetry

The experimental strategy to extract quantitative information is the same as that adopted in the previous studies for Au(111)-OTA^+/Br^- system. In series A chronocoulometry experiments, a variable OTA^+ concentration and a constant bromide (1 mM) concentration were used whereas in series B the bromide concentration was varied while retaining a constant OTA^+ concentration (1 mM). Preliminary analyses were done using cyclic voltammetry and differential capacity. Cyclic voltammograms in Figure 7.12 show the adsorption behavior of OTA^+ in the presence of 1 mM bromide for the (100) crystal. It should be noted that the voltammograms presented here are not the true representation of bromide adsorption on an unreconstructed Au(100) surface as minor amounts of reconstruction may happen as the electrode was cycled through negative potentials. Though precautions have been taken to reduce reconstruction effects, scanning to negative potentials can cause limited surface reconstruction to occur during the measurement and hence the peak corresponding to lifting of reconstruction can be seen in the cyclic voltammograms at E ~ -150 mV. In accordance with the previous discussion on Au(111), an increase in OTA^+ bulk concentration causes the shift in adsorption peaks

to further negative potentials even in the presence of bromide. The sharp peak P1 corresponding to the lifting of reconstruction followed by the formation of two dimensional adlayer of bromide is diminished and shifted to more positive potentials (ΔE ~ 25 mV in the presence of 1 mM OTA^+) with an increase in OTA^+ concentration. A second sharp peak, P2 that corresponds to commensurate bromide layer formation is shifted significantly to more positive potentials (~ +75 mV shift with the addition of 1 mM OTA^+). After the addition of the cationic surfactant, a broad plateau region is developed between peaks P1 and P2, suggesting the formation of a condensed layer of adsorbate in that region. Cyclic voltammograms corresponding to variable bromide bulk concentrations in the presence of 1 mM OTA^+ bulk concentration are shown in the inset of Figure 7.12. Here it is shown that the OTA^+ adsorption peak does not shift with increased bromide concentration in the bulk, but the bromide adlayer formation and phase transition peak shifts to further negative potentials with increasing bromide concentration.

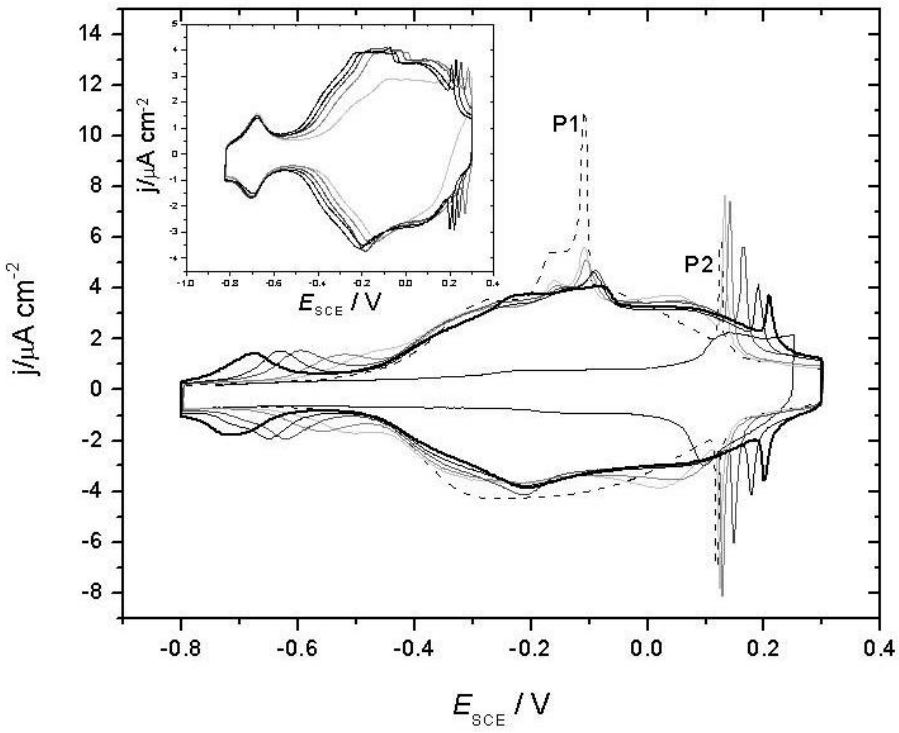

Fig. 7.12

Cyclic voltammograms of 1 mM Br^- (dotted line) and 1 mM Br^- with variable concentrations of OTA^+ from 0.025 mM (light gray line) to 1.5 mM (bold black line) at Au(100)/0.1 M NaF interface.

7.4.2 Chronocoulometry

In Figure 7.13a, the charge curves for series A chronocoulometry experiments are shown. The curve corresponding to 1 mM Br^- (i.e. in the absence of surfactant) indicates significant adsorption of bromide on the surface at potentials more positive of -500 mV. The charge curves for variable OTA^+ concentrations show that the surfactant starts adsorbing at potentials more negative to the onset of bromide adsorption on the Au(100) surface. At 1 mM bulk concentration, the surfactant starts adsorbing at -800 mV. The general qualitative trend of this charge curve is very similar to that observed for the same set of measurements on Au(111). Charge curves for series B measurements shown in Figure 7.13b indicate significant bromide adsorption at potentials positive to -400 mV.

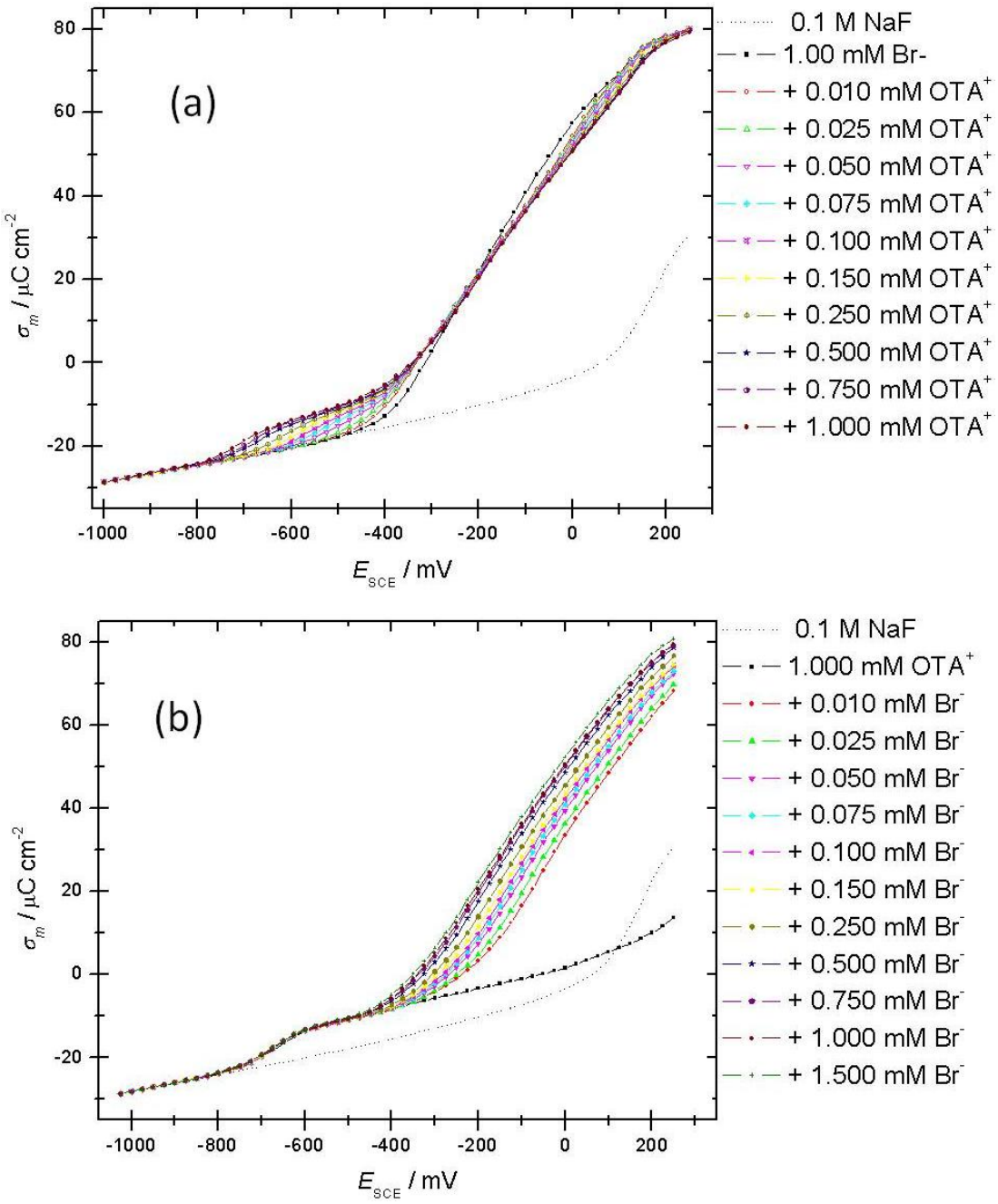

Fig. 7.13

(a) Charge density versus electrode potential curves for Au(100) in 0.1 M NaF supporting electrolyte (----), 1 mM NaBr (■) and following OTA^+ concentrations: 0.01 mM (○), 0.025 mM (△), 0.05 mM(▽), 0.075 mM(◈), 0.10 mM(⊠), 0.15 mM(▷), 0.25 mM(◫), 0.5 mM(★), 0.75 mM(◗), 1 mM(●).

(b) Charge density versus electrode potential curves for Au(100) in 0.1 M NaF supporting electrolyte (----), 1 mM OTA^+ (■) and following Br^- concentrations: 0.01 mM (○), 0.025 mM (△), 0.05 mM(▽), 0.075 mM(◈), 0.10 mM(⊠), 0.15 mM(▷), 0.25 mM(◫), 0.5 mM(★), 0.75 mM(◗), 1 mM(●), 1.5 mM(+).

7.4.3 Gibbs surface excesses for OTA+Br- on Au(100)

The charge density data was analyzed as described above for the Au(111) crystal. The Gibbs surface excess of OTA^+ in the presence of 1 mM Br^- on Au(100) determined from the charge curves in Figure 7.13a is plotted in Figure 7.14a. The maximum Gibbs excess is obtained at ~ -350 mV and a quasi-plateau region with slightly lower Gibbs excess can be observed at ~-100 mV, which presumably indicates a different adsorption state. After +50 mV, the surface excess further drops to another quasi-plateau region. The surface excess of bromide in the presence of OTA^+ is determined from the charge curve in Figure 7.13b and is plotted in Figure 7.14b. From the plot it is clear that there is predominant adsorption of bromide on the surface at potentials more positive than -400 mV. As before, the Gibbs excess of OTA^+ as a function of metal charge density has also been evaluated and is plotted in Figures 7.15a and 7.15b. It can be seen that the maximum adsorption of OTA^+ is achieved when the surface is weakly or nearly non-polarized and there is a minimal amount of bromide adsorbed on the surface. Both OTA^+ and Br^- are adsorbed on the surface at positive charge densities, but there is a significant drop in the surface concentration of OTA^+ at positive charge densities even in the presence of bromide.

The Gibbs surface excess of OTA^+ and Br^- on the surface due to adsorption from a solution containing a 1:1 mixture of 1 mM OTA^+/Br^- is plotted against metal charge density in Figure 7.16 for comparison purposes. It can be observed that the maximum amount of surfactant is adsorbed at potentials where bromide just begins to adsorb on the surface. The surfactant surface excess is relatively low at more positive potentials, where an ordered layer of bromide is adsorbed on the surface.

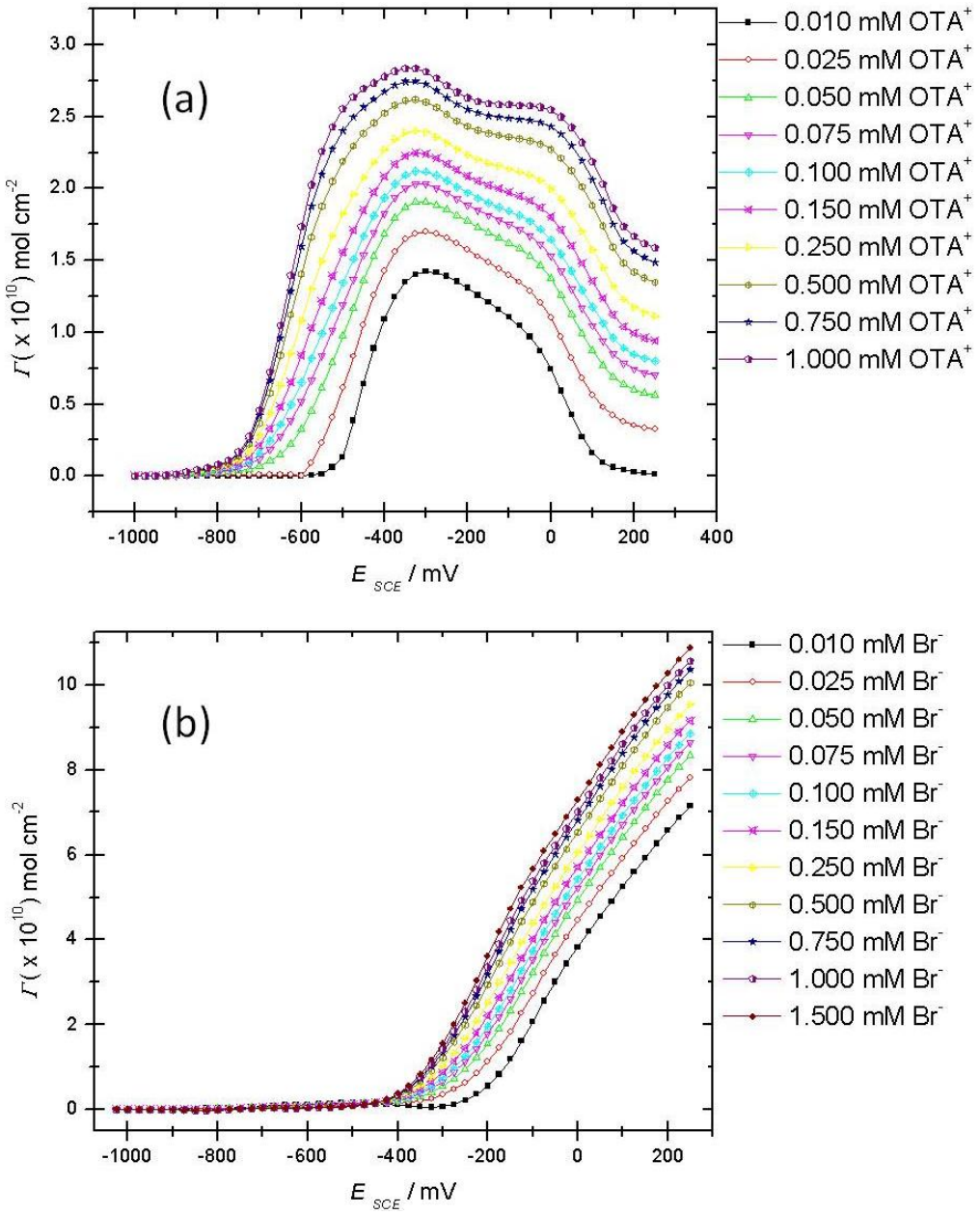

Fig. 7.14

(a) Plots of the Gibbs surface excess of OTA^+ in the presence of 1 mM NaBr bulk concentration at the Au(100)/solution interface versus electrode potential for the following bulk OTA^+ concentrations: 0.01 mM (■), 0.025 mM (○), 0.050 mM(△), 0.075 mM(▽), 0.10 mM(◈), 0.15 mM(⊠), 0.25 mM(▷), 0.50 mM(⬡), 0.75 mM(★), 1 mM(◗).

(b) Gibbs surface excess plots of Br^- in the presence of OTA^+ at the Au(100)/solution interface versus electrode potential for the following bulk Br^- concentrations: 0.01 mM (■), 0.025 mM (○), 0.050 mM(△), 0.075 mM(▽), 0.10 mM(◈), 0.15 mM(⊠), 0.25 mM(▷), 0.50 mM(⬡), 0.75 mM(★), 1 mM(◗), 1.5 mM (●).

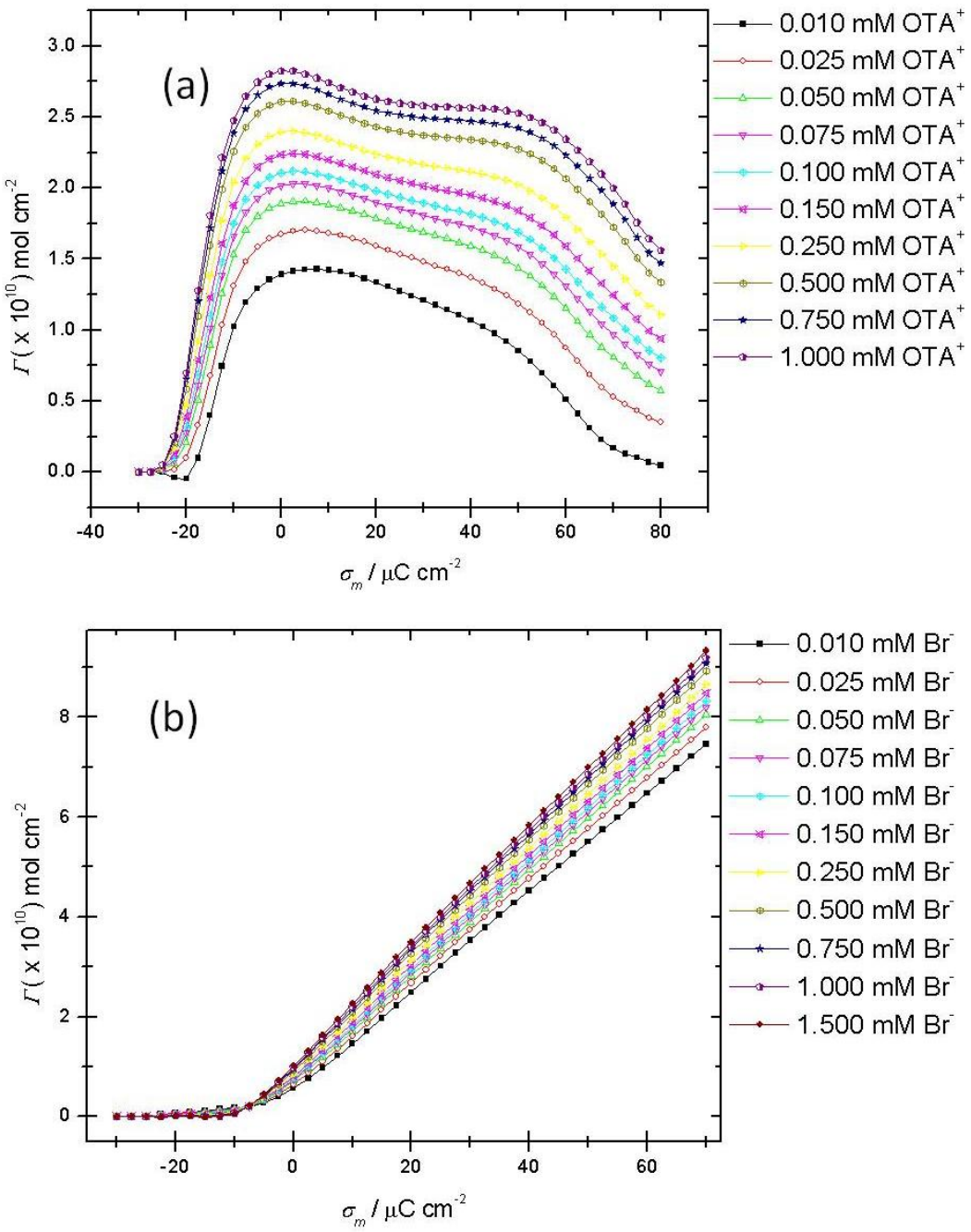

Fig. 7.15

(a) Gibbs surface excess plots of OTA^+ in the presence of 1 mM NaBr bulk concentration at the Au(100)/solution interface versus metal charge density for the following bulk OTA^+ concentrations: 0.01 mM (■), 0.025 mM (○), 0.050 mM(△), 0.075 mM(▽), 0.10 mM(◈), 0.15 mM(⊠), 0.25 mM(▷), 0.50 mM(⬡), 0.75 mM(★), 1 mM(◑).
(b) Gibbs surface excess plots of Br^- in the presence of OTA^+ at the Au(100)/solution interface versus metal charge density for the following bulk Br^- concentrations: 0.01 mM (■), 0.025 mM (○), 0.050 mM(△), 0.075 mM(▽), 0.10 mM(◈), 0.15 mM(⊠), 0.25 mM(▷), 0.50 mM(⬡), 0.75 mM(★), 1 mM(◑), 1.5 mM (●).

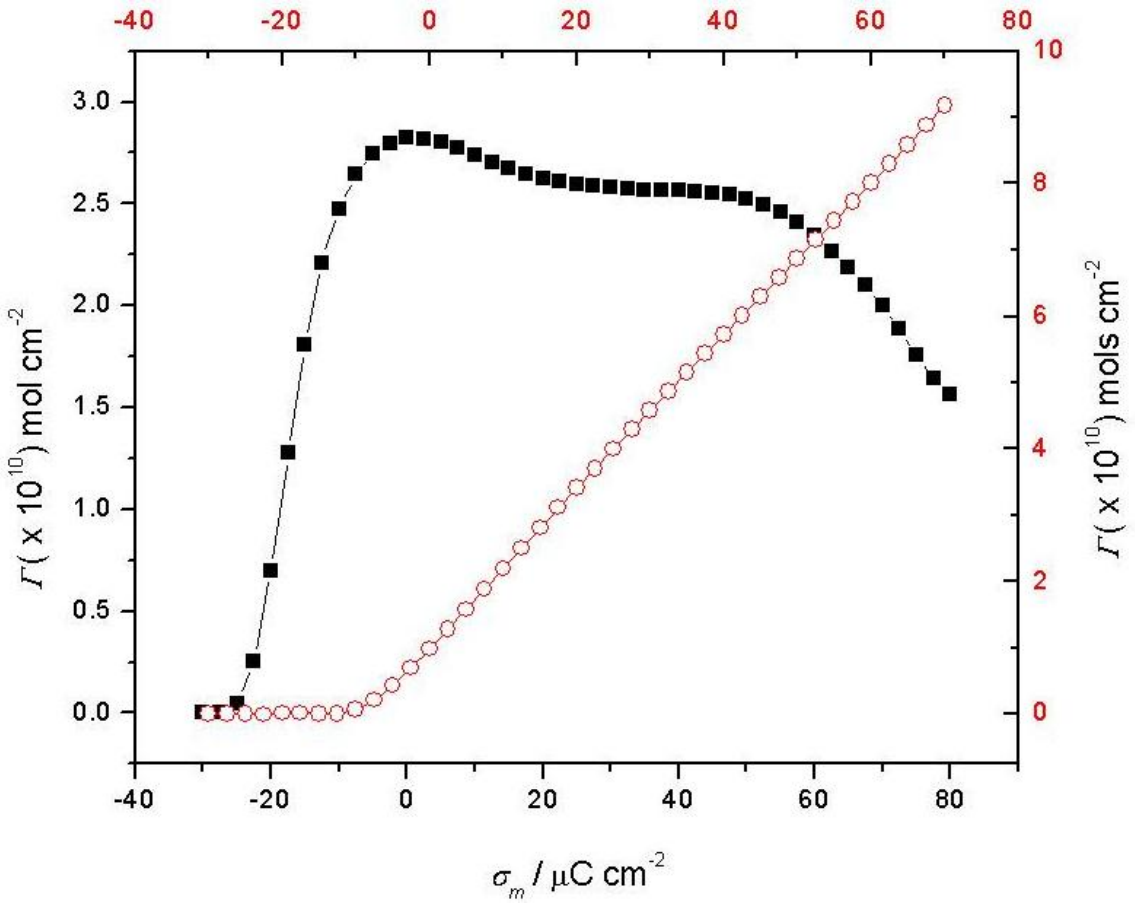

Fig. 7.16

Gibbs surface excess vs metal charge density plots of OTA^+ (■)and Br^- (⊙) corresponding to 1 mM bulk concentrations of OTA^+/Br^-.

7.5 Gibbs surface excesses of OTA+/Br- on Au(111) and Au(100)

Having the surface concentration data for OTA^+/Br^- on both Au(111) and Au(100) surfaces, it is possible to evaluate the influence of crystallography on the magnitude of surfactant adsorption. Since the potential of zero charge of the two crystals is significantly different, this has to be taken into account when comparing Gibbs excess as a function of potentials on these two crystals. The Gibbs surface excess for 1 mM

OTA^+/Br^- bulk concentration is plotted on a rational potential scale (E-E_{pzc}) in Figure 7.17a. Surprisingly, the data suggests that within the experimental error (the estimated error in surface excess using the chronocoulometry back integration technique is 10%)[35], there is no significant difference in the adsorption behavior of OTA^+/Br^- on the two crystals. At positively charged surfaces there is more bromide adsorbed on the Au(111) surface compared to the Au(100) surface in the presence of OTA^+ (Figure 7.17a, inset). However, this is not unexpected as Wandlowski and coworkers have shown that even in the absence of any other specifically adsorbing species, the surface concentration of bromide is higher on Au(111) compared to Au(100).[36] The Gibbs surface excess of OTA^+/Br^- corresponding to 1 mM bulk concentration is plotted against metal charge density in Figure 7.17b, which shows that the surfactant starts adsorbing at slightly more negative potentials on Au(111), and the Gibbs excess of bromide adsorbed on Au(111) is higher than that on Au(100) surface (Figure 7.17b, inset) at constant metal charge density.

Based on this quantitative analysis of OTA^+/Br^- on Au(111) and Au(100) faces, no preferential adsorption of the quaternary ammonium surfactant on Au(100) over Au(111) for the range of potentials (or charges) examined is observed. It has to be noted that if a comparison was made without taking the difference in pzc into consideration, it

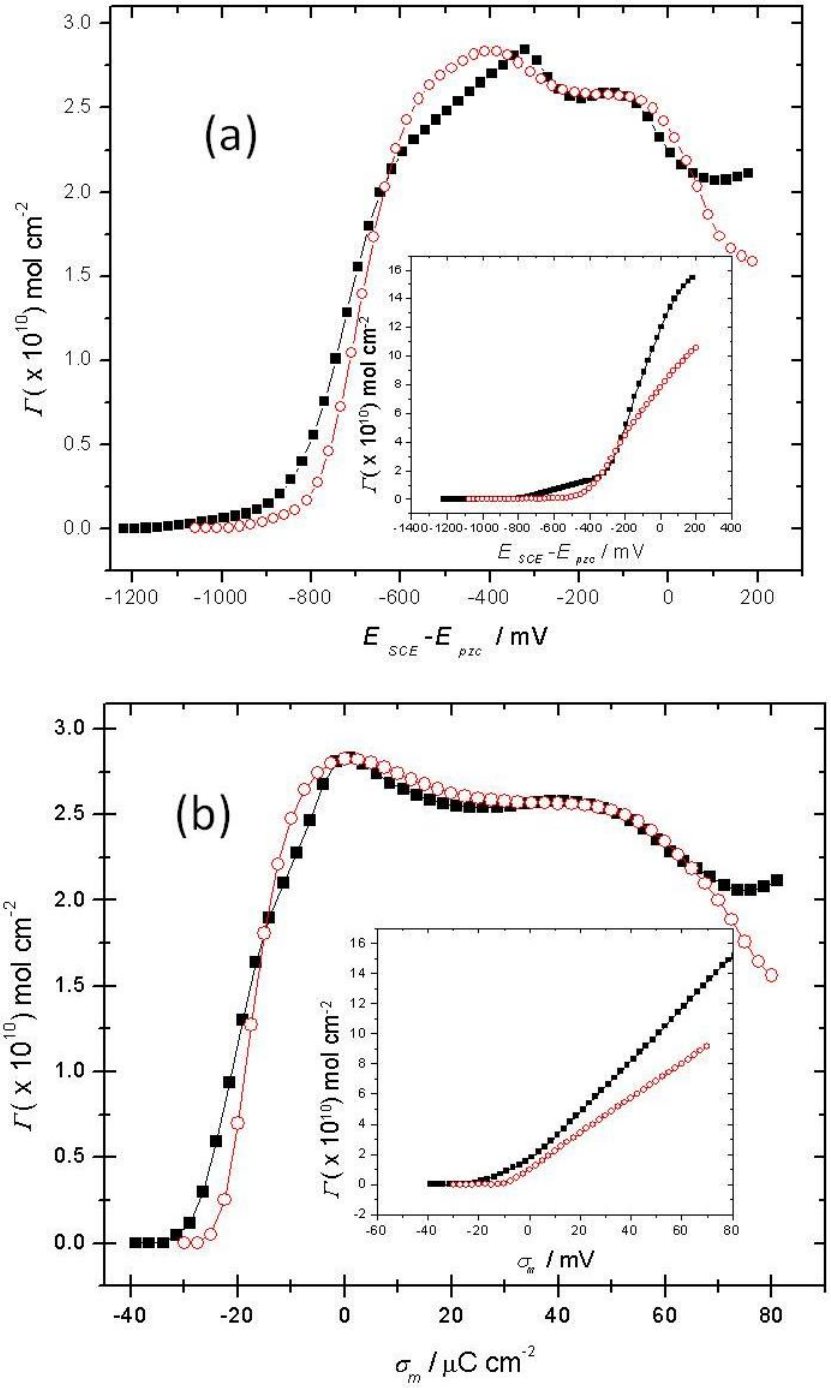

Fig. 7.17

(a) Gibbs surface excess vs electrode potential plots of OTA^+ (and Br^- in the inset) at Au(111) (■) and Au(100) (○) interfaces corresponding to 1 mM bulk concentrations of OTA^+/Br^-.

(b) Gibbs surface excess vs metal charge density plots of OTA^+ (and Br- in the inset) at Au(111) (■) and Au(100) (○) interface corresponding to 1 mM bulk concentrations of OTA^+/Br^-.

may appear that there is a higher surface concentration of the surfactant on Au(100) at negative potentials (-600 mV > *E* > -400 mV), in comparison to Au(111). Comparison of the Gibbs excess *versus* metal charge density plot also shows no significant difference in the adsorption behavior of the surfactant on both crystals. Also, the analysis of bromide adsorption in the presence of a quaternary ammonium surfactant shows that the surface concentration of bromide is larger on Au(111) compared to Au(100). This is not very surprising as electrosorption studies of bromide on Au(111) and Au(100) surfaces reported in the literature also show similar results.[36] As noted earlier, if the comparison was not made on a rational potential scale, it would again (erroneously) suggest a preferential adsorption of bromide on Au(100) at negative potentials.

Based on these results, it appears that even in the presence of bromide ions, quaternary ammonium surfactants show no significant preferential adsorption on Au(100) surfaces. The popular postulate for nanorod growth based on the preferential adsorption of bromide on Au(100) facet over Au(111) seems unlikely. The anisotropic growth of gold nanorod must be following a more complex mechanism. Other species present in the medium (gold salt, ascorbic acid, etc.) may have a significant role in determining the anisotropy. For instance the cationic surfactant might form complexes with ascorbic acid and/or gold salt, which may have dramatic preferential adsorption on different faces of the seed crystal. The results in this chapter suggests that a mechanism based on "pristine" quaternary ammonium bromide adsorption on different facets of gold seed crystal is highly unlikely, further investigation with more sophisticated techniques is necessary to determine the actual growth mechanism of gold nanorods.

7.6 Summary and Conclusions

In the first part of this chapter, the effect of bromide on the surface concentration of a quaternary ammonium surfactant on gold surfaces has been studied. It has been demonstrated that the surface coverage of OTA^+ increases in the presence of adsorbed bromide. The surface concentration of OTA^+ and Br^- on Au(111) and Au(100) were obtained using chronocoulometry studies, for a range of concentrations from 0.01 mM to 1 mM. The surface concentration of OTA^+/Br^- on Au(111) and Au(100) surfaces were provided as a function of metal charge densities, as well as on a rational potential scale. A comparison of the surface concentration plots indicate that even in the presence of bromide there is no significant difference between the adsorption of OTA^+ on Au(111) and Au(100) crystal faces. There is moderately higher bromide coverage on Au(111) compared to Au(100) in the presence of OTA^+. These results show that the current popular perception of gold nanorod growth, based on the preferential adsorption of quaternary ammonium bromide on Au(100) over Au(111) is highly unlikely.

Reference List

1. Brosseau, C. L.; Sheepwash, E.; Burgess, I. J.; Cholewa, E.; Roscoe, S. G.; Lipkowski, J. Adsorption of N-Decyl-N,N,N-trimethylammonium Triflate (DeTATf), a Cationic Surfactant, on the Au(111) Electrode Surface. *Langmuir* **2006,** *23* (4), 1784-1791.

2. Shi, Z.; Lipkowski, J.; Mirwald, S.; Pettinger, B. Electrochemical and second harmonic generation study of bromide adsorption at the Au(111) electrode surface. *Journal of Chemical Society , Faraday Trans.* **1996,** *92* (20), 3737-3746.

3. Wandlowski, T.; Wang, J. X.; Magnussen, O. M.; Ocko, B. M. Structural and Kinetic Aspects of Bromide Adsorption on Au(100). *The Journal of Physical Chemistry* **1996,** *100* (24), 10277-10287.

4. Magnussen, O. M. Ordered Anion Adlayers on Metal Electrode Surfaces. *Chemical Reviews* **2002,** *102* (3), 679-726.

5. Jaschke, M.; Butt, H. J.; Gaub, H. E.; Manne, S. Surfactant Aggregates at a Metal Surface. *Langmuir* **1997,** *13* (6), 1381-1384.

6. Uskokovic, V.; Drofenik, M. Synthesis of materials within reverse micelles. *Surface Review & Letters* **2005,** *12* (2), 239-277.

7. Sau, T. K.; Murphy, C. J. Seeded High Yield Synthesis of Short Au Nanorods in Aqueous Solution. *Langmuir* **2004,** *20* (15), 6414-6420.

8. Jana, N. R.; Gearheart, L.; Murphy, C. J. Wet Chemical Synthesis of High Aspect Ratio Cylindrical Gold Nanorods. *The Journal of Physical Chemistry B* **2001,** *105* (19), 4065-4067.

9. Jana, N. R.; Gearheart, L.; Murphy, C. J. Wet chemical synthesis of silver nanorods and nanowires of controllable aspect ratio. *Chemical Communications* **2001,** (7), 617-618.

10. Busbee, B. D.; Obare, S. O.; Murphy, C. J. An Improved Synthesis of High-Aspect-Ratio Gold Nanorods. *Advanced Materials* **2003,** *15* (5), 414-416.

11. Yu; Chang, S. S.; Lee, C. L.; Wang, C. R. C. Gold Nanorods:GÇë Electrochemical Synthesis and Optical Properties. *The Journal of Physical Chemistry B* **1997,** *101* (34), 6661-6664.

12. Wu, H. Y.; Huang, W. L.; Huang, M. H. Direct High-Yield Synthesis of High Aspect Ratio Gold Nanorods. *Crystal Growth & Design* **2007,** *7* (4), 831-835.

13. Murphy, C. J.; Sau, T. K.; Gole, A. M.; Orendorff, C. J.; Gao, J.; Gou, L.; Hunyadi, S. E.; Li, T. Anisotropic Metal Nanoparticles: Synthesis, Assembly, and Optical Applications. *The Journal of Physical Chemistry B* **2005,** *109* (29), 13857-13870.

14. Zhi-Chuan Xu et al Wet chemical synthesis of gold nanoparticles using silver seeds: a shape control from nanorods to hollow spherical nanoparticles. *Nanotechnology* **2007,** *18* (11), 115608.

15. Park, W. M.; Huh, Y. S.; Hong, W. H. Aspect-ratio-controlled synthesis of high-aspect-ratio gold nanorods in high-yield. *Current Applied Physics* **2009,** *9* (2, Supplement 1), e140-e143.

16. Gao, J.; Bender, C. M.; Murphy, C. J. Dependence of the Gold Nanorod Aspect Ratio on the Nature of the Directing Surfactant in Aqueous Solution. *Langmuir* **2003,** *19* (21), 9065-9070.

17. Smith, D. K.; Korgel, B. A. The Importance of the CTAB Surfactant on the Colloidal Seed-Mediated Synthesis of Gold Nanorods. *Langmuir* **2008,** *24* (3), 644-649.

18. Kawasaki, H.; Nishimura, K.; Arakawa, R. Influence of the Counterions of Cetyltrimetylammonium Salts on the Surfactant Adsorption onto Gold Surfaces and the Formation of Gold Nanoparticles. *The Journal of Physical Chemistry C* **2007,** *111* (6), 2683-2690.

19. Filankembo, A.; Giorgio, S.; Lisiecki, I.; Pileni, M. P. Is the Anion the Major Parameter in the Shape Control of Nanocrystals. *The Journal of Physical Chemistry B* **2003,** *107* (30), 7492-7500.

20. Sau, T. K.; Murphy, C. J. Role of ions in the colloidal synthesis of gold nanowires. *Philosophical Magazine* **2007,** *87* (14), 2143-2158.

21. Lofton, C.; Sigmund, W. Mechanisms Controlling Crystal Habits of Gold and Silver Colloids. *Advanced Functiona Materials* **2005,** *15* (7), 1197-1208.

22. Link, S.; El-Sayed, M. A. Optical properties and ultrafast dynamics of metallic nanocrystals. *Annual Review of Physical Chemistry* **2003,** *54* (1), 331-366.

23. Nikoobakht, B.; El-Sayed, M. A. Preparation and Growth Mechanism of Gold Nanorods (NRs) Using Seed-Mediated Growth Method. *Chemistry of Materials* **2003,** *15* (10), 1957-1962.

24. Wei, Z.; Zamborini, F. P. Directly Monitoring the Growth of Gold Nanoparticle Seeds into Gold Nanorods. *Langmuir* **2004,** *20* (26), 11301-11304.

25. Johnson, C. J.; Dujardin, E.; Davis, S. A.; Murphy, C. J.; Mann, S. Growth and form of gold nanorods prepared by seed-mediated, surfactant-directed synthesis. *Journal of Materials Chemistry* **2002,** *12* (6), 1765-1770.

26. Garg, N.; Scholl, C.; Mohanty, A.; Jin, R. The Role of Bromide Ions in Seeding Growth of Au Nanorods. *Langmuir* **2010,** *26* (12), 10271-10276.

27. Lu, X.; Rycenga, M.; Skrabalak, S. E.; Wiley, B.; Xia, Y. Chemical Synthesis of Novel Plasmonic Nanoparticles. *Annual Review of Physical Chemistry* **2009,** *60* (1), 167-192.

28. Ha, T. H.; Koo, H. J.; Chung, B. H. Shape-Controlled Syntheses of Gold Nanoprisms and Nanorods Influenced by Specific Adsorption of Halide Ions. *The Journal of Physical Chemistry C* **2006,** *111* (3), 1123-1130.

29. Orendorff, C. J.; Murphy, C. J. Quantitation of Metal Content in the Silver-Assisted Growth of Gold Nanorods. *The Journal of Physical Chemistry B* **2006,** *110* (9), 3990-3994.

30. Sek, S.; Chen, M.; Brosseau, C. L.; Lipkowski, J. In Situ STM Study of Potential-Driven Transitions in the Film of a Cationic Surfactant Adsorbed on a Au(111) Electrode Surface. *Langmuir* **2007,** *23* (25), 12529-12534.

31. Miller, D. D.; Bellare, J. R.; Kaneko, T.; Evans, D. F. Control of aggregate structure with mixed counterions in an ionic double-chained surfactant. *Langmuir* **1988,** *4* (6), 1363-1367.

32. Horvath, L.; Mihaljevic, B.; Tomasic, V.; Risovic, D.; Filipovic-Vincekovic, N. Counterion Binding to Ionic Micelles: Effects of Counterion Specificity. *Journal of Dispersion Science and Technology* **2001,** *22* (2), 221-229.

33. Retter, U.; Avranas, A. On Anion-Induced Formation of Hemicylindrical and Hemispherical Surface Micelles of Amphiphiles at the Metal/Electrolyte Interface. *Langmuir* **2001,** *17* (16), 5039-5044.

34. Parsons, R. The electrical double layer: recent experimental and theoretical developments. *Chemical Reviews* **1990,** *90* (5), 813-826.

35. Lipkowski, J. In *Adsorption of molecules at metal electrodes*, Lipkoski, J., Ross, P. N., Eds.; VCH: New York, 1992; pp 171-238.

36. Ocko, B. M.; Magnussen, O. M.; Wang, J. X.; Adic, R. R.; Wandlowski, T. The structure and phase behavior of electrodeposited halides on single-crystal metal surfaces. *Physica B: Condensed Matter* **1996,** *221* (1-4), 238-244.

Chapter 8

Summary and Conclusions

8.1 Summary of Work Presented

The use of interfacial electrochemistry to elucidate certain elementary aspects of nanoparticle formation and stability has been exemplified in this thesis. It has been demonstrated that a study in this direction, i.e. comparing the nanoparticle/solution interface to an analogous electrode/electrolyte system, provides insightful information about the interface of a nanoparticle. Two projects in this regard have been discussed in this thesis: (1) Stability of nanoparticles in different chemical environments by evaluating the halide induced aggregation of dimethylaminopyridine (DMAP) stabilized gold nanoparticles at different solution pHs, (2) Addressing the popular postulate concerning the growth mechanism of quaternary ammonium bromide stabilized gold nanorods by studying the relative adsorption on Au(111) and Au(100) surfaces. While efforts towards accomplishing these two major goals have been the highlight of this thesis, relevant fundamental studies on the adsorbate layer as well as the structure of the electrode surface have also been the subject of discussion in several chapters.

Halide induced aggregation of water dispersible gold nanoparticles stabilized by DMAP was the first system chosen for an electrochemical evaluation and was instigated from the observation that the identity of the halide ions has a strong influence on the extent of aggregation of these gold nanoparticles. Differential capacity measurements on two-dimensional electrode surfaces showed that the aggregation is primarily resultant from the displacement of DMAP molecules by halides ions at the metal/solution

interface. It has been demonstrated that the extent of DMAP replacement by halide ions at the gold/solution interface follows the order $I^->Br^->Cl^->F^-$. A detailed quantitative evaluation of DMAP displacement by halide ions has been done using chronocoulometry, providing the surface concentration of both DMAP and chloride as a function of the electrical state of the gold surface. By comparing this electrochemical data with zeta potential measurements of DMAP stabilized nanoparticles done under identical conditions, an evaluation of the DMAP/halide surface concentration on gold surfaces has been made. This study has also revealed that the positive charge on the nanoparticle does not arise from the adsorbed DMAP layer, but rather from a positive charge on the metal surface itself.

The unique ability of quaternary ammonium bromide surfactants to induce anisotropic growth of gold nanorods has been a scientific curiosity among nanoparticle researchers in recent years. A popular postulate is that the anisotropy of gold nanorods results primarily from the differences in the adsorption of quaternary ammonium surfactant between (100) and (111) faces of the gold nanoparticle during the growth process. Notably, there is as of yet no direct evidence in the literature that provide information about the relative adsorption of these surfactants on different gold facets. Hence this postulate was tested by evaluating the surface concentration of a quaternary ammonium surfactant in the presence of bromide ions on Au(100) and Au(111) surfaces. The results summarized in Chapter 7 show that neither quaternary ammonium ions nor bromide ions show a considerable difference in the surface concentrations between (111) and (100) faces of gold. The comparison was made on a rational potential scale as well as by plotting the surface concentration against the metal charge densities for both surfaces.

The observation that there is no considerable difference in the adsorption of quaternary ammonium bromide between these two faces of gold, suggests that an explanation based on the relative adsorption of quaternary ammonium bromide surfactant on different gold facets is implausible for the mechanism of gold nanorod growth. Alternatively, it could be that the anisotropy results from the relative adsorption of some intermediates formed during the nanoparticle growth process *viz.* a gold-quaternary ammonium complex rather than unembellished quaternary ammonium bromide adsorption. Here no conclusive remark on the growth mechanism of gold nanorods can be unequivocally made and one can only caution that the relative adsorption of "pristine" quaternary ammonium bromide surfactant cannot be the primary factor inducing the anisotropic growth of gold nanorods.

Apart from the interest emanating from the nanoparticle research, understanding the adlayer structure as well as the extent of adsorption at the metal/solution interface itself is a fundamental problem in surface science and interfacial electrochemistry. Against the backdrop of the projects that directly address some issues in the nanoparticle world *viz.* the stability of DMAP stabilized gold nanoparticles as well as anisotropic growth of gold nanorods, three problems of fundamental interest have also been discussed in this thesis. The pH and crystallography dependent orientation of DMAP molecules on gold surfaces has been discussed in Chapter 4. It has been demonstrated that the adsorption states of DMAP on gold surfaces have strong pH dependence. At high pH, DMAP orients horizontally on Au(111) at negative potentials and reorients to a vertical state of adsorption at more positive potentials. At low pH, only the horizontal state of adsorption could be observed on Au(111) within the range of potentials studied.

The stability of the horizontal state of adsorption of DMAP on gold surfaces follows the order Au(111) > Au(100) > Au(poly) in both acidic and basic environments.

A quantitative evaluation of the effect of surface reconstruction on the adsorption of octyltrimethylammonium triflate Au(100) has been discussed in Chapter 5. This work showed that there is no significant difference in the surface concentration of the adsorbed OTA-Tf, between reconstructed and unreconstructed surfaces of Au(100) when the comparison was made on a rational potential scale. In Chapter 6, potential induced restructuring of OTA-Tf on Au(111) surfaces has been demonstrated using chronocapacity and chronocoulometry measurements. The transition of hemicylindrical surface aggregates of OTA-Tf at negative potentials to a vertical adsorbed layer at relatively more positive potentials has been portrayed in this chapter.

8.2 Scope for Further Research

The thought that analysis of the processes happening at the electrode/electrolyte interface can give insightful information about analogous nanoparticle interface can be further explored using *in-situ* microscopy or spectroscopy techniques. Techniques that are popularly being used *in-situ* with electrochemical techniques include reflection absorption spectroscopy (RAS)[1], surface enhanced Raman scattering (SERS),[2] surface enhanced infrared absorption spectroscopy (SEIRS),[3,4] neutron reflectivity studies[5] and electrochemical scanning tunneling microscopy / atomic force microscopy (EC-STM / EC-AFM)[6,7]. These *in-situ* techniques offer complimentary and/or supplementary information about the processes happening at the interface. For instance, a future direction for the investigation on the gold nanorod growth mechanism is to study the relative adsorption of the quaternary ammonium bromide-gold complex on different

crystal planes of gold, which could be done by creating identical reaction conditions in an electrochemical system. Analysis of such a multi-component system cannot be done solely with the simple electrostatic models and the thermodynamics of adsorption as was detailed in this thesis. The use of suitable *in-situ* spectroscopy techniques is viable for this kind of analyses as the information about the species adsorbed at the interface can be obtained directly using these methods. Furthermore, a real-time analysis of the process happening at the nanoparticle interface is extremely challenging, hence the importance of the studies on analogous surfaces is compelling.

Another plausible future direction is to use the information obtained in this thesis regarding surfactant adsorption on electrode surfaces to design new synthetic strategies for nanoparticles. In fact, these investigations on DMAP adsorption on gold surfaces have been helpful for nanoparticle researchers in designing their synthetic strategies[8]. Furthermore, studies on the adsorption of DMAP on gold surfaces have demonstrated that DMAP shows strong crystallography and pH dependent adsorption on gold surfaces. According to the current understanding of anisotropic growth of nanoparticles, the relative adsorption of surfactants on different faces of the nanoparticle during the growth process has a crucial role in determining particle anisotropy. In this view, DMAP stabilized gold nanoparticles synthesized under appropriate experimental conditions may form anisotropic nanostructures. In part, the success of this approach is primarily dependent on the validity of proposed mechanisms of anisotropic growth of the nanoparticles. Nonetheless such an approach for designing synthetic strategies for nanoparticles resulting from a very good understanding of the processes happening at the

interface is essential for developing tailor-made protocols for the shape selective synthesis of anisotropic nanoparticles.

Reference List

1. Zamlynny, V.; Lipkowski, J. Quantitative SNIFTIRS and PM IRRAS of Organic Molecules at Electrode Surfaces. In *Advances in Electrochemical Science and Engineering*, Wiley-VCH Verlag GmbH: 2006; pp 315-376.

2. Tian, Z. Q.; Ren, B. Adsorption and Reaction at Dlectrochemical Interfaces as Probed by Surface-Enhanced Raman Spectroscopy. *Annual Review of Physical Chemistry* **2004,** *55* (1), 197-229.

3. Osawa, M. In-situ Surface-Enhanced Infrared Spectroscopy of the Electrode/Solution Interface. In *Advances in Electrochemical Science and Engineering*, Wiley-VCH Verlag GmbH: 2006; pp 269-314.

4. Rosendahl, S. M.; Danger, B. R.; Vivek, J. P.; Burgess, I. J. Surface Enhanced Infrared Absorption Spectroscopy Studies of DMAP Adsorption on Gold Surfaces. *Langmuir* **2009,** *25* (4), 2241-2247.

5. Majewski, J.; Smith, G. S.; Burgess, I.; Zamlynny, V.; Szymanski, G.; Lipkowski, J.; Satija, S. Neutron reflectivity studies of electric field driven structural transformations of surfactants. *Applied Physics A: Materials Science & Processing* **2002,** *74* (0), s364-s367.

6. Burgess, I.; Jeffrey, C. A.; Cai, X.; Szymanski, G.; Galus, Z.; Lipkowski, J. Direct Visualization of the Potential-Controlled Transformation of Hemimicellar Aggregates of Dodecyl Sulfate into a Condensed Monolayer at the Au(111) Electrode Surface. *Langmuir* **1999,** *15* (8), 2607-2616.

7. Sek, S.; Chen, M.; Brosseau, C. L.; Lipkowski, J. In Situ STM Study of Potential-Driven Transitions in the Film of a Cationic Surfactant Adsorbed on a Au(111) Electrode Surface. *Langmuir* **2007,** *23* (25), 12529-12534.

8. Muench, F.; Kunz, U.; Neetzel, C.; Lauterbach, S.; Kleebe, H. J.; Ensinger, W. 4-(Dimethylamino)pyridine as a Powerful Auxiliary Reagent in the Electroless Synthesis of Gold Nanotubes. *Langmuir* **2010,** *27* (1), 430-435.